Cyclotron Production of Radioscandium from Enriched Calcium Targets for Cancer Imaging Applications

By

Kaelyn V. Becker

A dissertation submitted in partial fulfillment of
the requirements for the degree of

Doctor of Philosophy

(Medical Physics)

at the

UNIVERSITY OF WISCONSIN - MADISON

2023

Date of final oral examination: 17th of May, 2023

The dissertation is approved by the following members of the Final Oral Committee:
Jonathan W. Engle, Associate Professor, Medical Physics
Bryan P. Bednarz, Professor, Medical Physics
Bradley T. Christian, Professor, Medical Physics
Paul A. Ellison, Assistant Professor, Medical Physics
Heather M. Hennkens, Assistant Professor

ACKNOWLEDGMENTS

Throughout my tenure in the Cyclotron group, I have grown as a scientist and as a person in so many ways thanks to all the amazing people around me.

First, thank you to my committee for providing support and guidance throughout this project. Heather Hennkens, thank you for so selflessly answering my email and supporting my pursuits with ^{161}Tb with both your time and resources. To Paul Ellison, thank you for always being available to patiently walk me through tricky problems and offer your advice. Brad Christian, your patience, and advice regarding all my PET-related problems has taught me so much. Bryan Bednarz, thank you for your support on the T32 grant and connecting me with invaluable resources. And to Jon Engle, thank you for your endless hours of patient guidance. You treated me as an independent scientist and taught me to form my own ideas, and that made all the difference.

I was very fortunate to have many mentors beyond my committee members. To Ali Pirasteh, thank you for teaching me that failure is both expected and okay. To Eduardo Aluicio-Sarduy, thank you for the countless hours you spent sharing your knowledge, advice, and support, and showing me that having a positive attitude can fix any bad day. To Jerry, Todd, Jason, and Margarita, thank you for your advice, support, and kindness that made every day coming into the lab a positive experience.

To my incredible lab mates: Aeli, Kendall, Wilson, Molly, and Chris, thank you for your support and friendship. You all made the lab such a warm and welcoming place and never failed to offer your support and empathy for a ruined experiment or bad results (no matter how busy you yourselves were). A special thank you to Aeli and Kendall. You both have been here for the entirety of my graduate career and your friendship is something I am incredibly grateful for.

Thank you so much to my family and friends. To my mom, dad, and brother Jonan, thank you all for your unconditional support. Even if you only followed half of what I was saying, you would always offer to watch my practice talks and provide the encouragement and confidence I needed. And finally, I want to express my truest gratitude to my best friend and love of my life, Tim. Thank you for braving the cold Wisconsin winters, the late-night hours, and for listening to every talk (at least) 5 times to ease my nerves. You being there for rubber-duck debugging, helping me fix my scripts, and reassuring me every step of the way is appreciated more than you'll ever know.

I absolutely could not have done this without all of you, thank you.

ABSTRACT

This dissertation investigates the positron-emitting radioisotopes of scandium: ^{43}Sc ($t_{1/2}$ = 3.891 h, β^+_{mean} = 476 keV) and ^{44g}Sc ($t_{1/2}$ = 3.97 h, β^+_{mean} = 632 keV), and establishes their potential as alternatives to the well-established PET radionuclide ^{68}Ga ($t_{1/2}$ = 67.71 m, β^+_{mean} = 829.5 keV). ^{44g}Sc emits a high energy gamma of 1157 keV (I_γ = 99.9%) which delivers excess dose to patients and may reduce image quality. Thus, ^{43}Sc, which has lower energy gamma emissions (E_γ = 372.9 keV; I_γ = 22.5%), may be preferred in clinical settings. We, and others, have investigated methods to produce ^{44g}Sc, but production of ^{43}Sc has largely been neglected due to the need for deuterons and/or enriched material. ^{43}Sc and ^{44g}Sc's roughly four-hour half-lives allow for biodistribution images > 4 hours post-injection and may be transported to nearby clinics without a cyclotron on-site. Both $^{43/44g}$Sc exist primarily in the +3-oxidation state similar to therapeutic isotopes such as ^{177}Lu and ^{161}Tb. The chemical similarity of scandium to light lanthanides suggests that scandium-labeled agents may have comparable biodistributions to the same agents labelled with ^{177}Lu or ^{161}Tb. This dissertation explores cyclotron production methods for $^{43/44g}$Sc on enriched ^{4x}CaO targets, comparing production yields and radionuclidic purity between several production routes accessible on a small cyclotron. This work also investigates ^{43}Sc's and ^{44g}Sc's potential *in vitro* and *in vivo* for cancer imaging applications. Phantom studies were performed on clinical PET/CT scanners to compare contrast and recovery between ^{43}Sc/^{44g}Sc and other conventionally used positron-emitting radionuclides. Additionally, [$^{43/44g}$Sc]Sc-FAPI-46 and [^{68}Ga]Ga-FAPI-46 PET/CT imaging were compared in a murine model of pancreatic ductal adenocarcinoma. Finally, the uptake and biodistribution of [^{44g}Sc]Sc-DOTA-TATE, [^{68}Ga]Ga-DOTA-TATE and [^{161}Tb]Tb-DOTA-TATE was compared through *in vitro* and *in vivo* PET/CT and SPECT/CT studies to assess theranostic potential in neuroendocrine tumors.

TABLE OF CONTENTS

ACKNOWLEDGMENTS i

ABSTRACT iii

LIST OF TABLES vii

LIST OF FIGURES x

Chapter 1: Introduction 1

1.1 Organization of the Dissertation *6*

Chapter 2: Optimization of Cyclotron Production of $^{43/44g}$Sc 8

2.1 Introduction *8*

2.1.2 Motivation 15

2.2 Materials and Methods *17*

2.2.1 Chemicals 17

2.2.1 Measurement of the ^{42}Ca(d,n)^{43}Sc cross section 20

2.2.2 Target fabrication 24

2.2.3 Production yield measurements 26

2.2.4 HPGe spectrometry 29

2.2.5 Radiochemical isolation of $^{43/44g}$Sc 29

2.2.6 Isotopically enriched calcium recovery 30

2.2.7 Apparent molar activity measurements and trace metals analysis 32

2.3 Results and Discussion *33*

2.3.1 Measurement of the ^{42}Ca(d,n)^{43}Sc cross section 33

2.3.2 CaO target development and current limit tests 38

2.3.3 ^{43}Sc and ^{44g}Sc production yield measurements 39

2.3.4 Radiochemical isolation of $^{43/44g}$Sc 43

2.3.5 Isotopically enriched calcium recovery 44

2.3.6 Apparent molar activity measurements and trace metals analysis 46

2.4 Conclusions *49*

Chapter 3: Investigation of [$^{43/44g}$Sc]Sc-FAPI as a Model to Image PDAC 52

3.1 Introduction *52*

3.1.2 Motivation 56

3.2 Materials and Methods *57*

3.2.1 Chemicals 57
3.2.2 Production and Radiosynthesis of [$^{43/44g}$Sc]Sc-FAPI-46 and [^{68}Ga]Ga-FAPI-46 57
3.2.3 PDAC murine model 60
3.2.4 PET/CT imaging and *ex vivo* biodistribution 62
3.2.5 Partial volume effect investigation 66
3.2.6 Comparison of $^{43/44g}$Sc to conventionally used PET radionuclides on clinical scanners 69
3.3 Results and Discussion *74*
3.3.1 Production and Radiosynthesis of [$^{43/44g}$Sc]Sc-FAPI-46 and [^{68}Ga]Ga-FAPI-46 74
3.2.3 PET/CT imaging and *ex vivo* biodistribution 77
3.2.4 Tumor detection in an orthotopic mouse model 85
3.2.5 Comparison of $^{43/44g}$Sc to conventionally used PET radionuclides on clinical scanners 98
3.4 Conclusions *108*

Chapter 4: Evaluation of the Theranostic Combination of [^{44g}Sc]Sc-DOTA-TATE and [^{161}Tb]Tb-DOTA-TATE 112

4.1 Introduction *112*
4.1.2 Motivation 119
4.2 Materials and Methods *120*
4.2.1 Chemicals 120
4.2.2 DOTA-TATE radiolabeling 120
4.2.3 *In vitro* cell studies 123
4.2.5 Lipophilicity measurements 126
4.2.6 *In vivo* PET/CT and SPECT/CT imaging 126
4.2.7 [^{161}Tb]Tb-DOTA-TATE toxicity 129
4.2.8 [^{161}Tb]Tb-DOTA-TATE dosimetry estimations 129
4.3 Results and Discussion *134*
4.3.1 DOTA-TATE radiolabeling 134
4.3.2 *In vitro* cell studies 136
4.3.3 Lipophilicity measurements 139
4.3.4 *In vivo* PET/CT and SPECT/CT imaging 140
4.3.7 [^{161}Tb]Tb-DOTA-TATE toxicity 149
4.3.8 [^{161}Tb]Tb-DOTA-TATE dosimetry estimations 150

4.4 Conclusions *153*

Chapter 5: Conclusions and future directions 159

Appendix A: Cross section measurements for proton induced reactions on natural lanthanum..... 164

Appendix B: Optimization of automatic chemistry FASTLab module for ^{89}Zr and ^{68}Ga 192

REFERENCES 208

LIST OF TABLES

Table 1: Decay properties and example tracers of conventional PET radionuclides [1]. 1
Table 2: Decay properties of various PET radionuclides [1]. 2
Table 3: Isotopic enrichment (%) of enriched $CaCO_3$ material received from the DOE National Isotope Development Center..... 18
Table 4: Spectrographic analysis of the enriched $^{4x}CaCO_3$ (M = major; T = trace). 20
Table 5: Properties of radionuclides quantified in both experiments [1]..... 23
Table 6: Fit and theoretical half-lives for ^{61}Cu and ^{43}Sc [1]. 36
Table 7: Observed production yields for the 5 routes investigated along with target masses and energy thickness [82, 35]* [92]$^{+}$..... 41
Table 8: Measured beam intercepts for the proton and deuteron beams on a 9.5 mm target. 43
Table 9: Trace metals analysis of an eluted fraction of $^{43/44g}$Sc using MP-AES..... 49
Table 10: Activity concentrations used to fill the partial volume effect phantom..... 68
Table 11: Physical decay characteristics, effective half-life, and positron intensity of the radionuclides used in this study [1]. 70
Table 12: Filled radioactivity for the hot spheres (same solution used for the Derenzo phantom) and background regions derived from dose calibrator and HPGe recorded activities and measured volumes. 71
Table 13: Calibration sample activities measured on the Capintec dose calibrator and an HPGe detector. Correction factors were applied to the dose calibrator-derived activities..... 71
Table 14: Measured distribution coefficients for each radioligand studied in this work..... 76
Table 15: Tumor dimensions for the mice orthotopically implanted with tumors that were allowed to develop for 10, 17, and 25 days. 85
Table 16: Tumor dimensions for the orthotopically implanted tumors permitted to grow for 4.5 weeks..... 94
Table 17: Tumor dimensions of the two mice with 9-week orthotopically injected tumors. 96
Table 18: Ex vivo tumor uptake for each tumor model for mice injected with [^{68}Ga]Ga-FAPI-46 and [^{44g}Sc]Sc-FAPI-46. 98
Table 19: Background recovery coefficients for each radionuclide on the two GE PET/CT scanners investigated here..... 101

Table 20: Scatter fraction for each radionuclide on both GE PET/CT scanners. 103
Table 21: Fit half-life for the 373 keV and 511 keV peaks. 106
Table 22: Fit decay parameters for the biexponential fit of the 511 keV peak. 107
Table 23: Chemical properties of several +3 metal ions [146]. 117
Table 24: Average and maximum positron range in tissue for ^{68}Ga and ^{44g}Sc [150]. 119
Table 25: Organ masses and S-values used for ^{161}Tb dosimetry estimations [162, 160, 159]. . 134
Table 26: Receptor density measured using [^{44g}Sc]Sc-DOTA-TATE for both cell lines investigated here. 137
Table 27: Measured AR42J receptor binding affinity for [^{68}Ga]Ga-DOTA-TATE, [^{44g}Sc]Sc-DOTA-TATE, and [^{161}Tb]Tb-DOTA-TATE..... 138
Table 28: Log$D_{7.4}$ values for the three radiotracers investigated in this work. 140
Table 29: Time-dependent tissue uptake of [^{68}Ga]Ga-DOTA-TATE in AR42J tumor bearing mice. 142
Table 30: Time-dependent tissue uptake of [^{44g}Sc]Sc-DOTA-TATE in AR42J tumor bearing mice. 142
Table 31: Time-dependent tissue uptake of [^{161}Tb]Tb-DOTA-TATE in AR42J tumor-bearing mice. 143
Table 32: Description of each element in the stacked target 169
Table 33: Tabulated nuclear decay data used in this work [1]. *An error equivalent to the magnitude of the last digit provided was assumed when no uncertainty was provided. 173
Table 34: Tabulated measured cross sections for all Cerium radioisotope excitation functions. 173
Table 35: Tabulated measured cross sections for all remaining radioisotope excitation functions. 174
Table 36: Effects on activity distribution from sequence optimization. 198
Table 37: Assessment of the final ^{89}Zr product from the FASTLab separation (n = 20). 199
Table 38: Microwave plasma – atomic emission spectrometry trace metals analysis of ^{89}Zr from FASTLab separation procedure (n = 15). 199
Table 39: Activity distribution for each sequence optimization step..... 204
Table 40: Yield and apparent molar activity of final ^{68}Ga produced from FASTLab separation. 205

Table 41: Microwave plasma – atomic emission spectrometry trace metals analysis of ^{89}Zr from FASTLab separation procedure (n = 4). 206

LIST OF FIGURES

Figure 1: Nuclear reactions for proton and deuteron bombardment of enriched $^{42/43/44}$Ca targets to produce ^{43}Sc and ^{44g}Sc. 9

Figure 2: Experimentally measured and predicted values for ^{44g}Sc cross sections on calcium targets [28-31]. 10

Figure 3: Experimentally measured and predicted values for ^{43}Sc cross sections on calcium targets [28-29, 31-32]..... 10

Figure 4: Experimentally measured and predicated values for ^{44g}Sc cross sections on titanium targets [28, 202]. 12

Figure 5: Experimentally measured and predicted values for ^{43}Sc cross sections on titanium targets [28-29, 202-213]..... 13

Figure 6: Experimentally measured and predicted cross sections for the ^{42}Ca(d,n)^{43}Sc reaction [32, 82, 31, 88]. 16

Figure 7: Sample ^{nat}CaO target on nickel backing (left) and copper backing (right) mounted to aluminum frame. 20

Figure 8: **^{nat}**CaO targets evaporated on copper foil backings and mounted to aluminum frames. 21

Figure 9: Kapton®-covered ^{nat}CaO target on copper backing. 22

Figure 10: (A) $CaCO_3$ powder in graphite crucible; (B) Crucible placed in quartz tube under argon gas flow lowered into preheated vertical tube furnace (900°C); (C) CaO powder in graphite crucible following conversion; (D) CaO powder placed in pocket of niobium target; (E) Hydraulic press forming the target; (F) Pressed CaO target. 25

Figure 11: Niobium crucible containing approximately 60 mg of pressed CaO powder (left) and covered with 50 μm niobium cover foil (right). 26

Figure 12: Cross sections for the ^{42}Ca(d,n)^{43}Sc and ^{43}Ca(d,n)^{44g}Sc reactions [82, 87, 88]. Energy range investigated is highlighted in gray. 27

Figure 13: Cross sections for the ^{43}Ca(p,n)^{43}Sc and ^{44}Ca(p,n)^{44g}Sc reactions [35, 87, 36, 89, 88]. Energy range investigated is highlighted in gray. 28

Figure 14: CaO target that was left exposed to ambient room conditions overnight. 28

Figure 15: Ca/Sc separation strategy utilizing Eichrom branched DGA resin. 30

Figure 16: Calcium recycling procedure: (A) CaO target in dissolution block; (B) Branched DGA resin; (C) Dissolved calcium in HCl with addition of saturated ammonium carbonate solution; (D) $CaCO_3$ precipitating out of solution; (E) Centrifuged $CaCO_3$ pellet; (F) Dried $CaCO_3$; (G) Recycled $CaCO_3$ in graphite crucible; (H) CaO powder; (I) Hydraulic press forming CaO target in niobium crucible; (J) Recycled CaO target. 31
Figure 17: (Left) HPGe spectrum of the nickel-backed ^{nat}CaO target irradiated with 3 MeV deuterons. (Right) Zoomed in spectrum showing the 373 keV peak from ^{61}Cu and ^{43}Sc decay.. 33
Figure 18: (Left) $^{60}Ni(d,n)^{61}Cu$ cross section measured in this work and IAEA recommended cross sections. (Right) $^{42}Ca(d,n)^{43}Sc$ cross section measured from subtracted 373 keV peak plotted with TALYS-based TENDL_19 predictions and measured cross section data from Carzaniga et al. [33] [28]. 34
Figure 19: Decay curves for ^{61}Cu and ^{43}Sc on each nickel-backed target. 35
Figure 20: Copper-backed ^{nat}CaO target 12 covered with Kapton® tape before (left) and after (center) irradiation. (Right) Autoradiograph of target 12 illustrating damaged target material. .. 36
Figure 21: $^{42}Ca(d,n)^{43}Sc$ cross sections measured in this work alongside TENDL-19 predictions and previously reported measurements [33] [28]. 37
Figure 22: Peak pressure on the target as the current was increased (left). ^{nat}CaO (middle) and $^{nat}CaCO_3$ (right) targets immediately after 20 μA proton irradiation. 39
Figure 23: Activities of each radioisotope of scandium that was present in the full target at EoB for each of the 5 reaction routes that were investigated..... 40
Figure 24: Measured production yields compared to literature reported cross sections fitted to TENDL_19 predicted curves [82, 35, 87, 36, 89, 88]. 42
Figure 25: Elution profile for the Ca^{+2}/Sc^{+3} radiochemical separation used in this work. Overall eluted fraction remains consistent (right) but activity distribution in each of the 4 eluted fractions varies with each experiment (left)..... 44
Figure 26: Calcium elution profile from rinses of 6 M HCl off a loaded b-DGA column..... 45
Figure 27: Eppendorf vials used for drying down recycled $CaCO_3$. (A and B) Dried $(NH_4)_2CO_3$ crystals forming on walls of vial. (C) Properly decanted $CaCO_3$ drying to powdery substance.. 46
Figure 28: Autoradiography of the titration with a fixed amount of ^{44g}Sc activity mixed with increasing concentrations of DOTA run in EDTA. 47
Figure 29: Radio-HPLC chromatogram of [^{44g}Sc]Sc-DOTA-TATE. 48

Figure 30: PDAC tumor microenvironment (created with BioRender.com)..... 55
Figure 31: Labelling procedure for [$^{43/44g}$Sc]Sc-FAPI-46. 58
Figure 32: Labeling procedure for [^{68}Ga]Ga-FAPI-46. 59
Figure 33: Linear channel, spherical partial volume effect phantom purchased from Phantech. (Left) PVE phantom filled with dye; (center) CAD drawing; (right) PET scan of the phantom filled with ^{68}Ga. 67
Figure 34*:* Setup orientation of the spherical phantom (left) and Derenzo phantom (right) on the beds of the PET/CT scanners used in this study. 72
Figure 35: [$^{43/44g}$Sc]Sc-FAPI-46 labeling dependence on pH (left) and time (right). 74
Figure 36: Radio-HPLC traces for [^{68}Ga]Ga-FAPI-46 (left) and [$^{43/44g}$Sc]Sc-FAPI-46 (right). [^{44g}Sc]Sc-FAPI-46 has an identical radio-HPLC trace to [^{43}Sc]Sc-FAPI-46. 75
Figure 37: Radio-HPLC chromatogram of the [^{43}Sc]Sc-FAPI-46 reaction at 0 h (left), 4 h (center), and 12 h (right) in PBS. 75
Figure 38: MIP PET/CT images of a representative mouse injected with [^{68}Ga]Ga-FAPI-46 (top left and bottom left), [^{43}Sc]Sc-FAPI-46 (top right), and [^{44g}Sc]Sc-FAPI-46 (bottom right). 77
Figure 39: MIP PET/CT images of a tumor-bearing mouse and Matrigel® control mouse injected with [^{44g}Sc]Sc-FAPI-46 (left) and [^{68}Ga]Ga-FAPI-46 (right) at 1 h p.i. 78
Figure 40: (A-C) Time dependent uptake of [^{68}Ga]Ga-FAPI-46 (A), [^{43}Sc]Sc-FAPI-46 (B), and [^{44g}Sc]Sc-FAPI-46 (C) in organs of interest. (D-E) Time dependent uptake of [^{68}Ga]Ga-FAPI-46 (green diamond), [^{43}Sc]Sc-FAPI-46 (blue circle), and [^{44g}Sc]Sc-FAPI-46 (orange square) in the tumor (D) and kidneys (E) at each imaging time-point. (F) Image-derived %IA/g in each tissue at 2 h p.i. for [^{68}Ga]Ga-FAPI-46 (green hash, right-most), [^{43}Sc]Sc-FAPI-46 (blue hash, left-most), [^{44g}Sc]Sc-FAPI-46 (orange dots, center)..... 79
Figure 41: (A-C) Ex-vivo biodistribution verification for each radiotracer investigated here. (D-F) PET/CT ROI-derived %IA/g adjusted for partial volume effect compared to ex-vivo biodistribution data. 80
Figure 42: Partial volume effect phantom PET images for ^{68}Ga and ^{44g}Sc (left). Recovery coefficient versus sphere diameter for ^{68}Ga and ^{44g}Sc (right). 81
Figure 43: Uptake in emptied stomach and intestines (red hash) and full intestines and stomach (blue dots). Tumor uptake was included to ensure comparable experimental conditions. 84

Figure 44: MIP PET/CT images of [^{44g}Sc]Sc-FAPI-46 injected mice bearing orthotopically implanted tumors that have developed for 10 days. 87
Figure 45: MIP PET/CT images of [^{44g}Sc]Sc-FAPI-46 injected mice bearing orthotopically implanted tumors that have developed for 17 days. 88
Figure 46: MIP PET/CT images of [^{44g}Sc]Sc-FAPI-46 injected mice bearing orthotopically implanted tumors that have developed for 25 days. 89
Figure 47: A representative mouse bearing orthotopically implanted tumors injected with [^{68}Ga]Ga-FAPI-46 (left) followed by [^{44g}Sc]Sc-FAPI-46 (right) one day later. 90
Figure 48: Ex-vivo biodistribution of [^{44g}Sc]Sc-FAPI-46 in mice (n = 6) bearing orthotopically implanted tumors. 91
Figure 49: Radio-HPLC chromatogram of the pre-injection formulation for the 4.5-week tumor development mouse cohort. 93
Figure 50: Tumor uptake in each mouse from the 4.5-week tumor development cohort measured through ex-vivo biodistribution using a calibrated gamma counter. 94
Figure 51: MIP PET/CT images of the mice bearing orthotopically implanted tumors allowed to develop for 9 weeks. 95
Figure 52: Ex-vivo biodistribution of [^{44g}Sc]Sc-FAPI-46 in an orthotopic model versus the heterotopic model..... 97
Figure 53: Cross-sectional PET/CT image of the Derenzo phantom filled with each radionuclide and scanned on the GE Discovery 710. 99
Figure 54: Calculated contrast measured from the Derenzo phantom filled with each radionuclide and scanned on the GE Discovery 710 (left) and GE Discovery MI (right)..... 100
Figure 55: Cross-sectional PET/CT image of the Derenzo phantom filled with each radionuclide and scanned on the GE Discovery MI. 100
Figure 56: Cross-section image of the spherical phantom filled with each radionuclide and scanned on the GE Discovery MI. 102
Figure 57: Cross-sectional image of the spherical phantom filled with each radionuclide and scanned on the GE Discovery 710. 102
Figure 58: Calculated recovery coefficients for each sphere diameter for all the radionuclides investigated here on the GE Discovery 710 (left) and GE Discovery MI (right). 103

Figure 59: Recovery coefficient versus sphere diameter for the GE Discovery 710 and MI compared to the Siemens Biograph Horizon PET/CT. 104
Figure 60: HPGe spectra of final ^{43}Sc formulation used to fill the phantoms. 105
Figure 61: Decay data for the 373 keV and 511 keV peak with exponential fits. 106
Figure 62: Biexponential fit of the decay of the 511 keV peak. 107
Figure 63: Decay of signal measured by the xenon gas well counter coupled with a Keithley 6517B electrometer and the corresponding fit. 108
Figure 64: Radiopharmaceutical design composed of a radionuclide labeled with a chelator and a linker that attaches the radiometal to a targeting molecule. 113
Figure 65: Synthesis procedure for [M]-DOTA-TATE, where [M] = ^{68}Ga, ^{44g}Sc, or ^{161}Tb. 122
Figure 66: Binding saturation assay procedure for determining receptor density and binding affinity (created with BioRender.com). 124
Figure 67: Internalization experimental workflow (created with BioRender.com)..... 125
Figure 68: Tumor xenograft and radioligand injection (created with BioRender.com). 127
Figure 69: Autoradiography image of a TLC plate spotted with free ^{161}Tb (left lane) and [^{161}Tb] Tb-DOTA-TATE labeled at 3.7 MBq/nmol (10 nmol/mCi) DOTA-TATE..... 135
Figure 70: [^{161}Tb]Tb-DOTA-TATE stability in PBS and human serum. 136
Figure 71: Radio-HPLC chromatograms of [^{161}Tb] Tb-DOTA-TATE reaction (A), stability in PBS after 24 h (B), and stability in human serum after 24 h (C). 136
Figure 72: Binding saturation assay results along with their fits. 138
Figure 73: In-vitro internalization of bound M-DOTA-TATE into AR42J cells versus time for all three M-DOTA-TATE ligands investigated here. 139
Figure 74: Uptake of [^{68}Ga]Ga-DOTA-TATE, [^{44g}Sc]Sc-DOTA-TATE, and [^{161}Tb]Tb-DOTA-TATE in several organs of interest. 144
Figure 75: (Top row) Time-dependent uptake of the three radio-lignads investigated here determined from ROI analysis on CT-attenuation corrected PET and SPECT images. (Bottom row) Ex-vivo biodistribution of the corresponding radio-ligand measured with a calibrated gamma counter. 145
Figure 76: Activity recovery versus feature diameter. 146
Figure 77: PVE-corrected uptake from PET/CT and SPECT/CT images compared to ex-vivo-derived data. 146

Figure 78: MIP PET/CT imaged of AR42J tumor-bearing mice injected with [^{68}Ga]Ga-DOTA-TATE (left) and [^{44g}Sc]Sc-DOTA-TATE (right). Scale bars are given in units of Bq/mL. 147
Figure 79: MIP SPECT/CT images of [^{161}Tb]Tb-DOTA-TATE uptake in AR42J tumor-bearing mice. 148
Figure 80: White blood cell counts for two mice before and after injection of [^{161}Tb]Tb-DOTA-TATE. 150
Figure 81: Estimated [^{161}Tb]Tb-DOTA-TATE dose to female human organs based on [^{68}Ga]Ga-DOTA-TATE and [^{44g}Sc]Sc-DOTA-TATE PET/CT imaging and [^{161}Tb]Tb-DOTA-TATE SPECT/CT imaging. 152
Figure 82: [^{161}Tb]Tb-DOTA-TATE dose estimates for female human organs at 4 h (left) and 8 h (right) p.i. 153
Figure 83: Aluminum foil affixed to an acrylic holder with 3M acrylic lined Kapton polyimide film tape. 166
Figure 84: Fluences before (left) and after (right) minimization. 176
Figure 85: Result of varying exit energy of the protons to minimize the variance between the predicted fluences among the 5 monitor reactions measured. 176
Figure 86: Experimental and theoretical cross sections for ^{132}Ce [88]. 178
Figure 87: Experimental and theoretical cross sections for ^{133m}Ce [188, 88]. 179
Figure 88: Experimental and theoretical cross sections for ^{134}Ce [188, 189, 88]. 180
Figure 89: Experimental and theoretical cross sections for ^{135}Ce [188, 189, 88]. 181
Figure 90: Experimental and theoretical cross sections for ^{137}Ce [188, 189, 88]. 182
Figure 91: Experimental and theoretical cross sections for ^{137m}Ce [188, 189, 88]. 183
Figure 92: Experimental and theoretical cross sections for ^{139}Ce [188, 189, 190, 88]. 185
Figure 93: Experimental and theoretical cross sections for ^{135}La [188, 189, 88]. 185
Figure 94: Experimental and theoretical cross sections for ^{131}Ba [188, 88]. 186
Figure 95: Experimental and theoretical cross sections for ^{133}Ba [188, 189, 88]. 187
Figure 96: Experimental and theoretical cross sections for ^{133m}Ba [188, 189, 88]. 188
Figure 97: Experimental and theoretical cross sections for ^{132}Cs [188, 189, 88]. 189
Figure 98: Yields calculated from a combination of experimental and theoretical data. 190
Figure 99: ARTMS QiS™ target transfer and dissolution system (left) and GE FASTlab (right). 193

Figure 100: FASTLab cassette for the $^{nat}Y/^{89}Zr$ radiochemical separation, labeling key components. 194
Figure 101: Spot-welded ^{nat}Y foil target on a tantalum backing. 194
Figure 102: Separation scheme used for radiochemical isolation of ^{89}Zr from Y targets. 196
Figure 103: Activity distribution of the final, optimized $^{nat}Y/^{89}Zr$ FASTLab separation sequence. 197
Figure 104: HPGe spectrum of a final ^{89}Zr product sample. No detectable peaks from ^{88m}Zr were present. 200
Figure 105: Electroplated ^{68}Zn target. 201
Figure 106: Final $Zn/^{68}Ga$ FASTLab sequence. 202
Figure 107: $Zn/^{68}Ga$ FASTLab cassette layout on the GE FASTLab developer platform software. 203
Figure 108: Activity distribution of the final, optimized FASTLab $Zn/^{68}Ga$ separation sequence. 205
Figure 109: Sample ^{68}Ga HPGe spectrum of the final product vial. 207

Chapter 1: Introduction

Positron emission tomography (PET) imaging collects valuable physiological information for oncology, cardiology, neurology, and other areas of medicine. When PET is used alongside anatomical imaging modalities such as computed tomography (CT) and magnetic resonance imaging (MRI), physiological properties such as receptor expression, uptake, and clearance of a molecule can be investigated in addition to anatomical features such as size and location. For decades, PET imaging primarily utilized four main cyclotron-produced β^+-emitters: ^{11}C, ^{13}N, ^{15}O, and ^{18}F (see Table 1).

Radionuclide	**Half-life**	**β^+ BR (%)**	**β^+ Avg. Energy (keV)**	**Tracers**	**Applications**
^{11}C	1221.8(8) s	99.7669(25)	385.7(4)	$[^{11}C]C_5H_{14}NO^+$ (Choline) $[^{11}C]C_2H_3O_2^-$ (Acetate)	Prostate cancer, cardiology
^{13}N	9.965(4) min	99.8036(20)	491.82(12)	$[^{13}N]NH_3$ (Ammonia)	Cardiac, brain, liver
^{15}O	122.24(16) s	99.003(10)	735.28(23)	$[^{15}O]OH_2$ (Water)	Blood flow and volume
^{18}F	109.77(5) min	96.73(4)	249.8(3)	$[^{18}F]$FDG (Flurodeoxyglucose)	Oncology

Table 1: Decay properties and example tracers of conventional PET radionuclides [1].

The potential of PET imaging extends beyond radionuclides listed in Table 1. In the past 20 years, the rate of new publications on PET radiohalogens other than ^{18}F and radiometals has been steadily increasing [2]. Ligands such as somatostatin analogues and prostate-specific membrane antigen- (PSMA) targeting agents can be labeled with radiometals through a bifunctional chelator that binds to the radiometal and has a second terminus that can form a covalent bond with the molecule of interest [3]. Radiometals typically have longer half-lives (Table 2) than the traditional PET radionuclides listed in Table 1 making them compatible with long biological half-life (> 1 d) molecules such as antibodies [4].

Radionuclide	**Half-life**	**β^+ BR (%)**	**β^+ Avg. Energy (keV)**
^{43}Sc	3.891(12) h	88.1(8)	476(6)
^{44g}Sc	3.97(4) h	94.27(5)	632.0(10)
^{51}Mn	46.2(1) min	97.09(3)	962.8(5)
^{52g}Mn	5.591(3) d	29.4(4)	242(5)
^{55}Co	17.53(3) h	76(3)	570(4)
^{61}Cu	3.336(10) h	61(4)	500(5)
^{64}Cu	12.7006(20) h	17.49(15)	278(3)
^{66}Ga	9.49(3) h	57(4)	1750(18)
^{68}Ga	67.71(8) min	88.91(9)	829.5(13)
^{69}Ge	39.05(10) h	24(5)	490(15)
^{72}As	26.0(1) h	87.8(2.2)	1170(5)
^{76}Br	16.2(2) h	55(3)	1180(9)
^{86}Y	14.74(2) h	31.9(2.1)	660(8)
^{89}Zr	78.41(12) h	22.74(0.24)	396(6)
^{124}I	4.1760(3) d	22.7(1.3)	820(7)

Table 2: Decay properties of various PET radionuclides [1].

The following properties are desired for ideal imaging agents: high specificity and binding affinity, fast clearance from non-target tissues, low toxicity, high stability *in vivo*, favorable physical decay characteristics, and accessibility. An ideal imaging agent has high binding affinity for target regions to increase the signal from the target of interest (high sensitivity). In addition, the tracer should have high specificity to reduce background signal and toxicity to healthy structures. Radiopharmaceuticals are typically cleared through the kidneys (through the renal pathway), the liver (through the hepatobiliary pathway), or through both depending on properties such as their lipophilicity, charge, size, etc. [5]. Rapid clearance of a tracer from the blood and off-target tissues both reduces dose to the patient and decreases the background signal, increasing tissue to background ratios. The amount of imaging agent needed for diagnostic quality images should also not pose biological harm to the patient (this amount varies depending on the radionuclide and targeting molecule). Additionally, the radiopharmaceutical must be stable *in vivo* before reaching the target. The biological half-life of peptides and antibodies can range from minutes to days, so the stability of the radiopharmaceutical in the presence of plasma and enzymes in target tissues needs to exceed the circulation time of the radiopharmaceutical [6]. The half-life of the radionuclide must also be suitable for the circulation time of the molecule. Longer-lived radionuclides ($t_{1/2}$ > 12 h) are necessary for longer circulating molecules such as antibodies but shorter half-lives are easier to handle from a radioactive waste and patient safety perspective. The emission of prompt gammas and the energy of the emitted positron also affect PET image quality. Higher positron energies reduce the image resolution, and the emission of prompt gammas increases patient exposure and scatter, which degrades image quality. Finally, for radiopharmaceuticals to be clinically feasible, the radionuclide must be accessible. Short-lived ($t_{1/2}$ < 1 h) cyclotron-produced radionuclides are limited to facilities with on-site cyclotrons

(or local distribution), but longer-lived radionuclides may be distributed to regional facilities without a cyclotron on site. Radionuclides producible via generators further expands their accessibility.

In addition to diagnostic applications, pairing chemically similar radionuclides as radiolabels of diagnostic and therapeutic drugs ("theranostics") is an increasingly popular approach to cancer therapy and has accelerated the use of PET radiometals. Imaging of ^{68}Ga- ($t_{1/2}$ = 67.71 min; β^{+}_{Eavg} = 829.5 keV; $\beta^{+}_{intensity}$ = 88.91%) labeled somatostatin analogs in neuroendocrine tumors and PSMA-targeting ligands in prostate cancer has been used to monitor response to ^{177}Lu- ($t_{1/2}$ = 6.644 d; β^{-}_{Eavg} = 133.6 keV; $\beta^{-}_{intensity}$ = 100.0%) based therapy [7, 8, 9], to select potential patients for treatment [10], and to improve lesion detection relative to ^{177}Lu single photon emission tomography (SPECT) [11]. However, ^{68}Ga's high average positron energy and short half-life limit its clinical applications. Because ^{68}Ga's half-life is too short to transport, clinics require an on-site cyclotron or ^{68}Ge/^{68}Ga generator to provide patient doses while ^{68}Ga's high positron energy reduces detectability of small lesions compared to radionuclides with shorter positron ranges.

Peptide receptor radionuclide therapy (PRRT) takes advantage of overexpressed receptors on tumor cell surfaces relative to healthy tissue to deliver dose preferentially to the site of disease. However, patient populations have varying degrees of receptor expression, impacting the dose delivered to the tumor given a standard injection. For example, Lutathera® ([^{177}Lu]Lu-DOTA-TATE) is a somatostatin receptor targeting drug that is used to treat gastroenteropancreatic neuroendocrine tumors that are positive for the hormone receptor somatostatin [12]. Studies measuring patient-specific dose to several organs from [^{177}Lu]Lu-DOTA-TATE therapy have concluded that there is deviation in tracer uptake between patients [13, 14]. Thus, while

radiopharmaceutical therapy is currently administered without personalized dosimetry, several published works support the use of pre-treatment dosimetry to prescribe individualized treatments [14, 15, 16]. Studies have shown that uptake of [^{68}Ga]Ga-DOTA-TATE is weakly correlated to absorbed [^{177}Lu]Lu-DOTA-TATE dose at 1 h post-injection (p.i.) and can be predictive of treatment response [17, 18]. However, the short half-life of ^{68}Ga limits its use for accurately predicting absorbed dose to target and non-target tissues for [^{177}Lu]Lu-DOTA-TATE therapy because the tumor uptake of [^{177}Lu]Lu-DOTA-TATE peaks at several hours p.i. when [^{68}Ga]Ga-DOTA-TATE imaging is no longer feasible [17].

Radioisotopes of scandium are promising alternatives for ^{68}Ga. Two positron-emitting radioisotopes are currently considered for clinical use: ^{43}Sc ($t_{1/2}$ = 3.891 h; β^+_{mean} = 476 keV; $\beta^+_{intensity}$ = 88.1%) and ^{44g}Sc ($t_{1/2}$ = 3.97 h; β^+_{mean} = 632 keV; $\beta^+_{intensity}$ = 94.27%) [19, 20, 21]. Both ^{43}Sc and ^{44g}Sc have longer half-lives than ^{68}Ga, facilitating imaging at later time points p.i. past the peak tumor uptake of ^{177}Lu-labeled somatostatin receptor targeting agents and providing more potential for dosimetric evaluation [17]. The ionic radius and coordination behavior of scandium are also better matched to lutetium compared with gallium [22] making it a viable diagnostic analogue for ^{177}Lu-based radiopharmaceuticals. Furthermore, ^{43}Sc and ^{44g}Sc can be paired with ^{47}Sc ($t_{1/2}$ = 3.3492 d; β^-_{mean} = 162 keV; $\beta^-_{intensity}$ = 100.0%), which emits β^- particles suitable for therapy, forming a chemically identical theranostic pair.

Production of ^{44g}Sc is possible through proton irradiation (5 – 20 MeV) of natural metallic calcium targets [23, 24], but longer-lived ($t_{1/2}$ = 44 h – 84 d) radioisotopes of scandium (^{46}Sc, ^{47}Sc, ^{48}Sc) are co-produced due to the many stable isotopes of calcium (^{40}Ca, 96.94%; ^{42}Ca, 0.647%; ^{43}Ca, 0.135%; ^{44}Ca, 2.09%; ^{46}Ca, 0.004%; ^{48}Ca, 0.187%) [1]. To produce more radionuclidically pure ^{43}Sc or ^{44g}Sc with proton or deuteron irradiations, isotopically enriched

targets are necessary. Enriched target material facilitates several reaction routes with either proton or deuteron bombardment: ^{42}Ca(d,n)^{43}Sc, ^{43}Ca(p,n)^{43}Sc, ^{43}Ca(d,n)^{44g}Sc, ^{44}Ca(p,n)^{44g}Sc, ^{44}Ca(p,2n)^{43}Sc, and ^{44}Ca(d,2n)^{44g}Sc. Current published literature on these production routes will be discussed in further detail in Chapter 2.

The goal of this work is to investigate and optimize the possible production routes of both ^{43}Sc and ^{44g}Sc using enriched calcium targets irradiated on a small cyclotron capable of accelerating 16 MeV protons and 8 MeV deuterons (Chapter 2) and to compare their image qualities on clinical PET/CT scanners. Additionally, *in vivo* and *in vitro* studies with $^{43/44g}$Sc-labelled compounds for cancer imaging applications are presented in Chapters 3 and 4.

1.1 Organization of the Dissertation

Chapter 2 reviews currently employed production pathways and radiochemical isolation strategies for ^{43}Sc and ^{44g}Sc production. The radionuclidic purity, production yields, and accessibility of the ^{43}Sc and ^{44g}Sc reaction routes possible on the University of Wisconsin, Madison's GE PETtrace cyclotron were compared and measured: ^{42}CaO(d,n)^{43}Sc, ^{43}CaO(p,n)^{43}Sc, ^{43}CaO(d,n)^{44g}Sc, ^{44}CaO(p,n)^{44g}Sc, and ^{44}CaO(p,2n)^{43}Sc. Additionally, an efficient procedure to convert $CaCO_3$ to CaO, a material that can withstand higher power density irradiations, along with a radiochemical isolation procedure for $^{43/44g}$Sc using extraction chromatography and a method for efficient recovery of enriched calcium target material is presented.

Chapter 3 discusses the potential for scandium-labeled fibroblast activation protein inhibitors ([^{43}Sc]Sc-FAPI-46 and [^{44g}Sc]Sc-FAPI-46) to image pancreatic ductal adenocarcinoma in a mouse model. The mechanism of FAP-targeting and benefits of FAPI-based PET imaging over standard-of-care procedures are discussed. An *in vivo* study comparing the potential of ^{68}Ga-,

^{43}Sc-, and ^{44g}Sc-labelled FAPI for imaging pancreatic ductal adenocarcinoma via PET/CT imaging in a heterotopic and an orthotopic murine model is described. Chapter 3 also covers a phantom study on two clinical PET/CT scanners using clinical spherical and Derenzo phantoms filled with a variety of positron-emitting radionuclides (^{18}F, ^{64}Cu, ^{68}Ga, ^{43}Sc, ^{44g}Sc, and a mixture of $^{43/44g}$Sc). Recovery coefficients and contrast were compared across the different radionuclides on both scanners.

Chapter 4 reviews neuroendocrine tumor targeting with ^{177}Lu and discusses the possibility of ^{161}Tb-based treatment. Studies investigating ^{44g}Sc's potential to act as an imaging analogue for ^{177}Lu in PSMA-617 based therapy and imaging are discussed as well. The work in Chapter 4 outlines the investigation of ^{68}Ga's and ^{44g}Sc's potential to act as an imaging analogue for the therapeutic radionuclide ^{161}Tb when labelled with the somatostatin receptor targeting agent DOTA-TATE. Lipophilicity measurements along with receptor affinity and internalization studies with AR42J cells (derived from rat pancreatic tumors) are reported for each radiotracer. Additionally, biodistribution at various timepoints were compared via PET/CT imaging for [^{68}Ga]Ga- and [^{44g}Sc]Sc-DOTA-TATE and SPECT/CT imaging for [^{161}Tb]Tb-DOTA-TATE. [^{161}Tb]Tb-DOTA-TATE dosimetry estimates to female human organs using the murine biodistribution data from [^{68}Ga]Ga-DOTA-TATE, [^{44g}Sc]Sc-DOTA-TATE, and [^{161}Tb]Tb-DOTA-TATE imaging are also discussed.

Appendix A presents the cross-section measurements for radionuclides produced from proton bombardment of natural lanthanum targets at the Los Alamos National Laboratory. Appendix B describes an automated chemistry for the separation of ^{nat}Y/^{89}Zr and $^{nat/68}$Zn/^{68}Ga using a GE FASTLab module and ARTMS QiS™ target transfer and dissolution system.

Chapter 2: Optimization of Cyclotron Production of $^{43/44g}$Sc

2.1 Introduction

Natural calcium is comprised of ^{40}Ca (96.94%), ^{42}Ca (0.647%), ^{43}Ca (0.135%), ^{44}Ca (2.09%), ^{46}Ca (0.004%), and ^{48}Ca (0.187%) [1]. While natural calcium is predominantly ^{40}Ca, proton or deuteron bombardment of ^{40}Ca produces radionuclides with half-lives on the order of milliseconds that will decay to negligible quantities under 10 minutes. Thus, ^{44g}Sc can be produced through proton bombardment of natural calcium targets (which are both widely accessible and relatively inexpensive) due to the large fraction of ^{44}Ca compared to other stable isotopes of calcium [23, 25]. However, irradiating calcium targets with protons co-produces the isomer ^{44m}Sc ($t_{1/2}$ = 58.61 h; IT = 98.80% , ε = 1.20%, 86.74% 271.241 keV γ) and other longer-lived radioisotopes of scandium such as ^{46}Sc ($t_{1/2}$ = 83.79 d; β^-_{mean} = 111.8 keV; $\beta^-_{intensity}$ = 100%; 99.99% 1120.5 keV γ), ^{47}Sc ($t_{1/2}$ = 3.35 d; β^-_{mean} = 162.0 keV; $\beta^-_{intensity}$ = 100%; 68.3% 159.38 keV γ), and ^{48}Sc ($t_{1/2}$ = 43.71 h; β^-_{mean} = 220.5 keV; $\beta^-_{intensity}$ = 100%; 100% 1312.12 keV γ) that cannot be chemically separated from $^{43/44g}$Sc.

The presence of small quantities of $^{46/47/48}$Sc is of negligible concern when ^{44g}Sc is labeled with high *in vivo* stability, short biological half-life molecules such as peptides (fast clearance from the body) because the $^{46/47/48}$Sc will clear from the body with the targeting molecule. However, if the radiopharmaceutical is not stable *in vivo*, or has a long biological half-life (such as antibodies), there is potential for the $^{46/47/48}$Sc to become detached from the targeting molecule and accumulate in off-target tissue. Benabdallah et. al and Valdovinos showed that $^{44g}ScCl_3$ primarily accumulated in the liver, kidneys, and cardiac structures such as the blood, heart, aorta, and vena cava [26, 27]. $^{44g}ScCl_3$ had longer circulation characteristics compared to complexed ^{44g}Sc (such as ^{44g}Sc-citrate and ^{44g}Sc-NODAGA) indicative of plasma binding [26]. While

complexed ^{44g}Sc cleared through the kidneys rapidly, free $^{44g}ScCl_3$ was slowly cleared through the liver. Because $^{46/47/48}$Sc are isotopes of ^{44g}Sc, they would also accumulate in the liver and kidneys and deliver additional dose to these off-target healthy tissues.

Nuclear reactions

Higher radionuclidic purity ^{43}Sc and ^{44g}Sc is achievable through irradiation of enriched ^{42}Ca, ^{43}Ca, and ^{44}Ca (compared to ^{nat}Ca). However, due to the scarcity and expensive nature of this material, efficient recycling methods must be in place for enriched target productions to be economically feasible. With natural and enriched calcium targets, ^{44g}Sc can be produced through the ^{nat}Ca(p,x)^{44g}Sc, ^{44}Ca(p,n)^{44g}Sc, ^{44}Ca(d,2n)^{44g}Sc, or ^{43}Ca(d,n)^{44g}Sc reactions while ^{43}Sc can be produced through the ^{nat}Ca(α,x)^{43}Sc, ^{42}Ca(d,n)^{43}Sc, ^{43}Ca(p,n)^{43}Sc, or ^{44}Ca(p,2n)^{43}Sc reactions (enriched reaction routes investigated in this work are shown in Figure 1). Experimentally measured and theoretical predictions for the cross sections of these reactions are shown in Figures 2 and 3.

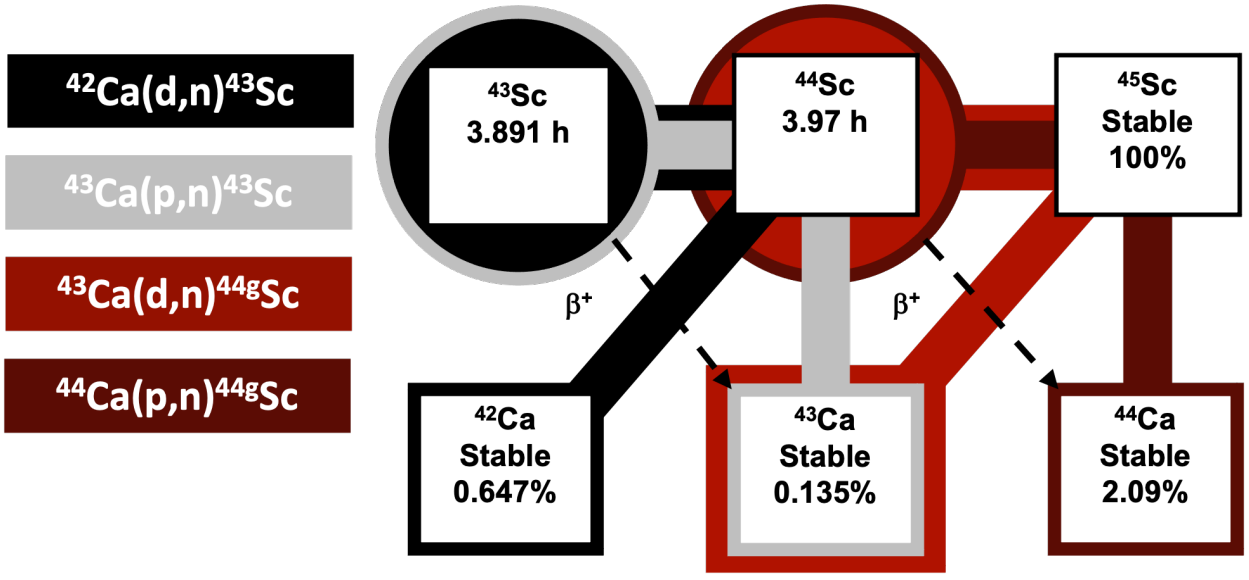


Figure 1: Nuclear reactions for proton and deuteron bombardment of enriched $^{42/43/44}$Ca targets to produce ^{43}Sc and ^{44g}Sc.

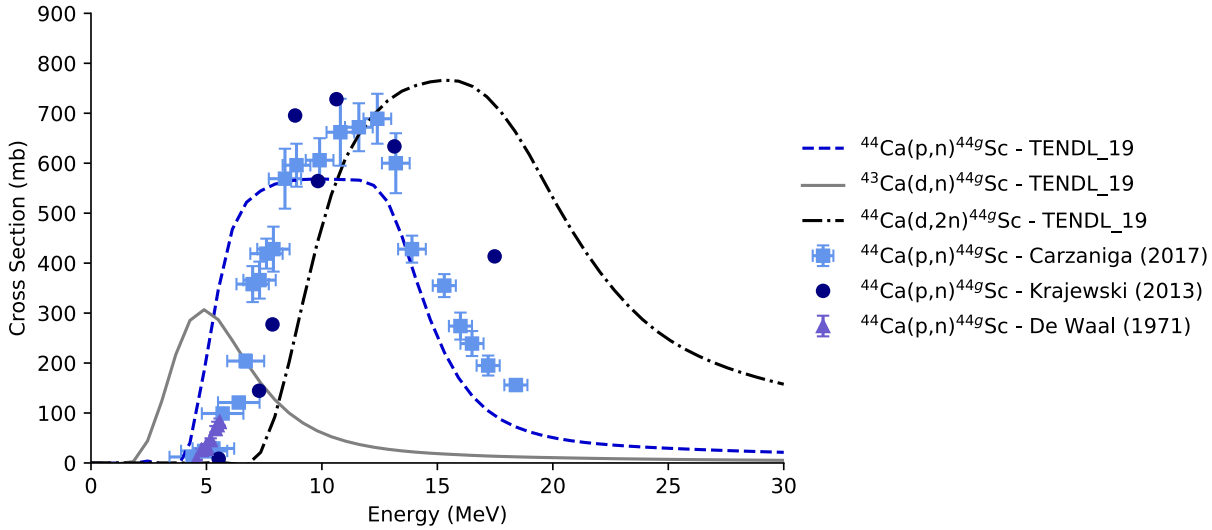


Figure 2: Experimentally measured and predicted values for ^{44g}Sc cross sections on calcium targets [28-31].

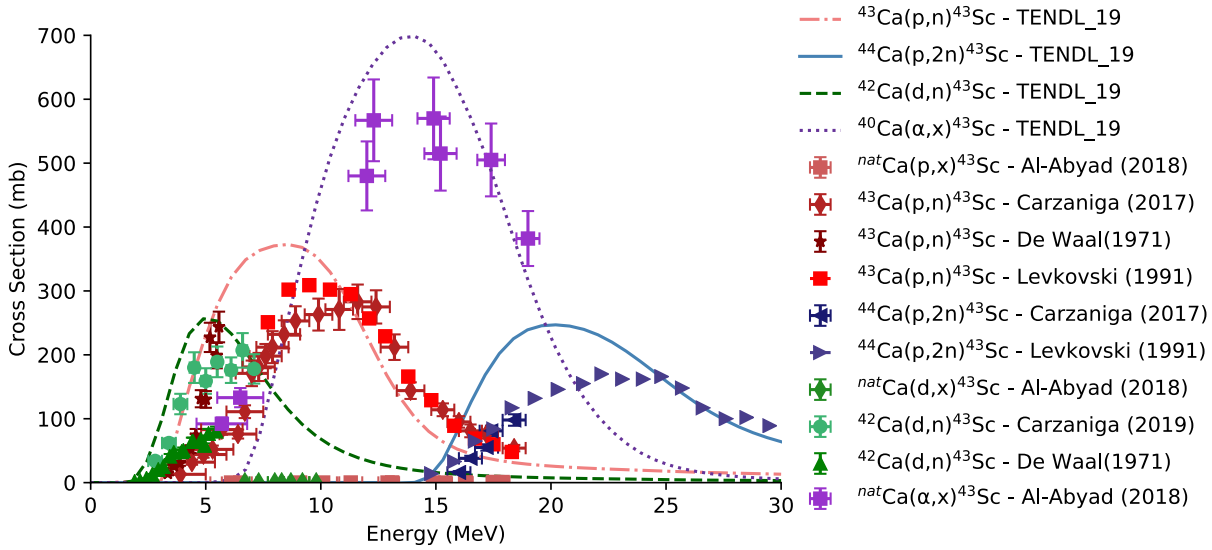


Figure 3: Experimentally measured and predicted values for ^{43}Sc cross sections on calcium targets [28-29, 31-32].

TALYS-based, TENDL-19 cross sections suggest that the maximum yield for ^{44g}Sc is through deuteron irradiation of ^{44}Ca targets with incident energies above 12 MeV via the ^{44}Ca(d,2n)^{44g}Sc reaction (Figure 2, black) [28]. Alliot et al. irradiated enriched $^{44}CaCO_3$ targets (470 μm thick) with 12 MeV deuterons and measured yields comparable to TALYS-based predictions (220 vs 240 MBq/μAh) [34]. One drawback to deuteron bombardment vs proton bombardment of ^{44}Ca targets at this energy is the increase in ^{44m}Sc/^{44g}Sc ratio for the ^{44}Ca(d,2n)^{44g}Sc reaction compared to ^{44}Ca(p,n)^{44g}Sc (Figure 2, blue). Alliot et. al. measured a relative cross section between ^{44m}Sc/^{44g}Sc of 33% for ^{44}Ca(d,2n)^{44g}Sc compared to 7.77% for the proton route. For sites lacking deuterons > 12 MeV, the ^{44}Ca(p,n)^{44g}Sc reaction provides yields approaching the ^{44}Ca(d,2n)^{44g}Sc route but also lower ^{44m}Sc impurities. Finally, deuteron bombardment of ^{43}Ca targets is possible through the ^{43}Ca(d,n)^{44g}Sc reaction (Figure 2, gray), but the yields are lower than ^{44}Ca(p,n)^{44g}Sc and ^{44}Ca(d,2n)^{44g}Sc and this route also requires more expensive target material.

Predicted cross sections taken from the TALYS-based TENDL-19 library and measured cross sections suggest that the maximum yield of ^{43}Sc is achieved through alpha irradiation of natural calcium targets at energies around 15 MeV (Figure 3, purple) [28, 32]. While this reaction uses inexpensive target material and produces high yields, alpha accelerators are rare. Alternatively, proton bombardment of ^{43}Ca targets results in high yields (Figure 3, red) [35, 31, 36], but ^{43}Ca is in lower natural isotopic abundance and more expensive than ^{42}Ca and ^{44}Ca target material. However, with efficient target recycling, this reaction route becomes more economical. Deuteron bombardment of ^{42}Ca targets is also possible for sites with an accelerator capable of > 5 MeV deuterons and provides yields slightly lower than the two aforementioned routes (Figure 3, green). Finally, proton bombardment of ^{44}Ca at energies > 16 MeV produces

^{43}Sc through the ^{44}Ca(p,2n)^{43}Sc reaction but this will be co-produced with ^{44g}Sc (Figure 2, blue) [35, 36].

Production of ^{43}Sc and ^{44g}Sc is also possible through proton irradiation of titanium targets (Figures 4 and 5) [37, 38]. Like the calcium target routes, it is possible to use ^{nat}Ti targets, but enriched titanium (^{46}Ti and ^{47}Ti) target materials are required to reduce co-production of long-lived isotopes of scandium (^{46}Sc, ^{47}Sc, ^{48}Sc) due to the several stable isotopes of titanium (^{46}Ti, 8.25%; ^{47}Ti, 7.44%; ^{48}Ti, 73.72%; ^{49}Ti, 5.41%; ^{50}Ti, 5.18%). The ^{46}Ti(p,α)^{43}Sc (Figure 5, purple) and ^{47}Ti(p,α)^{44g}Sc reaction routes (Figure 4, gray) have lower cross sections than proton reactions on calcium, but ^{46}Ti and ^{47}Ti are cheaper than the enriched calcium material [21]. Theoretical predictions and experimentally measured cross sections for production of ^{43}Sc and ^{44g}Sc off titanium targets are shown in Figures 4 and 5.

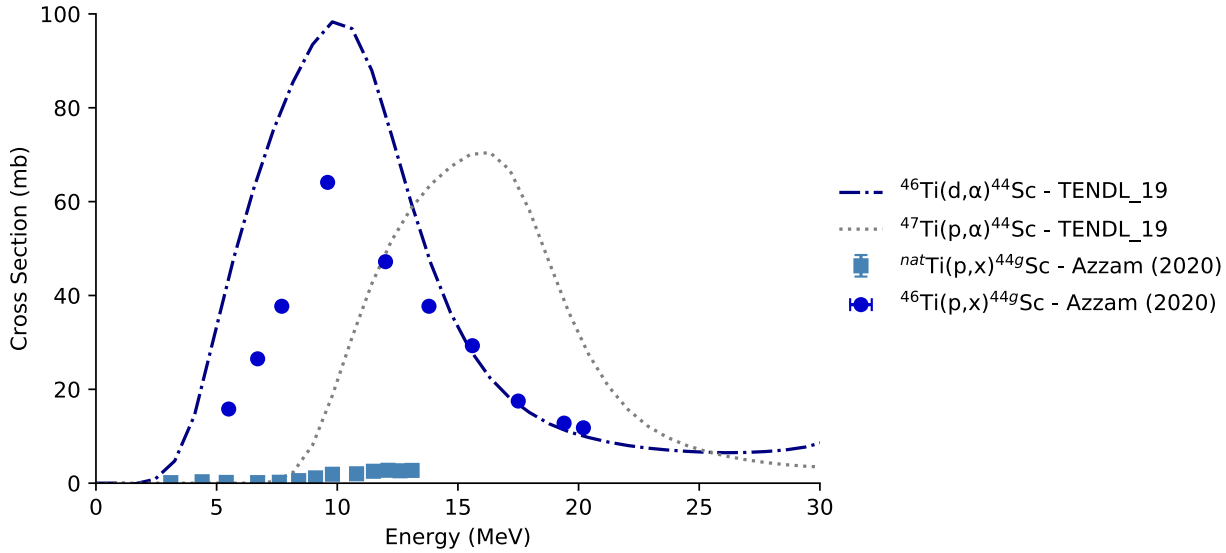


Figure 4: Experimentally measured and predicated values for ^{44g}Sc cross sections on titanium targets [28, 202].

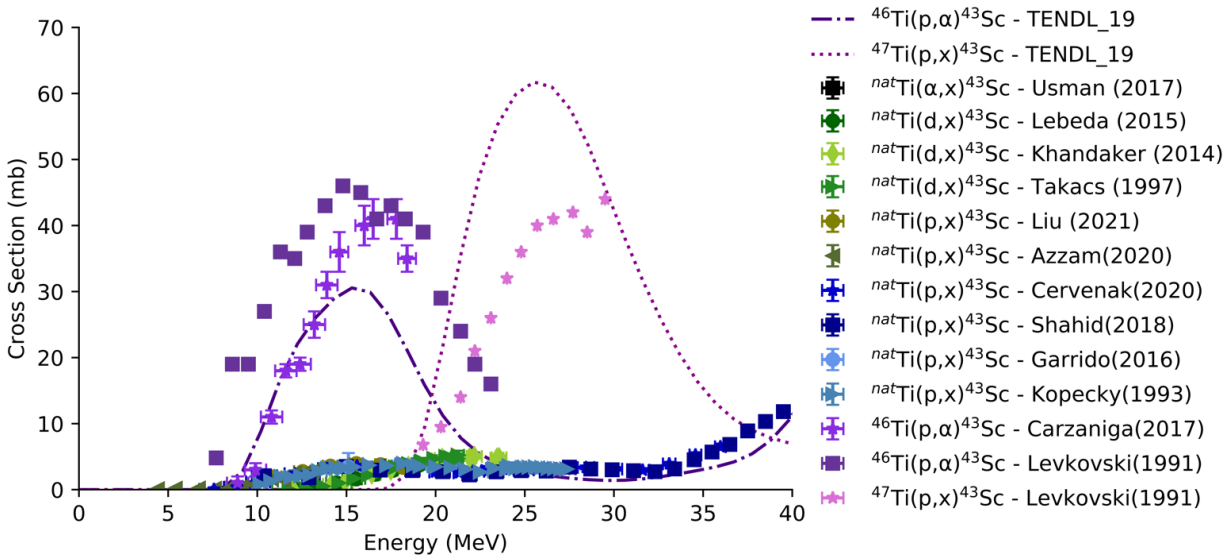


Figure 5: Experimentally measured and predicted values for ^{43}Sc cross sections on titanium targets [28-29, 202-213].

For sites that do not have access to an accelerator, a generator system from ^{44g}Sc's long-lived parent ^{44}Ti ($t_{1/2}$ = 59.1 y) has been developed [39-46, 19]. ^{44}Ti's long half-life, the potential for high efficiency elutions (> 97%) [41], and lack of ^{44m}Sc make the ^{44}Ti/^{44g}Sc generator system appealing. Producing ^{44g}Sc from cyclotron irradiation of natural and enriched calcium targets will always result in the co-production of ^{44m}Sc whereas beta decay of ^{44}Ti results solely in ^{44g}Sc. There has also been development towards a ^{47}Ca/^{47}Sc (^{47}Ca $t_{1/2}$ = 4.536 d) generator system for the therapeutic radioisotope of scandium [45, 47-51]. However, to produce ^{47}Ca, enriched ^{48}Ca material is needed which is both expensive and not widely available.

Cyclotron production of ^{47}Sc is also possible through proton bombardment of titanium targets (^{nat}Ti(p,x)^{43,44g,47}Sc, ^{48}Ti(p,2n)^{47}Sc, ^{50}Ti(p,α)^{47}Sc). These reactions suffer from co-production of ^{46}Sc and ^{48}Sc at high energies so care should be taken to use lower proton energies (< 30 - 35 MeV) [21]. There are also two reaction routes to produce ^{47}Sc from calcium target material:

$^{48}Ca(p,2n)^{47}Sc$ and $^{44}Ca(\alpha,p)^{47}Sc$ [52-56]. However, both ^{48}Ca target material and alpha accelerators are not widely accessible and these reactions routes will likely not have widespread use. Other alternative production paths to ^{47}Sc include photonuclear reactions via electron linear accelerators ($^{48}Ti(\gamma,p)^{47}Sc$) [57-60] and reactor production with fast ($^{47}Ti(n,p)^{47}Sc$) or thermal ($^{46}Ca(n,\gamma)^{47}Ca \rightarrow {}^{47}Sc$) neutrons [61].

Radiochemistry

Several methods for isolating radioscandium from calcium and titanium targets have been reported. Following target irradiation, calcium targets can be readily dissolved in hydrochloric acid [21]. After dissolution, calcium and scandium may be separated using analytical extraction chromatography resins such as UTEVA® [62], N,N,N',N'-tetra-n-octyldiglycolamide (DGA) [34], and hydroxamate or Zr-resin® (Triskem) [23]. Ion exchange resins such as Dowex® 50W-X8 can be used in combination with extraction chromatography resin such as DGA to further remove trace metal impurities [63-65]. Additionally, one source reports precipitation followed by filtration to isolate the radioscandium [66].

Methods for separating radioscandium and titanium begin with digesting the titanium. While natural titanium metal targets can be dissolved in hot HCl, H_2SO_4, or HF, it has been reported that enriched TiO_2 targets are more difficult to dissolve and require additional steps such as heating or the addition of excess sulfate salt [21]. Once the target has been dissolved, the radioscandium may be isolated using extraction chromatography with DGA [58, 61] or ion exchange resins such as Dowex® 50WX4, BioRad AG® 1-X8, AG® 50W-X8, AG® 50W-X4, AG® MP-50, or Chelex 100 [57, 67-69].

Radiolabeling

Once radiochemically separated from the target material, ^{44g}Sc has been successfully complexed and exhibited high *in vivo* stability with the commonly used chelators 1,4,7,10-tetraazacyclododecane-1,4,7,10-tetraacetic acid (DOTA) and diethylenetriamine pentaacetatate (DTPA) [20, 70]. Novel chelators such as the heptadendate AAZTA ligands, the nonmacrocyclic H_4pypa chelator, and the triaza-macrocycle-based picolinate-functionalized chelator H_3mpatcn (which can be labelled with scandium at room temperature) have been designed specifically for scandium [71-75].

In vivo and in vitro studies

^{44g}Sc has been investigated *in vitro* and *in vivo* when labeled with DOTA-based peptides [64, 76-78] and conjugated AAZTA-PSMA peptides [79, 80]. Some additional work has also investigated using antibody fragments in conjunction with ^{44g}Sc to image tumor-bearing mice [81, 71].

2.1.2 Motivation

Accurate nuclear data is essential for optimizing cyclotron production and maximizing yields. Figure 3 in the section above show cross section data collected for production of ^{43}Sc from calcium targets from several reactions where the data and predictions pertaining to the ^{42}Ca(d,n)^{43}Sc reaction are shown in green (and highlighted in Figure 6). There are three measured sets of cross section data, but they are inconsistent and do not cover energies above 10 MeV. Additional data covering energies up to 15 MeV would validate previously measured data and inform optimal incident beam energy.

Additionally, while previous works have investigated cross section measurements of various proton- and deuteron-induced reactions on calcium [31, 33, 35-36, 82], there is a lack of

comprehensive studies comparing the various radionuclidic purities and production yields for small cyclotron-produced ^{43}Sc and ^{44g}Sc. Carzaniga et. al. has published detailed work on cross-section measurements for several deuteron- and proton- induced reactions on calcium targets but did not compare radionuclidic purity or measure thick target yields [82, 35]. Duchemin et. al. measured cross sections for deuteron bombardment of calcium targets to produce $^{44g/44m}$Sc and predicted thick target yields based on these measurements to compare to previously reported proton-induced reaction yields [83]. However, they did not investigate ^{43}Sc production or measure production yields to verify their cross-section measurements.

Production yields and radionuclidic purities for several reactions to produce ^{43}Sc and ^{44g}Sc on enriched $^{42/43/44}$Ca calcium were measured on a GE PETtrace cyclotron (capable of accelerating 16 MeV protons and 8 MeV deuterons) and compared to achieve this goal. Furthermore, enriched calcium is currently only available as $CaCO_3$, a suboptimal material for cyclotron irradiation due to $CaCO_3$'s low thermal conductivity and decarboxylation (and subsequent release of CO_2 at high temperatures) in beam. This work investigates CaO as an alternative target

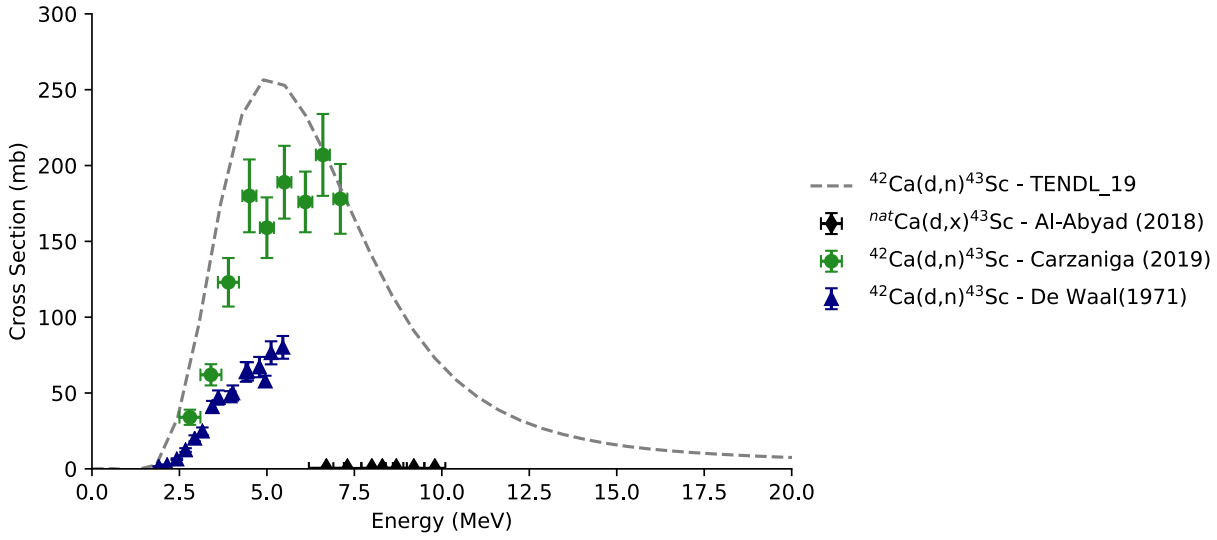


Figure 6: Experimentally measured and predicted cross sections for the ^{42}Ca(d,n)^{43}Sc reaction [32, 82, 31, 88].

material with the goal of increasing beam tolerance and raising production yields.

Even in reactions where the cross section is large, the amount of radioscandium that is produced is on the order of tens of nanograms while the target material is on the order of 100 milligrams. Additionally, several impurities may be present in reagents that are used to dissolve the target material so it is essential to isolate the radioscandium from impurities that may lower labeling efficiencies before moving to preclinical and clinical studies. Efficient recycling methods were also investigated to reduce target material loss with each production. To achieve these goals, this work utilized a radiochemical isolation method using branched DGA resin to recover the enriched calcium and isolate the radioscandium from trace metal impurities to result in high molar activity $^{43/44g}$Sc.

2.2 Materials and Methods

2.2.1 Chemicals

Enriched $^{42}CaCO_3$, $^{43}CaCO_3$, and $^{44}CaCO_3$ material was obtained from the Department of Energy National Isotope Development Center with an isotopic purity of 93.58%, 83.93%, and 98.89%, respectively (Table 3). The presence of stable contaminants identified via spectrographic analysis is listed in Table 4. Solutions were prepared with optima grade HCl and HNO_3 purchased from Fisher Chemical and 18 MΩ cm^{-1} water. Branched DGA resin was purchased from Eichrom. DOTA chelator and DOTA-(Tyr^3)-octreotate (DOTA-TATE) were purchased from Macrocyclics.

Calcium isotope	**$^{42}CaCO_3$**	**$^{43}CaCO_3$**	**$^{44}CaCO_3$**
^{40}Ca	5.24 ± 0.02	10.13 ± 0.08	1.04 ± 0.01
^{42}Ca	93.58 ± 0.05	0.78 ± 0.006	0.036 ± 0.003
^{43}Ca	0.33 ± 0.02	83.93 ± 0.10	0.026 ± 0.002

^{44}Ca	0.84 ± 0.01	5.06 ± 0.03	98.89 ± 0.02
^{46}Ca	< 0.01	< 0.001	< 0.001
^{48}Ca	0.01 ± 0.01	0.09 ± 0.001	< 0.001

Table 3: Isotopic enrichment (%) of enriched $CaCO_3$ material received from the DOE National Isotope Development Center.

Element (ppm)	**$^{42}CaCO_3$**	**$^{43}CaCO_3$**	**$^{44}CaCO_3$**
Ag		< 50	
Al		< 200 T	1
Au		< 500	
B		< 100	5
Ba		< 100 T	
Be		< 10	
Bi		< 200	
Ca	M	M	M
Ce		< 1000	
Cd		< 500	
Cl			3
Co		< 200	< 1
Cr		< 200	3
Cs		< 500	
Cu	15	< 100	< 1
Dy		< 1000	
Er		< 50	
Eu		< 50	
Fe	15	< 200 T	20
Ga		< 200	
Gd		< 200	
Ge		< 200	

Hg	< 500	
Ho	< 500	
In	< 500	
K	< 100	1
La	< 200	
Li	< 50	
Lu	< 50	
Mg	<= 100	< 3
Mn	< 100	< 1
Mo	< 100	< 1
Na	< 100T	10
Nb	< 500	
Nd	< 500	
Ni	< 200	< 1
P		1
Pb	< 200	
Pr	< 500	
Pt	< 500	
Rb	< 200	
S		10
Sb	< 500	
Si	< 100T	< 3
Sm	< 500	
Sn	< 200	
Sr	5000	
Ta	< 500	
Tb	< 500	
Te	< 500	
Tm	< 500	
Ti	< 100	< 1
V	< 200	< 1

W	< 500	
Y	< 50	
Yb	< 20	
Zn	< 500	
Zr	< 200	< 1

Table 4: Spectrographic analysis of the enriched $^{4x}CaCO_3$ (M = major; T = trace).

2.2.1 Measurement of the $^{42}Ca(d,n)^{43}Sc$ cross section

Natural isotopic enrichment CaO targets (2.4 – 3.0 μm thick; 9.5 mm diameter) were evaporated on thin nickel (1.3 μm thick) foils at Argonne National Laboratory. Nickel was chosen for the well-defined $^{60}Ni(d,n)^{61}Cu$ IAEA monitor reaction to confirm beam energy and current [84]. The CaO-nickel targets were then mounted to aluminum frames (21.6 x 17.2 x 0.8 mm) as seen in Figure 7 (left).

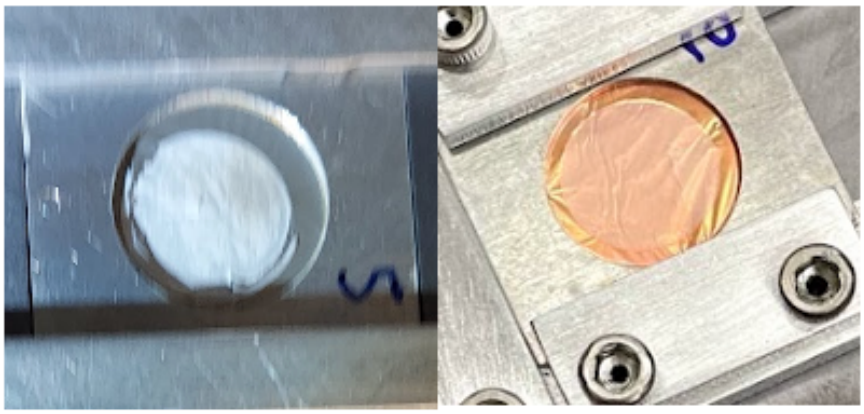


Figure 7: Sample ^{nat}CaO target on nickel backing (left) and copper backing (right) mounted to aluminum frame.

Twelve nickel-backed targets were irradiated on the University of Notre Dame's FN Tandem Van de Graff accelerator with 4 - 11 MeV deuterons and currents between 200 - 500 nA. Targets were irradiated for 1.5 - 4 hours. Following irradiation, samples were transferred to the low

background counting room and counted on a Canberra model GC3518 HPGe detector to quantify ^{43}Sc and monitor reaction product quantities.

Analysis of the acquired spectrum from the irradiated nickel-backed targets revealed that

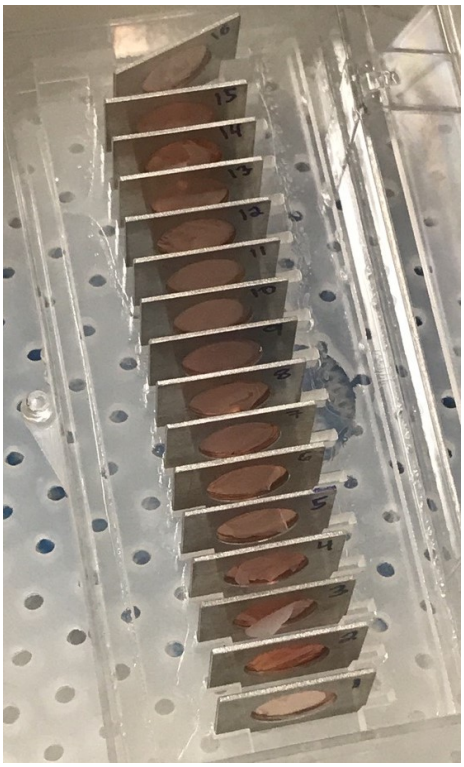


Figure 8: ^{nat}CaO targets evaporated on copper foil backings and mounted to aluminum frames.

^{43}Sc's 372.9 keV (22.5%) gamma peak was much larger than expected. This was due to the high activity of ^{61}Cu produced that also emits a 373.0 keV (2.14%) gamma. Following this observation, 16 new ^{nat}CaO targets were fabricated on thin copper foil (1.1 ± 0.1 μm thick) backings using the same evaporated calcium (3.0 μm thick; 9.5 mm diameter) technique at Argonne National Laboratory (Figures 7 and 8) to avoid co-production of ^{61}Cu. Copper backings were selected for the ^{nat}Cu(d,x)^{6x}Zn monitor reactions and the lack of a co-produced gamma

close in energy to ^{43}Sc's characteristic 372.9 keV gamma. These targets were similarly irradiated at the University of Notre Dame's FN Tandem.

Prior to irradiation, the copper-backed ^{nat}CaO targets were stored in a vacuum-sealed

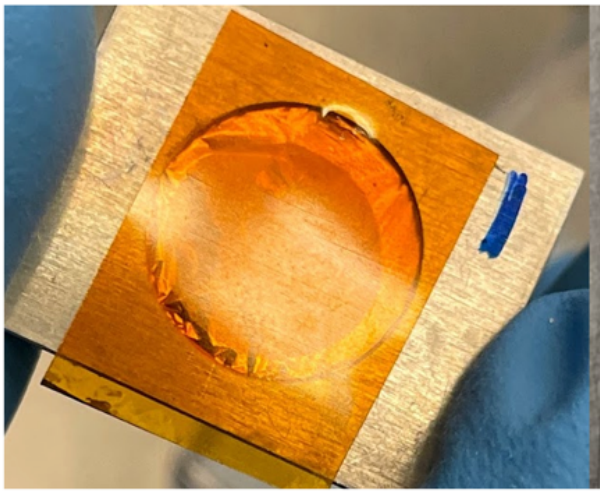


Figure 9: Kapton®-covered ^{nat}CaO target on copper backing.

container with desiccant to prevent moisture absorption by the targets during transportation. However, despite these efforts, some of the ^{nat}CaO targets absorbed water during transfer and delaminated from the copper backings. This was hypothesized to be a larger problem for the copper-backed targets than the nickel-backed targets due to the difference in humidity when the targets were irradiated (January for nickel-backed targets and July for copper-backed targets). To prevent further delamination, 1 Mil Kapton® tape was placed on top of the aluminum frame covering the 9.5 mm aperture and the ^{nat}CaO deposits. A thin slit was cut in the tape to allow gas produced during irradiation to escape. A sample Kapton®-covered target is shown in Figure 9. Six out of the 16 targets were deemed unusable due to loss of target material or rips in the backing foil. The remaining ten targets were irradiated for 1 - 5 hours with 3.5 – 11 MeV deuterons with currents ranging from 100 – 400 nA. Following irradiation, targets were

transferred to the counting room and measured on the same HPGe detector as the nickel-backed targets. Targets were individually counted for 2 – 5 hours to obtain high counting statistics ($\frac{\sqrt{N}}{N} <$ 5%).

Activities for both sets of experiments were quantified by gamma spectrometry using the Al-windowed HPGe detector described above and MAESTRO (Ortec) software. The detector energies and efficiencies were calibrated with a ^{152}Eu check source within one week following target measurements. A Gaussian function was used to fit the peak ROIs using a non-linear least squares optimization within the spectra:

$$Peak = B + Ae^{\frac{-(x-\mu)^2}{2\sigma^2}} \quad (1)$$

The number of counts in each peak was determined by integrating the fit curve above minus the background, B. The primary gammas and decay properties of all radionuclides investigated are listed below in Table 5.

Radionuclide	**Type**	**Half-life**	**Reaction**	**γ_{Energy} (keV)**	**γ_{BR} (%)**
^{43}Sc	Target	3.891(12) h	^{42}Ca(d,n)^{43}Sc	372.9(3)	22.5
^{61}Cu	Monitor	3.336(10) h	^{nat}Ni(d,x)^{61}Cu	282.956(10)	12.7(20)
				373.050(10)	2.14(33)
^{56}Co	Monitor	77.236(26) d	^{nat}Ni(d,x)^{56}Co	846.770(6)	99.9399
^{58}Co	Monitor	70.86(6) d	^{nat}Ni(d,x)^{58}Co	810.7593(20)	99.450
^{62}Zn	Monitor	9.193(15) h	^{nat}Cu(d,x)^{62}Zn	596.56(13)	26.0
^{63}Zn	Monitor	38.47(5) min	^{nat}Cu(d,x)^{63}Zn	669.62(5)	8.2
^{65}Zn	Monitor	243.93(9) d	^{nat}Cu(d,x)^{65}Zn	1115.539(2)	50.04(10)

Table 5: Properties of radionuclides quantified in both experiments [1].

Cross sections were calculated from the activities measured from activation of the ^{nat}CaO targets and beam currents measured on an electrically isolated station attached to the beam dump and target holder. Measured activities were decay corrected to end of bombardment (EoB) using the standard decay formula:

$$A(t) = A_0 e^{-\lambda t} \quad (2)$$

HPGe spectra were saved every 15 minutes and decay plots were created and fit with an exponential to confirm radionuclide identity by half-life. The cross section was then determined by:

$$\sigma = \frac{A_0}{I\rho x(1-e^{-\lambda t})} \quad (3)$$

where σ is the cross section (m^2), A_0 is the EoB activity (Bq), I is the deuteron fluence (deuterons/s), ρ is the density of the target (kg/m^3), and x is the thickness (m).

2.2.2 Target fabrication

Enriched $CaCO_3$ targets can withstand proton currents up to 50 μA when kept relatively thin and of low mass (0.1 - 0.2 mm, < 10 mg) [64]. However, this material is very hygroscopic and readily absorbs water from the atmosphere. Additionally, when sufficiently heated in beam, $CaCO_3$ decarboxylates, forming CaO, offgassing CO_2, potentially damaging the target and reducing accelerator beam transmission. When transitioning from preclinical to clinical demands, optimization of irradiation lengths and production yields can be achieved through use of larger target masses and/or increased beam currents. To compensate for the increased power deposition required for larger-scale $^{43/44g}$Sc productions, CaO was investigated as an alternative target material to $CaCO_3$. CaO was produced through decarboxylation of $CaCO_3$ in a vertical tube furnace (Thermansys) heated in an inert atmosphere to 900 - 950 °C. Approximately 150 - 300 mg of $CaCO_3$ was placed in a small graphite crucible and lowered into a flat-bottomed quartz

tube. The graphite crucible prevented powder loss to the sides of the quartz tube and facilitated removal of the powder. A compression fitting with an argon gas line was connected to the quartz tube to prevent degradation of the graphite crucible during heating. The crucible and quartz tube were placed in the preheated furnace under argon gas flow and baked for 60 - 90 minutes. To confirm complete thermal decomposition of the $CaCO_3$ material, the mass of the crucible and powder was measured before and after heating and decomposition of the graphite crucible was accounted for. Following the decarboxylation procedure, the CaO was quickly pressed into a 9.5 mm diameter niobium crucible with a hydraulic press (250 kg/cm^2). This process is outlined in Figure 10.

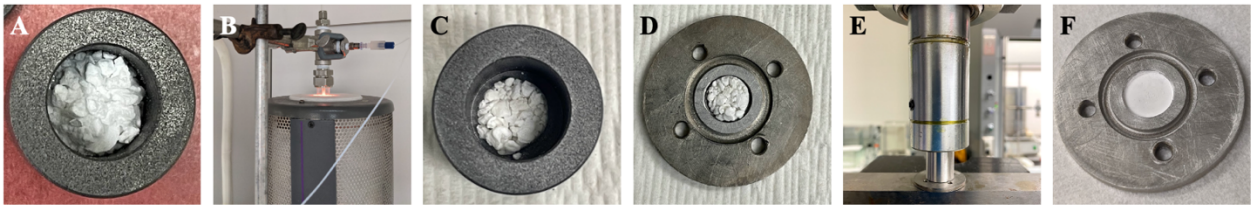


Figure 10: (A) $CaCO_3$ powder in graphite crucible; (B) Crucible placed in quartz tube under argon gas flow lowered into preheated vertical tube furnace (900°C); (C) CaO powder in graphite crucible following conversion; (D) CaO powder placed in pocket of niobium target; (E) Hydraulic press forming the target; (F) Pressed CaO target.

2.2.3 Production yield measurements

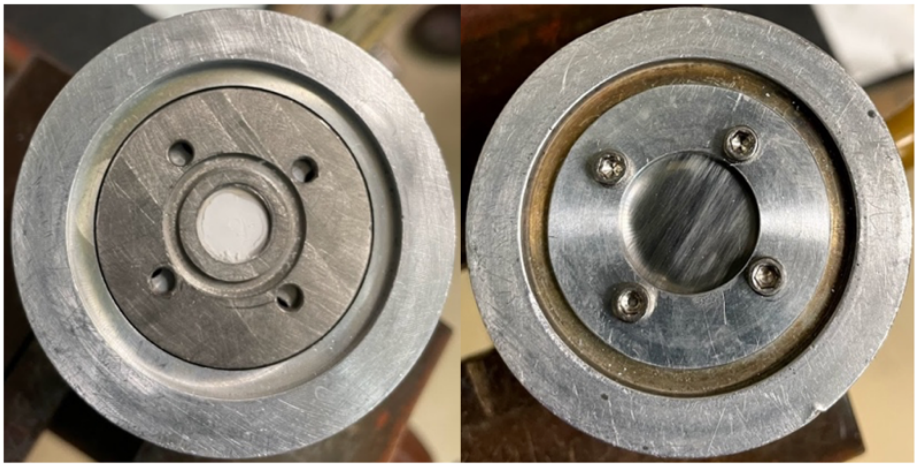


Figure 11: Niobium crucible containing approximately 60 mg of pressed CaO powder (left) and covered with 50 μm niobium cover foil (right).

Targets were covered with either a 50 μm or 150 μm thick niobium cover foil to confine the target material (Figure 11) and to degrade the incident proton/deuteron energy. The 50 μm thick foil degraded the incident 16 MeV protons to 15.2 MeV and the 150 μm thick niobium cover foil degraded the incident energy to 13.6 MeV (calculated using SRIM) [85]. Additionally, the 50 μm thick foil degraded the incident 8 MeV deuterons to 5.8 MeV. These cover foil thicknesses were chosen to minimally degrade the 16 MeV proton beam (incident energy of 15.2 MeV) and 8 MeV deuteron beam (incident energy of 5.8 MeV) and to cover the peak of the cross-section curve (incident energy of 13.6 MeV) as seen in Figures 12 and 13. Energy loss through the CaO targets was calculated using the Bethe-Bloch formula [86]:

$$-\frac{dE}{dx} = \frac{4\pi}{m_e c^2} * \frac{nz^2}{\beta^2} * \left(\frac{e^2}{4\pi\varepsilon_0}\right)^2 * \left[ln\left(\frac{2m_e c^2 \beta^2}{I * (1-\beta^2)}\right) - \beta^2\right] \quad (4)$$

where E is energy of the particle, x is distance travelled, n is electron density of the material the particle is traversing through, z is the charge of the particle, v is the velocity of the particle, I is the mean excitation energy, c is the speed of light, ε_0 is the vacuum permittivity, m_e is the mass of an electron, e is the charge of an electron, and $\beta = v/c$.

The pressed target was then loaded immediately on the University of Wisconsin, Madison's GE PETtrace cyclotron or placed under vacuum in a furnace preheated to >100 °C to keep the target from absorbing moisture (Figure 14 below illustrates an example of a CaO target that was not placed under vacuum and left exposed to humidity). For the $CaCO_3$ targets, 75 - 150 mg $CaCO_3$ was first heated in a polypropylene centrifuge tube at 90° C for 30 minutes to ensure that the material was dry and then pressed directly into the niobium crucible. All targets were irradiated for 15 mins to 1 hour with 5 - 20 μA protons or 3 - 10 μA deuterons with water jet cooling on the back of the target.

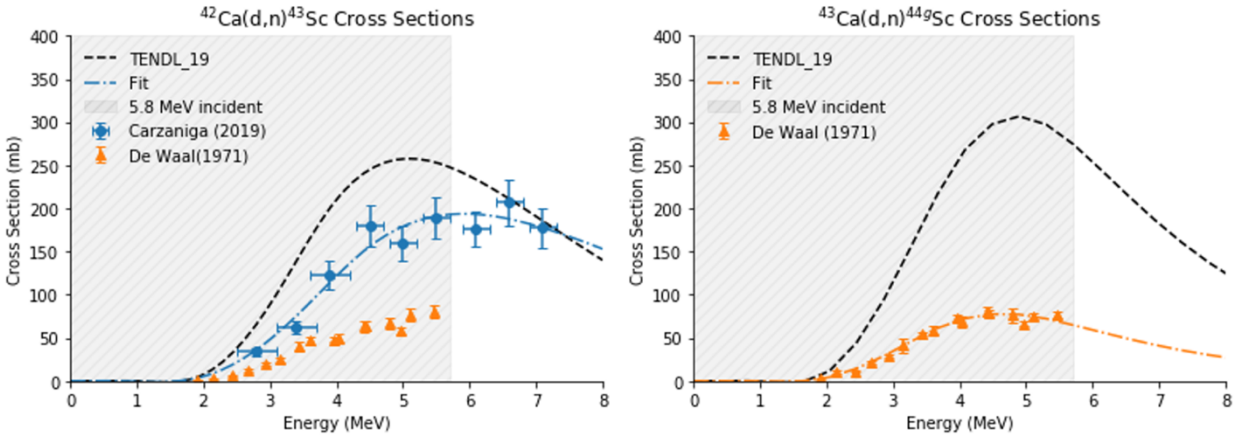


Figure 12: Cross sections for the ^{42}Ca(d,n)^{43}Sc and ^{43}Ca(d,n)^{44g}Sc reactions [82, 87, 88]. Energy range investigated is highlighted in gray.

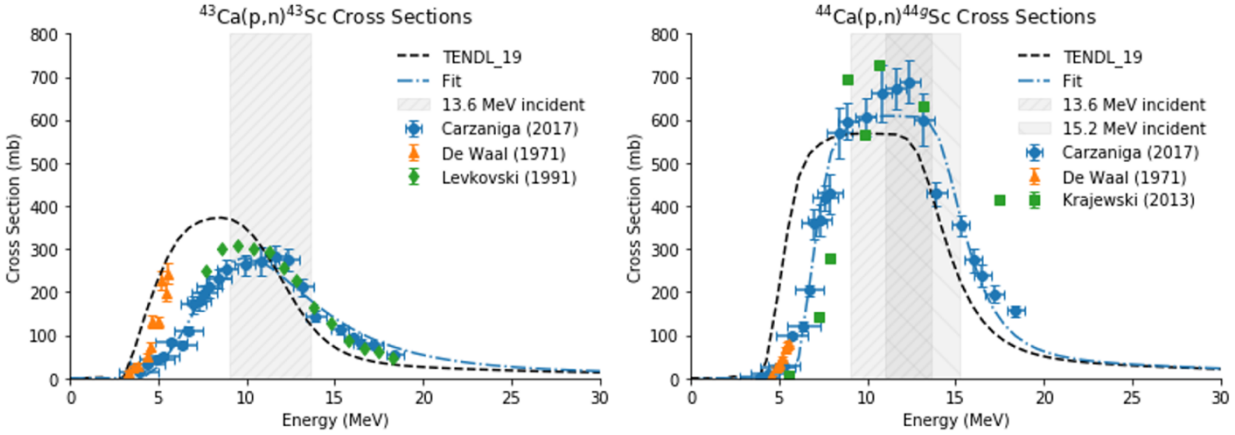


Figure 13: Cross sections for the ^{43}Ca(p,n)^{43}Sc and ^{44}Ca(p,n)^{44g}Sc reactions [35, 87, 36, 89, 88]. Energy range investigated is highlighted in gray.

To compare current tolerances, pressed powder $^{nat}CaCO_3$ and ^{nat}CaO targets of equal thickness were irradiated with 13.6 MeV protons. Cyclotron vacuum pressure was monitored during irradiation and peak and stabilized pressure were recorded as the current was increased in 1 μA increments during the irradiation.



Figure 14: CaO target that was left exposed to ambient room conditions overnight.

2.2.4 HPGe spectrometry

Targets were assayed via HPGe gamma spectrometry with an aluminum-windowed detector (Ortec) coupled to a Canberra Model C1519 research amplifier and multi-channel analyzer (full-width half-maximum at 1333 keV = 1.8 keV) to quantify radionuclide activities 10 - 30 mins after irradiation. ^{241}Am, ^{133}Ba, ^{152}Eu, ^{137}Cs, and ^{60}Co check sources traceable to NIST were used to energy and efficiency calibrate the detector. Full targets were measured 200 - 400 cm from the detector face to quantify $^{43/44g/44m}$Sc activity and longer-lived radioisotopes of scandium (^{46}Sc, ^{47}Sc, ^{48}Sc) were quantified through 250 µL aliquots of the dissolved target (5 mL) measured overnight approximately 20 cm from the detector face. To determine EoB yields of long-lived scandium radioisotopes, the activity of ^{43}Sc or ^{44g}Sc quantified in the aliquot provided a correction factor to obtain $^{46/47/48}$Sc full target activity.

2.2.5 Radiochemical isolation of $^{43/44g}$Sc

Targets were dissolved in 5 mL 9 M HCl heated at 80 °C with magnetic stir bar agitation for 30 - 45 mins. Radiochemical separation of $^{43/44g}$Sc from $^{42/43/44}$CaO target material used single-column extraction chromatography with branched DGA (132.3 ± 67 mg, 5.5 mm column diameter) resin (Eichrom) pre-conditioned with 3 mL 0.01 M HCl followed by 5 mL 9 M HCl. The 5 mL dissolved target solution was loaded on to the conditioned resin using a peristaltic pump (1.6 mL/min) and collected for target recycling along with a 10 mL rinse of 6 M HCl. To remove trace metals, a 12 mL 1 M HNO_3 rinse was performed and $^{43/44g}$Sc was subsequently eluted with four 500 µL fractions of 0.01 M HCl [90, 34]. The radiochemical separation strategy is illustrated in Figure 15.

Activities were assayed in a Capintec CRC-15R dose calibrator (^{43}Sc setting #825; ^{44g}Sc setting #938). Capintec dose calibrator settings were taken from the user's manual and confirmed via cross-calibration with HPGe spectroscopy.

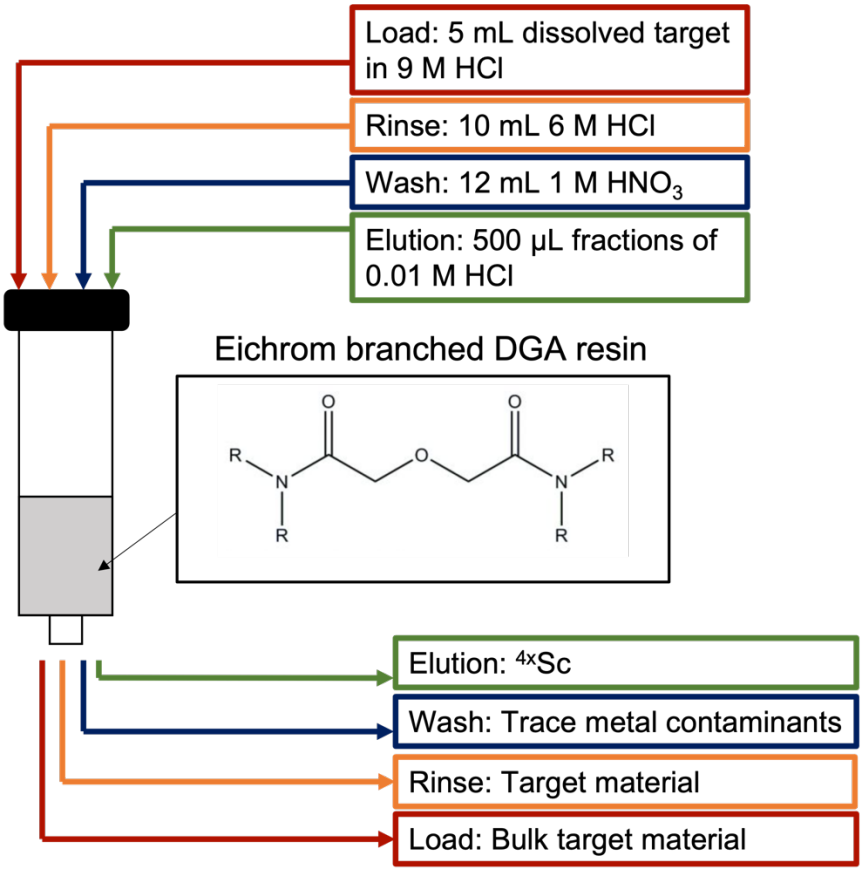


Figure 15: Ca/Sc separation strategy utilizing Eichrom branched DGA resin.

2.2.6 Isotopically enriched calcium recovery

The enriched calcium target material was recovered through precipitation from the 5 mL load and 10 mL rinse solutions. The calcium was precipitated as $CaCO_3$ through careful drop-wise addition of saturated $(NH_4)_2CO_3$ solution (approximately 25 mL), allowing 10 to 30 seconds for the solution to settle and CO_2 to be released between drops of $(NH_4)_2CO_3$. Once the solution

became cloudy and additional drops of $(NH_4)_2CO_3$ did not produce more precipitate, an additional 5 mL of $(NH_4)_2CO_3$ was added to ensure full precipitation. Because the solubility of $CaCO_3$ decreases with temperature, the vial containing the precipitate was refrigerated at approximately 3 °C for > 24 h to further precipitate $CaCO_3$ from solution [91]. The precipitate was then centrifuged, decanted, and dried under argon at 120 °C. Care was taken to remove as much liquid as possible to avoid the formation of $(NH_4)_2CO_3$ crystals on the edges of the vials. The dried $CaCO_3$ could then be decarboxylated to CaO for future irradiations following the same procedure described above. The full calcium recycling procedure is shown in Figure 16.

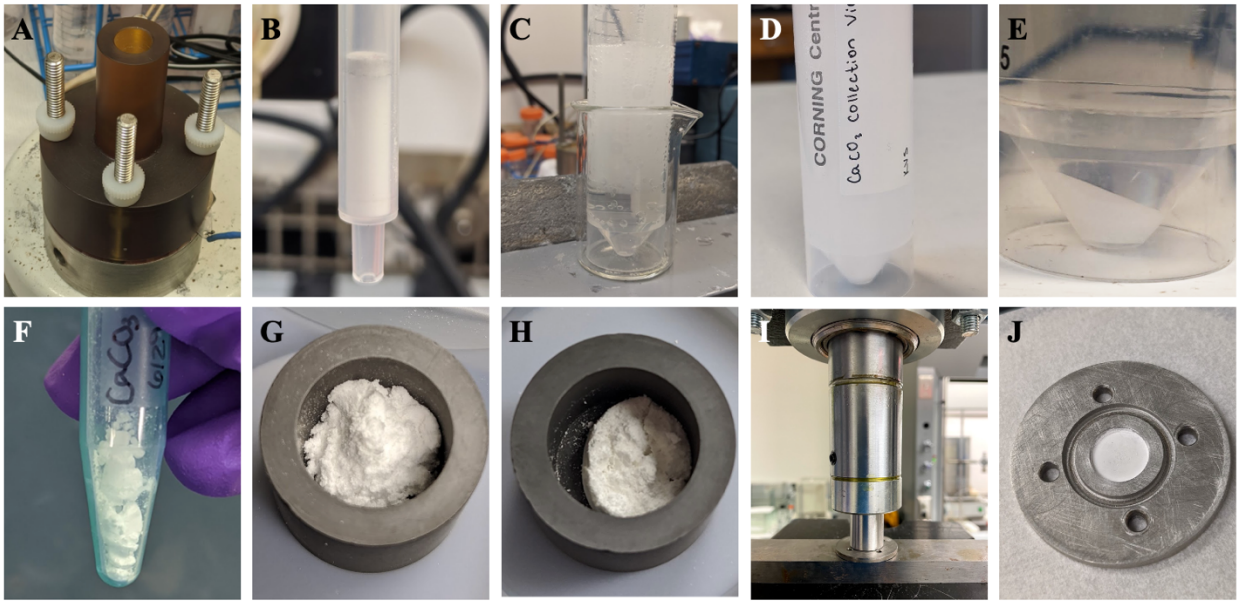


Figure 16: Calcium recycling procedure: (A) CaO target in dissolution block; (B) Branched DGA resin; (C) Dissolved calcium in HCl with addition of saturated ammonium carbonate solution; (D) $CaCO_3$ precipitating out of solution; (E) Centrifuged $CaCO_3$ pellet; (F) Dried $CaCO_3$; (G) Recycled $CaCO_3$ in graphite crucible; (H) CaO powder; (I) Hydraulic press forming CaO target in niobium crucible; (J) Recycled CaO target.

2.2.7 Apparent molar activity measurements and trace metals analysis

Trace metals analysis on the eluted $^{43/44g}$Sc solutions was performed by microwave plasma-atomic emission spectrometry (MP-AES) using an Agilent Technologies 4200 spectrometer. Calibration standards containing 10 ppb to 100 ppm of iron, zinc, copper, and calcium were prepared in 0.01 M HCl solutions from 1000 mg/l standards purchased from Sigma-Aldrich.

The apparent molar activity of the eluted $^{43/44g}$Sc solutions was determined through titration by reaction with varying concentrations of DOTA chelator. Polypropylene centrifuges tubes containing increasing concentrations of DOTA dissolved in 18 MΩ cm^{-1} water (100 µL, 0 - 100 µg/mL) were prepared and small aliquots (10 - 15 µL, 3.7 ± 0.04 MBq) of $^{43/44g}$Sc eluate were added to each vial. Additionally, 2 - 5 µL of 1.5 M NaOAc (pH = 4.5) buffer were added to each vial to reach a final pH between 4 - 4.5. The solutions were then vortexed and heated on a shaker plate at 80 °C and 300 RPM for 30 mins. $^{43/44g}$Sc complexation with DOTA was determined through thin layer chromatography (TLC) using aluminum backed silica gel plates (TLC Silica gel 60 F_{254}, Sigma-Aldrich). Activity was spotted onto the silica gel plates and developed in 50 mM ethylenediaminetetraacetic acid (EDTA). Plates were imaged with storage phosphor autoradiography (Packard Cyclone). Under these conditions, the radiolabeled Sc-DOTA stayed at the origin (retention factor, R_f = 0) while the free radioscandium travelled with the mobile front (R_f = *1)*. The apparent molar activity of $^{43/44g}$Sc with DOTA was found by dividing the activity of $^{43/44g}$Sc in each vial by twice the number of moles of DOTA required to complex 50% of the activity.

Radiolabeling experiments were also performed with the DOTA-based peptide DOTA-TATE following the same radiolabeling conditions listed above for DOTA. Briefly, 100 µL $^{43/44g}$Sc was vortexed with 2 - 3 µL DOTA-TATE (5 nmol/mCi; 7.4 MBq/nmol) and 2 - 5 µL 1.5 M NaOAc

pH 4.5 buffer and heated to 80° C while shaking at 300 RPM for 15 - 30 mins. Percent complexation was determined through radio-TLC and high-performance liquid chromatography (HPLC) using a C18 column (4.6 x 250 mm, Dionex 5µm 120 Å; ThermoFisher) and a water (0.1% Trifluoroacetic acid, TFA) to acetonitrile gradient (5% MeCN, 0 - 3.5 min; 5% - 35% MeCN, 3.5 - 13 min; 35% - 90% MeCN, 13 - 15 min; 90% MeCN, 15 - 19 min; 90% - 5% MeCN, 19 - 20 min; 5% MeCN, 20 - 25 min) flowing at 1 mL/min.

2.3 Results and Discussion

2.3.1 Measurement of the ^{42}Ca(d,n)^{43}Sc cross section

A sample HPGe spectrum from the nickel-backed ^{nat}CaO target irradiated with 3 MeV deuterons is shown in Figure 17. The peak seen at 373 keV has contributions from both ^{61}Cu and ^{43}Sc decay. The energies (373.050 ± 0.010 and 372.9 ± 0.3 keV respectively) and half-lives (3.336 ± 0.010 and 3.891 ± 0.012 hours respectively) [1] are too similar to deconvolve the peak by energy or decay.

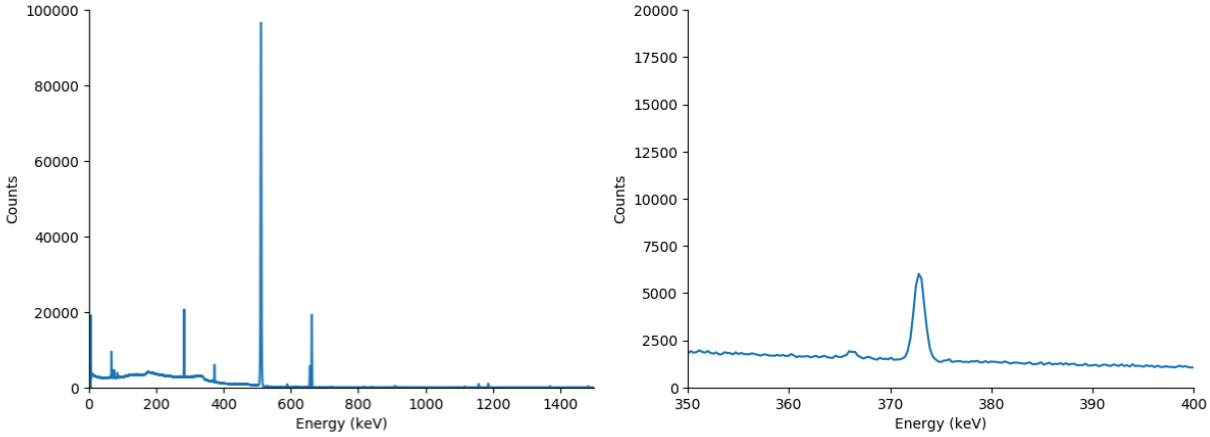


Figure 17: (Left) HPGe spectrum of the nickel-backed ^{nat}CaO target irradiated with 3 MeV deuterons. (Right) Zoomed in spectrum showing the 373 keV peak from ^{61}Cu and ^{43}Sc decay.

Thus, ^{43}Sc cross sections were calculated by first measuring ^{61}Cu EoB activity from its 282.96 keV (12.7%) gamma and calculating the number of counts ^{61}Cu would contribute to the 373 keV peak from its 373.0 keV (2.14%) gamma based on branching ratio and detector efficiency at 373 keV. Cross sections for the ^{60}Ni(d,x)^{61}Cu reaction were also calculated from the EoB ^{61}Cu activity and agreed well with IAEA recommended cross sections within error (Figure 18 (left)). The resulting estimated ^{42}Ca(d,n)^{43}Sc cross sections are shown in Figure 18 (right).

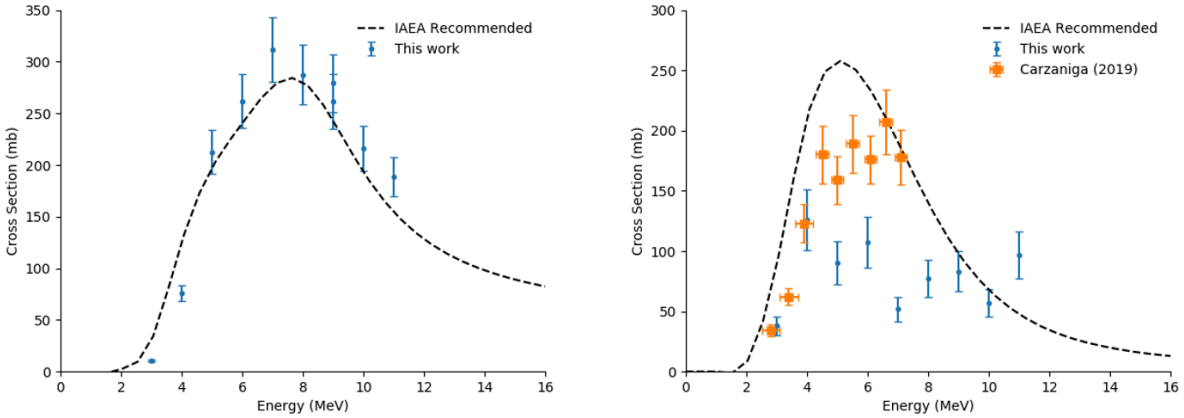


Figure 18: (Left) ^{60}Ni(d,n)^{61}Cu cross section measured in this work and IAEA recommended cross sections. (Right) ^{42}Ca(d,n)^{43}Sc cross section measured from subtracted 373 keV peak plotted with TALYS-based TENDL_19 predictions and measured cross section data from Carzaniga et al. [33] [28].

Measured ^{42}Ca(d,n)^{43}Sc cross sections in this work do not match predicted or previously measured data and are consistently low. To verify that the corrected counts were solely from ^{43}Sc, an exponential function was fit to the decay data (Figure 19). The fit half-life for ^{61}Cu using its 282.96 keV gamma matched the theoretical half-life well, whereas the fitted ^{43}Sc half-life from the corrected 373 keV peak counts deviated greatly from theoretical values shown in Table

6 (values from the 7 MeV irradiated foil were excluded for the ^{43}Sc half-life measurement). Due to the inconsistency between the measured and theoretical half-lives for ^{43}Sc, we could not be confident that the corrected counts in the 373 keV peak were solely from ^{43}Sc.

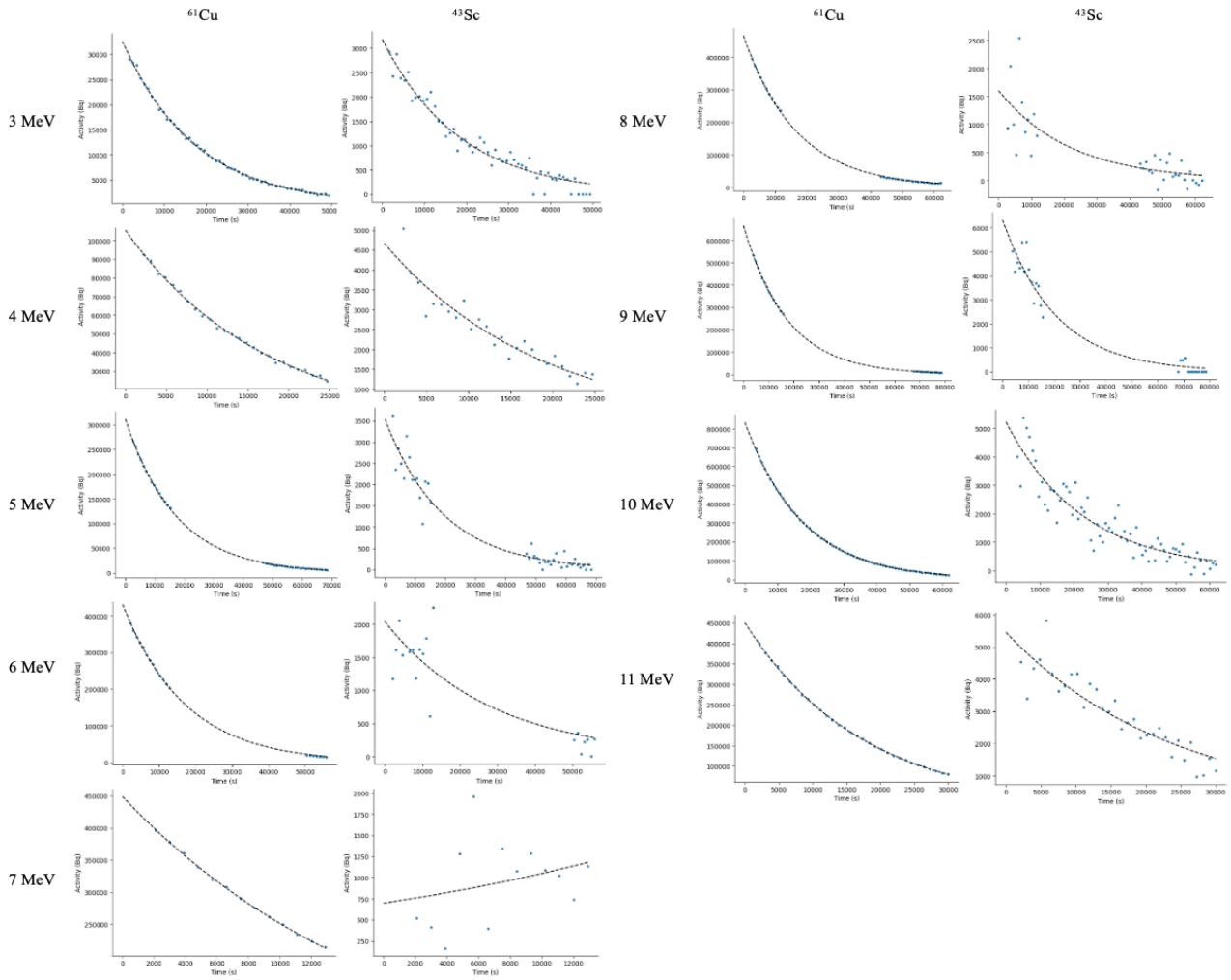


Figure 19: Decay curves for ^{61}Cu and ^{43}Sc on each nickel-backed target.

Radionuclide	Theoretical Half-life	Measured Half-life
^{61}Cu	3.336 ± 0.010 h	3.31 ± 0.04 h
^{43}Sc	3.891 ± 0.012 h	4.19 ± 0.63 h

Table 6: Fit and theoretical half-lives for ^{61}Cu and ^{43}Sc [1].

An additional set of ^{nat}CaO targets with copper backings rather than nickel backings were fabricated and irradiated to remedy the ^{61}Cu co-production issue. However, these ^{nat}CaO targets absorbed moisture in the high humidity environments and delaminated from the copper backings. While Kapton® tape was placed over the target face to prevent further target loss, irradiation of the covering resulted in burns and holes in the tape, allowing the fragile ^{nat}CaO target to fall through the opening. Figure 20 shows target 12 before and after irradiation where the dark discoloration in the center image is burnt tape surrounding a hole in the covering. Autoradiography of the targets showed that the ^{nat}CaO target was broken into small pieces and displaced following irradiation.

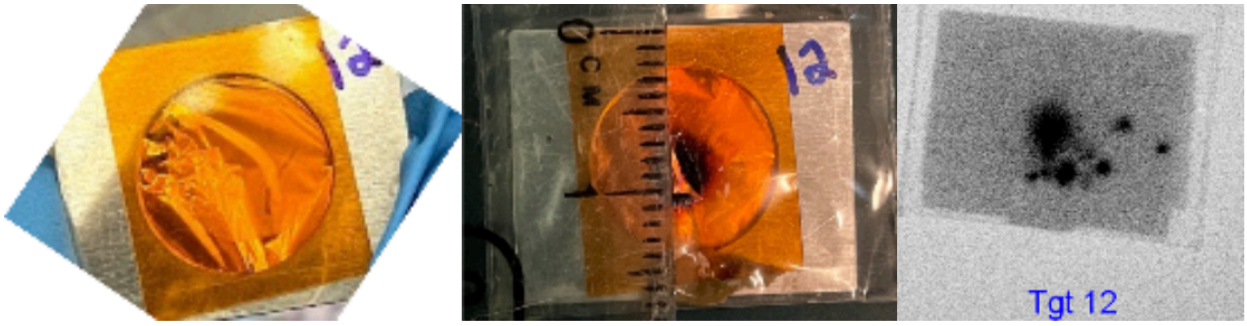


Figure 20: Copper-backed ^{nat}CaO target 12 covered with Kapton® tape before (left) and after (center) irradiation. (Right) Autoradiograph of target 12 illustrating damaged target material.

Cross sections for the $^{42}Ca(d,n)^{43}Sc$ reaction at each energy were calculated from the measured ^{43}Sc EoB activities and beam currents measured on an electrically isolated station attached to the beam dump and target holder (Figure 21). Cross sections measured in this work are lower than those reported by Carzaniga et al. [33] which is consistent with our observations of lost target material following irradiation.

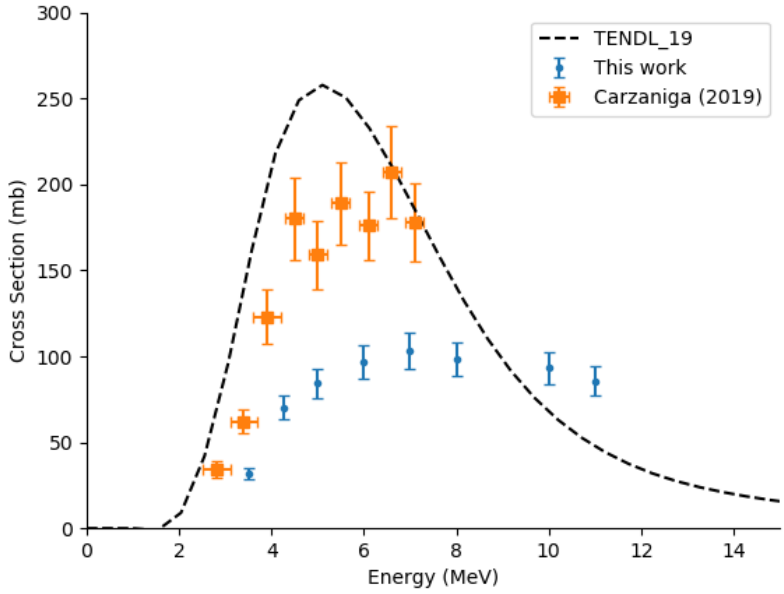


Figure 21: $^{42}Ca(d,n)^{43}Sc$ cross sections measured in this work alongside TENDL-19 predictions and previously reported measurements [33] [28].

Future work fabricating suitable targets to reattempt the $^{42}Ca(d,n)^{43}Sc$ cross section measurement would be beneficial to confirm reported experimental work and to measure the cross section at energies above 10 MeV. Monitor backing foils must be chosen with care to avoid production of radionuclides with gamma emissions near ^{43}Sc's characteristic 372.9 keV (22.5%) gamma due to the low branching ratio of ^{43}Sc's other gamma emissions. The co-production of ^{61}Cu from deuteron bombardment of the nickel backing foils in this work was significant and prohibited accurate quantification of produced ^{43}Sc activity. As a result, the calculated cross-

sections derived from estimated ^{43}Sc activities were lower than predicted and previously measured values. Further work on target fabrication techniques that can withstand humidity is also warranted due to calcium's highly hygroscopic nature. Exposed, evaporated calcium deposits absorbed moisture and delaminated from their copper backings, resulting in difficulty irradiating even with low deuteron currents (< 500 nA). Due to target fabrication challenges, the remainder of the nuclear data collection work in this chapter focused on measuring production yields from proton and deuteron bombardment of enriched ^{4x}CaO targets and comparing to previously measured cross section work.

2.3.2 CaO target development and current limit tests

To compare current tolerances, pressed powder $^{nat}CaCO_3$ and ^{nat}CaO targets of equal thickness (0.63 ± 0.02 mm) were fabricated and irradiated with 13.6 MeV protons. The targets were initially bombarded with 1 μA protons and the current was increased in 1 μA increments during the irradiation, allowing time for the cyclotron vacuum pressure to stabilize between increases until a current of 20 μA was reached. The time required to reach 20 μA for the $^{nat}CaCO_3$ target was 61 min and 23 min for the ^{nat}CaO target. The $^{nat}CaCO_3$ targets generated more gas load on the cyclotron's vacuum system, slowing their progression to 20 μA. The peak pressure versus current for both targets is shown Figure 22 (left). Following irradiation, the targets were examined for physical damage. Minimal damage was seen on the ^{nat}CaO target with no loss of enriched material (Figure 22 (center)), but the $^{nat}CaCO_3$ was found to be severely cracked following irradiation at 20 μA (Figure 22 (right)).

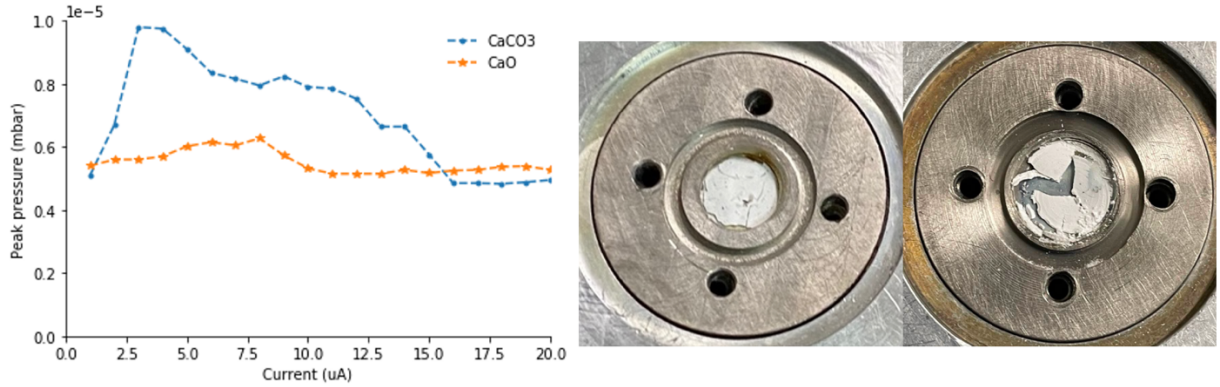


Figure 22: Peak pressure on the target as the current was increased (left). ^{nat}CaO (middle) and $^{nat}CaCO_3$ (right) targets immediately after 20 µA proton irradiation.

2.3.3 ^{43}Sc and ^{44g}Sc production yield measurements

$^{42/44}$CaO targets that were thick to the 5.8 MeV deuteron beam (61 ± 3 mg) were fabricated for deuteron production yield measurements. For proton production yield measurements, $^{43/44}$CaO targets that were 4.7 MeV thick (149 ± 2 mg) to the 13.6 MeV beam were fabricated to capture the flat region of the cross section curve for the ^{43}Ca(p,n)^{43}Sc and ^{44}Ca(p,n)^{44g}Sc reactions [35]. The ^{44}Ca(p,2n)^{43}Sc reaction has a predicted energy threshold close to the maximum 16 MeV protons that the GE PETtrace can accelerate, so the thin 50 µm niobium foil was used to minimally degrade the proton energy to 15.2 MeV for the irradiations designed to observe the ^{44}Ca(p,2n)^{43}Sc reaction (targets were kept the same mass and were consequently only 4.3 MeV thick for this reaction).

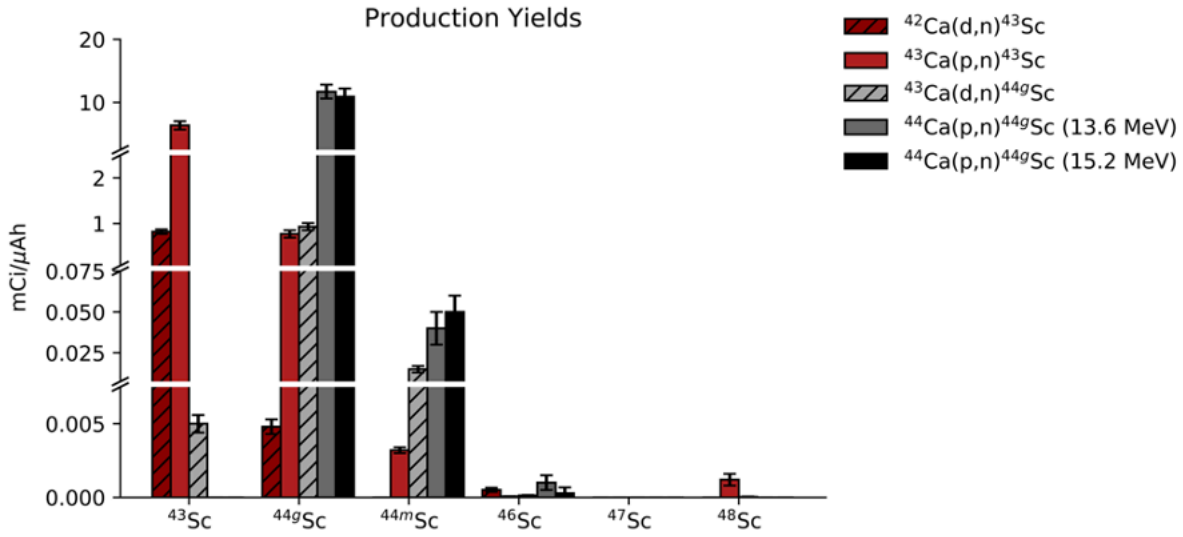


Figure 23: Activities of each radioisotope of scandium that was present in the full target at EoB for each of the 5 reaction routes that were investigated.

The pressed powder targets were irradiated with either 5 μA protons or 3 μA deuterons with a total charge between 0.5 and 1.6 μAh. Production yields for the ^{42}Ca(d,n)^{43}Sc, ^{43}Ca(p,n)^{43}Sc, ^{43}Ca(d,n)^{44g}Sc, ^{44}Ca(p,n)^{44g}Sc, and ^{44}Ca(p,2n)^{43}Sc reactions are shown in Table 7 (n = 3 per reaction route). No ^{43}Sc from the ^{44}Ca(p,2n)^{43}Sc was observed, indicating that 15.2 MeV is below the threshold from the reaction. This result agrees with previously reported data [35] where Carzaniga et. al. reports no ^{43}Sc production at an incident energy of 15.3 MeV.

Reaction	Isotopic enrichment	Incident energy (MeV)	Target mass (mg)	Target thickness (MeV)	Production yield (mCi/μAh)	Yield corrected for beam intercept (mCi/μAh)	Predicted yield (mCi/μAh)	Radionuclidic purity (%)
^{42}Ca(d,n)^{43}Sc	93.58 ± 0.05 %	5.8	62 ± 4	5.8	0.82 ± 0.05	1.49 ± 0.09	1.66*	99.36 ± 0.05
^{43}Ca(p,n)^{43}Sc	83.93 ± 0.10 %	13.6	148 ± 1	4.6	6.19 ± 0.81	12.64 ± 0.92	15.41*	87.81 ± 0.03
^{43}Ca(d,n)^{44g}Sc	83.93 ± 0.10 %	5.8	61 ± 2	5.8	0.93 ± 0.08	1.69 ± 0.14	0.74+	98.08 ± 0.08
^{44}Ca(p,n)^{44g}Sc	98.89 ± 0.02 %	13.6	150 ± 2	4.7	11.71 ± 1.09	23.92 ± 0.50	36.83*	99.71 ± 0.05
^{44}Ca(p,2n)^{43}Sc	98.89 ± 0.02 %	15.2	151 ± 2	4.3	0	0	0	--
^{44}Ca(p,n)^{44g}Sc	98.89 ± 0.02 %	15.2	151 ± 2	4.3	10.92 ± 1.34	22.60 ± 0.57	34.30*	99.51 ± 0.06

Table 7: Observed production yields for the 5 routes investigated along with target masses and energy thickness [82, 35]* [92]+.

Targets were also evaluated for radionuclidic purity via HPGe spectrometry. Figure 23 shows the production yield at EoB (mCi/μAh) for each radioisotope of scandium and the radionuclidic purity in percent total activity at EoB is listed in Table 7 (n = 3 per reaction route).

The GE PETtrace proton and deuteron beams intersect an area on the target that is larger than the 9.5 mm target diameter and thus, the measured total charge on target (μA·h) is an overestimation of that impinging on $^{43/44}$Ca. To account for this, the niobium cover foil was used to determine the percentage of the beam that intercepted the target. After irradiation, a beam profile was obtained through autoradiography, and an ROI with a width of 9.5 mm was drawn and centered on the beam profile. A larger > 20 mm diameter ROI was also drawn encompassing the entire beam spot. Additionally, four other 9.5 mm ROIs with an offset of up to 1.5 mm from center were drawn around the central region to determine the variance in beam intersection that may be caused from the beam drifting from the center. These values were independently

measured for the proton and deuteron beams and were also evaluated before and after a cyclotron ion source puller electrode replacement that occurred during the measurement of these production yields. The measured beam intersections and the max difference between the offset regions are listed in Table 8 with a correction to the measured production yields listed in Table 7.

Figure 24 shows the predicted physical yields versus target thickness for a 13.6 MeV proton (left) and 5.8 MeV deuteron beam (right). Dashed lines are predicted yields taken from a fit to published cross section values and TALYS-based TENDL_19 cross sections [88]. The fit cross sections used for this calculation are shown in blue and orange in Figures 12 and 13. Experimentally measured, beam-spot corrected yields are additionally shown in Figure 24.

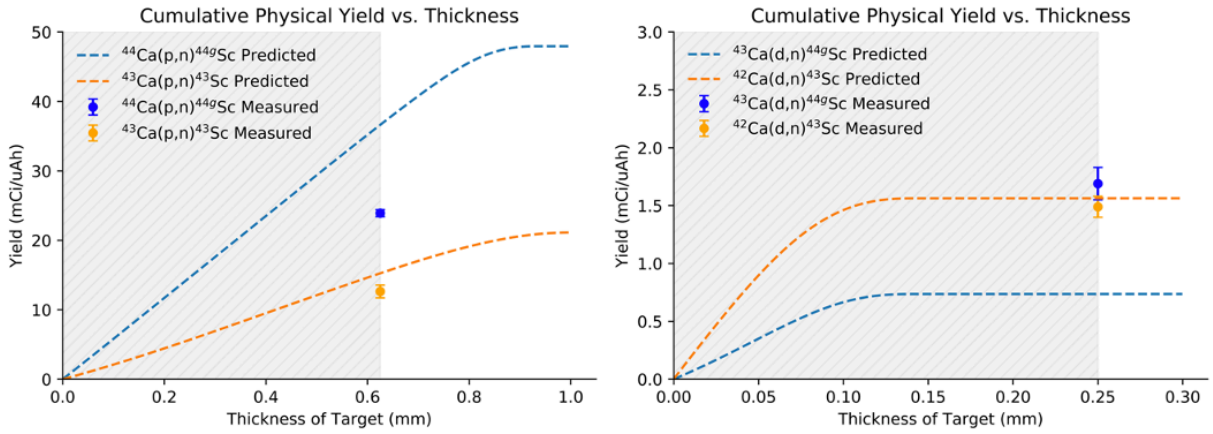


Figure 24: Measured production yields compared to literature reported cross sections fitted to TENDL_19 predicted curves [82, 35, 87, 36, 89, 88].

Puller	Incident Particle	% Beam Intercept
Original puller	proton	46 ± 1%
Original puller	deuteron	53 ± 5 %
New puller	proton	55 ± 3 %
New puller	deuteron	54 ± 5 %

Table 8: Measured beam intercepts for the proton and deuteron beams on a 9.5 mm target.

2.3.4 Radiochemical isolation of $^{43/44g}$Sc

Figure 15 in section 2.2.5 illustrates the separation strategy used for isolating the Sc^{+3} ions from the Ca^{+2} ions. The low affinity for Ca^{+2} ions on the branched DGA resin permitted efficient recycling from the 5 mL load and 10 mL 6 M HCl rinse stages of the separation [34]. Other +2 metals (such as Cu^{+2}) are also rinsed from the resin in this step. The 1 M HNO_3 wash removes metals such as iron and zinc due to the low affinity for these ions in 1 M HNO_3, and minimal loss of Sc^{+3} was observed as seen in the elution profile in Figure 25 [34]. Elution with 2 mL of 0.01 M HCl effectively removes 92.8 ± 4.0 % of the loaded scandium (Figure 25 (right)). However, there is large variation (Figure 25 (left)) in the activity in each 0.01 M HCl elution fraction (n = 10), perhaps due to variations in volumes of liquid being used to elute the activity (residual liquid may be left in tubing or on walls in parts of the system).

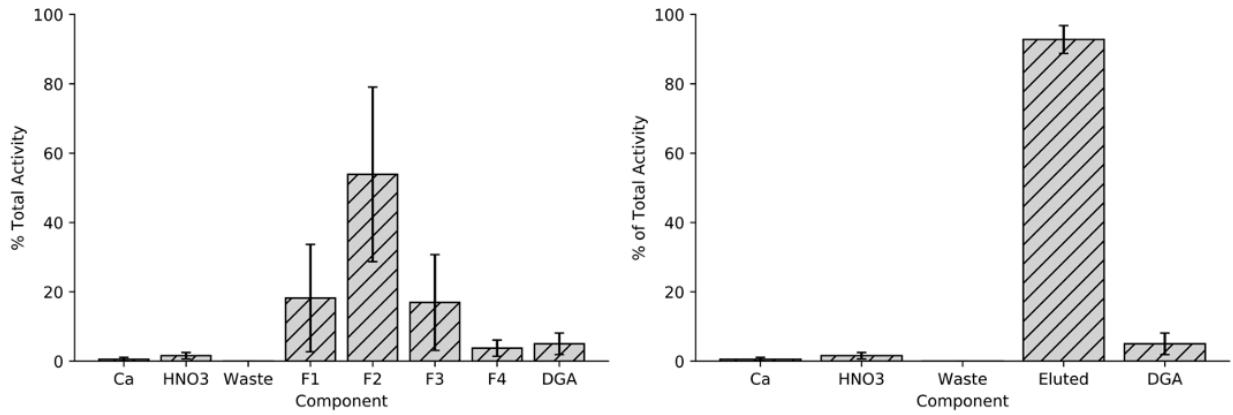


Figure 25: Elution profile for the Ca^{+2}/Sc^{+3} radiochemical separation used in this work. Overall eluted fraction remains consistent (right) but activity distribution in each of the 4 eluted fractions varies with each experiment (left).

2.3.5 Isotopically enriched calcium recovery

A calcium elution profile from the branched DGA resin used during calcium/scandium radiochemical isolation is shown in Figure 26. Calcium mass contained in each 1 mL elution fraction was determined via MP-AES with calibrated calcium standard. By mass, 99.47% of the calcium was recovered in the first 5 mL rinse and 99.84% in a total of 15 mL. Thus, the enriched $^{42/43/44}Ca$ was recovered from the first 5 mL rinse to reduce volumes and $(NH_4)_2CO_3$ consumption. An additional 10 mL rinse was incorporated in the separation strategy to collect residual calcium in case sufficient recovery was not seen in the first 5 mL rinse.

$^{42/43/44}Ca$ was recovered as $^{42/43/44}CaCO_3$ through slow addition of $(NH_4)_2CO_3$ to the collected 5 mL fraction. The enriched $^{42/43/44}CaCO_3$ target material was recovered with an efficiency of 95 ± 2% (n = 20). The recycled $^{42/43/44}CaCO_3$ could then be converted back to $^{42/43/44}CaO$ through decarboxylation in a vertical tube furnace (900 °C for 60 - 90 mins) for future irradiations. If

argon gas is passed over the graphite crucible during the decarboxylation procedure, the crucible surface remains smooth and losses from transferring and heating are < 1%.

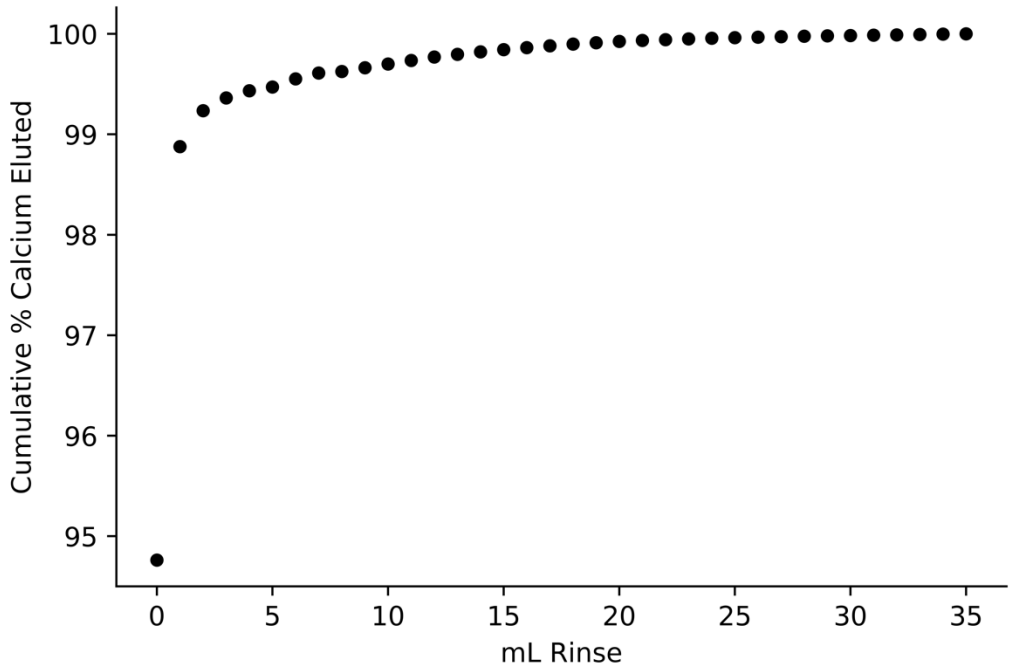


Figure 26: Calcium elution profile from rinses of 6 M HCl off a loaded b-DGA column.

Initial recycling attempts resulted in calcium recoveries > 100% when final mass in the recovery vial was compared to initial target mass. Careful investigation of the recovery tubes showed white, crystalline structures forming around the edges of the polypropylene centrifuge tube vial used during dry down (Figure 27). This was due to the presence of excess $(NH_4)_2CO_3$ that was not removed when transferring the $CaCO_3$ pellet to the dry down vessel in the initial procedure. Once excess liquid was removed from the dry down vessel, recoveries remained below 100% and there were no $(NH_4)_2CO_3$ crystals forming on the walls of the vessel. Figure 27 shows examples of the recovery vials with and without the excess $(NH_4)_2CO_3$ crystals on the walls.

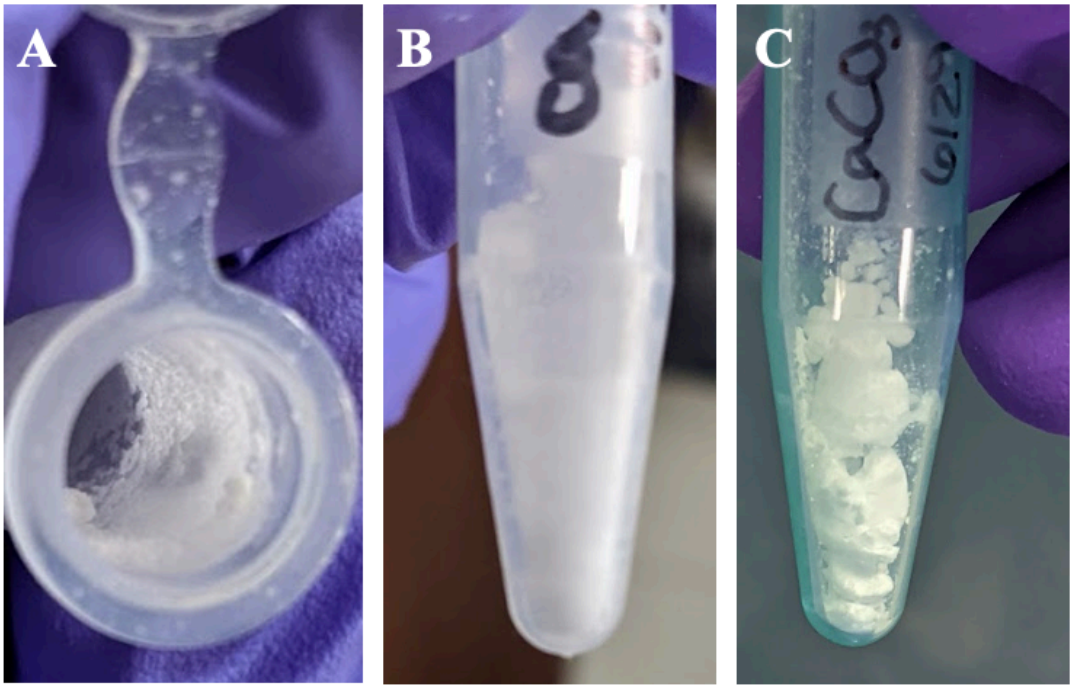


Figure 27: Eppendorf vials used for drying down recycled $CaCO_3$. (A and B) Dried $(NH_4)_2CO_3$ crystals forming on walls of vial. (C) Properly decanted $CaCO_3$ drying to powdery substance.

2.3.6 Apparent molar activity measurements and trace metals analysis

The quality of the final $^{43/44g}Sc$ eluent was determined through titrimetric reactions with the chelator DOTA and the ability to label with the DOTA-based peptide DOTA-TATE. Initial experiments (n = 8) were run in pH 5 and yielded a molar activity of 11.8 ± 10.4 GBq/µmol (0.32 ± 0.28 Ci/µmol). However, pH plays a critical role in scandium labelling as scandium will form hydroxide complexes such as $Sc(OH)^{2+}$, $Sc(OH)_2^{+}$, and $Sc(OH)_3$ in pH above 4.5 while other similar lanthanides such as lanthanum only exist as Ln^{3+} [93]. Once the labeling protocol was revised to pH 4, results showed a molar activity of 70 ± 11 GBq/µmol (1.9 ± 0.3 Ci/µmol) (n = 3) at EoB. An example autoradiography of the TLC plate used for apparent molar activity measurement is shown in Figure 28.

Additionally, 3.7 ± 0.4 MBq (100 ± 10 μCi) aliquots of $^{43/44g}$Sc were labeled with DOTA-TATE at a molar activity of 0.14 nmol/MBq (5 nmol/mCi) and assayed using HPLC. Radio-HPLC chromatograms (Figure 29) show near quantitative labeling (> 98%). Free radioscandium eluted with the solvent front (4 min) and $^{43/44g}$Sc-DOTA-TATE eluted at 15.6 min.

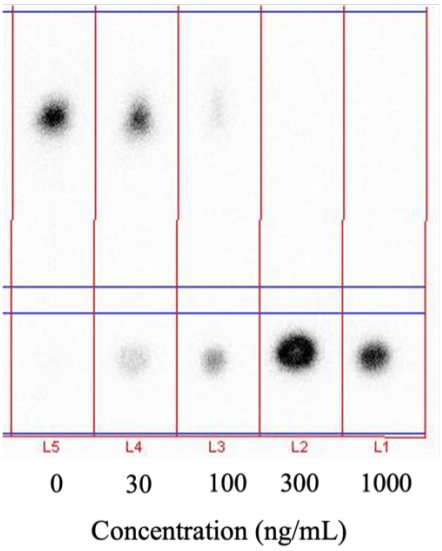


Figure 28: Autoradiography of the titration with a fixed amount of ^{44g}Sc activity mixed with increasing concentrations of DOTA run in EDTA.

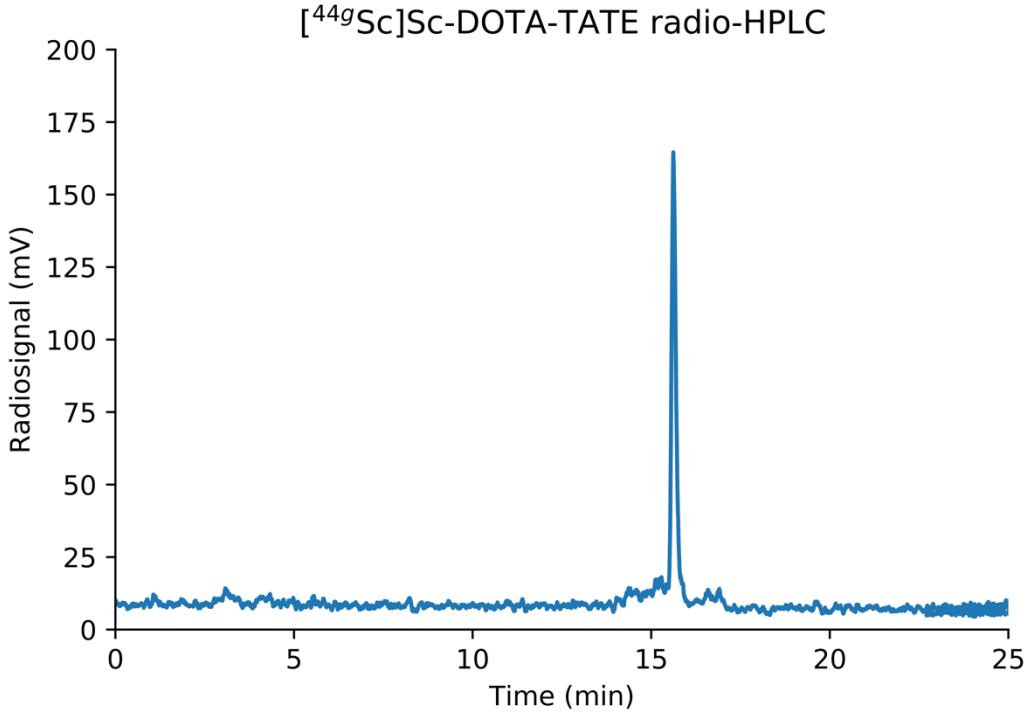


Figure 29: Radio-HPLC chromatogram of [^{44g}Sc]Sc-DOTA-TATE.

Amounts of calcium and commonly seen metals such as iron, zinc, and copper that may affect Sc-labelling were measured through MP-AES and are listed in Table 9 (n = 5). The efficient removal of metals such as iron, zinc, and copper in the radiochemical isolation strategy resulted in the high apparent molar activity observed with $^{43/44g}$Sc and DOTA. The mass of calcium that remained on the column and was co-eluted with the ^{4x}Sc resulted in minimal enriched material loss (< 0.5 mg).

Element	Impurities (ppb or µg/L)
Iron	0.7 ± 0.9
Zinc	1.7 ± 1.3
Copper	1.4 ± 0.1
Calcium	226.5 ± 45.6

Table 9: Trace metals analysis of an eluted fraction of $^{43/44g}$Sc using MP-AES.

2.4 Conclusions

The goal of this work was to optimize $^{43/44g}$Sc production and compare production yields and radionuclidic purity between various ^{43}Sc and ^{44g}Sc production routes. The ^{42}Ca(d,n)^{43}Sc cross section measurement was also attempted using two different target backing approaches. However, poor backing material selection and high humidity conditions resulted in the incomplete measurement of the cross section in both experimental attempts.

Production yield and radionuclidic purity data were collected for several ^{43}Sc and ^{44g}Sc reaction routes. While there are six possible reactions to produce ^{43}Sc and ^{44g}Sc with protons and deuterons on small cyclotrons, the ^{44}Ca(p,2n)^{43}Sc and ^{44}Ca(d,2n)^{44g}Sc reactions are only possible at higher energies (> 15.2 MeV protons and > 5.8 MeV deuterons). The proton-induced reactions investigated here (^{43}Ca(p,n)^{43}Sc and ^{44}Ca(p,n)^{44g}Sc) had significantly higher production yields (by approximately a factor of 10) than the deuteron-induced reactions (^{42}Ca(d,n)^{43}Sc and ^{43}Ca(d,n)^{44g}Sc), but were performed with higher mass targets (approximately 150 mg versus 60 mg CaO) and higher incident energies (13.6 or 15.2 MeV protons versus 5.8 MeV deuterons). The peak of the cross-section curves for the deuteron-induced reactions were not fully captured with the energies and target thickness used here (Figures 12 and 13, gray bar). Therefore, accelerators capable of accelerating higher energy deuterons would be able to capture more of

the cross-section curve and produce higher yields through these routes. Thick target yields for the proton-induced reactions were not investigated in this work due to the large masses (~250 mg CaO) required to degrade the proton energy in the target from 13.6 MeV to 4 MeV where the cross section approaches zero [35].

Due to the relatively low isotopic purity of available ^{43}Ca (83.93%), an EoB radionuclidic purity of only 87.81 ± 0.03% ^{43}Sc was achievable through proton bombardment of ^{43}Ca. The main radioisotopic contaminants from this reaction are ^{44g}Sc at 12.16 ± 0.03 % total activity and ^{48}Sc ($t_{1/2}$ = 43.71 h; β^-_{mean} = 220.5 keV; $\beta^+_{intensity}$ = 100%) at 0.02 ± 0.01% total activity at EoB. The production of ^{44g}Sc results from a (p,n) reaction on the 5.06% ^{44}Ca present in the enriched ^{43}Ca target material and could be minimized through use of higher purity ^{43}Ca target material. With 100% isotopically pure ^{43}Ca, ^{44g}Sc would be removed and ^{43}Ca(p,n)^{43}Sc measured yields would increase to 7.38 mCi/μAh (or 15.06 mCi/μAh when corrected for beam intercept). Considering the alternative deuteron-induced reaction, ^{42}Ca(d,n)^{43}Sc, the radionuclidic purity at EoB was 99.36 ± 0.05% ^{43}Sc at EoB with no co-production of ^{44g}Sc's metastable state ^{44m}Sc. However, this route will require longer irradiation lengths and a cyclotron capable of accelerating deuterons to produce the same EoB activity as the proton-induced route.

The ^{44}Ca(p,n)^{44g}Sc route results both in higher production yields and greater radionuclidic purity than ^{43}Ca(d,n)^{44g}Sc with the conditions investigated in this work. This is partially due to the low purity of the ^{43}Ca and the smaller mass of the target. Cyclotrons capable of accelerating higher energy deuterons (> 8 MeV) along with higher purity and thicker ^{43}Ca targets would increase the production yields compared to those reported here. However, the higher predicted cross sections for the ^{44}Ca(p,n)^{44g}Sc reaction compared to ^{43}Ca(d,n)^{44g}Sc (Figures 12 and 13) suggest that the highest yields of ^{44g}Sc would still be through proton bombardment of ^{44}Ca. The

presence of longer-lived radioisotopes of scandium such as ^{46}Sc are also comparable in both reaction routes in the target thickness and energy range investigated herein: at EoB, there was 0.007 ± 0.003% ^{46}Sc for ^{44}Ca(p,n)^{44g}Sc and 0.013 ± 0.003% ^{46}Sc for ^{43}Ca(d,n)^{44g}Sc.

When considering translation to clinical studies, long-lived radioisotopes of scandium (^{46}Sc, ^{47}Sc, ^{48}Sc) should be minimized to avoid patient dose and handling of radioactive waste. The threshold for ^{68}Ge ($t_{1/2}$ = 270.8 d) impurity set by the European Pharmacopoeia in ^{68}Ge/^{68}Ga generator elutions is 0.001% [94]. The presence of ^{46}Sc ($t_{1/2}$ = 83.79 d), ^{47}Sc ($t_{1/2}$ = 3.3492 d), and ^{48}Sc ($t_{1/2}$ = 43.71 h) for the reaction routes at the irradiation parameters investigated herein are lower than the 0.001% ^{68}Ge limit at EoB with the exception of ^{43}Ca(p,n)^{43}Sc which results in 0.0012% ^{48}Sc at the end of bombardment and ^{43}Ca(d,n)^{44g}Sc which results in 0.013 ± 0.003% ^{46}Sc at end of bombardment, indicating that the lower isotopic enrichment of the ^{43}Ca target material results in lower radionuclidic purity.

Radiochemical isolation was performed using branched DGA resin. From the calcium mass that was measured via MP-AES, the separation factor for this separation is on the order of ~10^5 which is sufficient for simple and efficient target recycling and high radiochemical yields (95 ± 2% enriched calcium recovery and 92 ± 4% $^{43/44g}$Sc activity in 2 mL 0.01 M HCl). Quantitative labeling with DOTA-TATE and high apparent molar activities with DOTA were achieved with this separation strategy and minimal trace metals were observed through MP-AES analysis.

This work demonstrated that isotopically enriched $^{42/43/44}$CaO targets can be used to produce high yield and high radionuclidic purity ^{43}Sc and ^{44g}Sc through proton and deuteron bombardment. While several reaction routes are possible to produce either ^{43}Sc or ^{44g}Sc, the needs of the situation will dictate which reaction route to use (target material costs, yields, radionuclidic purity, etc.).

Chapter 3: Investigation of [$^{43/44g}$Sc]Sc-FAPI as a Model to Image PDAC

3.1 Introduction

Pancreatic ductal adenocarcinoma (PDAC) is an aggressive form of cancer with 5-year survival rates between 5 and 10% [95, 96]. Although the rate of pancreatic cancer amongst all types of cancer is only 3.2%, it makes up 8.2% of all cancer-related deaths [97] with PDAC being the most common type of pancreatic cancer [98]. Multiple factors contribute to the poor prognosis of PDAC: early local tumor spread, lack of effective treatments, absence of a screening biomarker, and failure of contemporary state-of-the-art imaging techniques in early detection [99]. PDAC diagnosis is primarily performed using computed tomography (CT), magnetic resonance imaging (MRI), endoscopic ultrasound (EUS), or positron emission tomography (PET), but traditional methods often miss early-stage disease with only 12% of disease being local at the time of detection [97]. Unfortunately, strategies such as surgical resection are only available when the disease is diagnosed in early stages, and few treatment options are viable once the cancer has metastasized. Approximately 10% of patients already exhibit signs of metastasis at the time of surgery, and of those undergoing surgery, 12.5% develop disease recurrence within 6 months post-surgery [98].

Clinicians frequently use contrast-enhanced CT (CE-CT) for diagnosis and staging of pancreatic cancer [100, 101]. However, small tumor sizes and similar attenuation between PDAC and healthy pancreatic tissue can mask early disease on CT scans. CE-CT has an overall sensitivity of 89% and a specificity of 90% when imaging PDAC [101], but for small (< 2 cm), self-attenuating tumors, the sensitivity drops to 58-77% [101]. Overall, the sensitivity for MRI (84%) is comparable to CE-CT and the choice between CE-CT versus MRI is often decided

based on equipment availability, expertise, and patient eligibility (presence of metal in the body or contrast allergy) [102].

Vascular involvement and pancreatic duct dilation, which are important distinguishing features between pancreatitis and malignant disease, are also often missed on CE-CT and MRI [103]. One retrospective study found that, of 257 cases of PDAC investigated, 66 initial examinations had missed findings and 49 had misinterpreted findings [103]. Misdiagnosis places patients at a higher risk of advanced disease when diagnosed. Thus, early detection of PDAC is important for improving patient outcomes [103].

Like anatomical imaging, currently employed molecular imaging techniques also have limitations when imaging PDAC. The National Comprehensive Cancer Network (NCCN) does not currently recommend [^{18}F]-Fluorodeoxyglucose ([^{18}F]-FDG) as an initial imaging modality for PDAC, and [^{18}F]-FDG is typically only used for high-risk patients [104]. The sensitivity and specificity for [^{18}F]-FDG PET/CT are around 73-92% and 68-86%, respectively, and there have been no conclusive clinical benefits to its use in addition to CT or MRI for staging or diagnosis of PDAC [102].

[^{18}F]-FDG is a glucose analogue with a fluorine-18 atom replacing the hydroxyl group at the C-2 position in a normal glucose molecule. Glucose transporters and hexokinase can still transport and phosphorylate [^{18}F]-FDG similar to glucose [100]; however, once phosphorylated, [^{18}F]-FDG cannot undergo the subsequent steps of glycolysis and accumulates within the cell [105]. [^{18}F]-FDG PET imaging of solid tumors takes advantage of the Warburg effect where cancer cells preferentially produce ATP through glycolysis even in the presence of oxygen [106]. This metabolic pathway is much less efficient than typical aerobic metabolism utilizing the Krebs cycle and the electron transport chain, and, because of this, the rate of glucose uptake is

much higher in cancer cells than healthy cells [106]. However, glucose intolerance is a common symptom of PDAC which causes high levels of blood glucose [100]. Elevated glucose levels lead to lower [^{18}F]-FDG tumor uptake and can result in false negative scans [100]. Pancreatitis and other forms of inflammation also have increased [^{18}F]-FDG uptake and have resulted in false positives [100]. Furthermore, [^{18}F]-FDG's low sensitivity for detecting involved lymph nodes (30-49%) and liver metastases (42.9-60%) limit its applications when determining surgical eligibility [104].

Dense growth of fibrous or connective tissue (demoplasia) containing cancer associated fibroblasts (CAFs) characterize PDAC [107, 108]. These CAFs promote tumor-growth and invasion through sustained proliferative signaling leading to metastases and have been shown to contribute to PDAC's therapy resistance [109]. As opposed to normal fibroblasts, CAFs express fibroblast activation protein-α (FAP), a type II membrane-bound serine protease, on their surfaces [110, 108]. Because FAP is almost exclusively related to pathological conditions (including fibrosis, arthritis, and cancer), it is a promising novel target for PET imaging of PDAC and other epithelial tumors [111, 110]. Labeling FAP-inhibitors (FAPI) with positron emitters enables PET imaging of the FAP-expressing CAFs correlated with tumor development and progression in PDAC (Figure 30) [108]. Because CAFs are so integrated in the development of PDAC (through their tumor proliferating qualities), FAPI-PET imaging could provide useful physiological information for staging the disease [108].

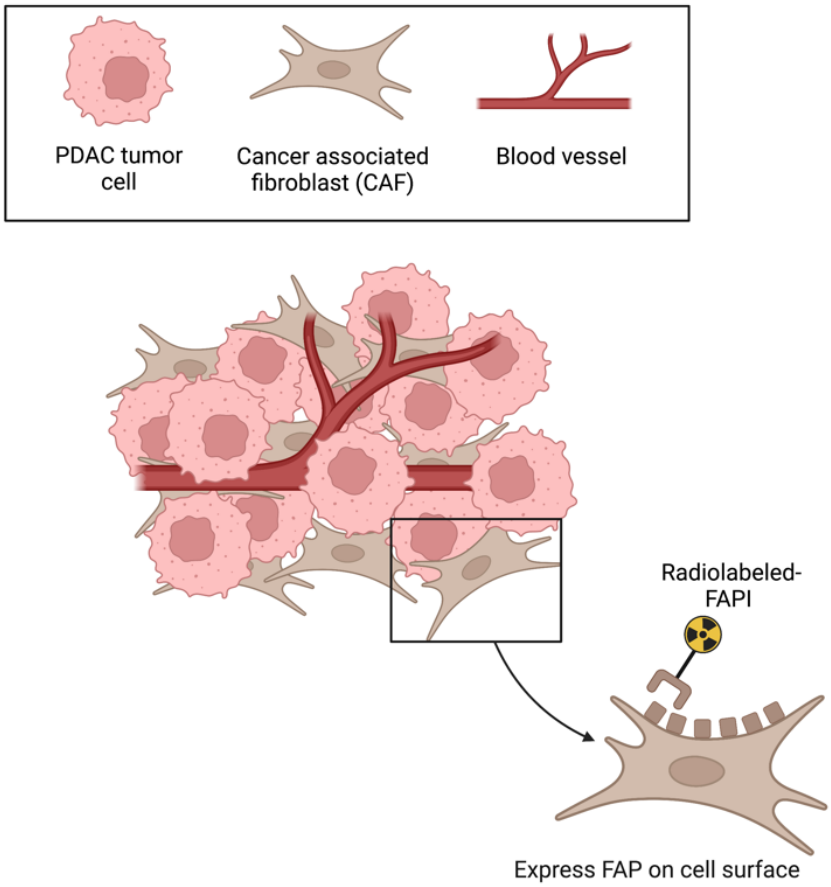


Figure 30: PDAC tumor microenvironment (created with BioRender.com).

^{68}Ga-labeled FAPI PET/CT is better at detecting and staging PDAC than conventional anatomical imaging and [^{18}F]-FDG [110, 112]. However, ^{68}Ga's ($t_{1/2}$ = 67.71 m; β^{+}_{mean} = 829.5 keV; $\beta^{+}_{intensity}$ = 88.91%) relatively high positron energy and short half-life limit its potential and make it suboptimal for imaging early/small lesions. Scandium's two positron-emitting radioisotopes have longer half-lives and lower mean positron energies than ^{68}Ga, potentially enabling longer time-point imaging and higher PET resolution, respectively.

In this study, [^{43}Sc]Sc-FAPI-46's and [^{44g}Sc]Sc-FAPI-46's potential at detecting PDAC in a murine model was compared with [^{68}Ga]Ga-FAPI-46. It was hypothesized that ^{43}Sc and ^{44g}Sc in

place of ^{68}Ga could improve the image quality and potentially lead to detection of smaller lesions/earlier levels of disease.

In addition to Sc-FAPI PET/CT imaging, ^{43}Sc and ^{44g}Sc are of broader clinical interest due to their favorable decay characteristics and theranostic applications in conjunction with ^{47}Sc and other light lanthanides (^{177}Lu, ^{161}Tb, etc.). Physical decay characteristics such as emitted positron energy (and consequently, positron range), co-emitted gammas, etc. affect the reconstructed image quality. While several studies have compared ^{44g}Sc image quality with other clinically used positron-emitting radionuclides [38, 113-115], few studies have investigated ^{43}Sc image quality, and they are limited to preclinical PET/CT scanners [38, 115]. In this work, image contrast and activity recovery between ^{43}Sc, ^{44g}Sc, a mixture of ^{43}Sc and ^{44g}Sc, ^{18}F, ^{64}Cu, and ^{68}Ga using spherical and Derenzo phantoms on two clinical PET/CT scanners was compared.

3.1.2 Motivation

Current standard-of-care imaging techniques for PDAC are insufficient at detecting PDAC early enough for interventional approaches to be effective for many patients. Anatomical imaging modalities such as CE-CT and MRI often miss metastases and small lesions while [^{18}F]-FDG PET provides little benefit over CT imaging and often provides false positives for patients with inflammation. Finding a novel, more effective, imaging modality to detect PDAC early may offer patients more opportunities for curative options such as surgical resection. While [^{68}Ga]Ga-FAPI PET is a promising novel PET radiotracer, ^{68}Ga has several qualities that make it a suboptimal PET radionuclide. It was hypothesized that [$^{43/44g}$Sc]Sc-FAPI will provide a more effective imaging technique for PDAC than [^{68}Ga]Ga-FAPI due to ^{43}Sc and ^{44g}Sc's lower positron energies (and thus higher PET resolution) and longer half-lives (facilitating later time-point imaging).

Additionally, the physical properties of radionuclides (such as positron energy, positron branching ratio, gamma energies, etc.) affect the quality of reconstructed PET images. Various PET image characteristics between ^{43}Sc and ^{44g}Sc with ^{18}F, ^{64}Cu, and ^{68}Ga were compared to determine the clinical relevancy of ^{43}Sc and ^{44g}Sc compared to other potential clinical PET radionuclides.

3.2 Materials and Methods

3.2.1 Chemicals

All solutions were prepared using 18 MΩ cm^{-1} water, and Optima grade hydrochloric and nitric acid purchased from Fisher Chemical. Trace metal free sodium acetate was purchased from Sigma Aldrich, and reagent grade sodium ascorbate was purchased from Fisher Chemical. Branched DGA resin was purchased from Eichrom. Reagent grade ethanol and n-octanol was purchased from Sigma Aldrich. Phosphate-buffered saline (PBS) was purchased from Fisher Chemical. Enriched calcium carbonate ($^{42}CaCO_3$, $^{43}CaCO_3$, and $^{44}CaCO_3$) was obtained from the Department of Energy National Isotope Development Center (see Chapter 2, Table 3 for isotopic enrichment). FAPI-46 precursor (chelating agent: DOTA) was provided by SOFIE (Dulles, VA).

3.2.2 Production and Radiosynthesis of [$^{43/44g}$Sc]Sc-FAPI-46 and [^{68}Ga]Ga-FAPI-46

^{43}Sc was produced through deuteron bombardment of enriched ^{42}CaO targets via the ^{42}Ca(d,n)^{43}Sc reaction on a 16 MeV (8 MeV deuteron) GE Healthcare PETtrace cyclotron at the University of Wisconsin, Madison as described in Chapter 2. Similarly, ^{44g}Sc was produced through proton bombardment of enriched ^{44}CaO targets via the ^{44}Ca(p,n)^{44g}Sc reaction. Radiochemical isolation of $^{43/44g}$Sc from the enriched calcium target material was performed by single-column extraction chromatography utilizing branched DGA resin and methodology described in Chapter 2. ^{68}Ga was obtained in the form of $^{68}GaCl_3$ through elution (5 mL, 0.1 M

HCl) of a GalliaPharm $^{68}Ge/^{68}Ga$ generator (Eckert & Ziegler, Inc.) at the University of Wisconsin's clinical radiopharmaceutical facility.

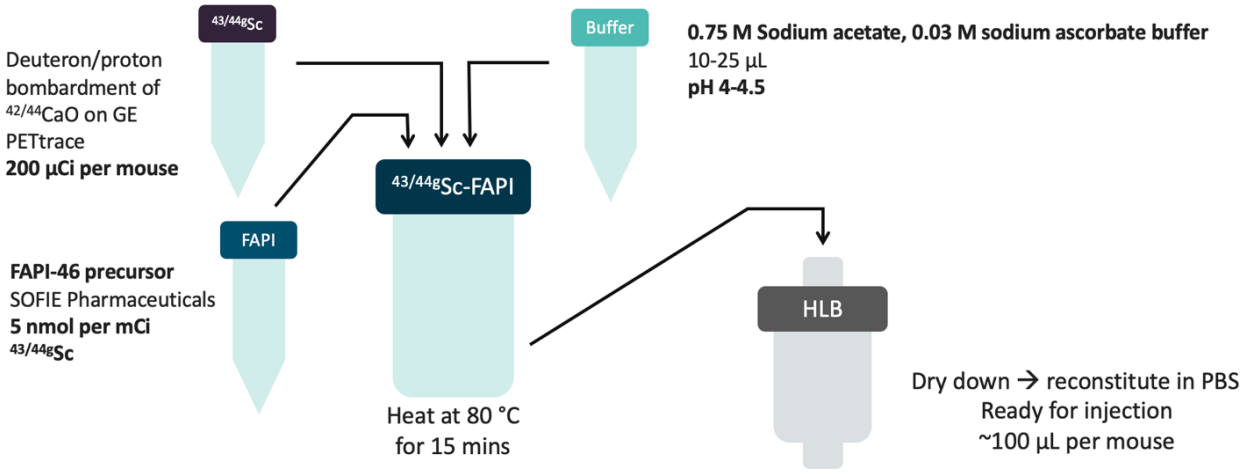


Figure 31: Labelling procedure for [$^{43/44g}$Sc]Sc-FAPI-46.

The [$^{43/44g}$Sc]Sc-FAPI-46 synthesis procedure is shown in Figure 31. Briefly, 37.0 - 64.8 MBq of $^{43/44g}$Sc (250 - 500 µL; 0.01M HCl) was mixed with FAPI-46 precursor (5 nmol/mCi; 7.4 MBq/nmol) and 2 - 25 µL 0.75 M sodium acetate, 0.03 M sodium ascorbate buffer solution (final pH 4 - 4.5) at 80 °C for 15 min under constant shaking (300 rpm). Following labeling, the [$^{43/44g}$Sc]Sc-FAPI-46 solution was purified with a reverse-phase, solid-phase-extraction Oasis HLB light cartridge (Waters) to remove all free $^{43/44g}$Sc. [$^{43/44g}$Sc]Sc-FAPI-46 was then eluted from the column in 1.5 mL absolute ethanol into a vial containing 1 mg/mCi (0.27 mg/MBq) sodium ascorbate to prevent radiolysis. The solution was then dried at room temperature under argon flow and reconstituted in 1 mL/mCi (0.027 mL/MBq) PBS. Radiochemical yield was determined through thin layer chromatography with 50 mM EDTA as a mobile phase. HPLC was also used to determine radiochemical purity using a C18 column (4.6 x 250 mm, Dionex 5µm 120 Å; ThermoFisher) and a water (0.1% Trifluoroacetic acid, TFA) to acetonitrile gradient

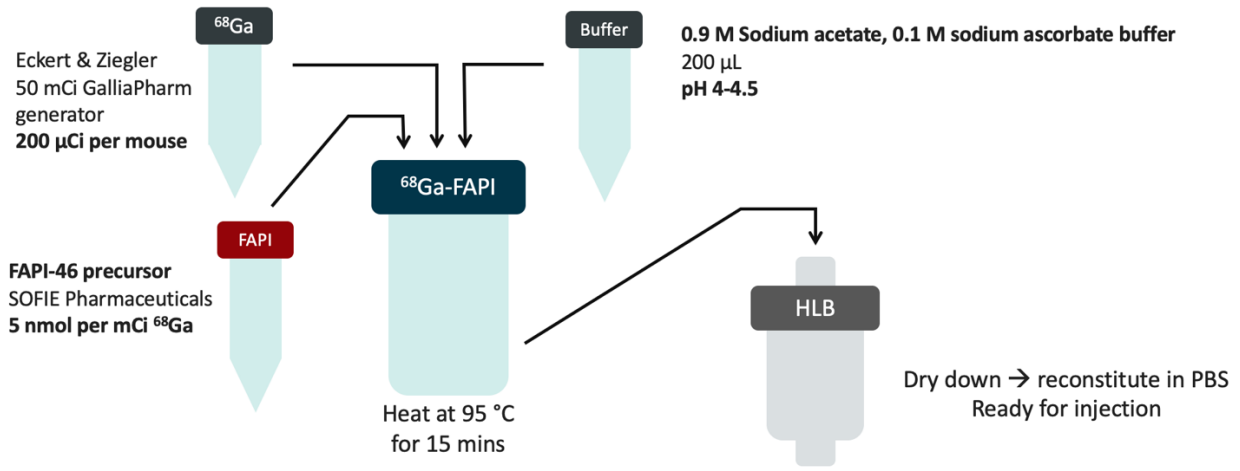


Figure 32: Labeling procedure for [^{68}Ga]Ga-FAPI-46.

(5% MeCN, 0 - 3.5 min; 5% - 35% MeCN, 3.5 - 13 min; 35% - 90% MeCN, 13 - 15 min; 90% MeCN, 15 - 19 min; 90% - 5% MeCN, 19 - 20 min; 5% MeCN, 20 - 25 min) flowing at 1 mL/min.

[^{68}Ga]Ga-FAPI-46 was labeled using a similar procedure to the one described above and is shown in Figure 32. A 1 mL $^{68}GaCl_3$ fraction (148 - 222 MBq) from a GalliaPharm generator was mixed with FAPI-46 precursor (5 nmol/mCi; 7.4 MBq/nmol) and 200 µL 0.9 M sodium acetate, 0.1 M sodium ascorbate buffer (final pH 4 – 4.5) at 95 °C for 15 min under constant shaking (400 rpm). Following labeling, the [^{68}Ga]Ga-FAPI-46 solution was loaded onto an Oasis HLB light cartridge, eluted in absolute ethanol into a vial containing 1 mg/mCi (0.27 mg/MBq) sodium ascorbate, dried, and resuspended in PBS. Radiochemical yield was determined through thin layer chromatography with 50 mM EDTA as a mobile phase. The same HPLC method listed above for [$^{43/44g}$Sc]Sc-FAPI-46 was used to determine radiochemical purity for the final [^{68}Ga]Ga-FAPI-46 formulation.

Lipophilicity measurement

The lipophilicity of [^{68}Ga]Ga-FAPI-46 and [$^{43/44g}$Sc]Sc-FAPI-46 were compared using a shake-flask method (n = 3). Following labeling and purification, 100 μL (5.6 - 7.4 MBq, 150 - 200 μCi) of purified M-FAPI-46 (M = ^{68}Ga, ^{43}Sc, or ^{44g}Sc) was mixed with 900 μL PBS. Additionally, 1 mL n-octanol was added, and the vials were shaken vigorously to combine the phases. Vials were left for 30 min and then centrifuged for 10 min for phase separation. Aliquots (100 μL) were taken from each phase for measurement via a calibrated gamma counter (Wizard 2480, Perkin Elmer). The lipophilicity was calculated using the formula:

$$logP = log(\frac{[solute]_{octanol}}{[solute]_{PBS}}) \quad (5)$$

where $[solute]_{octanol}$ was the counts per minute in the octanol aliquot and $[solute]_{PBS}$ was the counts per minute in the PBS aliquot.

3.2.3 PDAC murine model

Both heterotopic and orthotopic tumor xenograft models were investigated in this study. Heterotopic implantation is a relatively simple procedure that allows for easy and accurate tumor size monitoring and does not require anesthetic. While orthotopic implantation is more difficult and time consuming, the tumor environment for orthotopic models is generally more similar to naturally occurring tumors and is a better approximation for human tumors. All animal studies were conducted under a protocol approved by the University of Wisconsin Institutional Animal Care and Use Committee.

Cell model

A heterotopic murine PDAC model was provided to us by collaborators in the Department of Surgery at the University of Wisconsin School of Medicine and Public Health. Low-passage (< 5) murine pancreatic cancer cells derived from the Kras$^{G12D/+}$; TP53^{R172H}; Pdx1-Cre mouse

model (KPC cell line) (Ximbio, Westfield Stratford City, UK) were grown at 37 °C with 5% CO_2 in DMEM supplemented with 10% FBS (GeminiBio, West Sacramento, CA), L-glutamine (ThermoFisher, Waltham, MA), non-essential amino acids (ThermoFisher), and penicillin-streptomycin (ThermoFisher) [116].

Heterotopic model

To produce the heterotopic model, confluent cells were trypsinized, mixed 1:1 with Matrigel® (Corning Inc, Corning, NY), and 100,000 cells were injected into the right axilla of immunocompetent syngeneic 5 – 8-week-old C57Bl/6J mice (Jackson Laboratory, Bar Harbor, ME) by a surgical oncologist. Matrigel® with DMEM alone was injected in equal volume as an imaging control. Tumors were incubated for 19 - 21 days prior to imaging. Tumor presence was confirmed following imaging histopathologically with necropsy, formalin fixation and paraffin embedding, and H&E staining of tumor tissues by a board-certified gastrointestinal pathologist.

Orthotopic model

For the orthotopic model, detectability was investigated at various lengths of tumor growth and sizes. An orthotopic PDAC model was supplied to us by collaborators in the Department of Surgery performed with the following methodology:

Confluent cells were trypsinized, mixed 1:1 with Matrigel® (Corning Inc, Corning, NY), and 1,250 cells were injected into the pancreata of immunocompetent syngeneic 8–10-week-old C57Bl/6J mice (Jackson Laboratory, Bar Harbor, ME) as previously described [117]. In short, mice were anesthetized with isoflourane (Piramal Critical Care, Mumbai, India) and 0.6 mg/kg of Buprenorphine SR (ZooPharm LLC, Laramie, WY) was administered for pain control. Mice were placed onto a warming pad, shaved, and disinfected, and a 1 - 2 cm left flank incision was made, and the spleen and pancreas carefully exteriorized. A U-40 syringe with a 29.5 g needle

(Amsino International Inc, Pomona, CA) was used to inject 25 μL of cell solution containing 1,250 cells in into the tail of the pancreas. The skin was closed with absorbable 4 - 0 suture and wound clips. Tumors were allowed to develop, and the mice imaged at predetermined time points (10 days, 17 days, 25 days, 4.5 weeks, or 9 weeks following surgical implantation). Additional mice (n = 1 per imaging time point) were injected with Matrigel® and DMEM alone in equal volume as an imaging control.

3.2.4 PET/CT imaging and *ex vivo* biodistribution

Heterotopic model

In vivo imaging was performed on an Inveon small animal μPET/CT scanner (Siemens). Two groups of 4 mice (3 experimental, 1 Matrigel® control) were injected with either 7.2 ± 0.1 MBq (195 ± 3 μCi) [^{43}Sc]Sc-FAPI-46, followed by 7.7 ± 0.2 MBq (208 ± 5 μCi) [^{44g}Sc]Sc-FAPI-46 two days later, or 7.7 ± 0.1 MBq (208 ± 3 μCi) [^{68}Ga]Ga-FAPI-46 in 100 - 250 μL PBS. Access to water was restricted following the injections to reduce bladder volume. All mice underwent PET/CT imaging at 1 and 2 hours p.i., and mice injected with [^{43}Sc]Sc-FAPI-46 and [^{44g}Sc]Sc-FAPI-46 were additionally scanned at 5 and 8 hours p.i. Mice were imaged two at a time in the prone position under isoflurane anesthesia (3.5% induction, 2% maintenance) and PET scans were acquired with 40 - 80 million coincident events (time window 3.432 ns; energy window 350 - 650 keV). For [^{43}Sc]Sc-FAPI-46 scans, the energy window was adjusted to 400 - 650 keV to exclude ^{43}Sc's characteristic 372.9 keV (22.5%) gamma. CT scans were acquired before each PET scan to perform anatomical co-registration and CT attenuation-correction. Following imaging, CT attenuation-corrected PET images were reconstructed using a non-scatter corrected 3-D ordered subset expectation maximization / maximum a posteriori algorithm (OSEM3D/MAP). Radiotracer biodistribution was quantified with volume-of-interest analysis

(Inveon Research Workstation, Siemens) drawn manually and expressed as percent injected activity per gram of tissue (%IA/g). After the final scan, mice were euthanized with CO_2 asphyxiation (and cardiac exsanguination as a secondary method), and major organs were collected for *ex vivo* quantification using a scale and a calibrated gamma counter to validate image-derived data. Because the same mice were injected first with [^{43}Sc]Sc-FAPI-46 and then with [^{44g}Sc]Sc-FAPI-46 two days, *ex vivo* verification for [^{43}Sc]Sc-FAPI-46 was performed separately (n = 2). Tumor presence was confirmed by visual inspection and histologically through hematoxylin and eosin (H&E) staining.

Abdominal uptake investigation

Images from the heterotopic model study showed abdominal uptake in the mice injected with [^{43}Sc]Sc-FAPI-46 and [^{44g}Sc]Sc-FAPI-46 at later time points (> 1 h p.i.). To determine whether the cause for the abdominal intake was ingestion of excreted radiotracer, an additional study was performed. Two heterotopic tumor-bearing mice were injected with 5.9 ± 0.4 MBq (160 ± 10 μCi) [^{44g}Sc]Sc-FAPI-46 in 200 μL PBS 20 days after KPC cell inoculation and scanned on an Inveon μPET/CT at 1 and 3 h p.i. following the same procedure described above. After the final imaging time point, mice were euthanized, and tissues were collected for *ex vivo* biodistribution evaluation. For normal tissues collection procedures, the intestines and stomach were emptied of their contents to measure the uptake solely in the tissue. For this experiment, the contents of the intestines and stomach were collected along with the tissue to determine if there was activity that was ingested and digested. Uptake was expressed as %IA/g and intestinal and stomach uptake was compared between the full stomach and intestines and initial experiments (where just the tissue was measured).

Orthotopic model

Metallic surgical clips were used to seal the incision site in the orthotopic model and left on for 12 - 14 days following surgery. For the group of mice scanned at 10 days post-surgery, clips were removed 1 hour prior to the first PET/CT imaging time-point to avoid metallic CT artifacts. For all other mouse cohorts, surgical clips were removed prior to the day of scanning. Access to water for all mouse groups was restricted following injection to limit bladder volume.

In vivo imaging on an Inveon μPET/CT scanner was performed for each tumor development period. Due to relative ease of production and similar image quality observed during the heterotopic imaging study, mice were only injected with [^{44g}Sc]Sc-FAPI-46 for the orthotopic model studies as opposed to both [^{43}Sc]- and [^{44g}Sc]Sc-FAPI-46 (as was done for the heterotopic studies).

Mouse cohorts with 10-day, 17-day, and 25-day tumor development periods (n = 4 per group; 3 experimental, 1 Matrigel® control) were injected with 7.2 ± 0.3 MBq (195 ± 7 μCi) [^{44g}Sc]Sc-FAPI-46 in 250 μL PBS and scanned at 1, 3, and 4 h p.i. Like the heterotopic model, mice were imaged two at a time in the prone position under isoflurane anesthesia and PET scans were acquired with 40 - 80 million coincident events (time window 3.432 ns; energy window 350 - 650 keV). CT scans were acquired prior to PET acquisition to perform anatomical co-registration and CT-attenuation correction. CT-attenuation corrected PET images were reconstructed using non-scatter corrected OSEM3D/MAP. There was no appreciable difference in image quality at 3 and 4 h p.i. so mice with 4.5-week and 9-week tumor incubation periods were just scanned at 1 and 3 h p.i. Following the final imaging time-point, mice were euthanized using CO_2 asphyxiation (with cardiac exsanguination as a secondary method) and organs of interest were collected to verify image-derived data as described for the heterotopic model.

Tumor detectability was also compared between [^{68}Ga]Ga-FAPI-46 and [^{44g}Sc]Sc-FAPI-46 PET/CT at the 4.5-week tumor growth period. A group of 6 mice (5 experimental, 1 Matrigel® control) was first injected with 4.2 ± 0.9 MBq (113 ± 24 μCi) [^{68}Ga]Ga-FAPI-46 in 150 μL PBS and scanned at 1 h p.i. Mice were scanned, and PET/CT images reconstructed following the same protocol described above. One day later, the same cohort of mice were injected with 5.7 ± 0.1 MBq (155 ± 3 μCi) [^{44g}Sc]Sc-FAPI-46 in 150 μL PBS and scanned at 1 and 3 h p.i. Following the final imaging time-point, *ex vivo* biodistribution was analysis was performed as discussed previously.

The last cohort of mice (3 experimental, 1 Matrigel® control) had tumors that were allowed to develop for 9 weeks. Mice were injected with 7.7 ± 0.1 MBq (209 ± 3 μCi) [^{44g}Sc]Sc-FAPI-46 in 250 μL PBS and scanned at 1 and 3 h p.i. Mice were scanned, and PET/CT images reconstructed and analyzed following the same protocol described above.

Incisional uptake study

At the three earliest tumor development periods (10, 17, and 25 days), there was uptake on the left flank of each mouse where the surgical incision was made. The signal was strongest in the 10-day cohort scans and was no longer visible in the 9-week cohort images leading to the hypothesis that this was likely uptake from the incisions and not from pancreatic or tumor uptake. In normal wound healing, fibroblasts are recruited to the site of the wound to create new extracellular matrix and other structures to help close the wound [118]. The presence of these fibroblasts at the incision site would likely lead to M-FAPI-46 uptake. To confirm that the uptake in the images was from the incision, a small sample of the incision was taken for uptake analysis during *ex vivo* organ collection.

Gallbladder uptake investigation

During the 4.5-week scans, high uptake was observed in a region near the liver. This was suspected to either be liver, pancreatic, or gallbladder uptake. The gallbladder was not normally removed during *ex vivo* analysis for the other experiments. However, when high uptake in this region was observed during the early time-point scans, the decision was made to collect the gallbladder during *ex vivo* organ collection to compare uptake between the tumor, gallbladder, and liver to determine the source of the high uptake.

3.2.5 Partial volume effect investigation

When tracer uptake is quantified in small structures, the partial volume effect (PVE) can lead to underestimation of activity concentration in reconstructed PET images. There are two phenomena that contribute to the PVE: the finite spatial resolution of the imaging system and the range of the emitted positron before it annihilates. The finite spatial resolution of the system results in three-dimensional blurring of the source. As a result, the reconstructed feature becomes larger and lower intensity than the true object. The spatial resolution of the system primarily contributes to the PVE when the lesion or structure is less than three times the full width at half maximum (FWHM) [119]. Small animal PET scanners have better resolution than human scanners with spatial resolutions around 1.5 mm compared to approximately 5 mm on human scanners [120]. At the high spatial resolution of small animal PET scanners, the effect of the positron range becomes a larger factor than on human scanners. Several studies have investigated the accurate recovery of activity in phantoms with different radionuclides with varying positron energies and have consistently found that higher positron energies lead to lower recovery in small rod diameters [113, 114, 121].

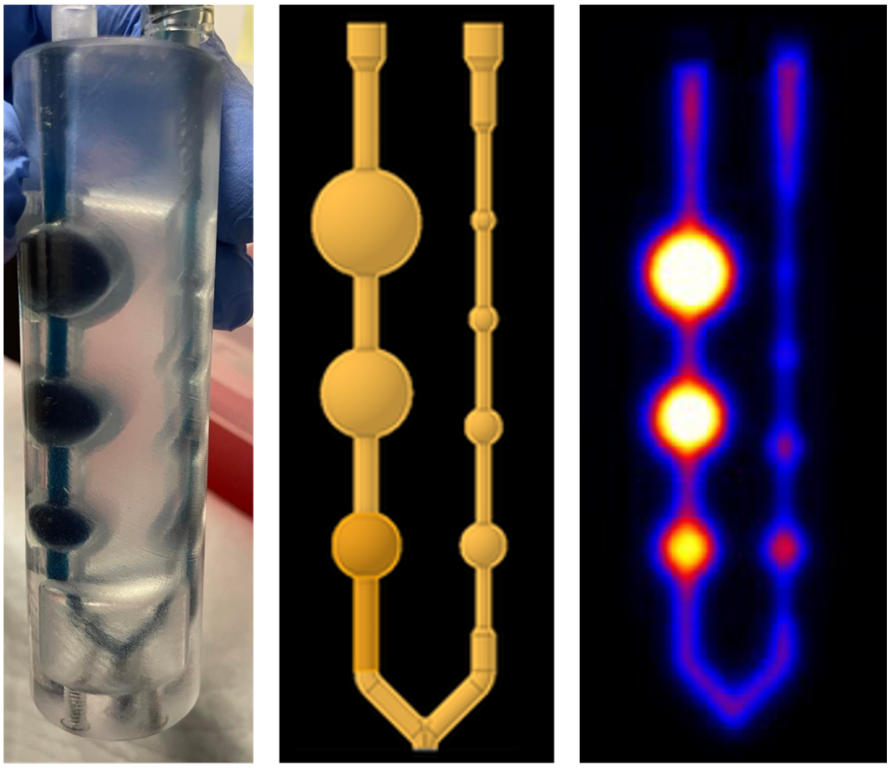


Figure 33: Linear channel, spherical partial volume effect phantom purchased from Phantech. (Left) PVE phantom filled with dye; (center) CAD drawing; (right) PET scan of the phantom filled with ^{68}Ga.

Rosar et. al measured recovery coefficients for phantoms filled with ^{68}Ga and ^{44g}Sc and found a 40.8 to 43.1% increase in recovery coefficients for ^{44g}Sc compared to ^{68}Ga when investigating diameters between 1 and 5 mm [114]. Ferguson et. al similarly compared recovery coefficients between ^{68}Ga, ^{44g}Sc, ^{64}Cu, and ^{18}F and found that ^{68}Ga had the lowest recovery coefficients (ranging from approximately 0.1 for 1 mm rods to 0.6 for 5 mm rods) with ^{44g}Sc having only slightly lower recoveries compared to ^{18}F (approximately 0.2 - 0.8 compared to 0.3 - 0.9) [113]. This study indicates that the effect of the positron range on spatial blurring decreases as the range of the positron approaches the intrinsic resolution of the system.

To assess activity quantification of small structures on the scale of the murine organs that were investigated in this study, a small linear channel spherical phantom (Figure 33) was scanned on the Inveon μPET/CT scanner used to image the mice in the previous section. The phantom was filled with a known concentration of ^{68}Ga and ^{44g}Sc, allowing time between scans for ^{68}Ga to completely decay away (> 12 hours) before filling with ^{44g}Sc. The ^{68}Ga and ^{44g}Sc concentrations used to fill the phantom are shown in Table 10. The filled phantom was placed in the center of the PET bed and static PET scans were acquired with 200 million coincident events (time window 3.432 ns; energy window 350 - 650 keV). Volumes of interest (VOIs) were drawn on CT-attenuation corrected, non-scatter corrected OSEM3D/MAP reconstructed PET/CT images using CT thresholding to select each spherical region of the phantom. The mean activity concentration in each VOI was divided by the known activity concentration to obtain a recovery coefficient:

$$RC_{sphere} = \frac{C_{mean,image}}{C_{filled}} \quad (6)$$

where $C_{mean,image}$ is the mean concentration from image derived VOIs and C_{filled} is the known activity concentration. The mean activity concentration rather than the max concentration was used in this formula to replicate the analysis procedure used for organ uptake quantification in the animal analysis discussed in the previous section.

Radionuclide	**Activity concentration**
^{68}Ga	291 μCi/mL (10.8 MBq/mL)
^{44g}Sc	367 μCi/mL (13.6 MBq/mL)

Table 10: Activity concentrations used to fill the partial volume effect phantom.

3.2.6 Comparison of $^{43/44g}$Sc to conventionally used PET radionuclides on clinical scanners

In this study, ^{43}Sc, ^{44g}Sc, and a mixture of ^{43}Sc and ^{44g}Sc ($^{43/44g}$Sc) were compared to other positron-emitting radionuclides (^{18}F, ^{68}Ga, and ^{64}Cu) in clinical Derenzo and spherical phantoms (acrylic) purchased from Phantech (Madison, WI). The University of Wisconsin, Madison's GE PETtrace cyclotron was used to produce ^{43}Sc (^{42}CaO(d,n)^{43}Sc), ^{44g}Sc (^{44}CaO(p,n)^{44g}Sc), ^{18}F ($H_2{}^{18}$O(p,n)^{18}F), and ^{64}Cu (^{64}Ni(p,n)^{64}Cu). The mixture of $^{43/44g}$Sc (88% ^{43}Sc, 12% ^{44g}Sc by activity at end of chemistry) was obtained through 13.6 MeV proton bombardment of 83.93% isotopically enriched ^{43}CaO targets containing 5.06% ^{44}Ca. ^{68}Ga was eluted from a GalliaPharm ^{68}Ge/^{68}Ga generator (5 mL, 0.1 M HCl, Eckert & Ziegler, Inc.) at the University of Wisconsin, Madison's radiopharmaceutical production facility. Table 11 lists the physical decay characteristics of the radionuclides used in this study and the effective half-life, positron branching ratio, and positron energy for the $^{43/44g}$Sc mixture.

The Derenzo phantom consisted of 6 sections of rods (diameters: 3.5, 4.0, 4.5, 5.0, 5.5, and 6.0 mm) and was filled with activities shown in Table 12. The concentrated activity solutions were prepared by first mixing 250 mL 18 MΩ cm^{-1} water, 200 µL Tween® 80 (Sigma-Aldrich), 25 µL 6 M HCl (final pH 4.5), and then adding the radioactivity (2.74 – 19.97 MBq; 0.075 – 2.16 mCi). Tween® was used to prevent bubbles from forming in the linear Derenzo phantom and the acid was added to prevent the radiometals from sticking to the walls of the phantom. Additionally, 2 - 3 drops of food coloring were added to facilitate detection of air bubbles when filling the small rods of the Derenzo phantom.

The spherical phantom was used to determine recovery coefficients (RC) in a large uniform background region as well as in spheres of varying diameters. The phantom consisted of six fillable spheres (diameters = 1, 1.3, 1.7, 2.2, 2.8, and 3.7 cm) surrounded by a uniform, fillable

background region of 3.1 L. While the lesion to background ratio was kept constant between radionuclides (approximately 5:1), filled activities were increased for low positron intensity radionuclides (^{64}Cu) and short-lived radionuclides (^{68}Ga and ^{18}F) to keep scan times consistent (under 15 minutes). The solutions for the background region were prepared with 3.1 L 18 MΩ cm^{-1} water, 200 μL 6 M HCL (final pH 4.5), and the radioactivity (6.73 – 51.05 MBq; 0.18 – 1.38 mCi). Filled activities along with the lesion to background ratio are shown in Table 12.

Radioactivity was drawn into 1 mL syringes and measured in a Capintec CRC-15R dose calibrator before and after adding to the prepared solutions. Dose calibrator settings for each radionuclide are shown in Table 13. In addition, small samples of radioactivity were independently drawn into syringes and cross-measured on the dose calibrator and an HPGe detector to determine correction factors (Table 13).

	^{43}Sc	**^{44g}Sc**	**$^{43/44g}$Sc**	**^{68}Ga**	**^{64}Cu**	**^{18}F**
Half-life	3.891(12) h	3.97(4) h	3.90 h	67.71(8) min	12.7006(20) h	109.77(5) min
β^+ ratio	0.881(8)	0.9427(5)	0.888	0.8891(9)	0.1749(15)	0.9673(4)
$E_{\beta+mean}$ (keV)	476(6)	632.0(10)	494.7	829.5(13)	278(3)	249.8(3)
E_γ (keV)	372.9(3) 22.5%	1157.020(15) 99.9(4)%	--	1077.34(5) 3.22%		

Table 11: Physical decay characteristics, effective half-life, and positron intensity of the radionuclides used in this study [1].

	Hot sphere and Derenzo activity concentration (kBq/mL)	**Background activity concentration (kBq/mL)**	**Lesion to background ratio**
^{43}Sc	13.04	2.73	4.78
^{44g}Sc	10.97	2.17	5.06
$^{43/44g}$Sc	15.43	3.12	4.95
^{68}Ga	26.23	5.93	4.43
^{64}Cu	79.87	16.47	4.85
^{18}F	43.85	8.58	5.11

Table 12: Filled radioactivity for the hot spheres (same solution used for the Derenzo phantom) and background regions derived from dose calibrator and HPGe recorded activities and measured volumes.

	Dose calibrator setting #	**Dose calibrator measured activity (µCi)**	**HPGe measured activity (µCi)**	**Correction factor**
^{43}Sc	825	9	9.1	1.01
^{44g}Sc	938	60	60.8	1.01
$^{43/44g}$Sc	825	29	30.9	1.07
^{68}Ga	416	25	23.6	0.94
^{64}Cu	015	57	52.8	0.93
^{18}F	455	37	29.5	1.07

Table 13: Calibration sample activities measured on the Capintec dose calibrator and an HPGe detector. Correction factors were applied to the dose calibrator-derived activities.

Both phantoms were scanned on a clinical GE Discovery 710 and GE Discovery MI PET/CT (GE Healthcare, Waukesha, WI) scanner (orientation of the phantoms shown in Figure 34). The GE Discovery 710 has 13824 lutetium-yttrium oxyorthosilicate (LYSO) scintillator crystals (4.2

x 6.3 x 25 mm^3) optically connected to photomultiplier tubes without a light-guide [122]. The axial field of view is 15.7 cm, and the transaxial field of view is 70 cm. The energy window is 425 - 650 keV with a coincidence window of 4.9 ns. The GE Discovery MI has 19584 LYSO scintillator crystals (3.95 x 5.3 x 25 mm^3) connected to arrays of silicon photomultiplier (SiPM) detectors through light-guides [123]. The axial field of view is 20 cm, and the transaxial field of view is 70 cm. The energy and coincidence windows are identical to the GE Discovery 710 at 425 - 650 keV and 4.9 ns, respectively. Ten million coincidences were collected for the Derenzo and 60 million coincidences for the spherical phantom regardless of which radionuclide the phantom was filled with. Data were reconstructed using an ordered subset expectation maximum – time of flight (OSEM-TOF) reconstruction algorithm (VPFX; without point spread function) with a 256 x 256 matrix size and 16 subsets, 8 iterations on the GE Discovery MI and 24 subsets, 5 iterations on the GE Discovery 710.

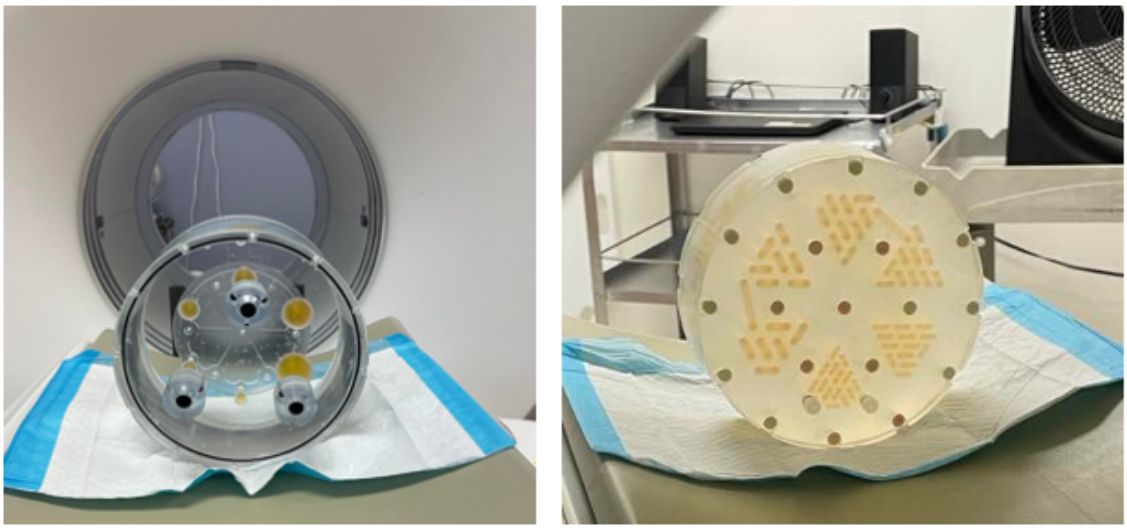


Figure 34*:* Setup orientation of the spherical phantom (left) and Derenzo phantom (right) on the beds of the PET/CT scanners used in this study.

Volumes of interest with diameters greater than the spherical inserts were manually drawn on CT-attenuation corrected PET scans (Horos) encompassing each region. The recovery coefficient was determined through the following formula:

$$RC_{sphere} = \frac{A_{sphere,measured}}{A_{sphere,filled}} \quad (7)$$

where $A_{sphere,measured}$ is the maximum measured voxel activity concentration within each sphere, and $A_{sphere,filled}$ is the expected activity concentration in each sphere. Additionally, $RC_{background}$ values were calculated for the uniform background region where no hot spheres were present. This was done by drawing 5 regions of interest (ROIs) of equal diameters in the center of the phantom and averaging the mean activity concentration and dividing by the known background activity concentration:

$$RC_{background} = \frac{A_{background,measured}}{A_{background,filled}} \quad (8)$$

where $A_{background,measured}$ is the image-derived mean activity concentration of the background and $A_{background,filled}$ is the expected background activity concentration.

Contrast was also compared across the six radionuclides using a linear channel Derenzo phantom. To determine contrast, a transverse slice in the center of the phantom was selected and a line profile was drawn from the center of one outermost rod to the center of the opposing outermost rod. The maximum and minimum values were then used to calculate the contrast:

$$C_{rod} = \frac{R_{max} - R_{min}}{R_{max} + R_{min}} \quad (9)$$

where R_{max} is the maximum value and R_{min} is the minimum value from the line profile.

3.3 Results and Discussion

3.3.1 Production and Radiosynthesis of [$^{43/44g}$Sc]Sc-FAPI-46 and [^{68}Ga]Ga-FAPI-46

[$^{43/44g}$Sc]Sc-FAPI-46 labeling was found to have a strong dependence on pH (Figure 35 (left)). When the pH of the labeling solution was too basic (> 4.5), labeling significantly decreased. As

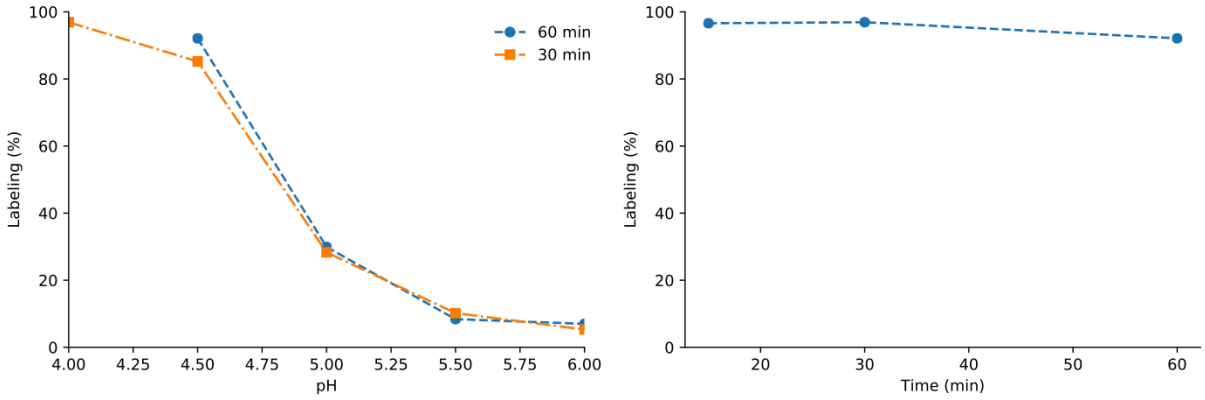


Figure 35: [$^{43/44g}$Sc]Sc-FAPI-46 labeling dependence on pH (left) and time (right).

discussed in section 2.3.6, pH plays a critical role in scandium labelling because scandium will form hydroxide complexes such as $Sc(OH)^{2+}$, $Sc(OH)_2^{+}$, and $Sc(OH)_3$ in pH above 4.5. In contrast, labeling was not found to have a significant dependence on reaction time above 15 minutes (Figure 35 (right)).

[^{43}Sc]Sc-FAPI-46, [^{44g}Sc]Sc-FAPI-46 and [^{68}Ga]Ga-FAPI-46 were produced with near quantitative yields (96 ± 1%) after a 15 min incubation period with an apparent molar activity of 5 nmol/mCi (7.4 MBq/nmol). Following purification, radio-HPLC showed a single peak (retention time = 12.24 min) corresponding to labeled [^{68}Ga]Ga-FAPI-46 (Figure 36 (left)) and for [$^{43/44g}$Sc]Sc-FAPI-46 (Figure 36 (right)).

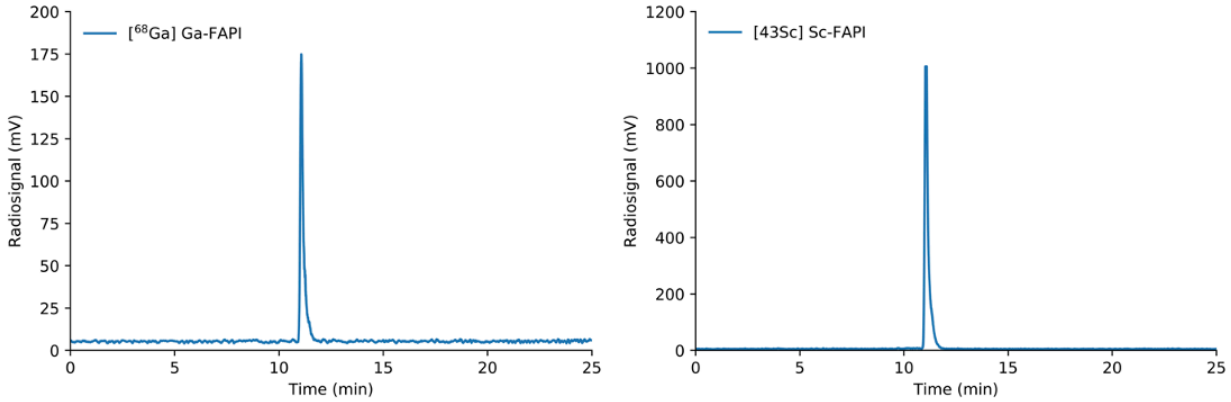


Figure 36: Radio-HPLC traces for [^{68}Ga]Ga-FAPI-46 (left) and [$^{43/44g}$Sc]Sc-FAPI-46 (right). [^{44g}Sc]Sc-FAPI-46 has an identical radio-HPLC trace to [^{43}Sc]Sc-FAPI-46.

The stability of [$^{43/44g}$Sc]Sc-FAPI-46 in PBS was evaluated up to 12 h by HPLC (Figure 37). Stabilities higher than 97% via TLC at 12 h were observed and a single radio peak was seen via HPLC at the retention time of [$^{43/44g}$Sc]Sc-FAPI-46 with no additional peaks, indicating minimal degradation of [$^{43/44g}$Sc]Sc-FAPI-46 in PBS.

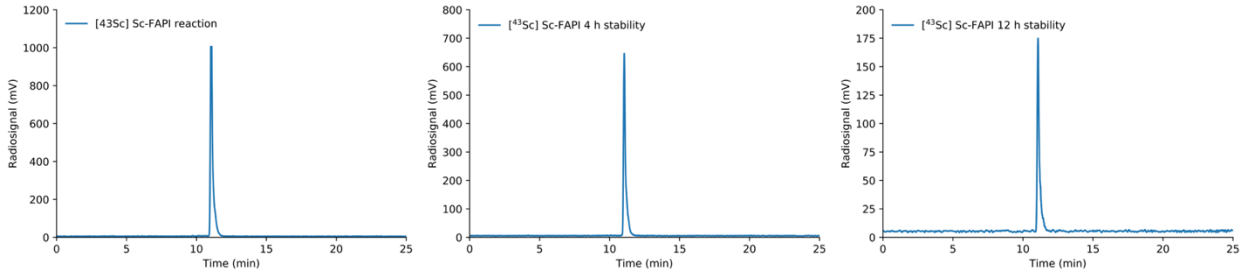


Figure 37: Radio-HPLC chromatogram of the [^{43}Sc]Sc-FAPI-46 reaction at 0 h (left), 4 h (center), and 12 h (right) in PBS.

Lipophilicity

Radioligand	**LogD$_{7.4}$**
[^{68}Ga]Ga-FAPI	-2.37 ± 0.09
[$^{43/44g}$Sc]Sc-FAPI	-2.39 ± 0.08

Table 14: Measured distribution coefficients for each radioligand studied in this work.

Differences in the lipophilicity between two molecules can have implications for clearance in the body (route and rate) and binding to off-target hydrophobic targets. The logD$_{7.4}$, n-octanol/PBS distribution coefficient was -2.37 ± 0.09 for [^{68}Ga]Ga-FAPI-46 and -2.39 ± 0.08 for [$^{43/44g}$Sc]Sc-FAPI-46 (Table 14). The identical logD$_{7.4}$ values indicate that both Ga-FAPI-46 and Sc-FAPI-46 have comparable lipophilicity and likely little to no difference in absorption or metabolic clearance.

3.2.3 PET/CT imaging and *ex vivo* biodistribution

Heterotopic Model

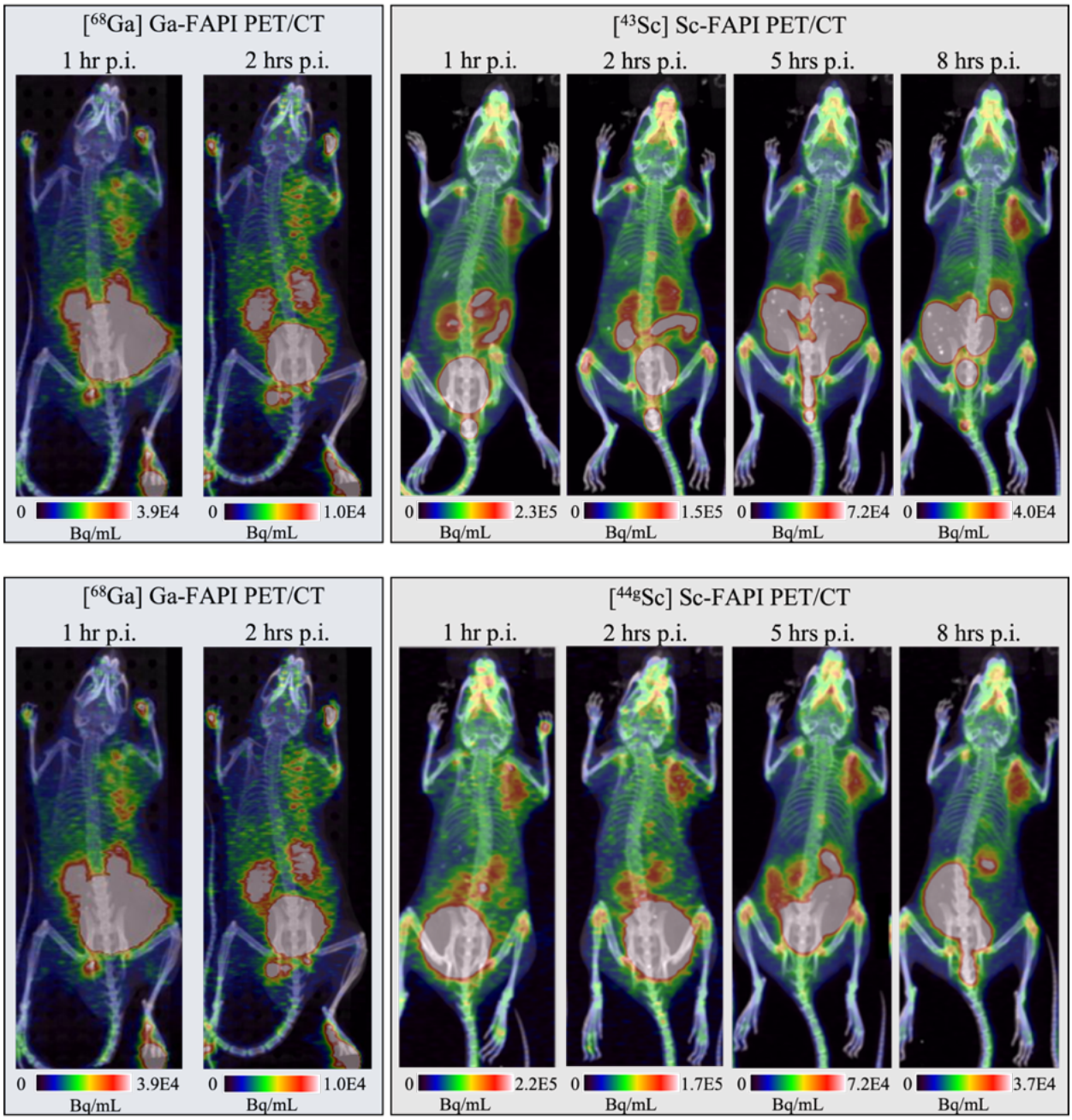


Figure 38: MIP PET/CT images of a representative mouse injected with [^{68}Ga]Ga-FAPI-46 (top left and bottom left), [^{43}Sc]Sc-FAPI-46 (top right), and [^{44g}Sc]Sc-FAPI-46 (bottom right).

Figure 38 contains maximum intensity projection (MIP) PET/CT images of a representative mouse injected with [^{68}Ga]Ga-FAPI-46, [^{43}Sc]Sc-FAPI-46, and [^{44g}Sc]Sc-FAPI-46 at each time point investigated (tumor located on right axilla of all mice). PET scales were adjusted to optimize tumor signal while minimizing bladder artifacts. Uptake of M-FAPI-46 can be seen in the tumor in all experimental animals at all imaging time points. In the mice injected with a Matrigel® control, no M-FAPI-46 uptake was seen in the injection area, indicating tumor-specific uptake (Figure 39).

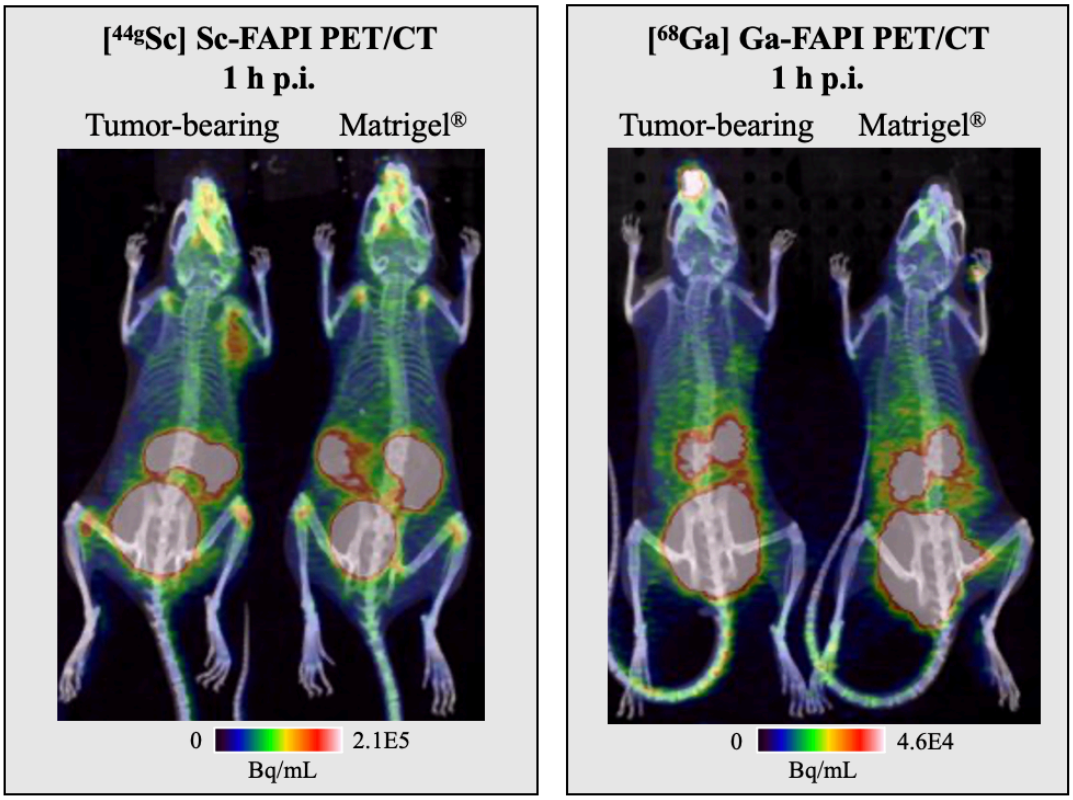


Figure 39: MIP PET/CT images of a tumor-bearing mouse and Matrigel® control mouse injected with [^{44g}Sc]Sc-FAPI-46 (left) and [^{68}Ga]Ga-FAPI-46 (right) at 1 h p.i.

Mice injected with both [^{43}Sc]Sc-FAPI-46 and [^{44g}Sc]Sc-FAPI-46 showed higher tumor uptake and subjectively higher image quality at both 1 and 2 hours p.i. compared to [^{68}Ga]Ga-FAPI-46. Additionally, images of the [^{68}Ga]Ga-FAPI-46 injected mice exhibited more artifacts from high bladder and kidney activity compared to the [$^{43/44g}$Sc]Sc-FAPI-46 injected mice. While the short half-life of ^{68}Ga prevented imaging at time points later than 2 hours p.i., mice injected with [$^{43/44g}$Sc]Sc-FAPI-46 were additionally scanned at 5 and 8 hours p.i. (Figure 38) and continued to exhibit high tumor uptake even at 8 hours p.i. Tumor signal, uptake, and image quality were similar across [^{43}Sc]Sc-FAPI-46 and [^{44g}Sc]Sc-FAPI-46.

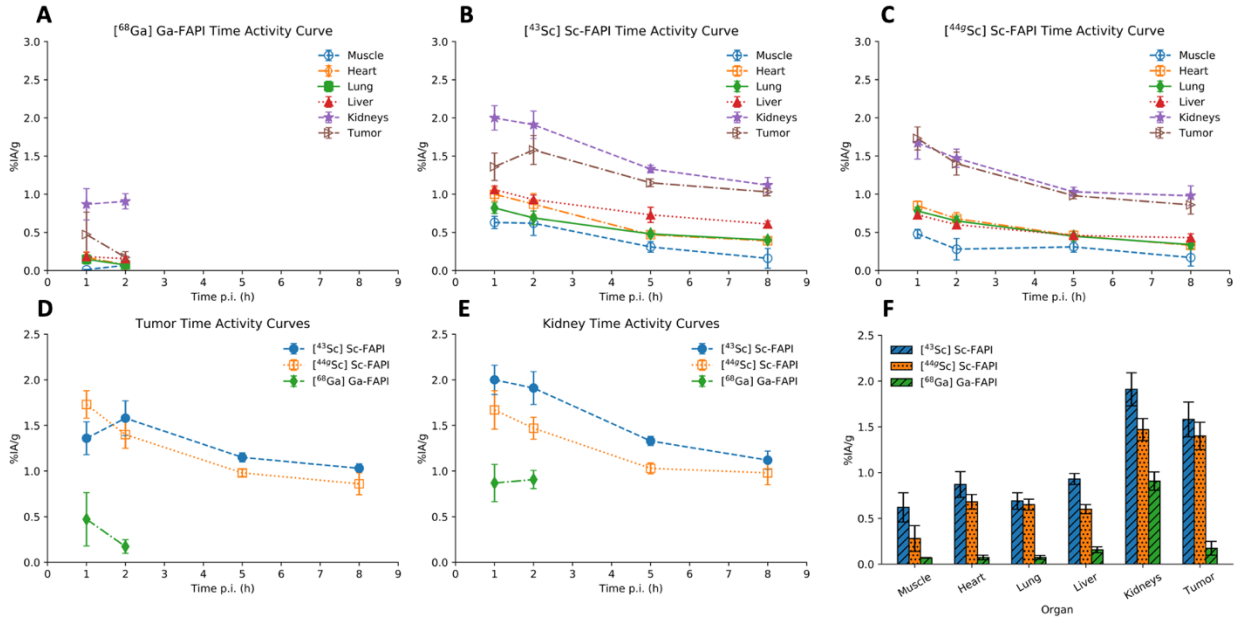


Figure 40: (A-C) Time dependent uptake of [^{68}Ga]Ga-FAPI-46 (A), [^{43}Sc]Sc-FAPI-46 (B), and [^{44g}Sc]Sc-FAPI-46 (C) in organs of interest. (D-E) Time dependent uptake of [^{68}Ga]Ga-FAPI-46 (green diamond), [^{43}Sc]Sc-FAPI-46 (blue circle), and [^{44g}Sc]Sc-FAPI-46 (orange square) in the tumor (D) and kidneys (E) at each imaging time-point. (F) Image-derived %IA/g in each tissue at 2 h p.i. for [^{68}Ga]Ga-FAPI-46 (green hash, right-most), [^{43}Sc]Sc-FAPI-46 (blue hash, left-most), [^{44g}Sc]Sc-FAPI-46 (orange dots, center).

Radiotracer biodistribution at each imaging time point was quantified through region of interest (ROI) analysis performed using Inveon Research Workstation and can be seen in Figure 40 (A-E). Figure 40 (F) additionally shows the image-derived uptake for [^{68}Ga]Ga-FAPI-46, [^{43}Sc]Sc-FAPI-46, and [^{44g}Sc]Sc-FAPI-46 at 2 h p.i. Uptake of [$^{43/44g}$Sc]Sc-FAPI-46 in target and non-target tissues was significantly higher compared with uptake of [^{68}Ga]Ga-FAPI-46. At 2 h p.i., uptake in tumor tissue was 1.6 ± 0.2 %IA/g for [^{43}Sc]Sc-FAPI-46 and 1.4 ± 0.2 %IA/g for [^{44g}Sc]Sc-FAPI-46 compared to 0.2 ± 0.1 %IA/g for [^{68}Ga]Ga-FAPI-46. Kidney uptake was more comparable at 2 h p.i. at 1.9 ± 0.2 %IA/g for [^{43}Sc]Sc-FAPI-46 and 1.5 ± 0.1 %IA/g for [^{43}Sc]Sc-FAPI-46 compared to 0.9 ± 0.1 %IA/g for [^{68}Ga]Ga-FAPI-46 (Figure 40, F).

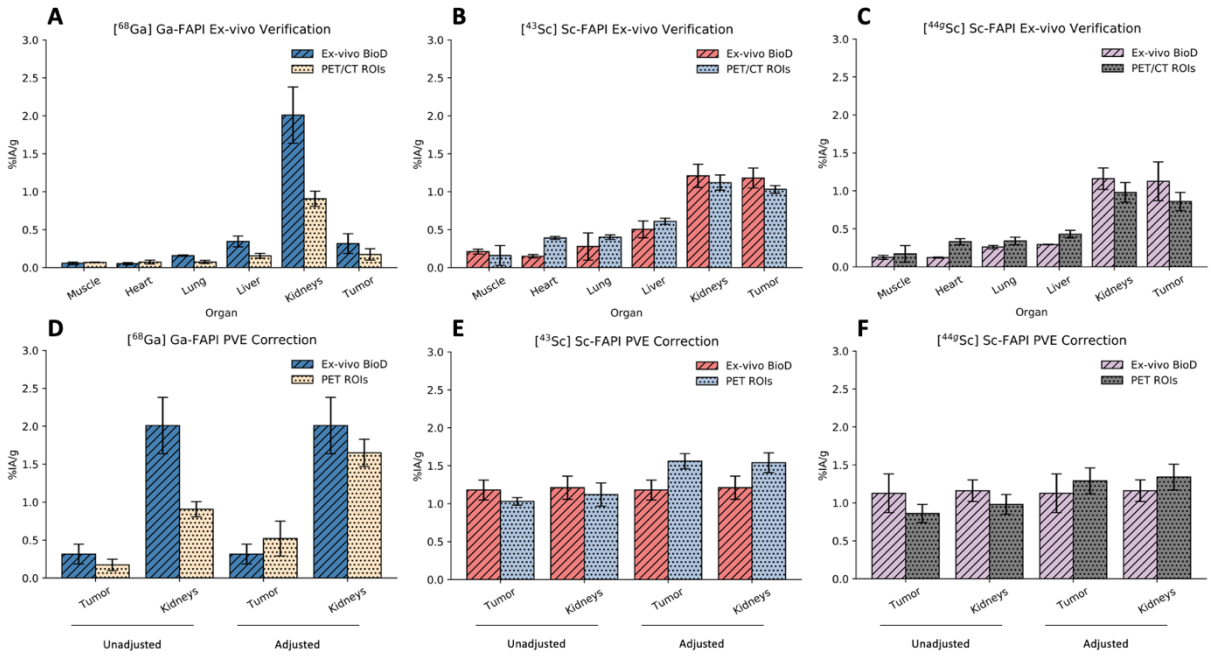


Figure 41: (A-C) *Ex vivo* biodistribution verification for each radiotracer investigated here. (D-F) PET/CT ROI-derived %IA/g adjusted for partial volume effect compared to *ex vivo* biodistribution data.

ROI-derived data were compared to *ex vivo* biodistribution measured with a scale and calibrated gamma counter (Figure 41, A-C). Image-derived data and *ex vivo* biodistribution %IA/g agree within error for [$^{43/44g}$Sc]Sc-FAPI-46 but differ for [^{68}Ga]Ga-FAPI-46 with image-derived %IA/g values lower than measured *ex vivo* values (Figure 41, A-C). As discussed in section 3.2.5, large positron ranges in tissue may result in a larger reconstructed spatial distribution of the activity than the true feature size. This results in an underestimation of activity from reconstructed images than the true uptake.

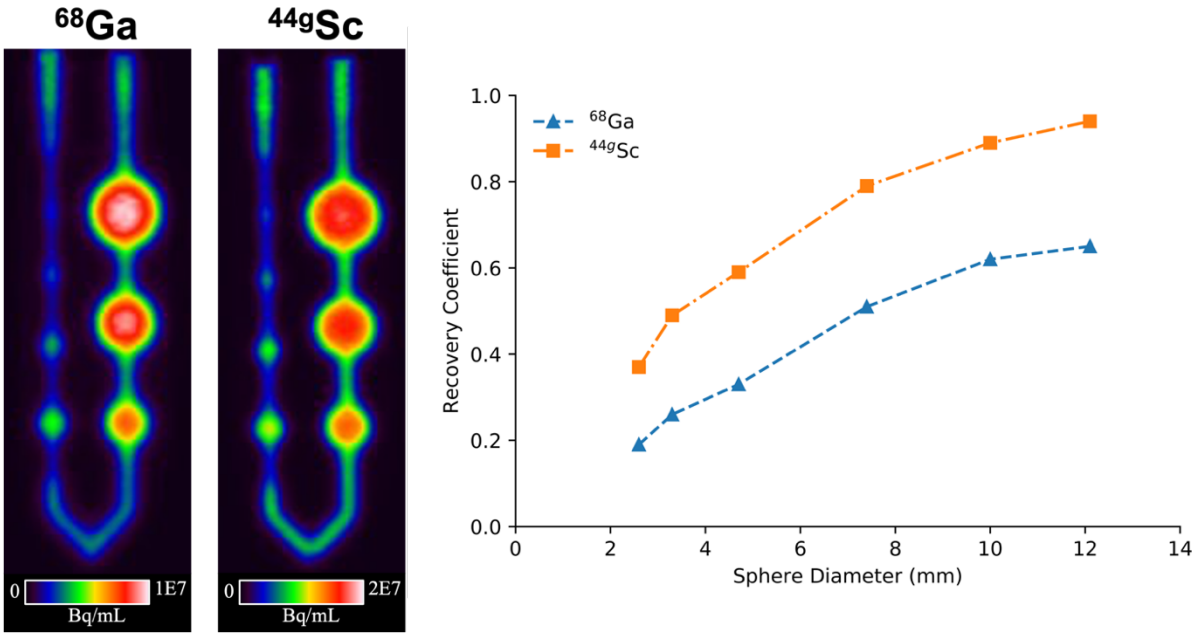


Figure 42: Partial volume effect phantom PET images for ^{68}Ga and ^{44g}Sc (left). Recovery coefficient versus sphere diameter for ^{68}Ga and ^{44g}Sc (right).

Figure 42 shows MIP PET/CT images of the Phantech linear PVE phantom filled with ^{68}Ga (left) and ^{44g}Sc (right). Qualitatively, the reconstructed activity in the ^{68}Ga-filled phantom is less uniform than the reconstructed ^{44g}Sc image. Additionally, the thin linear channel connecting the spherical chambers is lower intensity than the center of the spherical chamber for both images

but is more pronounced in the ^{68}Ga-filled phantom. Because the entire phantom is filled with the same activity concentration, if there were no partial volume effects, the entire reconstructed PET image would be uniform. The lower intensity in the thin linear channel and the smaller diameter spheres on the left side of the phantom are likely the result of both the positron range and the finite spatial resolution of the imaging system. As a result, the reconstructed activity is blurred and has a larger spatial distribution with a lower intensity than the original structure. This effect is less severe in larger diameter structures such as the largest 12 mm and 10 mm diameter spheres and for lower emitted positron energies (^{43}Sc and ^{44g}Sc vs ^{68}Ga).

The plot on the right of Figure 42 shows the percent recovery of the average activity concentration in each sphere. These results indicate that ^{68}Ga's high average positron energy results in the incomplete recovery of activity in small features (< 12 mm diameter). Recovery of ^{44g}Sc was also affected by feature size but the effects were less substantial with 94% of the activity recovered in the 12 mm sphere versus only 65% for ^{68}Ga.

Approximate spherical diameters for the tumors and kidneys were determined from organ mass and correction factors were derived from interpolating the recoveries versus sphere diameter seen in Figure 42. These correction factors were then applied to the image-derived %IA/g values and are shown in Figure 41 (D-F). When partial volume effects are accounted for, image-derived ^{68}Ga and *ex vivo* activity quantification agree within error supporting the hypothesis that the incomplete recovery of [^{68}Ga]Ga-FAPI-46 is primarily the result of the high positron energy.

Even when correcting for the larger PVE from ^{68}Ga imaging, [^{68}Ga]Ga-FAPI-46 tumor uptake was still lower than [$^{43/44g}$Sc]Sc-FAPI-46 tumor uptake. Applying an approximate (tumors are not exactly spherical) correction for PVE, tumor uptake was 1.56 ± 0.10 %IA/g for [^{43}Sc]Sc-

FAPI-46, 1.29 ± 0.17 %IA/g for [^{44g}Sc]Sc-FAPI-46, and 0.52 ± 0.23 %IA/g for [^{68}Ga]Ga-FAPI-46. Thus, the lower %IA/g seen in the tumor for mice injected with [^{68}Ga]Ga-FAPI-46 compared to [$^{43/44g}$Sc]Sc-FAPI-46 is not solely from PVE, but from the chemical differences between Ga-FAPI-46 and Sc-FAPI-46. Changing the radiometal labeled to the FAPI-46 molecule could potentially affect the metabolic clearance and lipophilicity of the ligand. If one radiopharmaceutical is cleared faster than another, the tumor uptake may be lower due to shorter circulation time. However, the lipophilicity of both radioligands were identical within error, indicating that the metabolic clearance is likely very similar between the two radiopharmaceuticals. Another potential cause for lower tumor uptake may be lower binding affinity. Future work comparing the FAP-binding affinity between Ga-FAPI-46 and Sc-FAPI-46 is warranted to determine if lower binding affinity is the cause of lower [^{68}Ga]Ga-FAPI-46 within the tumors observed in this work.

Intestinal uptake study

Uptake in the full intestines and stomach compared to the emptied organs is shown in Figure 43. The tumor uptake between the two experiments was compared as well to ensure that other organs had comparable uptake. In both experiments, the tumor uptake was comparable indicating similar experimental conditions.

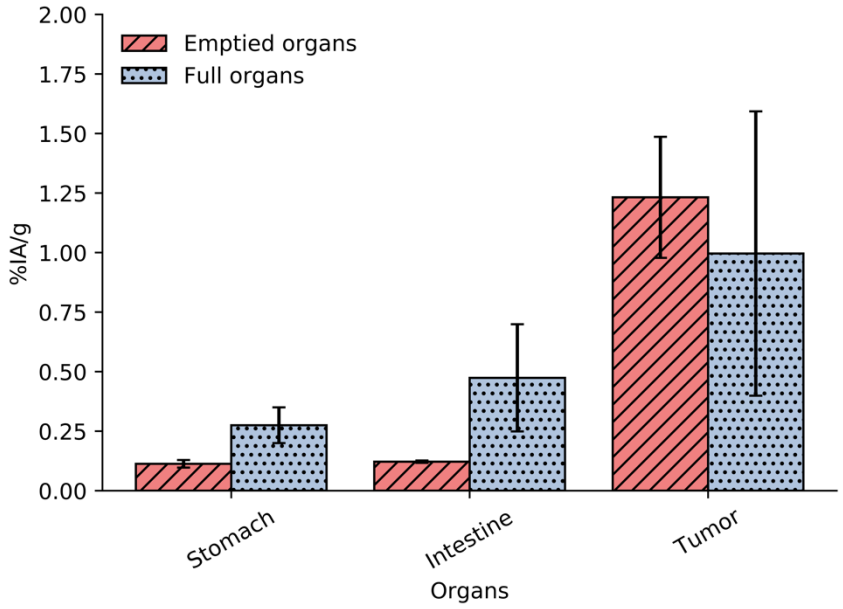


Figure 43: Uptake in emptied stomach and intestines (red hash) and full intestines and stomach (blue dots). Tumor uptake was included to ensure comparable experimental conditions.

If the mice were not consuming the excreted radiopharmaceutical, then the additional weight from the non-radioactive stomach and intestinal contents would increase the mass while not contributing to the measured activity. This would result in a decrease in %IA/g compared to the study where just the tissue was collected. However, there was an increase in %IA/g in the study where the full organs were collected, indicating that the contents of the stomach and intestines contained higher activity per gram than the tissue itself. This supports the hypothesis that the abdominal uptake observed in the later time point images is likely due to the mice ingesting bedding that contained excreted radiotracer through the mouse's urine.

The presence of M-FAPI-46 in the fecal matter increased background signal and could obscure abdominal metastases. Thus, for future murine experiments with M-FAPI-46 (especially when imaging late time points), the bedding should be removed following injection, or a grate should be installed to separate the mice from accessing the contaminated bedding.

3.2.4 Tumor detection in an orthotopic mouse model

10-, 17-, and 25-day incubation

Tumor development period	**Mouse 1 tumor dimensions**	**Mouse 2 tumor dimensions**	**Mouse 3 tumor dimensions**
10 days	2.73 x 2.34 mm	No visible tumor	No visible tumor
17 days	4.14 x 5.15 x 3 mm	3.78 x 1.97 x 2.62 mm	No visible tumor
25 days	3.24 x 2.67 x 1.75 mm	4.47 x 3.33 x 2.64 mm	No visible tumor

Table 15: Tumor dimensions for the mice orthotopically implanted with tumors that were allowed to develop for 10, 17, and 25 days.

Figures 44-46 show MIP PET/CT images of mice injected with [^{44g}Sc]Sc-FAPI-46 bearing orthotopically implanted tumors allowed to develop for 10, 17, and 25 days. Tumor presence was confirmed and measured *ex vivo* by a surgical resident. Measured tumor dimensions for each mouse are shown in Table 15. At 10 days, only one mouse presented a definitive tumor (dimensions: 2.73 x 2.34 mm) which was not visible on PET/CT (Figure 44). At 17 days, two of the three mice had definitive tumors (dimensions: 4.14 x 5.15 x 3 mm and 3.78 x 1.97 x 2.62 mm). Neither mouse had tumors visible on PET/CT scans at any time point (Figure 45). At 25 days, two of the three mice had definitive tumors (dimensions: 3.24 x 2.67 x 1.75 mm and 4.47 x

3.33 x 2.64 mm). Again, neither mouse had visible tumor uptake at the time points observed (Figure 46).

Most of the tumors were smaller in diameter than the heterotopic tumors imaged in the previous section (4 – 8 mm) so it was hypothesized that the absence of tumor signal in the PET/CT images may be due to smaller tumor diameters or location in a high background signal region (the abdomen).

The [^{44g}Sc]Sc-FAPI-46 uptake that is observed on the left flank of each mouse in Figures 44-46 was also seen in the Matrigel® control mouse and is located near the incision site suggesting that the high signal in the area is from [^{44g}Sc]Sc-FAPI-46 binding to fibroblasts that have been recruited to the wound site during normal wound healing processes. M-FAPI-46 uptake in the incision is discussed further in a later section.

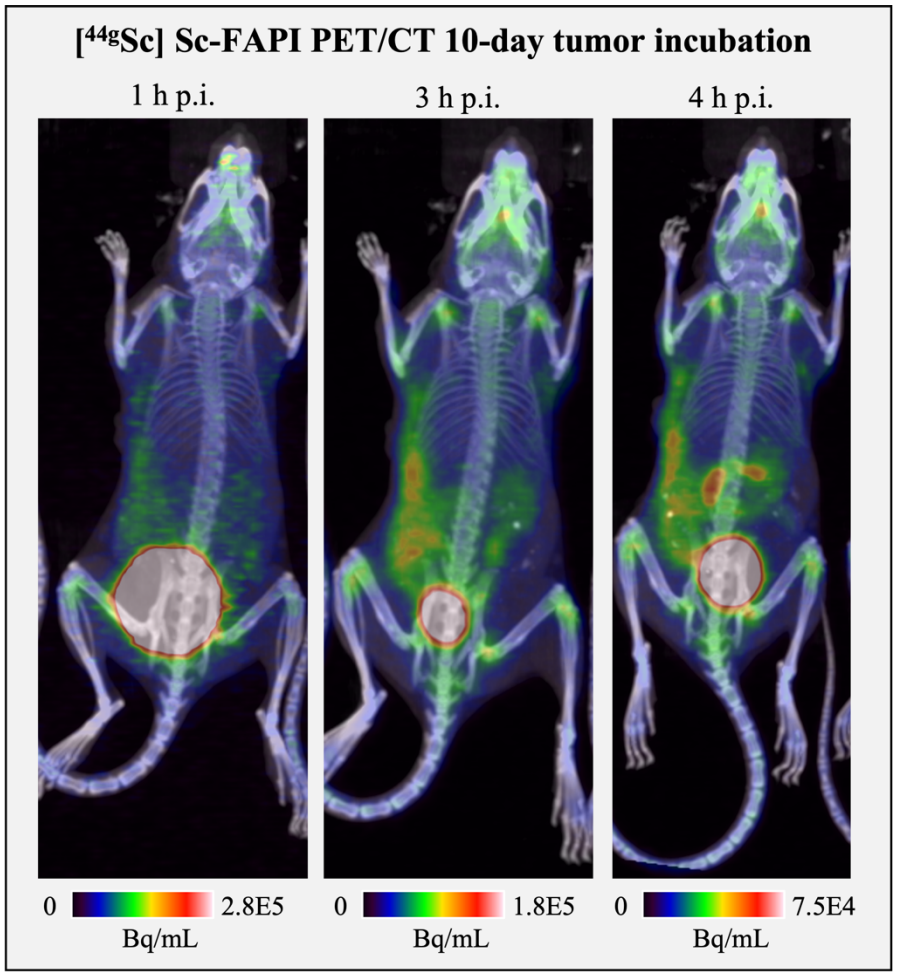


Figure 44: MIP PET/CT images of [^{44g}Sc]Sc-FAPI-46 injected mice bearing orthotopically implanted tumors that have developed for 10 days.

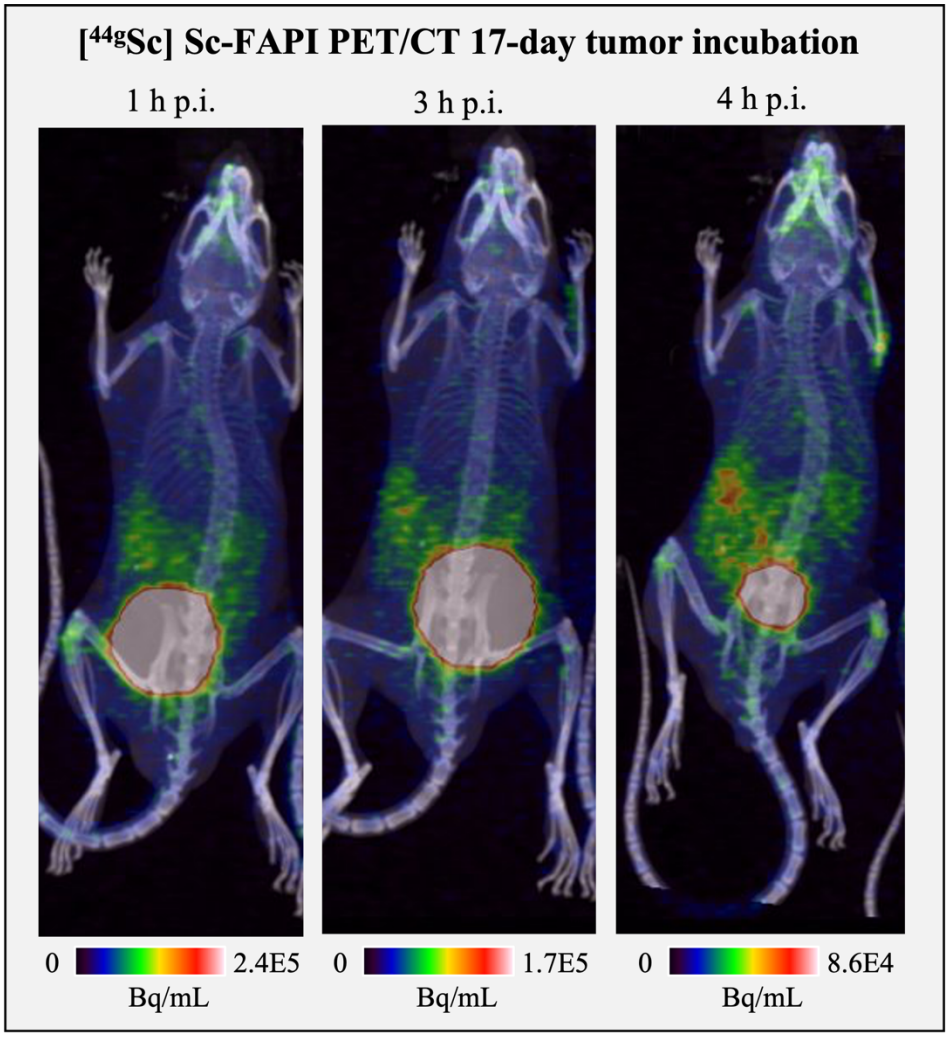


Figure 45: MIP PET/CT images of [^{44g}Sc]Sc-FAPI-46 injected mice bearing orthotopically implanted tumors that have developed for 17 days.

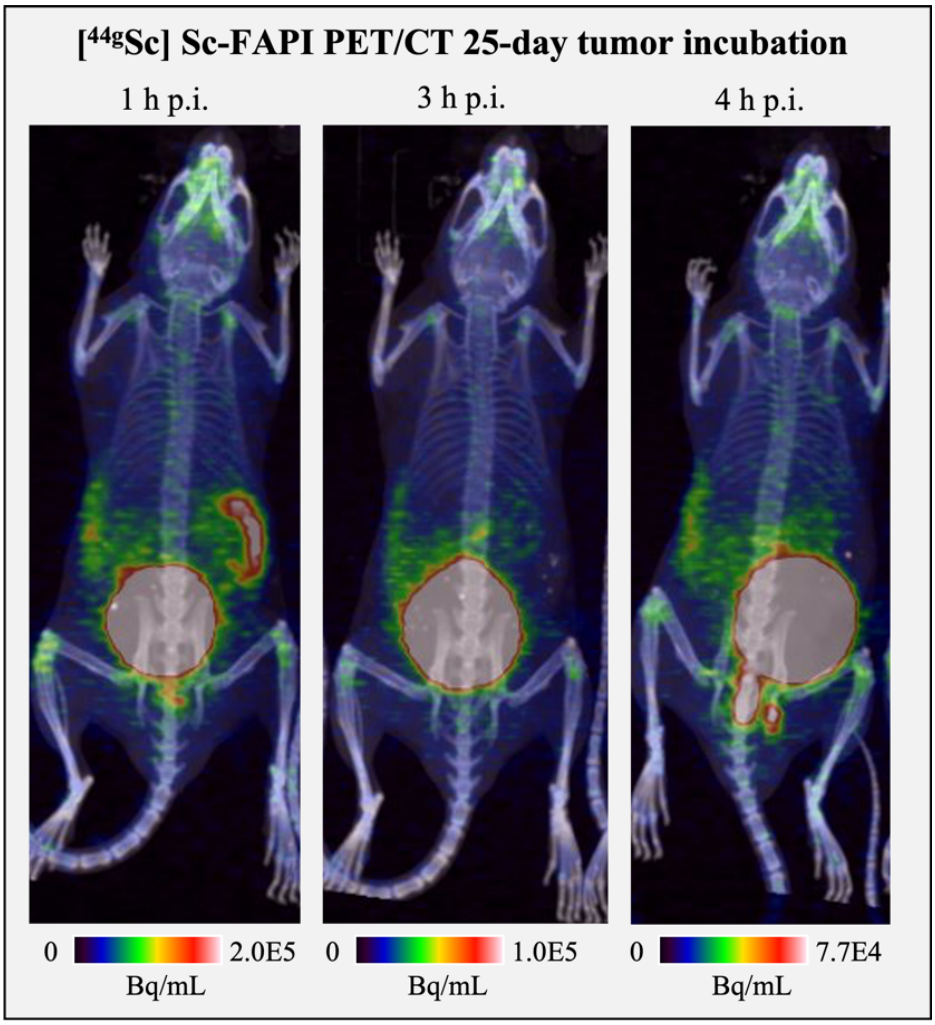


Figure 46: MIP PET/CT images of [^{44g}Sc]Sc-FAPI-46 injected mice bearing orthotopically implanted tumors that have developed for 25 days.

4.5-week tumor incubation

Figure 47 shows a representative mouse injected with [^{68}Ga]Ga-FAPI-46 (Figure 47 (left)) and scanned at 1 h p.i. followed by a [^{44g}Sc]Sc-FAPI-46 injection and scans at 1 and 3 h p.i. one day later (Figure 47 (right)). In all the mice in this cohort, an area of high uptake was seen in an area near the liver in both [^{44g}Sc]Sc-FAPI-46 scans but was absent in the [^{68}Ga]Ga-FAPI-46 scan.

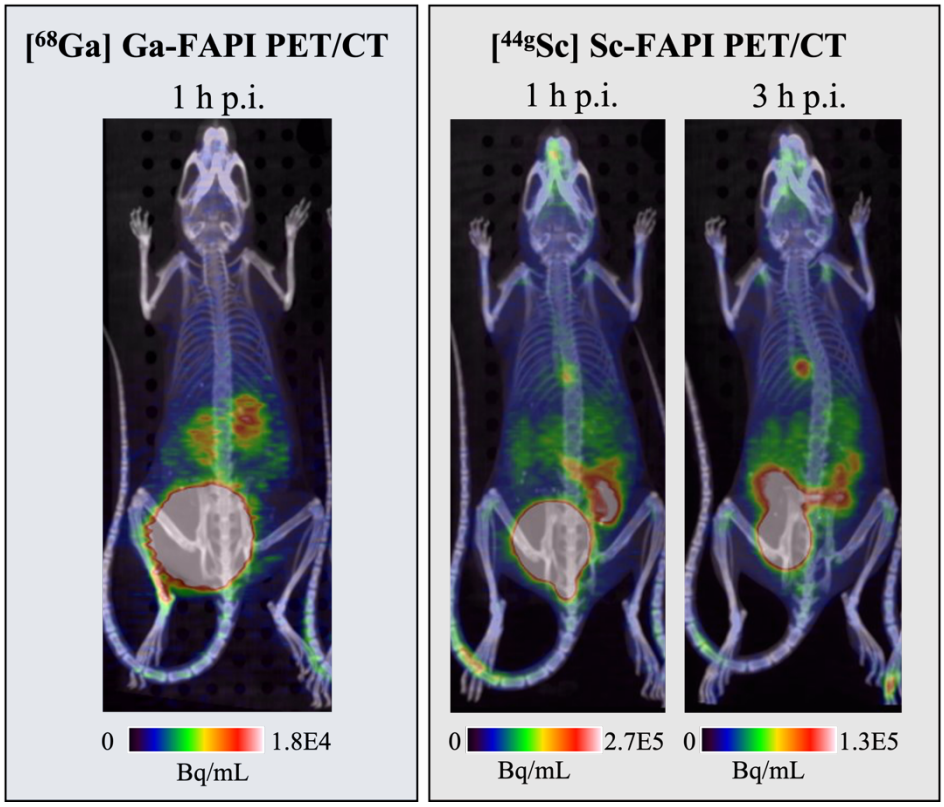


Figure 47: A representative mouse bearing orthotopically implanted tumors injected with [^{68}Ga]Ga-FAPI-46 (left) followed by [^{44g}Sc]Sc-FAPI-46 (right) one day later.

These areas of high uptake were absent in the 10-, 17-, and 25-day PET/CT images in the previous section, initially suggesting that the tumors were now large enough to be visible on PET/CT. However, the location of the high uptake was too superior in the body to be located within the pancreas. Figure 48 shows the *ex vivo* biodistribution of [^{44g}Sc]Sc-FAPI-46 after the 3 h p.i. imaging time point. Gallbladder uptake was higher than the kidneys, indicating that the bright areas on the PET/CT images are likely from gallbladder uptake. Because the high gallbladder uptake was only seen in the 4.5 week [^{44g}Sc]Sc-FAPI-46 scan and not the earlier

scans or the [^{68}Ga]Ga-FAPI-46 scan, it was hypothesized that there may have been radiolysis, or break down, of the [^{44g}Sc]Sc-FAPI-46 formulation.

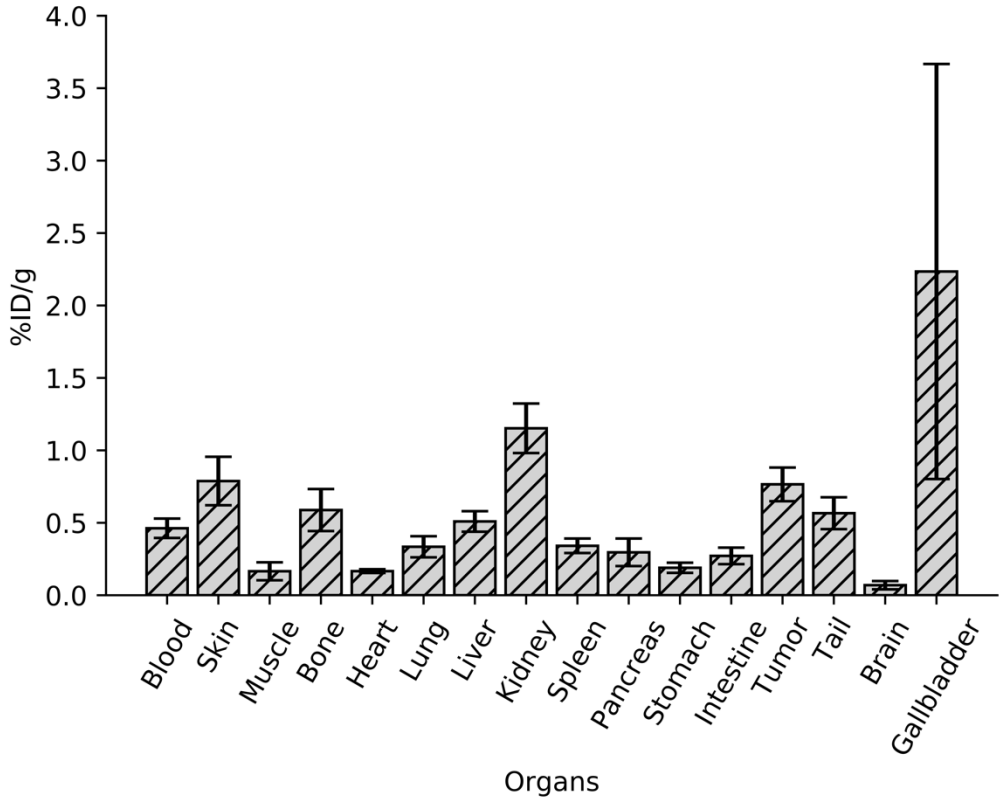


Figure 48: *Ex vivo* biodistribution of [^{44g}Sc]Sc-FAPI-46 in mice (n = 6) bearing orthotopically implanted tumors at 3 h p.i.

Figure 49 shows the pre-injection radio-HPLC chromatogram of the purified [^{44g}Sc]Sc-FAPI-46 compound used in this experiment. Two peaks are observed near the retention time of [^{44g}Sc]Sc-FAPI-46 (12.8 min and 13.3 min), indicative of radiolysis of some of the [^{44g}Sc]Sc-FAPI-46 molecule from ionizing radiation present in high concentration in the dry down vial. While ascorbic acid is added to the vial to act as a radical scavenger and prevent damage to the FAPI-46 molecule, it is possible that there was not enough present, or that the volume was dried

down to too low of a volume, increasing the activity concentration and resulting in radiolysis that was not seen in earlier formulations.

The resulting [^{44g}Sc]Sc-FAPI-46 fragments have a different affinity for the C-18 column than the full Sc-FAPI-46 molecule, and likely different logD values. Lipophilicity (along with size, charge, and other properties) influences clearance pathways and rates, so the radiolysis fragments will likely have different metabolic and physiological behavior *in vivo* than the full molecule. While FAPI-46 is primarily renally cleared, the radiolysis fragments may be excreted through different pathways if their lipophilicities are sufficiently different. Radiopharmaceuticals that are cleared through the biliary pathway are excreted into the bile which is stored in the gallbladder until it is cleared from the body through the gut. Biliary clearance of radiolysis fragments through the gallbladder is likely the cause for increased gallbladder uptake because this effect was observed in only the [^{44g}Sc]Sc-FAPI-46 images (not observed in the [^{68}Ga]Ga-FAPI-46 images) and only at the 4.5-week tumor incubation time-point (not seen in mice injected with [^{44g}Sc]Sc-FAPI-46 at 10-, 17-, 25-days or 9 weeks).

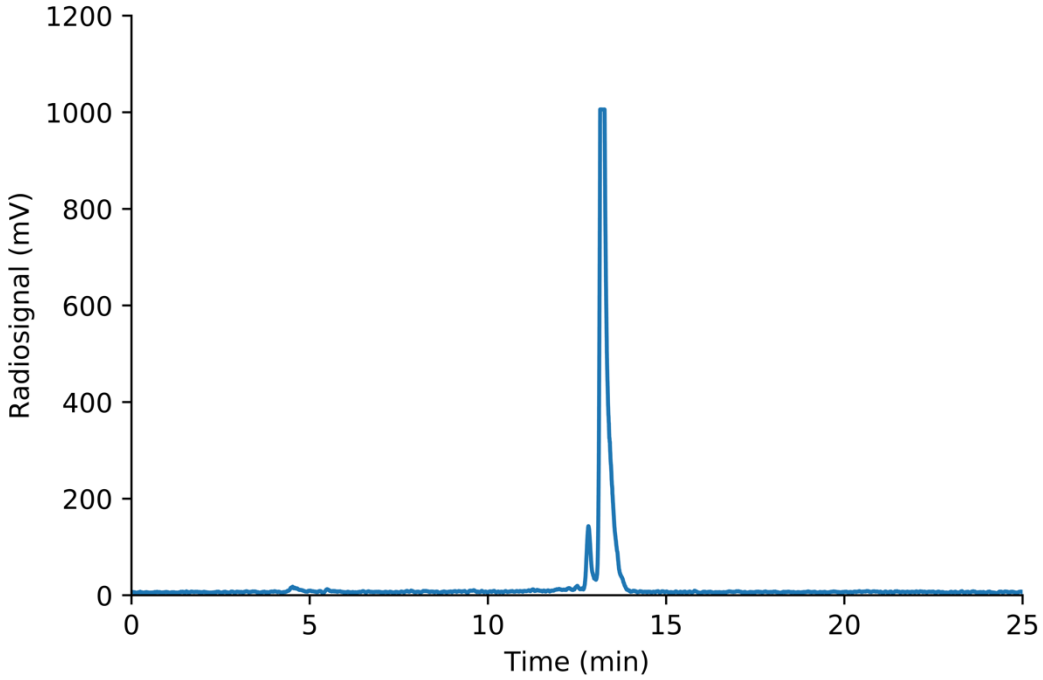


Figure 49: Radio-HPLC chromatogram of the pre-injection formulation for the 4.5-week tumor development mouse cohort.

All six experimental mice were confirmed to have tumors *ex vivo* and were measured by a surgical oncologist. Tumor dimensions are listed in Table 16 and ranged in size with an average diameter around 6 mm. However, tumors were not visible on any scans ([^{68}Ga]Ga-FAPI-46 or [^{44g}Sc]Sc-FAPI-46) at any time point even though they were roughly the same diameter as the heterotopic tumors that were seen in Figure 38.

Mouse identifier	Tumor dimensions (pancreatic)
C1	7 x 7 mm
C2	4 x 8 mm
C3	5 x 7 mm
C18	7 x 6 mm
C19	5 x 6 mm
C20	4 x 7 mm

Table 16: Tumor dimensions for the orthotopically implanted tumors permitted to grow for 4.5 weeks.

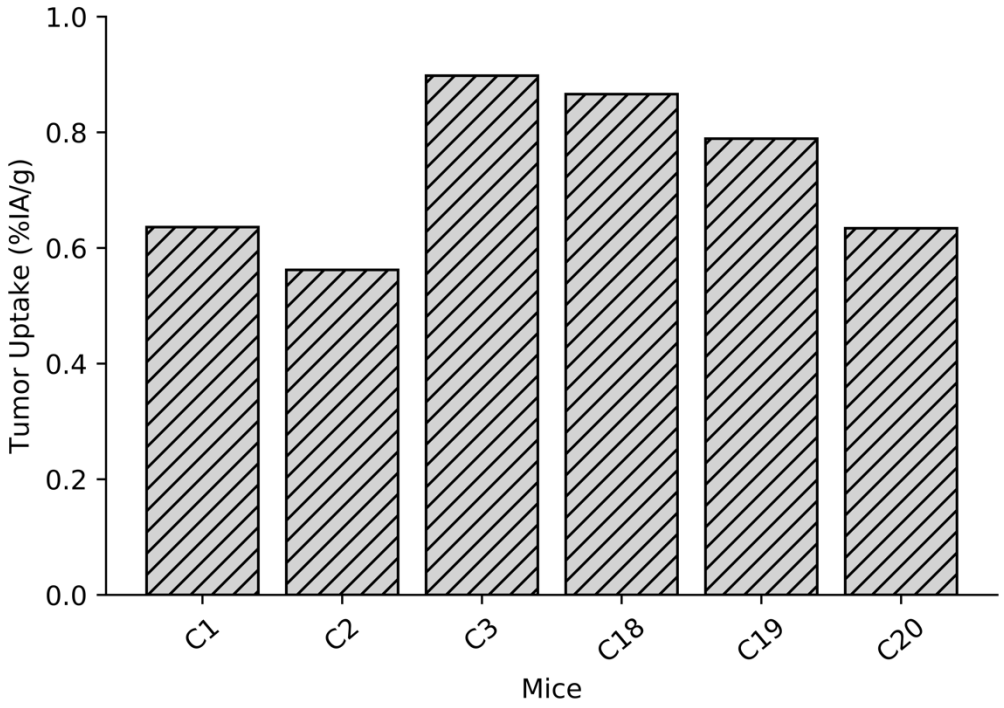


Figure 50: Tumor uptake in each mouse from the 4.5-week tumor development cohort measured through *ex vivo* biodistribution using a calibrated gamma counter.

The tumor uptake measured *ex vivo* is shown in Figure 50. Uptake is slightly lower than the [^{44g}Sc]Sc-FAPI-46 uptake seen in the heterotopic model (at 2 h p.i., [^{44g}Sc]Sc-FAPI-46 uptake was 1.4 ± 0.15 %IA/g), but higher than the [^{68}Ga]Ga-FAPI-46 heterotopic tumor uptake (0.32 ± 0.13 %IA/g from *ex vivo* biodistribution at 2 h p.i.). Heterotopically implanted tumors were visible at 1 and 2 h p.i. with [^{68}Ga]Ga-FAPI-46 scans, indicating that lower uptake is not the sole cause for the inability to visualize orthotopically implanted tumors. The high background from ingested [^{44g}Sc]Sc-FAPI-46, high bladder activity, and high kidney uptake are likely contributing factors to the inability to visualize tumors within the pancreas.

9-week tumor incubation

Of the 6 mice implanted with tumors and allowed to develop for 9 weeks, four did not survive to the imaging date due to complications from the tumor, including abdominal necrosis. MIP

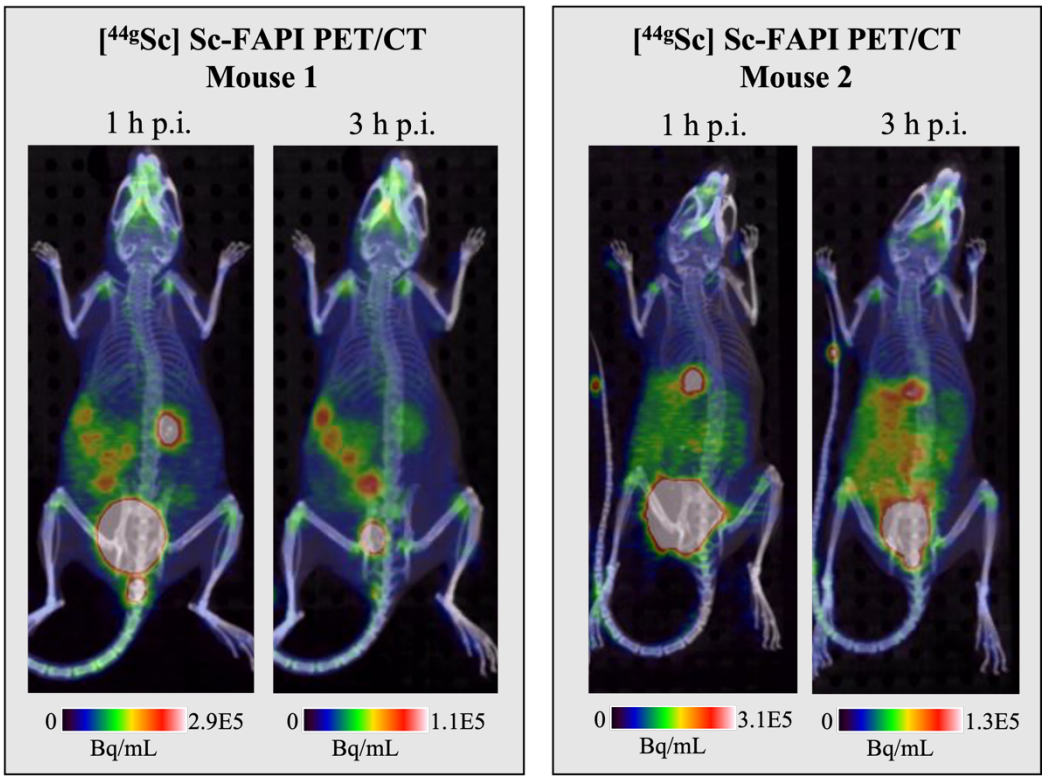


Figure 51: MIP PET/CT images of the mice bearing orthotopically implanted tumors allowed to develop for 9 weeks.

PET/CT images of the two surviving mice injected with [^{44g}Sc]Sc-FAPI-46 at the 9-week tumor incubation period are shown in Figure 51. There are several areas of high uptake in the abdominal region that persist between the 1 and 3 h p.i. time points in both mice initially suggesting that there were abdominal metastases present. No areas of high uptake were observed in the Matrigel® control mouse.

Ex vivo biodistribution studies revealed that both experimental mice had one tumor in the pancreas with no visible metastases confirmed by a surgical oncologist (tumor dimensions are shown in Table 17). The presence of one solid tumor and lack of metastases indicates that the areas of bright uptake on the PET/CT scan are likely not tumor uptake.

Mouse identifier	**Tumor dimensions**
723	2.1 x 2.5 cm
726	2.75 x 1.2 cm

Table 17: Tumor dimensions of the two mice with 9-week orthotopically injected tumors.

Mice that expired prior to the imaging date showed necrosis in the abdomen and were likely suffering from gastroparesis from the large tumors present in the pancreas. It is likely that the two mice in Figure 51 were also experiencing gastroparesis, a disorder that affects the movement of muscles in the stomach and delays food moving from the stomach to the small intestine. This would result in the fecal matter moving through the intestines at a slower rate than normal. The stomach and intestinal uptake study during the heterotopic imaging experiments confirmed that [$^{43/44g}$Sc]Sc-FAPI-46 was present in the fecal matter. Thus, it is likely that the areas of uptake visible on the PET/CT scans are from activity in the fecal matter of the mice that is more slowly moving through the intestines due to gastroparesis caused from the large pancreatic tumors rather than tumor uptake.

Like the 4.5-week tumor development cohort, the tumors measured in this study were larger than the heterotopic tumors visible on the PET/CT scans in the previous section. Identification of the tumor in the scans shown in Figure 51 is complicated by the presence of slow-moving fecal matter containing [^{44g}Sc]Sc-FAPI-46 and thus, tumor presence could not be confirmed via PET/CT image analysis.

Incisional uptake study

The *ex vivo* biodistribution of [^{44g}Sc]Sc-FAPI-46 in the orthotopic model versus the heterotopic model is shown in Figure 52 (note that there was no incision in the heterotopic model). The uptake in the orthotopic model incision is roughly the same as the heterotopic tumor uptake. Conversely, the tumor uptake in the orthotopic model was lower and much more variable than in the heterotopic model. The FAPI-46 targeting molecule binds to the fibroblast activation protein-

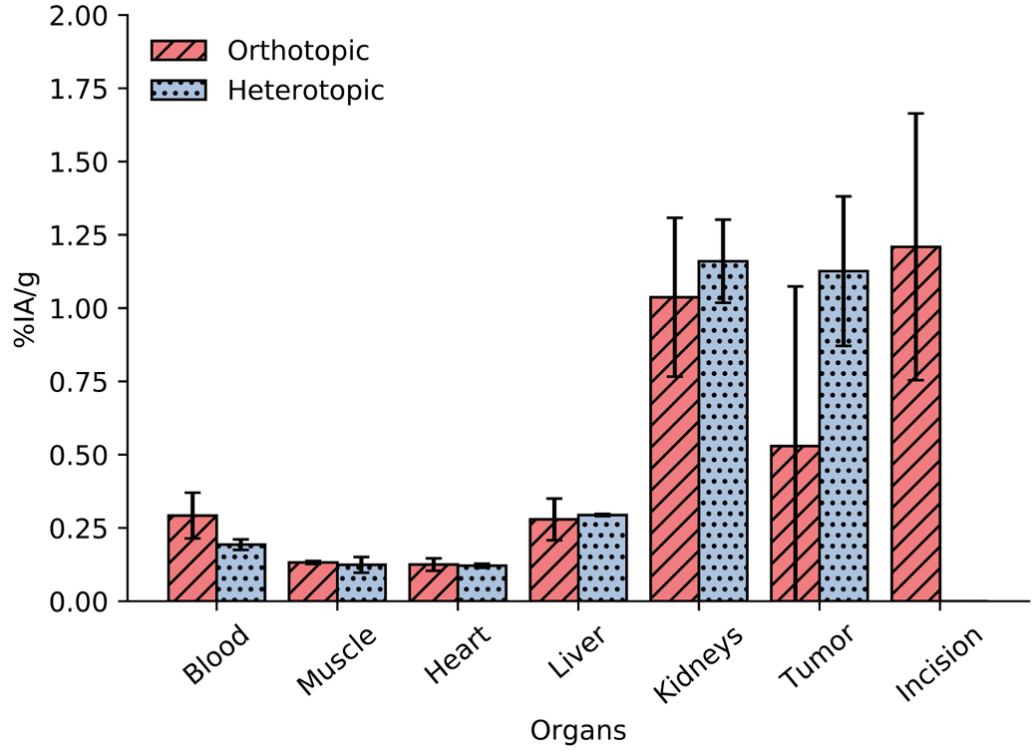


Figure 52: *Ex vivo* biodistribution of [^{44g}Sc]Sc-FAPI-46 in an orthotopic model versus the heterotopic model.

α expressed on the surfaces of recruited CAFs in the tumor microenvironment. If there are no (or reduced) CAFs within the tumor, the M-FAPI-46 uptake within the tumor will be lower. Future work investigating whether the orthotopic model develops the same tumor microenvironment, and whether the CAFs within the tumor microenvironment express fibroblast activation protein-α like the heterotopic model, is needed to further understand the cause for the decreased tumor uptake in the orthotopic model and the lack of signal on the PET/CT scans.

	[^{68}Ga]Ga-FAPI-46	**[^{44g}Sc]Sc-FAPI-46**
Heterotopic model	0.32 ± 0.13 %	1.13 ± 0.25 %
Orthotopic model	--	0.53 ± 0.55 %

Table 18: *Ex vivo* tumor uptake for each tumor model for mice injected with [^{68}Ga]Ga-FAPI-46 and [^{44g}Sc]Sc-FAPI-46.

The *ex vivo* measured tumor uptake for each tumor model and M-FAPI-46 ligand is shown in Table 18. The [^{44g}Sc]Sc-FAPI-46 orthotopic model tumor uptake was lower than the [^{44g}Sc]Sc-FAPI-46 heterotopic model and similar to the [^{68}Ga]Ga-FAPI-46 heterotopic model. Even though the tumor uptake was lower for the [^{68}Ga]Ga-FAPI-46 heterotopic model, tumors were still visible on the PET/CT scans. This indicates that lower uptake is not the only factor contributing to the decreased tumor visualization. The pancreas is in a region of high activity concentration (near the kidneys and bladder), reducing tumor visualization. Additionally, presence of [^{44g}Sc]Sc-FAPI-46 in the fecal matter contributes to high background in the region and complicates identification of tumors.

3.2.5 Comparison of $^{43/44g}$Sc to conventionally used PET radionuclides on clinical scanners

The contrast was compared between 6 radionuclides on two PET/CT scanners. Figure 53 shows a cross-sectional image of the reconstructed Derenzo phantom on the GE Discovery 710 and

Figure 54 shows the images from the Discovery MI. Qualitative differences can be seen between shorter-range positron-emitters such as ^{64}Cu and ^{18}F compared to the higher-range positron-emitter ^{68}Ga. All six sections of rods are easily distinguishable for ^{64}Cu and ^{18}F while the lower diameter rods (3.5 and 4 mm) are significantly blurred in the ^{68}Ga image. ^{43}Sc, ^{44g}Sc, and $^{43/44g}$Sc image quality was between the low and high positron range radionuclides where the smallest diameter rods are indistinguishable, but resolution improves with the 4 mm diameter rods. The calculated contrast values on each machine are shown in Figure 55 as well.

On both scanners, ^{64}Cu and ^{18}F demonstrated the greatest contrast across the varying rod diameters while ^{68}Ga performed the worst across all rod diameters, consistent with the positron energies listed in Table 10. Between ^{43}Sc, ^{44g}Sc, and $^{43/44g}$Sc, there is no significant difference in contrast, suggesting minimal benefit in contrast from ^{43}Sc's softer positron energy using these clinical PET/CT systems.

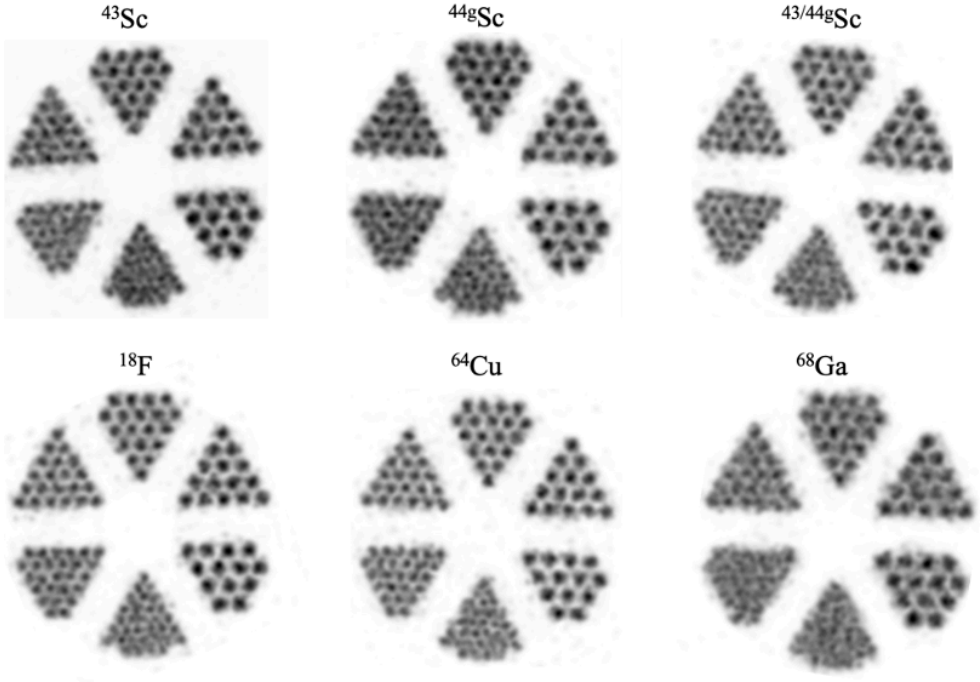


Figure 53: Cross-sectional PET/CT image of the Derenzo phantom filled with each radionuclide and scanned on the GE Discovery 710.

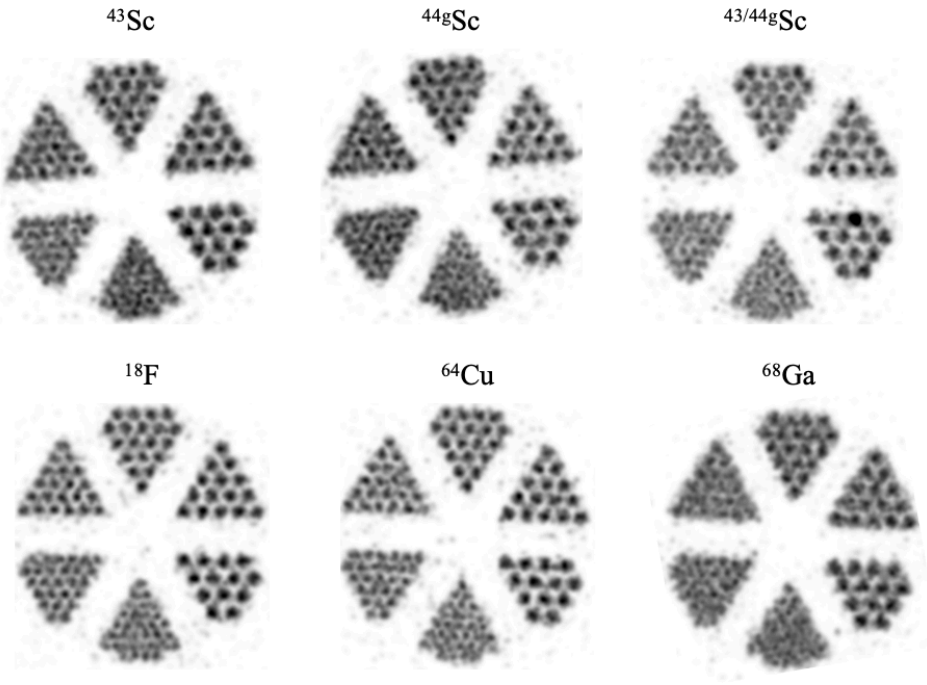


Figure 55: Cross-sectional PET/CT image of the Derenzo phantom filled with each radionuclide and scanned on the GE Discovery MI.

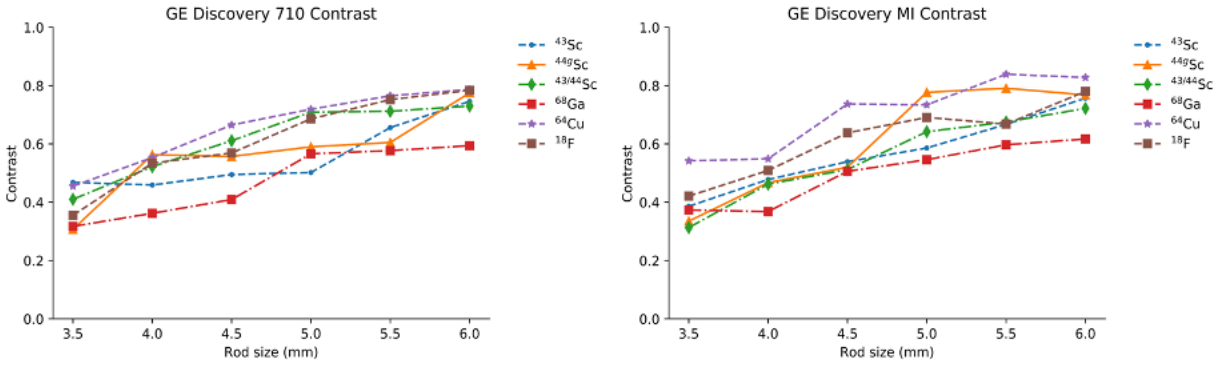


Figure 54: Calculated contrast measured from the Derenzo phantom filled with each radionuclide and scanned on the GE Discovery 710 (left) and GE Discovery MI (right).

Figures 56 and 57 show cross sectional images of the reconstructed spherical phantom filled with each radionuclide acquired on the GE Discovery 710 and GE Discovery MI PET/CT scanners. Recovery coefficients were calculated for each sphere and radionuclide and are plotted in Figure 58. Overall, RC_{sphere} decreased for each radionuclide as the sphere diameter decreased, consistent with the partial volume effect where the size of the feature approaches the range of the positron and results in activity "spilling" out of the region being quantified. For the phantoms filled either completely or partially with ^{43}Sc, the RC_{sphere} ranges between 1.08 at small diameters and 1.95 for the largest spheres. From our definition of RC_{sphere}, this indicates that the scanner is overestimating the activity in the larger spheres by nearly a factor of 2.

Radionuclide	**GE D710 RC_{bkgd}**	**GE DMI RC_{bkgd}**
^{43}Sc	1.53	2.19
^{44g}Sc	0.96	0.96
$^{43/44g}$Sc	1.56	1.59
^{18}F	0.93	0.97
^{64}Cu	0.95	0.96
^{68}Ga	1.04	1.04

Table 19: Background recovery coefficients for each radionuclide on the two GE PET/CT scanners investigated here.

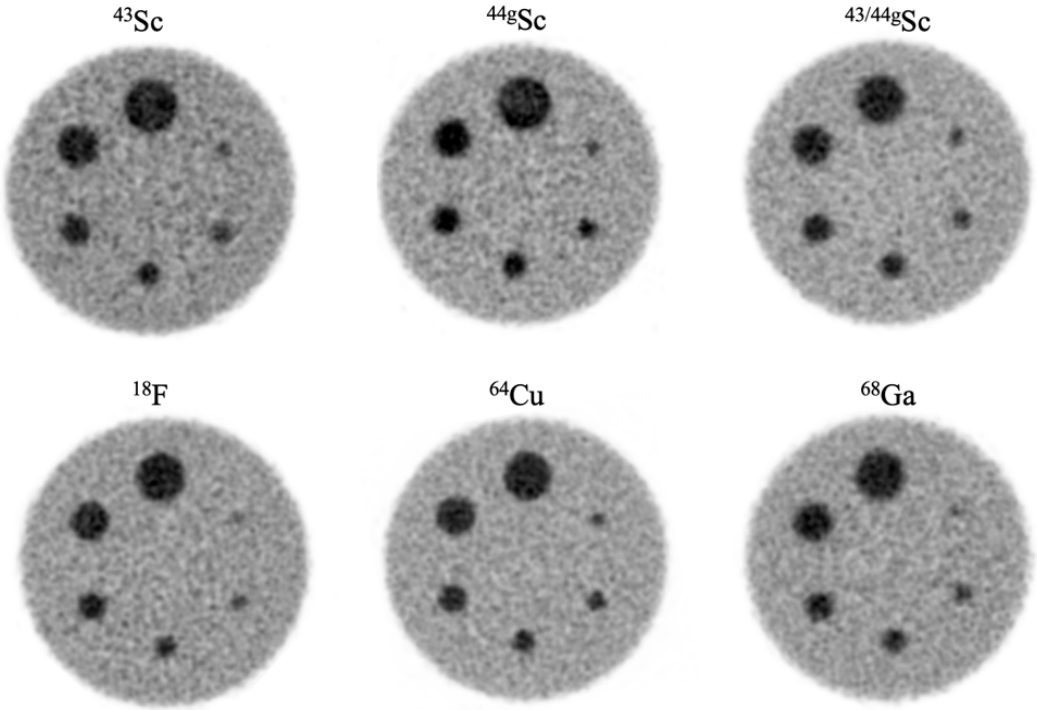


Figure 57: Cross-sectional image of the spherical phantom filled with each

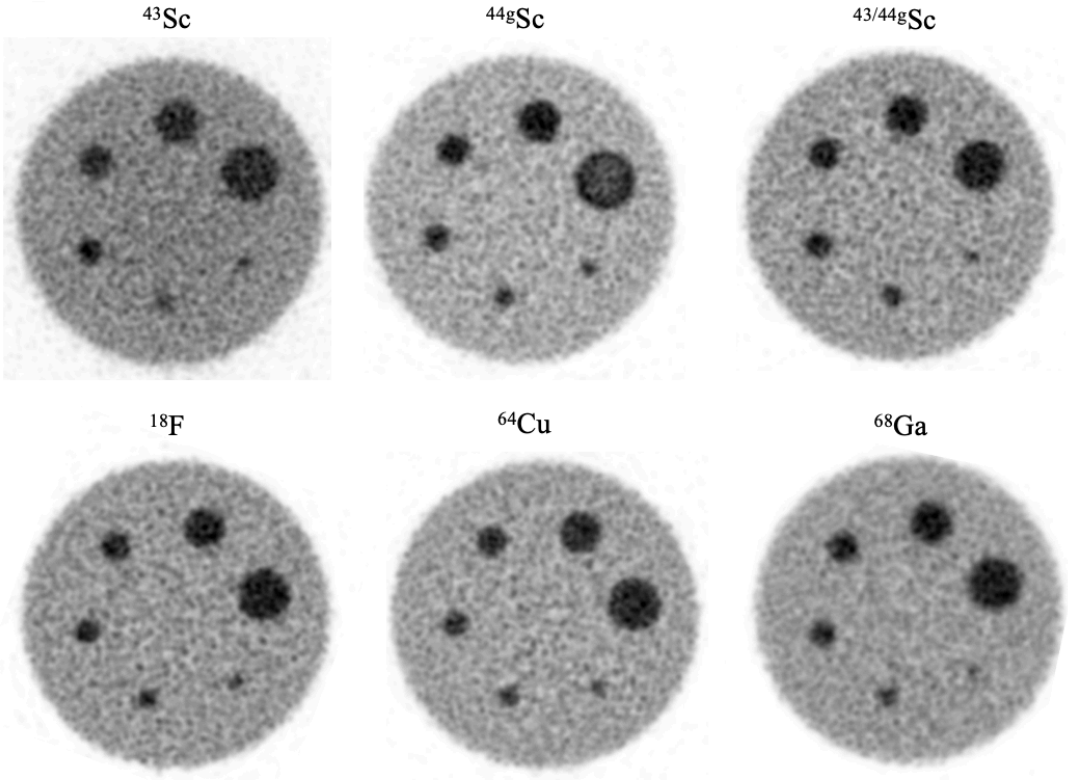


Figure 56: Cross-section image of the spherical phantom filled with each radionuclide and scanned on the GE Discovery MI.

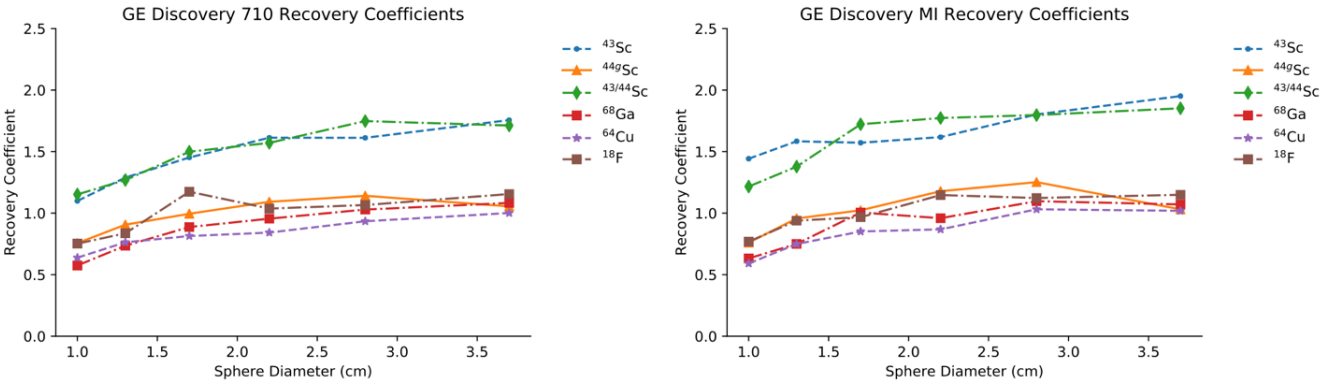


Figure 58: Calculated recovery coefficients for each sphere diameter for all the radionuclides investigated here on the GE Discovery 710 (left) and GE Discovery MI (right).

Radionuclide	**GE Discovery 710 scatter fraction**	**GE Discovery MI scatter fraction**
^{43}Sc	0.272	0
^{44g}Sc	0.318	0.385
$^{43/44g}$Sc	0.268	0.296
^{18}F	0.253	0.282
^{64}Cu	0.244	0.283
^{68}Ga	0.266	0.302

Table 20: Scatter fraction for each radionuclide on both GE PET/CT scanners.

Table 19 shows the background recovery coefficients from the uniform background region of the phantom. Both ^{43}Sc and $^{43/44g}$Sc are overestimated in the background region. Additionally, the GE Discovery MI overestimates the ^{43}Sc background activity by more than the GE Discovery 710. The scatter fraction returned by each scanner is recorded in Table 20. The GE Discovery MI returned a scatter fraction of 0 solely for the phantom filled with ^{43}Sc. An offline reconstruction was performed using GE's Duetto toolbox with the same reconstruction parameters used for the

online scanner reconstruction to see if the issue was reproduceable when reconstructing offline. The offline reconstruction found a scatter fraction of 0.313 indicating that there was an error with the scanner's online reconstruction method. The error was communicated to GE and the scanner's software was updated to resolve the issue. Following resolution of the miscalculated scatter, the GE Discovery 710 and GE Discovery MI background RCs agreed (1.53 for the GE Discovery 710 and 1.58 for the GE Discovery MI).

Siemens scanner comparison

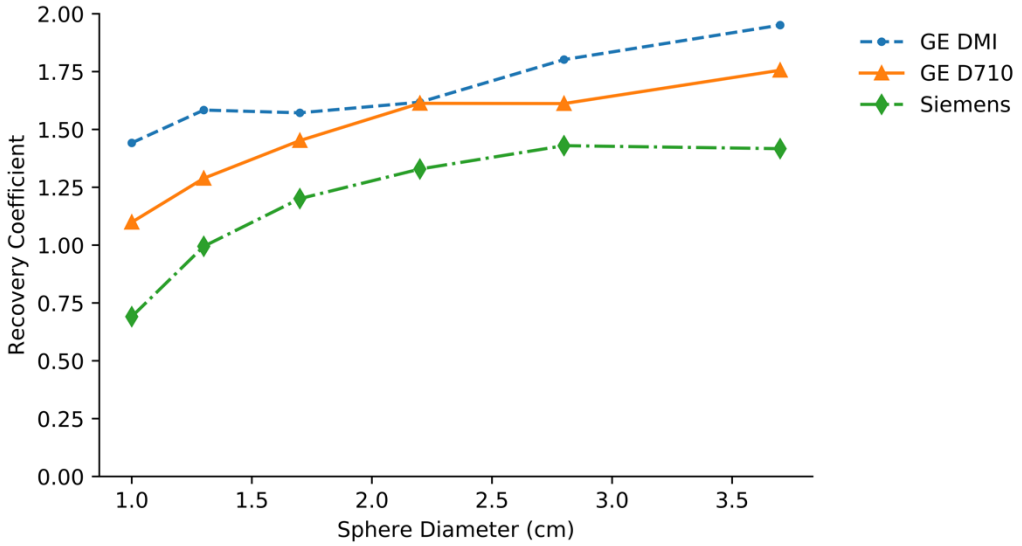


Figure 59: Recovery coefficient versus sphere diameter for the GE Discovery 710 and MI compared to the Siemens Biograph Horizon PET/CT.

Even when accounting for the GE Discovery MI's scatter fraction error, the reconstructed activity was still being overestimated in the spheres and background region for ^{43}Sc and $^{43/44g}$Sc. Figure 59 shows the recovery coefficients for each sphere size on the Siemens Biograph Horizon compared to the two GE Discovery PET/CTs. The activity was still overestimated on the Siemens scanner, but to a lesser degree than on the GE Discovery scanners. This indicates that

the scanner reconstruction method may be partly responsible for the incorrect quanitification of activity seen for ^{43}Sc.

A sample HPGe spectrum of the final ^{43}Sc formulation used to fill the phantoms is shown in Figure 60. The low energy x-rays (< 100 keV) are characteristic x-rays from the lead shielding surrounding the detector while the only other 2 peaks are at 373 keV and 511 keV from ^{43}Sc's characteristic gamma emission and the 511 keV from ^{43}Sc's emitted positrons. Thus, if there are contaminating positron-emitters contributing to the 511 keV peak and to the scanner signal, they must lack high branching ratio characteristic gamma emissions.

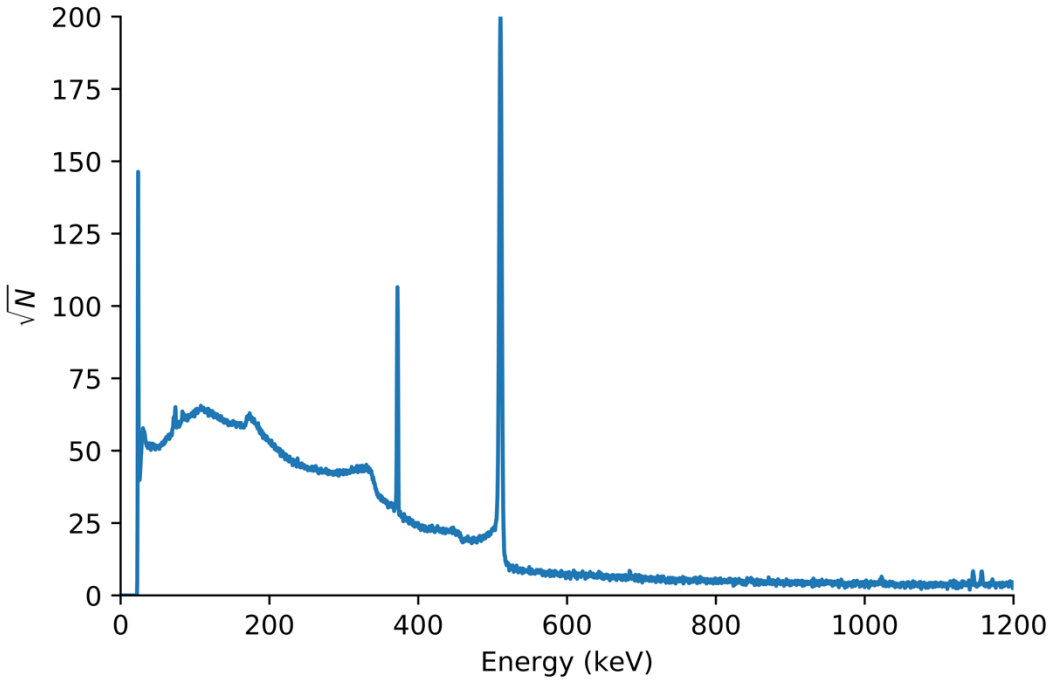


Figure 60: HPGe spectra of final ^{43}Sc formulation used to fill the phantoms.

Figure 61 shows the counts from both peaks over time along with an exponential fit. The fit half-lives and deviation from the true half-life are listed in Table 21. The 511 keV fit half-life deviates slightly more from the true half-life than the 373 keV peak, and the fit half-life appears

to be underestimated for later time points. A biexponential curve was fit to the 511 keV peak data to determine if there were two independent radionuclides contributing to the 511 keV peak:

$$A(t) = A_{0,1}e^{-\lambda_1 t} + A_{0,2}e^{-\lambda_2 t} \quad (8)$$

where λ_1 and λ_2 are the decay constants for independent radionuclides. The biexponential fit is shown in Figure 62.

Peak	Fit half-life	Deviation from true half-life
373 keV	3.94 h	1.24%
511 keV	4.02 h	3.35%

Table 21: Fit half-life for the 373 keV and 511 keV peaks.

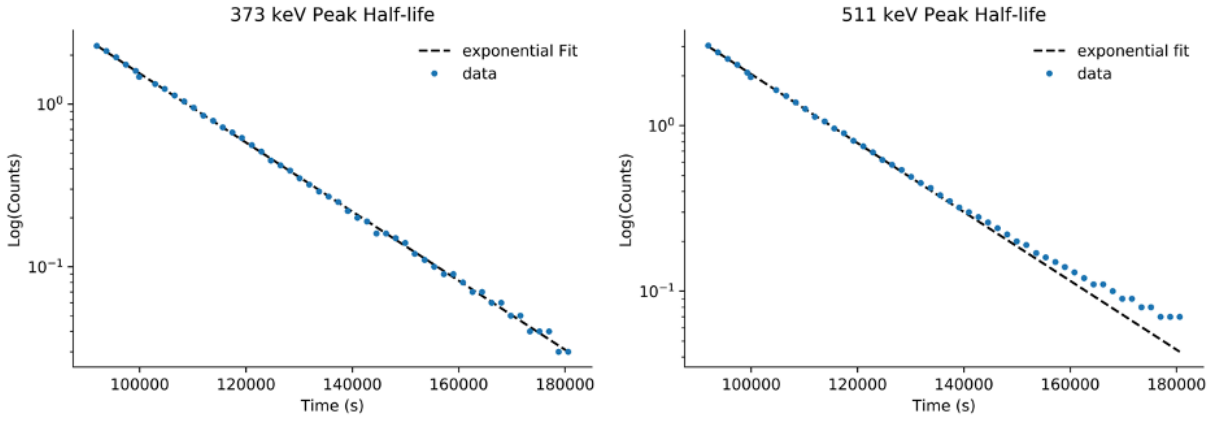


Figure 61: Decay data for the 373 keV and 511 keV peak with exponential fits.

The fit initial activities ($A_{0,1}$ and $A_{0,2}$) and fit decay constants for the biexponential fit are listed in Table 22. While a second half-life was fit, the fraction of initial activity is < 1 %. Thus, the deviation from ^{43}Sc's half-life at late time points is likely due to the background signal in the area where the detector is housed. Collected background spectra show approximately 1-2% of the counts from the 511 keV peak were from background sources, contributing to the error in fit

half-life and the deviation from the fit half-life at late time points when most of the ^{43}Sc has decayed.

A small aliquot (18 MBq, 487 μCi) of ^{43}Sc was also placed in a xenon gas well counter and the current was measured with a Keithley 6517B electrometer biased to 300 V. The current was recorded every 5 minutes and an exponential curve was fit to the data to determine the half-life. Figure 63 shows the signal decay and fit half-life. The fitted half-life was 3.887 h which is within 0.10% of the true half-life (3.891 h). Overall, this work suggests that no other positron-emitters are contributing to the 511 keV signal.

Radionuclide	**Half-life**	**Initial activity (A_0)**
^{43}Sc	3.71 h	322 μCi
Contaminant	7.72 h	3 μCi

Table 22: Fit decay parameters for the biexponential fit of the 511 keV peak.

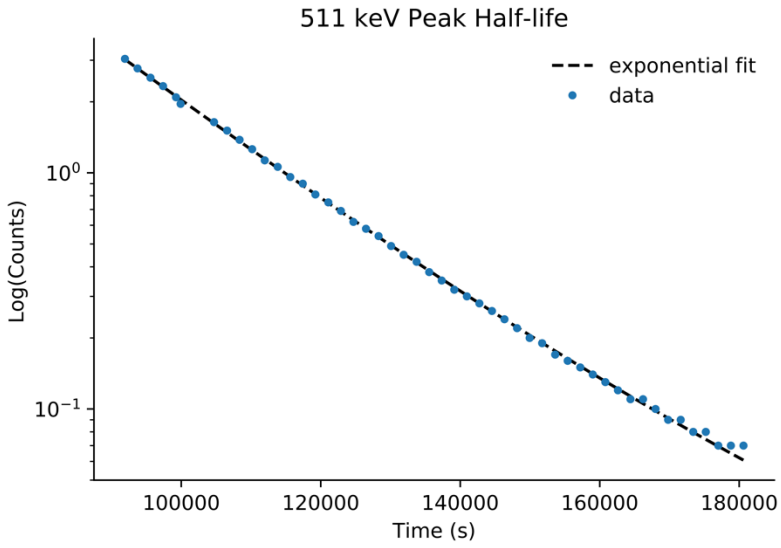


Figure 62: Biexponential fit of the decay of the 511 keV peak.

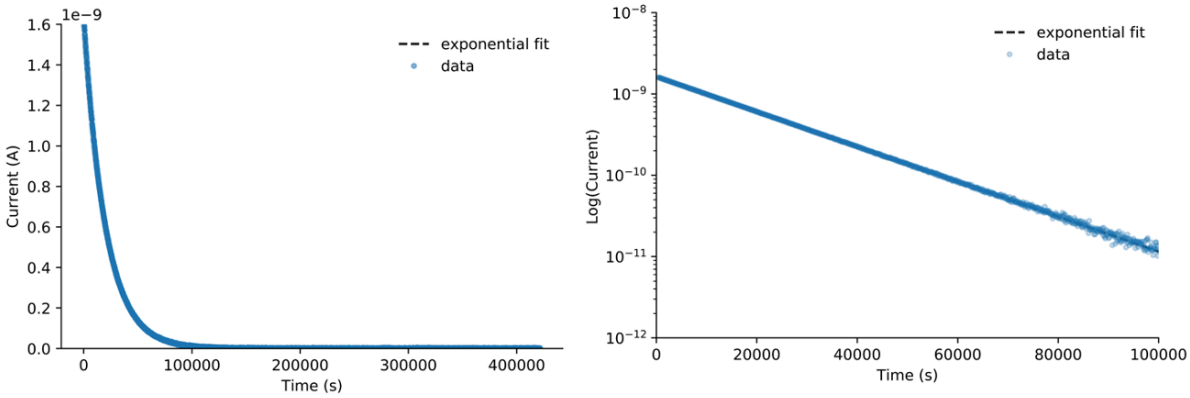


Figure 63: Decay of signal measured by the xenon gas well counter coupled with a Keithley 6517B electrometer and the corresponding fit.

3.4 Conclusions

PDAC is an aggressive form of cancer with limited options available for detection and screening. Early detection of the disease is essential for patient eligibility for treatments such as surgical resection. Anatomical imaging techniques such as CE-CT and MRI are the current standard of care for diagnosis and staging, but small lesions are difficult to detect on CE-CT and there is little contrast between PDAC and healthy pancreatic tissue due to similar attenuation between the two tissues [100, 101]. [^{68}Ga]Ga-FAPI has been gaining traction as a versatile imaging agent that has been shown to target many different types of cancers. It is particularly promising in imaging PDAC due to the disease's poor prognosis and lack of reliable imaging techniques needed to accurately stage the disease. Several groups have investigated the benefit of [^{68}Ga]Ga-FAPI-46 [124, 108]. However, [^{43}Sc]Sc-FAPI-46 and [^{44g}Sc]Sc-FAPI-46 showed increased clinical potential over [^{68}Ga]Ga-FAPI-46 in this work due to ^{43}Sc's and ^{44g}Sc's longer half-lives, higher tumor uptake, and superior image quality over ^{68}Ga.

The results described in this chapter showed that [^{68}Ga]Ga-FAPI-46, [^{43}Sc]Sc-FAPI-46, and [^{44g}Sc]Sc-FAPI-46 detected heterotopic PDAC tumor xenografts at all time points investigated.

Tumor uptake remained high over the 2 hours investigated for [^{68}Ga]Ga-FAPI-46 and 8 hours for [$^{43/44g}$Sc]Sc-FAPI-46. Tumor and normal tissue uptake were higher for [$^{43/44g}$Sc]Sc-FAPI-46 than [^{68}Ga]Ga-FAPI-46 at both 1 and 2 h p.i. At 2 h p.i., decay-corrected tumor uptake was approximately 7 times higher in mice injected with [^{43}Sc]Sc-FAPI-46 or [^{44g}Sc]Sc-FAPI-46 compared with [^{68}Ga]Ga-FAPI-46.

Reconstructed PET/CT image-derived %IA/g values were verified via *ex vivo* biodistribution. Image-derived uptake was found to be within error compared to *ex vivo* data for [$^{43/44g}$Sc]Sc-FAPI-46 but was lower than *ex vivo* values for [^{68}Ga]Ga-FAPI-46. A phantom with spherical chambers of increasing diameters was used to determine activity recovery based on feature size. Results indicated that ^{68}Ga's high positron energy causes a reduction in quantified activity, especially in smaller features. Even when adjusting for partial volume effects, [^{68}Ga]Ga-FAPI-46 uptake in the tumor was approximately 0.5 ± 0.2 %IA/g which is still 3 times lower than the observed [$^{43/44g}$Sc]Sc-FAPI-46 uptake.

When comparing [^{43}Sc]Sc-FAPI-46 and [^{44g}Sc]Sc-FAPI-46, both radioligands show similar image quality and have nearly identical half-lives. ^{44g}Sc emits a 1157 keV (99.9%) gamma and cyclotron production of ^{44g}Sc results in the co-production of the excited isomer ^{44m}Sc ($t_{1/2}$ = 58.61 h). On the other hand, ^{43}Sc production requires enriched ^{42}Ca or ^{43}Ca material which is more expensive than ^{nat}Ca or ^{44}Ca. Choice of ^{43}Sc or ^{44g}Sc will likely be specific to laboratory capabilities, access to resources, and specific circumstances as discussed in [125].

An orthotopic model was also investigated. Tumors were implanted surgically into the pancreas and grown for 10 d, 17 d, 25 d, 4.5 weeks, and 9 weeks. Tumors were not visible on PET/CT scans, including tumors that were larger than 2 cm in diameter for the 9-week tumor development cohort. Lower tumor uptake (potentially from differences in receptor expression in

an orthotopic environment) combined with location in a high activity region (the abdomen) complicating tumor visualization in the orthotopic model.

For future studies, withholding water for a longer time prior to scanning and attempting to void the bladder prior to imaging may reduce background activity. Removal of bedding or use of a grate to prevent ingestion of the excreted M-FAPI-46 will likely further reduce background abdominal signal. However, when moving from murine studies to larger animals (such as rats or pigs) or in-human trials, abdominal background is not as much of a concern. Finally, > 25 days of tumor development is likely needed to develop tumors large enough to visualize but care should be taken not to exceed 8 weeks to prevent complications such as gastroparesis.

PET image qualities were also compared between ^{43}Sc, ^{44g}Sc, $^{43/44g}$Sc and more conventional PET radionuclides such as ^{18}F, ^{64}Cu, and ^{68}Ga in a Derenzo and spherical phantom on two clinical PET/CT scanners. Because PET resolution is impacted by positron range (energy), ^{43}Sc has been hypothesized to have better PET resolution than ^{44g}Sc. Additionally, it has been suggested that ^{44g}Sc's higher energy gamma (1157 keV; 99.9%) as opposed to ^{43}Sc's lower energy gamma (373 keV; 22.5%) may degrade image quality due to the potential to scatter within a PET scanner's 511 keV window [35] and deliver extra dose to the patient. In this study there was no significant difference in contrast between ^{43}Sc, ^{44g}Sc, or the mixture $^{43/44g}$Sc.

^{44g}Sc activity recovery increased with increasing sphere diameter, approaching a value of 1, similar to the other radionuclides investigated. However, both GE Discovery PET/CT scanners overestimated the ^{43}Sc and $^{43/44g}$Sc activity by 50 - 100%. ^{43}Sc differs from ^{44g}Sc in that it releases a prompt gamma (373 keV, 22.5%) with an energy close to the acceptance window on the PET/CT scanners used (425 - 650 keV). The GE Discovery MI reconstruction algorithm initially returned an error when evaluating the scatter fraction for the spherical phantom filled

with ^{43}Sc, indicating that the characteristic gamma from ^{43}Sc may influence scatter calculations and influence recovered activity. Figure 60 showed a sample HPGe spectra of a ^{43}Sc sample produced from deuteron bombardment of a ^{42}CaO target. The two prominent peaks seen were from ^{43}Sc's characteristic 373 keV gamma and the 511 keV peak. No other large peaks are noted (besides a small 1157 keV peak from ^{44g}Sc) and the half-life of the 373 keV and 511 keV peaks both matched ^{43}Sc's half-life, suggesting that the only positron-emitters present are ^{43}Sc and a small fraction of ^{44g}Sc (~1-2% activity). Future work is needed to accurately quantify ^{43}Sc in clinical PET/CT scanners before moving to in-human clinical use.

Acknowledgements

We gratefully acknowledge Dr. Sean Ronnekleiv-Kelly and Dr. Patrick Schwartz for their help developing and providing the murine models used in this work.

Chapter 4: Evaluation of the Theranostic Combination of [^{44g}Sc]Sc-DOTA-TATE and [^{161}Tb]Tb-DOTA-TATE

4.1 Introduction

Peptide receptor radionuclide therapy (PRRT) is a rapidly evolving and exciting area of cancer treatment. Prolonged, selective delivery of radiation to the tumor with minimal toxicity to surrounding normal tissue is the goal of PRRT. Labeling a radionuclide (choice of which depends on emission characteristics, physical half-life, and chemical properties) to a targeting molecule via a linker (and commonly, a chelating agent in the case of radiometals) that targets the site of disease achieves this goal by delivering the source of radiation directly to the tumor (Figure 64) [126]. Unlike external beam radiation therapy or systemic chemotherapy, PRRT specifically targets the tumor on the molecular level with the goal of less toxicity from exposure to normal, healthy tissue [126].

Targeted radionuclide therapy first emerged in the 1940s when physicians were using post-surgery ^{131}I ablation to treat residual thyroid disease [127, 126]. Since then, the field has evolved and clinical practice is utilizing more radionuclides such as ^{131}I, ^{90}Y, ^{223}Ra, and ^{177}Lu. Additionally, several groups are investigating alpha-emitting radionuclides like ^{225}Ac and ^{212}Pb for therapy in preclinical research [128, 129]. There are currently two FDA-approved radioimmunotherapy drugs: ^{131}I-tositumomab (BEXXAR®, GlaxoSmithKline) and ^{90}Y-ibritumomab tiuxetan (Zevalin®, Biogen-Idec Pharmaceuticals), both of which are used to treat B-cell non-Hodgkin's lymphoma [130, 131]. Painful bone metastases can be treated with the FDA-approved β^--emitters, ^{153}Sm-lexidronam (Qudramet®) and ^{89}Sr-chloride (Metastron®) [132, 133]. However, the more recently FDA-approved, alpha-emitting ^{223}Ra-chloride (Xofigo®, Bayer) that also targets bone metastases for castration-resistant prostate cancer has

predominantly replaced ^{153}Sm-lexidronam and ^{89}Sr-chloride [134]. More recently, two ^{177}Lu-based radiopharmaceuticals have been FDA-approved: [^{177}Lu]Lu-PSMA-617 (Pluvicto™) for treating castration-resistant metastatic prostate cancer [135], and [^{177}Lu]Lu-DOTA-TATE (Lutathera®) for treatment of gastroenteropancreatic neuroendocrine tumors (GEP-NETs). In the case of unresectable somatostatin-receptor-positive neuroendocrine tumors, peptide receptor radionuclide therapy with ^{177}Lu ($t_{1/2}$ = 6.6443 d; β^-_{mean} = 133.6 keV; $\beta^-_{intensity}$ = 100.0%) has had promising clinical results with approximately 30% of patients having objective tumor response to Lutathera® treatment [136].

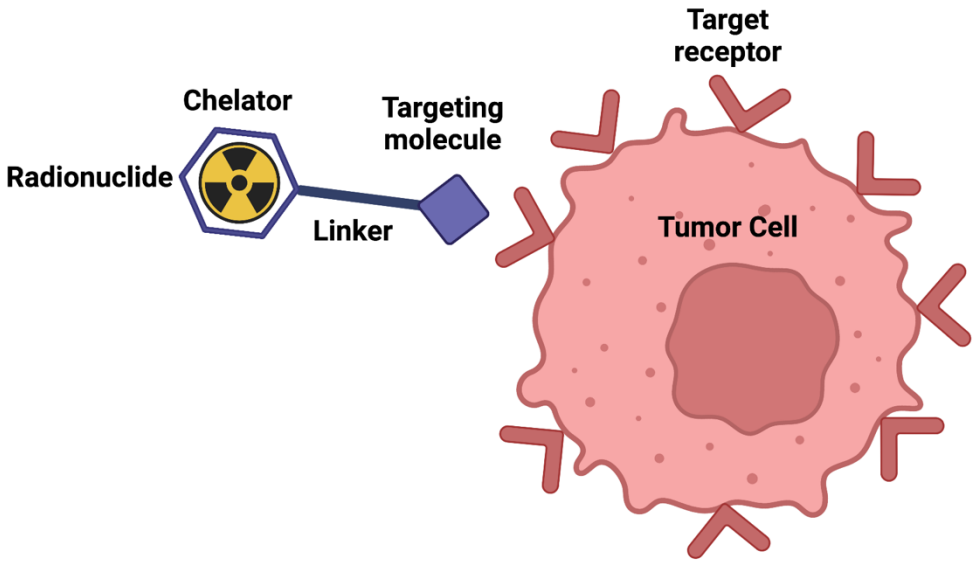


Figure 64: Radiopharmaceutical design composed of a radionuclide labeled with a chelator and a linker that attaches the radiometal to a targeting molecule.

Neuroendocrine tumors (NETs) are a group of tumors that originate from the endocrine and nervous systems with diverse characteristics [12]. NETs have several shared characteristics such as the presence of secretory granules, and they can form in a variety of organ systems. They are most often found in the lung (5%) or the gastroenteropancreatic region such as the small intestine, pancreas, and rectum (72%) [136, 12]. While NETs are relatively rare (2.5 to 5 per

100,000 people per year), the incidence of GEP-NETs has been increasing steadily and has more than doubled since 1985 [137]. The cause of the increase in NET diagnoses is unknown, but it is currently thought to be attributed to a combination of better diagnostic tools catching more disease (endoscopies, colonoscopies, and CT technology), and potential environmental factors [138].

Categorization of NETs divides disease into being either benign or malignant, and functional vs non-functional. Functional NETs secrete hormones and cause symptoms such as carcinoid syndrome; however, most NETs are non-functional and present few symptoms besides abdominal pain and are therefore difficult to diagnose [139, 140]. At the time of diagnosis, patients typically present vague, non-specific symptoms such as weight loss, diarrhea, or symptoms caused by metastases and large tumor mass (such as abdominal bleeding and pain) [12]. Because of the lack of early symptoms, NETs are often metastatic at the time of diagnosis, with only 40% of patients expressing local disease [12]. Currently, the only curative treatment technique is surgical resection, but this is not an option for patients with locally advanced or metastatic disease [12]. When surgery is not an option, patients are typically treated with a combination of chemotherapy, octreotide therapy, or other approaches [141, 12].

Many GEP-NETs overexpress somatostatin receptors (SSTRs) on their cell surfaces [142]. The hypothalamus releases somatostatin (a peptide hormone) which acts as a neurotransmitter and inhibits the release of growth hormone and growth factor secretion [142]. There are 5 different subtypes of SSTRs that are expressed in human tumors, but somatostatin receptor 2 (SST2) is the most frequently expressed subtype [142]. Additionally, somatostatin binds to SST2 with higher affinity than other SSTRs [12]. Tyr3-octreotide is an artificially developed somatostatin analogue with a similar affinity for SSTRs as somatostatin [12]. When linked to the

macrocyclic chelator DOTA, it forms the functionalized ligand DOTA-TOC. Octreotate is a newer artificial somatostatin analogue, with threonine replacing the C-terminus threonine alcohol in octreotide. Together with DOTA, this replacement results in a somatostatin analogue (DOTA-TATE) with 9 times higher affinity for SST2 than DOTA-TOC [12].

^{177}Lu-labeled DOTA-TATE (Lutathera®) enables the delivery of cytotoxic radiation in the form of β^- particles to GEP-NETs that overexpress SST2. The maximum tissue penetration of the emitted β^- particles is only 2 mm, resulting in minimal nearby healthy tissue toxicity while still being capable of reaching the nucleus of target cells [12]. Recently, the radionuclide ^{161}Tb ($t_{1/2}$ = 6.89 d; β^-_{mean} = 154 keV, $\beta^-_{intensity}$ = 101%) has been proposed as an alternative to ^{177}Lu for PRRT [143]. ^{161}Tb has similar physical decay characteristics to ^{177}Lu (half-life, mean β^- energy), but emits Auger and conversion electrons that may have additional therapeutic benefit. Müller et. al compared cell toxicity between ^{161}Tb-cm09 and ^{177}Lu-cm09 and found that a lower activity of ^{161}Tb-cm09 (1.7 - 4.5-fold decrease) achieved the same tumor killing effect (half-maximal inhibition of tumor cell viability) as ^{177}Lu-cm09 [144]. Additionally, ^{161}Tb-cm09 reduced tumor growth *in vivo* more efficiently when compared to ^{177}Lu-cm09 [144].

Terbium has a total of four clinically interesting radioisotopes: ^{149}Tb ($t_{1/2}$ = 4.12 h; α_{mean} = 3.967 MeV; $\alpha_{intensity}$ = 17%) for α-therapy, ^{152}Tb ($t_{1/2}$ = 17.5 h; β^+_{mean} = 1.14 MeV; $\beta^+_{intensity}$ = 20.3%) for PET imaging, ^{155}Tb ($t_{1/2}$ = 5.32 d; γ =86.55 keV (32.0%); γ = 105.32 keV (25.1%)) for SPECT imaging, and ^{161}Tb for β^- -therapy. While ^{161}Tb has chemically matched diagnostic analogues in ^{152}Tb and ^{155}Tb, these radionuclides are difficult to produce in large-scale quantities [145]. The ^{155}Gd(p,4n)^{152}Tb reaction results in yields up to 1.924 MBq/μAh of ^{152}Tb but requires enriched ^{155}Gd (14.8% natural isotopic abundance) material and incident energies of 30 - 66 MeV. Additionally, this route suffers from Dy and Tb contaminants. The ^{152}Gd(p,n)^{152}Tb is

another possibility and is accessible at much lower energies. However, the natural isotopic abundance of ^{152}Gd is low (0.20%) and ^{153}Tb is co-produced through ^{152}Gd(p,γ)^{153}Tb. Optimization of target thickness and careful selection of energy (12 MeV) reduces ^{153}Tb contamination to < 1%, though ^{152}Tb's high positron energy (> 1 MeV) limit its clinical applications.

For ^{155}Tb production, the indirect route ^{159}Tb(p,5n)^{155}Dy → ^{155}Tb produces ^{155}Tb but has the disadvantage that the ^{155}Tb would be inseparable from the bulk Tb target. Deuteron bombardment of natural Gd also produces ^{155}Tb through the ^{nat}Gd(d,x)^{155}Tb reaction but co-produces long-lived radioisotopes of Tb that cannot be chemically separated due to the many stable isotopes of Gd (^{152}Gd, 0.20%; ^{154}Gd, 2.18%; ^{155}Gd, 14.80%; ^{156}Gd, 20.47%; ^{157}Gd, 15.65%; ^{158}Gd, 24.84%; ^{160}Gd, 21.86%). Spallation reactions are another alternative route to produce both ^{152}Tb and ^{155}Tb. However, only a few centers are available worldwide, requiring large production yields and an established distribution network for this route to be clinically feasible.

Positron-emitting radioisotopes of scandium (^{43}Sc and ^{44g}Sc) may be suitable alternative diagnostic analogues for ^{161}Tb due to the several similarities between the trivalent ions of scandium, lutetium, and terbium. While scandium is a rare-earth metal, it has similar coordination preference and ionic bonding tendency to light lanthanides [146]. Table 23 lists several chemical properties of scandium and other trivalent cations discussed here. Scandium has a slightly smaller ionic radius than lutetium and terbium, but is closer to the light lanthanides than gallium. Additionally, scandium, lutetium, and terbium all have the same common coordination number of 8 while gallium has a coordination number of 6. Scandium's pKa is lower than lutetium and terbium and its high acid dissociation constant results in hydrolysis

($Sc^{+3}_{(aq)}$ → $Sc(OH)^{2+}$) beginning at pH 2 [146]. However, high molar activities with DOTA are possible with heat (80 °C) and reaction pH < 4.5.

Metal ion	Ionic radius	Coordination number	Hardness	pKa
Ga^{3+}	0.62	6	7.07	2.6
Sc^{3+}	0.87	8	10.49	4.3
Lu^{3+}	0.98	8	10.07	7.6
Tb^{3+}	1.04	8	10.07-10.30	7.9

Table 23: Chemical properties of several +3 metal ions [146].

Clinical studies have demonstrated the promising potential of [^{68}Ga]Ga-DOTA-TATE as a diagnostic tool for identifying primary tumors for treatment of NETs with [^{177}Lu]Lu-DOTA-TATE [147, 148]. However, the high positron energy and short half-life of ^{68}Ga ($t_{1/2}$ = 67.71 min, β^+_{mean} = 829.5 keV, $\beta^+_{intensity}$ = 88.91%) limit its resolution and ability to scan at late time points. Gallium's small ionic radius and lower coordination number compared to lutetium also suggest that it may not be an ideal match for lutetium. As mentioned in Chapter 1, while dosimetry guided PRRT is not currently the clinical standard, predicting tumor and healthy tissue dose from a pre-treatment diagnostic scan could tailor treatment to a patient's specific physiology. However, this approach requires the diagnostic radiopharmaceutical to have similar biodistribution and uptake in target and non-target tissues to the therapeutic radionuclide. Different ionic radii and coordination preference with chelators between different radiometals may affect the distribution and metabolic clearance of the radiopharmaceutical. Thus, diagnostic analogues for therapeutic radiopharmaceuticals should be chosen to closely match the chemical properties of the therapeutic radionuclide.

As mentioned above, scandium's ionic radius and coordination chemistry with DOTA may be better matched with light lanthanides used in therapeutic applications than gallium. Umbricht et. al compared *in vivo* biodistribution of [^{68}Ga]Ga-PSMA-11, [^{68}Ga]Ga-PSMA-617, [^{44g}Sc]Sc-PSMA-617, and [^{177}Lu]Lu-PSMA-617 in a mouse model with PC-3 PIP (PSMA^{pos}) tumors [149]. Their results indicate that the *in vivo* pharmacokinetics of [^{68}Ga]Ga-PSMA-617 were similar to [^{177}Lu]Lu-PSMA-617 except for increased [^{68}Ga]Ga-PSMA-617 uptake in the liver. Conversely, [^{44g}Sc]Sc-PSMA-617 and [^{177}Lu]Lu-PSMA-617 were found to have near identical *in vivo* biodistributions at all time points observed [149]. Due to the similar coordination chemistry with DOTA (the chelator used in both PSMA-617 and DOTA-TATE) and chemical properties between scandium, lutetium, and terbium, it was hypothesized that [^{44g}Sc]Sc-DOTA-TATE may also have more similar *in vivo* biodistribution to [^{161}Tb]Tb-DOTA-TATE compared to [^{68}Ga]Ga-DOTA-TATE.

In addition, ^{68}Ga's physical decay characteristics make it a less attractive diagnostic tool for PRRT. Its short half-life limits distribution except for local clinics and prevents delayed imaging following injection. ^{44g}Sc's four-fold longer half-life could facilitate regional production and distribution to clinics and facilities without a cyclotron. Its longer half-life also presents the opportunity to image at later time points when tumor-to-background ratios may improve and increase contrast. ^{68}Ga's higher positron energy compared to ^{44g}Sc also results in greater positron penetration in tissue. The mean and max positron ranges in tissue for ^{68}Ga and ^{44g}Sc are shown in Table 24 [150]. Higher positron ranges may lead to lower PET resolution and increase in partial volume effects when quantifying activity in small lesions (< 10 mm) or investigation in murine models. While the max range in tissue for these two radionuclides is between 7 and 10 mm, the

average range will be lower due to the torturous paths that positrons caused from deflections within the tissue.

Radionuclide	R_{mean} (mm)	R_{max} (mm)
^{68}Ga	3.559	10.273
^{44g}Sc	2.458	7.355

Table 24: Average and maximum positron range in tissue for ^{68}Ga and ^{44g}Sc [150].

4.1.2 Motivation

^{161}Tb is a novel alternative to ^{177}Lu in PRRT. Theoretical models have predicted that ^{161}Tb may be more effective than ^{177}Lu at treating very small lesions due to its emission of short-range Auger and conversion electrons [151, 152, 153]. *In vivo* studies comparing ^{161}Tb- and ^{177}Lu-labeled PSMA-617 showed similar tissue distribution between the two radiotracers but mice injected with [^{161}Tb]Tb-PSMA-617 demonstrated activity-dependent improvement in tumor response compared to mice injected with [^{177}Lu]Lu-PSMA-617 [154].

Terbium's radioisotopes suitable for PET (^{152}Tb) and SPECT (^{155}Tb) imaging are difficult to produce in large-scale quantities and have lower PET resolution when compared with ^{44g}Sc. Given ^{44g}Sc's relative ease of production in clinical-scale quantities compared to ^{152}Tb, its comparatively lower positron energy to both ^{68}Ga and ^{152}Tb, its longer half-life relative to ^{68}Ga, and its chemical similarities to light lanthanides, ^{44g}Sc may be a suitable diagnostic analogue to ^{161}Tb. In this work, [^{44g}Sc]Sc-DOTA-TATE's ability to act as a diagnostic analogue for [^{161}Tb]Tb-DOTA-TATE in an SST2-expressing murine model was investigated. Lipophilicity, internalization, binding affinity, and *in vivo* pharmacokinetics between [^{68}Ga]Ga-DOTA-TATE, [^{44g}Sc]Sc-DOTA-TATE, and [^{161}Tb]Tb-DOTA-TATE were also compared to determine whether

[^{44g}Sc]Sc-DOTA-TATE could act as a better diagnostic analogue for [^{161}Tb]Tb-DOTA-TATE than [^{68}Ga]Ga-DOTA-TATE.

4.2 Materials and Methods

4.2.1 Chemicals

All solutions were prepared with optima grade HCl and HNO_3 purchased from Fisher Chemical and 18 MΩ cm^{-1} water. Trace metal free sodium acetate was purchased from Sigma Aldrich and reagent grade sodium ascorbate was purchased from Fisher Chemical. Reagent grade ethanol and n-octanol was purchased from Sigma Aldrich. Branched DGA resin was purchased from Eichrom. DOTA chelator and DOTA-TATE were purchased from Macrocyclics. AR42J and NCI-H69 cell lines were purchased from ATCC. Isotopically enriched calcium carbonate ($^{44}CaCO_3$) was obtained from the Department of Energy National Isotope Development Center (See Chapter 2, Table 3 for isotopic enrichment).

4.2.2 DOTA-TATE radiolabeling

^{44g}Sc was produced through proton bombardment of enriched ^{44}CaO targets via the ^{44}Ca(p,n)^{44g}Sc reaction on a 16 MeV GE Healthcare PETtrace cyclotron at the University of Wisconsin, Madison following the procedure outlined in Chapter 2. Radiochemical separation of ^{44g}Sc from the enriched calcium target material was performed by single-column extraction chromatography utilizing branched DGA resin and methodology also described in Chapter 2. ^{68}Ga was obtained in the form of $^{68}GaCl_3$ through elution (5 mL, 0.1 M HCl) of a GalliaPharm ^{68}Ge/^{68}Ga generator (Eckert & Ziegler, Inc.) at the University of Wisconsin's clinical radiopharmaceutical facility. ^{161}Tb was produced at the University of Missouri's research reactor through neutron bombardment of enriched ^{160}Gd targets (^{160}Gd(n,γ)^{161}Gd → ^{161}Tb).

The [^{68}Ga]Ga-, [^{44g}Sc]Sc-, [^{161}Tb]Tb-DOTA-TATE synthesis procedure is shown in Figure 65. Briefly, 118 MBq of ^{68}Ga (3.2 mCi; 640 µL; 0.1 M HCl) was mixed with 23 µL DOTA-TATE (5 nmol/mCi; 7.4 MBq/nmol; 0.697 nmol/µL) and 5 - 10 µL 0.5 M NaOAc buffer (final pH 4 - 4.5) at 80 °C for 30 min under constant shaking (350 rpm). Due to the short half-life of ^{68}Ga compared to the length of the labeling procedure, ^{68}Ga was labeled with half the mass compared to ^{44g}Sc and ^{161}Tb so that the ratio of ^{68}Ga to cold ligand would be comparable at the time of injection. For [^{44g}Sc]Sc-DOTA-TATE synthesis, 60 MBq of ^{44g}Sc (1.6 mCi; 100 µL; 0.01 M HCl) was mixed with 48 µL DOTA-TATE (10 nmol/mCi; 3.7 MBq/nmol; 0.697 nmol/µL) and 2 - 5 µL 0.5 M NaOAc buffer (final pH 4 – 4.5) at 80 °C for 30 min under constant shaking (350 rpm). Similarly, 44 MBq of ^{161}Tb (1.2 mCi; 35 µL; 0.05 M HCl) was mixed with 36 µL DOTA-TATE (10 nmol/mCi; 3.7 MBq/nmol; 0.697 nmol/µL) and 2 - 5 µL 0.5 M NaOAc buffer (final pH 4 – 4.5) at 80 °C for 30 min under constant shaking (350 rpm).

Following labeling, the M-DOTA-TATE compounds were purified with a reverse-phase, solid-phase-extraction Oasis HLB light cartridge (Waters) to remove all free M = ^{68}Ga, ^{44g}Sc, or ^{161}Tb. [^{68}Ga]Ga-DOTA-TATE, [^{44g}Sc]Sc-DOTA-TATE, and [^{161}Tb]Tb-DOTA-TATE were eluted from the column in 1.5 mL absolute ethanol into a vial containing 1 mg/mCi (0.27 mg/MBq) sodium ascorbate to prevent radiolysis. The solution was dried at room temperature under argon flow (approximately 30 - 45 min) and reconstituted in 1 mL/mCi (0.027 mL/MBq) PBS. Radiochemical yield was determined through thin layer chromatography with 50 mM EDTA as a mobile phase. HPLC was also used to determine radiochemical purity using a C18 column (4.6 x 250 mm, Dionex 5µm 120 Å; ThermoFisher) and a water (0.1% Trifluoroacetic acid, TFA) to acetonitrile gradient (5% MeCN, 0 - 3.5 min; 5% - 35% MeCN, 3.5 - 13 min; 35%

- 90% MeCN, 13 - 15 min; 90% MeCN, 15 - 19 min; 90% - 5% MeCN, 19 - 20 min; 5% MeCN, 20 - 25 min) flowing at 1 mL/min.

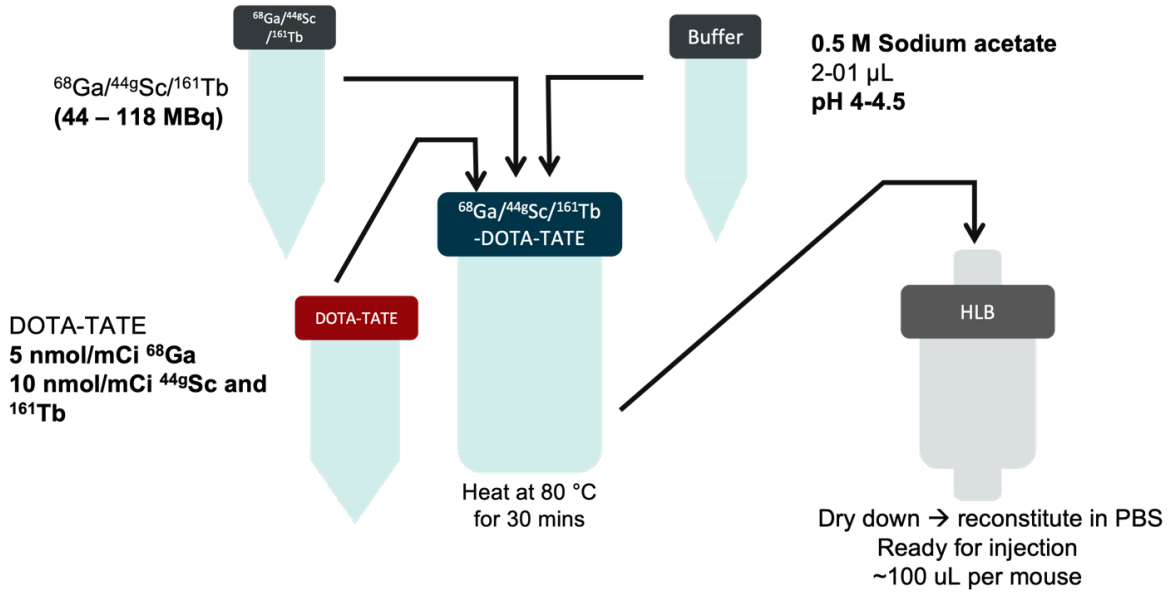


Figure 65: Synthesis procedure for [M]-DOTA-TATE, where [M] = ^{68}Ga, ^{44g}Sc, or ^{161}Tb.

Stability of [^{161}Tb]Tb-DOTA-TATE in PBS and human serum was additionally evaluated. Following HLB purification, ethanol dry-down, and reconstitution in PBS, one 100 µL (11.1 MBq, 300 µCi) fraction of [^{161}Tb]Tb-DOTA-TATE was added to 100 µL PBS at room temperature and a second 100 µL fraction was combined with 100 µL human serum and incubated at 37 °C. Samples from the PBS vial were taken at 30 min, 2 h, 6 h, and 24 h post incubation and spotted on aluminum-backed silica gel TLC plates and run in EDTA mobile phase. Similarly, for the human serum vials, at each time point, 20 µL samples were taken and mixed with 20 µL acetonitrile to precipitate all proteins. Vials were centrifuged for 5 mins and then spotted on TLC plates. Samples were taken at 30 min, 2 h, 6 h, and 24 h post incubation. Additionally, aliquots were taken from both vials at 0 h and 24 h post incubation for HPLC analysis.

4.2.3 *In vitro* cell studies

Cell culture

Most preclinical studies evaluating radiolabeled somatostatin analogues use the rat pancreatic cell line AR42J or the human small cell lung cancer cell line NCI-H69, which both natively express SST2 [155]. Both AR42J and NCI-H69 cell lines were purchased from ATCC. AR42J cells were grown at 37°C with 5.6% CO_2 in ATCC-formulated F-12K media supplemented with 20% FBS, 1% penicillin-streptomycin, and 1 mL (2.5 mg/mL) Plasmocin®. NCI-H69 cells were grown in ATCC-formulated RPMI-1640 medium supplemented with 10% FBS, 1% penicillin-streptomycin, and 1 mL (2.5 mg/mL) Plasmocin®.

Measurement of binding affinity and receptor density

Receptor density was compared across AR42J and NCI-H69 cell lines using [^{44g}Sc]Sc-DOTA-TATE and the binding affinity was compared across the three M-DOTA-TATE ligands using AR42J cells. Both properties were measured with saturation binding assays (n = 3 per M-DOTA-TATE ligand and cell line). The experimental procedure is shown in Figure 66. Cells were seeded into 96-well plates (50,000 cells/50 µL per well) with filter bottoms. Increasing concentration of M-DOTA-TATE (0.06 – 1000 nM) were added to each well (50 µL activity in PBS). Cells were incubated at 37 °C and shaken at 300 rpm for 2 hours (total volume, 100 µL). The supernatant was then removed, and filters were washed with three 200 µL rinses of PBS. Filters containing the cells were dried and counted in a calibrated gamma-counter for analysis. K_D values and receptor density was found by plotting the total (specific and non-specific) binding versus the radio-ligand concentration and performing non-linear regression using GraphPad Prism software. The formula used to determine K_D and B_{max} was:

$$y = \frac{B_{max} * x}{K_D + x} + (NS * X) + Background \quad (9)$$

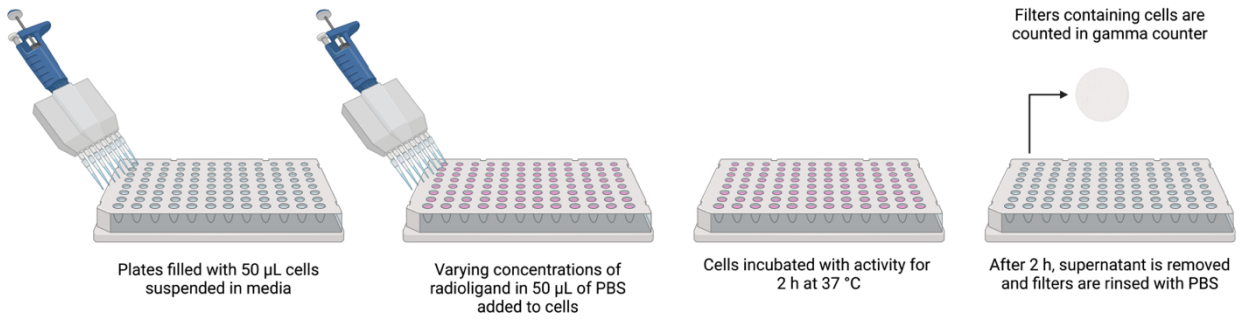


Figure 66: Binding saturation assay procedure for determining receptor density and binding affinity (created with BioRender.com).

where y is the total binding, x is the radioligand concentration, NS is the non-specific binding, K_D is the equilibrium dissociation constant (same units as x), and B_{max} is the maximum specific binding (same units as y). Because the measured K_D can change based on experimental setup, the binding affinity of [^{68}Ga]Ga-DOTA-TATE and [^{44g}Sc]Sc-DOTA-TATE was compared relatively with [^{161}Tb] Tb-DOTA-TATE as discussed by Reddy and Umbricht [156, 149]. Additionally, calibration samples were taken of the prepared stock radioligand concentrations (10 µL) to confirm added radioligand concentration.

Internalization

Internalization assays were performed at various time points by plating 50,000-100,000 AR42J cells (2 mL medium) in clear-bottom petri-dishes. Three dishes were plated per time point for each M-DOTA-TATE ligand. Internalization fraction was assessed at 30 min and 2 h for [^{68}Ga]Ga-DOTA-TATE, 30 min, 2 h, 4 h, and 8 h for [^{44g}Sc]Sc-DOTA-TATE, and 30 min, 2 h, 4 h, 8 h, and 24 h for [^{161}Tb]Tb-DOTA-TATE. Cells were incubated for at least 24 hours prior to the experiment to allow for adhesion and growth. The following day, 150 – 370 kBq (4 – 10 µCi) of purified M-DOTA-TATE (0.04 – 0.1 nmol) were added to each dish at the corresponding time point beginning with the latest time point. Following addition of radio-ligand, dishes were

returned to the 37 °C (5% CO_2) incubator and incubated for their designated lengths. Following incubation with M-DOTA-TATE, the supernatant was collected from all dishes along with a 3 mL PBS rinse to collect all unbound M-DOTA-TATE. After the dishes were rinsed, 1 mL 0.1 M sodium citrate was added to the dishes to remove the M-DOTA-TATE bound to the receptors of the cells. After 5 min, the 0.1 M sodium citrate fraction along with a 3 mL PBS rinse was collected, and 1 mL 0.25 M trypsin was added to each dish. Following a 5 min incubation period, the trypsinzed cells and a 3 mL PBS rinse was collected to measure the M-DOTA-TATE that was internalized into the cells. The full experimental procedure is shown in Figure 67. Each fraction was measured on a calibrated gamma counter. The internalized fraction was determined by dividing the internalized counts per second by the sum of the internalized and bound counts per second.

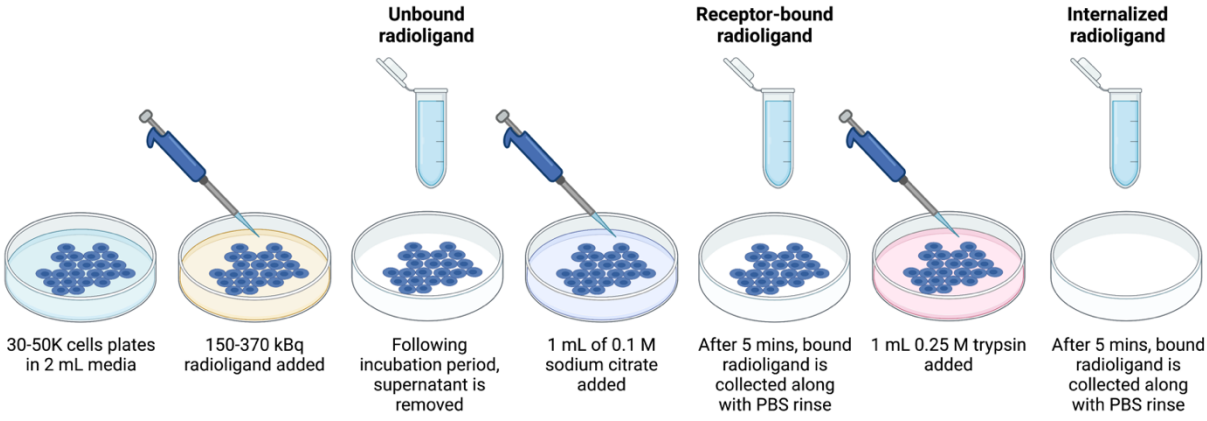


Figure 67: Internalization experimental workflow (created with BioRender.com).

4.2.5 Lipophilicity measurements

Following labeling and purification, the lipophilicity of [^{68}Ga]Ga-DOTA-TATE, [^{44g}Sc]Sc-DOTA-TATE, and [^{161}Tb]Tb-DOTA-TATE was measured using a shake-flask method (n = 3 per radioligand). Briefly, a 100 µL aliquot containing 3.7 MBq (100 µCi) of purified M-DOTA-TATE was added to 900 µL PBS. Additionally, 1 mL of n-octanol was added, and the vials were shaken vigorously to combine the two phases. Vials were allowed to sit for 30 min to permit phase separation and then centrifuged for 10 min. Small, 100 µL aliquots were taken from each phase and measured on a calibrated gamma counter. The lipophilicity was calculated as the log of the ratio of the counts per minute for the n-octanol phase divided by the counts per minute for the PBS phase.

4.2.6 *In vivo* PET/CT and SPECT/CT imaging

Tumor mouse model

Mice were purchased from The Jackson Laboratory (Bar Harbor, ME) and all animal studies were operated under an approved animal protocol with veterinarian supervision. For M-DOTA-TATE *in vivo* biodistribution comparison studies, three groups of female, 4 – 6-week-old NOD.Cg-*Prkdc*^{scid} *Il2rg*^{tm1Wjl}/SzJ (NSG™) mice (n = 4 per M-DOTA-TATE ligand) were subcutaneously injected with 1:1 mixture of AR42J cells (10^6 cells suspended in 40 µL PBS) and Matrigel® (40 µL; Corning) into their right shoulder (80 µL total volume) 18-21 days prior to imaging experiments (Figure 68).

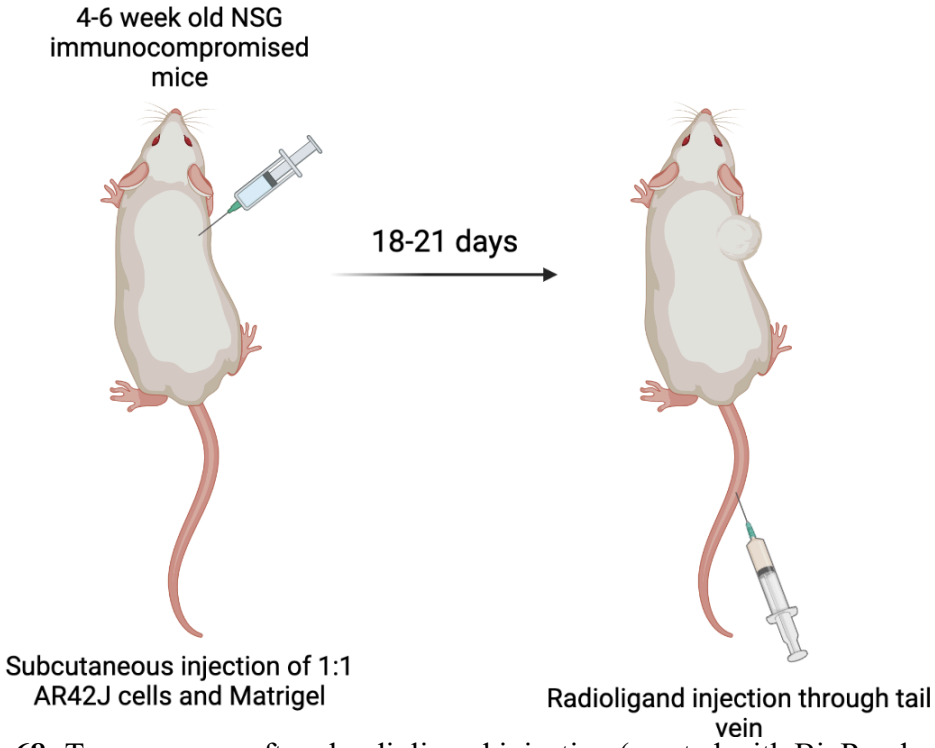


Figure 68: Tumor xenograft and radioligand injection (created with BioRender.com).

PET/CT imaging studies

[^{68}Ga]Ga-DOTA-TATE and [^{44g}Sc]DOTA-TATE PET/CT imaging studies were performed with an Inveon small animal μPET/μCT scanner (Siemens). Mice (n = 4) were injected with either 7.5 ± 0.3 MBq (203 ± 8 μCi; 2 nmol DOTA-TATE) [^{68}Ga]Ga-DOTA-TATE or 7.7 ± 0.2 MBq (207 ± 4 μCi; 2 nmol DOTA-TATE) [^{44g}Sc]Sc-DOTA-TATE 18 - 21 days following tumor inoculation. Mice were imaged two at a time in the prone position under isoflurane anesthesia (3.5% induction, 2% maintenance). CT scans were acquired to perform anatomical co-registration and CT-attenuation correction. Following an approximately 10 min CT scan, static, full body PET scans were performed with 40 - 80 million coincident events acquired (coincidence timing window 3.432 ns; energy window 350 - 650 keV). Following imaging, CT attenuation-corrected PET images were reconstructed using Inveon Acquisition Workplace (Siemens) using a non-scatter corrected 3-D ordered subset expectation maximization /

maximum a posteriori algorithm (OSEM3D/MAP). Radiotracer biodistribution for both M-DOTA-TATE ligands was quantified with volume-of-interest analysis drawn manually on reconstructed PET/CT imaged (Inveon Research Workstation, Siemens) and expressed as percent injected activity per gram of tissue (%IA/g). After the final scan, mice were euthanized with CO_2 asphyxiation (and cardiac exsanguination as a secondary method), and organs of interest were collected for *ex vivo* quantification using a scale and a calibrated gamma counter to validate image-derived data. Uptake was expressed as %IA/g.

SPECT/CT imaging studies

[^{161}Tb]Tb-DOTA-TATE imaging studies were performed with a small animal MILabs-USPECT/CT^{UHR} scanner. Mice (n = 4) were injected with 9 ± 2 MBq (230 ± 50 μCi; 2 nmol DOTA-TATE) [^{161}Tb]Tb-DOTA-TATE 18 days following tumor inoculation. Mice were imaged 4 at a time using an MILabs multimouse bed and a general-purpose rat and mouse collimator (GP-RM) with 1.5 mm pinhole size, < 0.85 mm reconstructed resolution, and > 700 cps/MBq sensitivity. Spiral, step-mode, 40-minute duration scans were collected with one time frame and 20 SPECT positions (2 mins scan length per position). Following SPECT acquisition, CT scans were collected for anatomical co-registration and CT-attenuation correction. Images were reconstructed using the 74.57 keV (10.2%) gamma (2.4% energy width) using a similarity-regulated ordered subsets expectation maximization (SROSEM) algorithm (0.4 mm isotropic voxels, 128 subsets, 5 iterations, 1.0 mm FWHM gaussian blurring). CT-attenuation corrected SPECT images were analyzed with VOI analysis manually drawn using Imalytics Preclinical 3.0 (Gremse) software and expressed as %IA/g. After the final time-point scan, mice were euthanized and organs of interest were collected, weighed, and measured on a calibrated gamma counter to verify image-derived data.

4.2.7 [^{161}Tb]Tb-DOTA-TATE toxicity

Base-line blood samples were taken from the sublingual vein of female, 6-week-old NSG™ mice (n = 2) and collected in MiniCollect® K3E K3EDTA tubes containing tri-potassium K3EDTA for complete blood cell (CBC) analysis on a VETSCAN® HM5 hematology analyzer. Three days after base-line blood samples were collected, the mice were injected with 350 µL of 19 ± 0.1 MBq (515 ± 4 µCi) low molar activity [^{161}Tb]Tb-DOTA-TATE (1.1 MBq/nmol; 30 nmol/mCi). Eight days after injection with [^{161}Tb]Tb-DOTA-TATE, additional blood samples were taken from the sublingual vein and CBC analysis performed using the same methodology as the base-line samples to compare [^{161}Tb]Tb-DOTA-TATE effects on white blood cell count.

4.2.8 [^{161}Tb]Tb-DOTA-TATE dosimetry estimations

Biodistribution from time activity curves discussed in section 4.2.6 in conjunction with the Medical Internal Radiation Dose (MIRD) formulism were used to estimate dose to human female organs [157, 158]. For each time point that the dose was estimated for (2 h, 4 h, and 8 h), the absorbed dose for select target organs was calculated by the sum:

$$d(r_T) = \frac{1}{A_0}\sum_S \tilde{A}(r_S) \times S(r_T \leftarrow r_S) \quad (10)$$

over each source organ where A_0 is the injected activity, $\tilde{A}(r_S)$ is the time-integrated activity in the entire organ r_S for each end point derived from murine time activity curves, and $S(r_T \leftarrow r_S)$ is the absorbed dose rate for target organ r_T per unit of radioactive decay in source organ r_S using the ICRP 110 AF model [159, 160]. Values for $S(r_T \leftarrow r_S)$ were taken from OpenDose [159] for ^{161}Tb for each female human source organ. Organ masses and S-values are listed in Table 25.

[^{68}Ga]Ga-DOTA-TATE and [^{44g}Sc]Sc-DOTA-TATE time activity curves were decay corrected back to time of injection and then decayed back to each time point using ^{161}Tb's half-life to estimate [^{161}Tb]Tb-DOTA-TATE biodistribution. Partial volume effects were accounted

for each organ using data from section 4.3.4 and the measured *ex vivo* masses to determine organ volume.

The spleen, stomach, and small-intestines were not delineated, so the time-averaged activity in these organs were assumed to be identical to the liver because they are all components of the hepatobiliary clearance pathway. Additionally, the tumor was assumed to be in the pancreas for cross-dose calculations to simulate a GEP-NET in a human. The dose for the urinary bladder was only calculated for the bladder wall due to the frequent excretion of bladder contents. Similarly for the heart, stomach, and intestines, the dose to the wall of each organ is reported (excluding dose to contents).

Evaluating human dose from murine time activity curves relies on the assumption that the percent injected activity in a whole organ is equal between humans and mice. Several physiological differences between mice and humans exist that could influence the biodistribution of a tracer. Mice have faster metabolism than humans and different enzymes that may break down injected peptides more or less preferentially compared to humans [161]. However, the assumption that the distribution is the same between mice and humans allows for a first order approximation of the dose in humans and is provided to demonstrate ^{68}Ga's and ^{44g}Sc's ability to estimate dose for ^{161}Tb rather than to provide absolute human dosimetry of [^{161}Tb]Tb-DOTA-TATE.

Source organ (S)	Mouse organ mass (g) [162]	Target organ (T)	S-value (mGy/MBq/s) [159]
Urinary bladder wall	0.07	Urinary bladder wall	7.7458E-4
		Kidneys	3.3202E-9
		Liver	9.3961E-10
		Lungs	1.1210E-10
		Spleen	6.3375E-10
		Stomach wall	1.7364E-9
		Small intestine wall	3.3371E-7
		Heart wall	1.64E-10
		Pancreas (tumor)	4.01E-09
Kidneys	0.74	Urinary bladder wall	3.2960E-9
		Kidneys	1.2169E-4
		Liver	2.6828E-7
		Lungs	2.48E-08
		Spleen	4.1819E-7
		Stomach wall	2.7576E-7
		Small intestine wall	2.5289E-7
		Heart wall	3.23E-08
		Pancreas (tumor)	7.29E-07
Liver	2.14	Urinary bladder wall	9.3217E-10

		Kidneys	2.6758E-7
		Liver	2.4583E-5
		Lungs	1.5874E-7
		Spleen	8.0167E-8
		Stomach wall	3.4177E-7
		Small intestine wall	8.1548E-8
		Heart wall	1.65E-07
		Pancreas (tumor)	3.27E-07
Lungs	0.14	Urinary bladder wall	1.19E-10
		Kidneys	2.4771E-8
		Liver	1.6138E-7
		Lungs	3.4837E-5
		Spleen	1.9387E-7
		Stomach wall	9.5014E-8
		Small intestine wall	6.2483E-9
		Heart wall	7.02E-07
		Pancreas (tumor)	2.20E-08
Spleen	0.13	Urinary bladder wall	6.4322E-10
		Kidneys	4.1551E-7
		Liver	7.9697E-8
		Lungs	1.9593E-7
		Spleen	2.5608E-4
		Stomach wall	1.1108E-6

		Small intestine wall	8.4998E-8
		Heart wall	1.63E-07
		Pancreas (tumor)	1.52E-07
Stomach wall	0.07	Urinary bladder wall	1.8067E-9
		Kidneys	2.8651E-7
		Liver	3.5222E-7
		Lungs	9.8272E-8
		Spleen	1.1499E-6
		Stomach wall	2.2944E-4
		Small intestine wall	3.4438E-7
		Heart wall	2.39E-07
		Pancreas (tumor)	1.54E-06
Small intestine wall	1.5	Urinary bladder wall	3.4415E-7
		Kidneys	2.6171E-7
		Liver	8.4089E-8
		Lungs	6.3374E-9
		Spleen	8.8585E-8
		Stomach wall	3.4302E-7
		Small intestine wall	5.4178E-5
		Heart wall	1.08E-08
		Pancreas (tumor)	7.01E-07
Heart contents	0.2	Urinary bladder wall	1.56E-10

		Kidneys	3.70E-08
		Liver	1.66E-07
		Lungs	3.94E-07
		Spleen	1.82E-07
		Stomach wall	2.14E-07
		Small intestine wall	1.18E-08
		Heart wall	2.97E-06
		Pancreas (tumor)	4.48E-08
Pancreas (tumor)	0.54	Urinary bladder wall	3.47E-09
		Kidneys	7.53E-07
		Liver	3.39E-07
		Lungs	2.25E-08
		Spleen	1.59E-07
		Stomach wall	1.54E-06
		Small intestine wall	7.02E-07
		Heart wall	4.12E-08
		Pancreas (tumor)	2.76E-04

Table 25: Organ masses and S-values used for ^{161}Tb dosimetry estimations [162, 160, 159].

4.3 Results and Discussion

4.3.1 DOTA-TATE radiolabeling

[^{68}Ga]Ga-DOTA-TATE was produced with near quantitative yields (> 97%) when labeled with 7.4 MBq/nmol DOTA-TATE (5 nmol/mCi) while [^{44g}Sc]Sc-DOTA-TATE and [^{161}Tb]Tb-DOTA-TATE were produced at near quantitative yields (> 96%) when labeled with 3.7

MBq/nmol DOTA-TATE (10 nmol/mCi) after a 30 min incubation period. A sample autoradiography image of a TLC plate spotted with free ^{161}Tb and labeled [^{161}Tb]Tb-DOTA-TATE is shown in Figure 69.

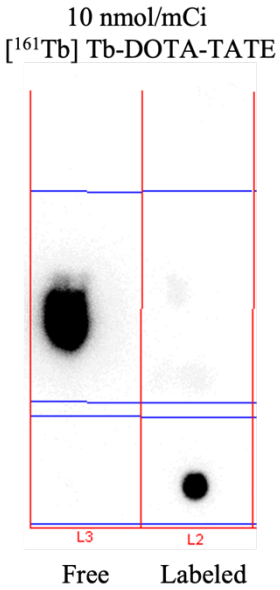


Figure 69: Autoradiography image of a TLC plate spotted with free ^{161}Tb (left lane) and [^{161}Tb] Tb-DOTA-TATE labeled at 3.7 MBq/nmol (10 nmol/mCi) DOTA-TATE.

The stability of [^{161}Tb]Tb-DOTA-TATE was evaluated in PBS and human serum up to 24 h post incubation and was evaluated by TLC and HPLC. Stabilities at 24 h were > 97% for the sample incubated in PBS and > 93% for the sample incubated in human serum via TLC. Radio-HPLC chromatograms show a single peak at the retention time of [^{161}Tb]Tb-DOTA-TATE with no additional peaks, indicating minimal degradation of [^{161}Tb]Tb-DOTA-TATE in PBS and human serum up to 24 h (Figure 70).

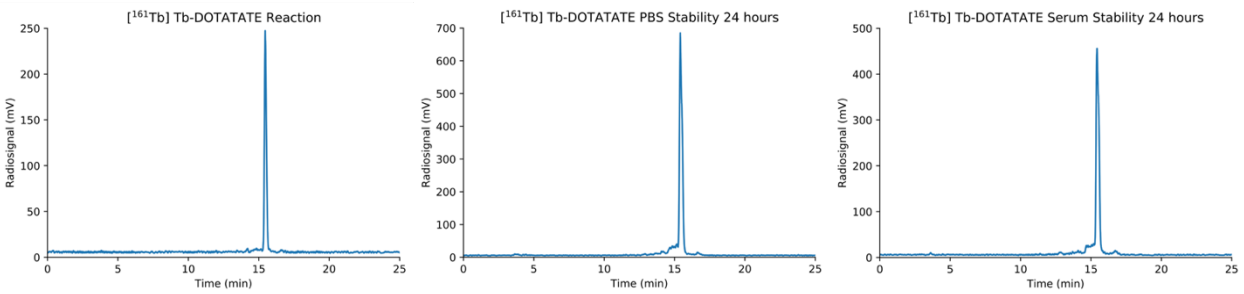


Figure 71: Radio-HPLC chromatograms of [^{161}Tb] Tb-DOTA-TATE reaction (A), stability in PBS after 24 h (B), and stability in human serum after 24 h (C).

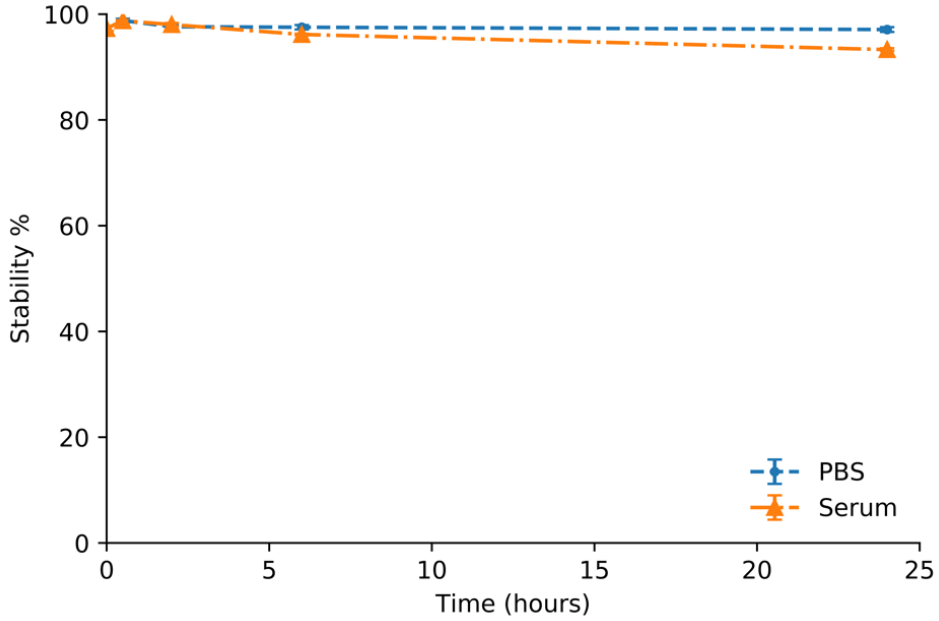


Figure 70: [^{161}Tb]Tb-DOTA-TATE stability in PBS and human serum.

4.3.2 *In vitro* cell studies

Measurement of binding affinity and receptor density

Receptor density was measured using [^{44g}Sc]Sc-DOTA-TATE and was compared between AR42J and NCI-H69 cell lines as shown in Table 26. The receptor density was a factor of 10 higher for AR42J cells (approximately 350,000 receptors per cell) compared to NCI-H69.

Similar receptor densities for AR42J cells were reported by Bestervelt et. al. (154 fmol per 2 x 10^5 cell; ~464,000 receptors per cell) [163]. Lower receptor density cells would result in lower uptake for an identical injected masse so AR42J cells were chosen for *in vitro* and *in vivo* comparison studies between [^{68}Ga]Ga-DOTA-TATE, [^{44g}Sc]Sc-DOTA-TATE, and [^{161}Tb]Tb-DOTA-TATE.

Cell line	**B_{max} (fmol)**	**Binding sites/cell**
AR42J	57.5 ± 9.6	346,300 ± 57,800
NCI-H69	7.2 ± 1.8	43,400 ± 10,800

Table 26: Receptor density measured using [^{44g}Sc]Sc-DOTA-TATE for both cell lines investigated here.

AR42J equilibrium dissociation constants (K_D) were compared in triplicate between the three M-DOTA-TATE ligands investigated. The measured K_D values along with the relative binding affinity are shown in Table 27. Figure 72 shows plots of the saturation binding assay with fits generated by GraphPad prism. All three radiotracers have comparable K_D values within error indicating comparable binding affinity with the SST2 receptors. The B_{max} for [^{68}Ga]Ga-DOTA-TATE appears to be higher than [^{44g}Sc]Sc-DOTA-TATE and [^{161}Tb]Tb-DOTA-TATE in Figure 72, suggesting that the receptors per cell were higher for the [^{68}Ga]Ga-DOTA-TATE experiments. However, this was due to a vacuum pump malfunction that caused poor rinsing of the filters and resulted in higher non-specific binding.

Radioligand	K_D (nM)	Relative binding affinity
[^{68}Ga]Ga-DOTA-TATE	1.02 ± 1.01	0.81
[^{44g}Sc]Sc-DOTA-TATE	0.96 ± 0.79	0.85
[^{161}Tb]Tb-DOTA-TATE	0.83 ± 0.52	1.00

Table 27: Measured AR42J receptor binding affinity for [^{68}Ga]Ga-DOTA-TATE, [^{44g}Sc]Sc-DOTA-TATE, and [^{161}Tb]Tb-DOTA-TATE.

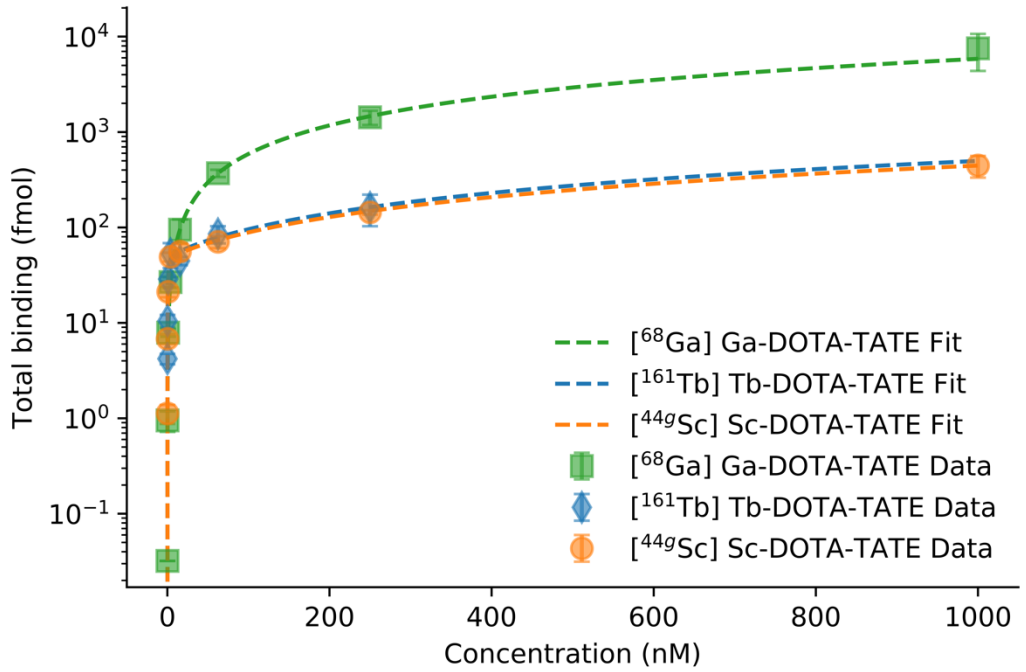


Figure 72: Binding saturation assay for AR42J cells along with fits.

Internalization

The rate of internalization into the cell was compared across the three M-DOTA-TATE ligands (Figure 73). The internalized fraction at early time points was comparable across the tracers with 17-22% of the bound radio-ligand being internalized into the cell at 30 mins. At 2 h, the internalization rate begins to deviate between the three M-DOTA-TATE ligands with 21 ± 2 % of the [^{161}Tb]Tb-DOTA-TATE being internalized compared to 34 ± 4 % of the [^{44g}Sc]Sc-DOTA-

TATE and 27 ± 4% of the [^{68}Ga]Ga-DOTA-TATE. At the 8 h incubation period, the difference is even larger with only 23 ± 2% of [^{161}Tb]Tb-DOTA-TATE was internalized compared to 39 ± 4% of [^{44g}Sc] Sc-DOTA-TATE, indicating that [^{161}Tb]Tb-DOTA-TATE may be internalized into AR42J cells at a slower rate than [^{44g}Sc]Sc-DOTA-TATE and [^{68}Ga]Ga-DOTA-TATE.

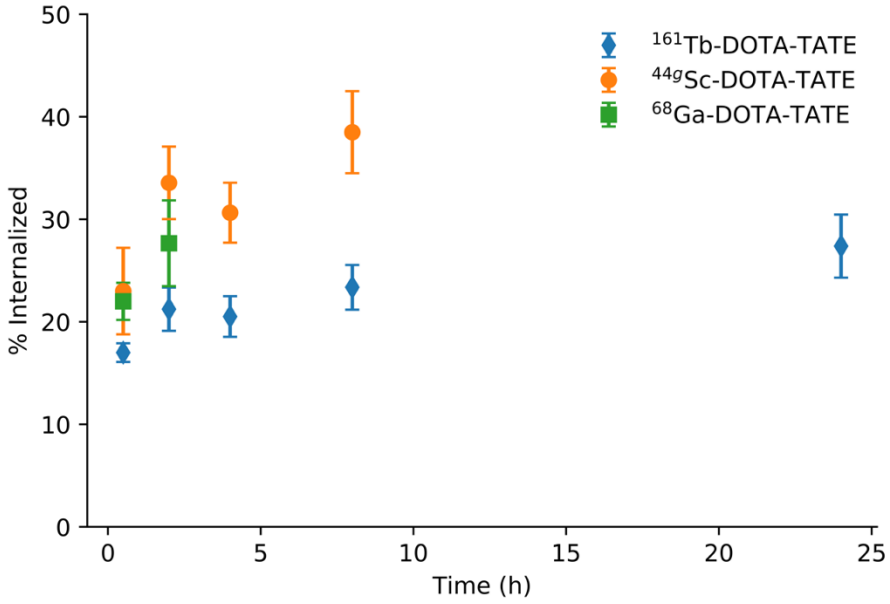


Figure 73: *In vitro* internalization of bound M-DOTA-TATE into AR42J cells versus time for all three M-DOTA-TATE ligands investigated here.

4.3.3 Lipophilicity measurements

Distribution coefficients (logD values) for each radio-ligand investigated in this work are shown in Table 28. The n-octanol/PBS distribution coefficients were similar across all three M-DOTA-TATE ligands with a slightly higher $logD_{7.4}$ value for [^{161}Tb]Tb-DOTA-TATE (-2.14 ± 0.03) compared to [^{68}Ga]Ga-DOTA-TATE (-2.32 ± 0.24) or [^{44g}Sc]Sc-DOTA-TATE (-2.36 ± 0.12). This indicates that [^{161}Tb]Tb-DOTA-TATE had a slightly higher affinity for the organic n-

octanol phase and is moderately more lipophilic compared to [^{68}Ga]Ga-DOTA-TATE or [^{44g}Sc]Sc-DOTA-TATE.

DOTA-TATE-based radiopharmaceuticals primarily clear through the kidneys using the renal clearance pathway [164]. Work done by Tafreshi et. al. demonstrated that increasing the lipophilicity of a compound reduced the uptake in the kidneys and slightly increased the uptake in the liver, suggesting that more lipophilic molecules are cleared through the hepatobiliary clearance route while less lipophilic molecules are cleared through the renal clearance route [165]. Thus, if a radiopharmaceutical is sufficiently more lipophilic than another, it may clear more through the liver than the kidneys. Tafreshi et. al. noted that molecules with logD values above -2.6 began to have increased hepatic route clearance [165]. However, as will be discussed in the next section, no increase in liver uptake was observed for [^{161}Tb]Tb-DOTA-TATE compared to [^{44g}Sc]Sc-DOTA-TATE or [^{68}Ga]Ga-DOTA-TATE indicating that its slightly higher $logD_{7.4}$ value was likely not significantly affecting its clearance route.

Radioligand	**Distribution coefficient**
[^{68}Ga] Ga-DOTA-TATE	-2.32 ± 0.24
[^{44g}Sc] Sc-DOTA-TATE	-2.36 ± 0.12
[^{161}Tb] Tb-DOTA-TATE	-2.14 ± 0.03

Table 28: $LogD_{7.4}$ values for the three radiotracers investigated in this work.

4.3.4 *In vivo* PET/CT and SPECT/CT imaging

PET/CT and SPECT/CT time activity curves

Tissue distribution in AR42J tumor-bearing mice was evaluated for [^{68}Ga]Ga-DOTA-TATE (30 min and 2 h p.i.), [^{44g}Sc]Sc-DOTA-TATE (30 min, 2 h, 4 h, and 8 h p.i.) and [^{161}Tb]Tb-DOTA-

TATE (30 min, 2 h, 4 h, 8 h, and 24 h p.i.). Time-dependent uptake in organs of interest derived from VOI quantification of CT-attenuation corrected PET and SPECT images are shown in Figures 74 and 75 (top row) with tabulated values in Tables 29-31. *Ex vivo* biodistribution data collected after the last time point are also shown in the bottom row of Figure 75.

As discussed in section 3.2.5, high positron energies (and consequently, large positron ranges in tissue) result in a larger reconstructed spatial distribution of the activity than the feature size, which can decrease the recovered activity from reconstructed images. From Table 14, the relatively high positron energy of ^{68}Ga ($E\beta^{+}_{mean}$ = 830 keV) results in an average range of 3.6 mm in tissue and a maximum range of 10.3 mm compared to ^{44g}Sc ($E\beta^{+}_{mean}$ = 632 keV) which has an average positron range of 2.5 mm and a maximum range of 7.4 mm. Because of this effect, image-derived tissue distribution underestimates activity recovery for ^{68}Ga to a greater degree than for ^{44g}Sc.

For SPECT imaging using ^{161}Tb, a similar effect is seen caused primarily by collimator performance rather than positron energy. SPECT collimators have a finite spatial resolution and collimators are typically designed balancing a tradeoff between high spatial resolution and high detection efficiency [166]. To measure this effect, the same Phantech partial volume effect phantom used for ^{68}Ga and ^{44g}Sc recovery coefficient quantification was filled with ^{161}Tb and scanned on the μSPECT/μCT scanner used for animal imaging.

Organ	**30 min p.i. (%IA/g)**	**2 h p.i. (%IA/g)**
Bone	0.35 ± 0.15	0.06 ± 0.04
Muscle	0.20 ± 0.13	0.05 ± 0.02
Heart	0.94 ± 0.31	0.13 ± 0.01
Lung	0.72 ± 0.16	0.28 ± 0.03

Liver	0.73 ± 0.22	0.24 ± 0.02
Kidneys	6.10 ± 2.38	2.98 ± 0.31
Tumor	4.80 ± 0.47	4.80 ± 0.98
Tumor-to-kidney ratio	0.87 ± 0.32	1.63 ± 0.33

Table 29: Time-dependent tissue uptake of [^{68}Ga]Ga-DOTA-TATE in AR42J tumor bearing mice.

Organ	**30 min p.i. (%IA/g)**	**2 h p.i. (%IA/g)**	**4 h p.i. (%IA/g)**	**8 h p.i. (%IA/g)**
Bone	0.50 ± 0.09	0.23 ± 0.05	0.04 ± 0.04	0.03 ± 0.01
Muscle	0.42 ± 0.24	0.23 ± 0.11	0.14 ± 0.14	0.02 ± 0.01
Heart	1.16 ± 0.27	0.21 ± 0.03	0.10 ± 0.05	0.04 ± 0.01
Lung	0.90 ± 0.24	0.27± 0.01	0.17 ± 0.09	0.09 ± 0.05
Liver	0.89 ± 0.17	0.33 ± 0.03	0.23 ± 0.09	0.19 ± 0.05
Kidneys	7.75 ± 1.38	5.00 ± 1.27	5.03 ± 1.39	4.25 ± 0.77
Tumor	4.18 ± 0.69	3.50 ± 0.67	3.18 ± 0.76	2.43 ± 0.29
Tumor-to-kidney ratio	0.54 ± 0.03	0.71 ± 0.05	0.64 ± 0.03	0.58 ± 0.09

Table 30: Time-dependent tissue uptake of [^{44g}Sc]Sc-DOTA-TATE in AR42J tumor bearing mice.

Organ	**30 min p.i. (%IA/g)**	**2 h p.i. (%IA/g)**	**4 h p.i. (%IA/g)**	**8 h p.i. (%IA/g)**	**24 h p.i. (%IA/g)**
Bone	0.28 ± 0.11	0.22 ± 0.16	0.17 ± 0.04	0.13 ± 0.05	0.05 ± 0.03

Muscle	0.10 ± 0.07	0.07 ± 0.06	0.03 ± 0.01	0.02 ± 0.02	0.04 ± 0.05
Heart	0.20 ± 0.05	0.06 ± 0.02	0.11 ± 0.06	0.07 ± 0.05	0.06 ± 0.03
Lung	0.33 ± 0.13	0.13 ± 0.05	0.14 ± 0.06	0.10 ± 0.05	0.09 ± 0.04
Liver	0.38 ± 0.21	0.15 ± 0.07	0.11 ± 0.04	0.12 ± 0.01	0.06 ± 0.02
Kidneys	3.64 ± 0.74	2.87 ± 0.91	2.12 ± 0.22	2.15 ± 0.76	0.95 ± 0.15
Tumor	2.56 ± 0.30	2.20 ± 0.40	1.94 ± 0.40	1.63 ± 0.49	1.17 ± 0.47
Tumor-to-kidney ratio	0.72 ± 0.12	0.80 ± 0.20	0.93 ± 0.24	0.85 ± 0.44	1.24 ± 0.43

Table 31: Time-dependent tissue uptake of [^{161}Tb]Tb-DOTA-TATE in AR42J tumor-bearing mice.

The activity recovery versus feature diameter is shown in Figure 76. The recovery coefficients for ^{68}Ga and ^{44g}Sc are similar to those reported by Rosar et. al and Disselhorst et. al using similar diameters and reconstruction methods [114, 121]. A correction factor to account for partial volume effects based on Figure 76 was applied to the image-derived uptake in kidneys and tumor at the final time point and compared to *ex vivo* biodistribution data in Figure 77. When the incomplete recovery is accounted for, the image-derived data match the *ex vivo*-derived data within error.

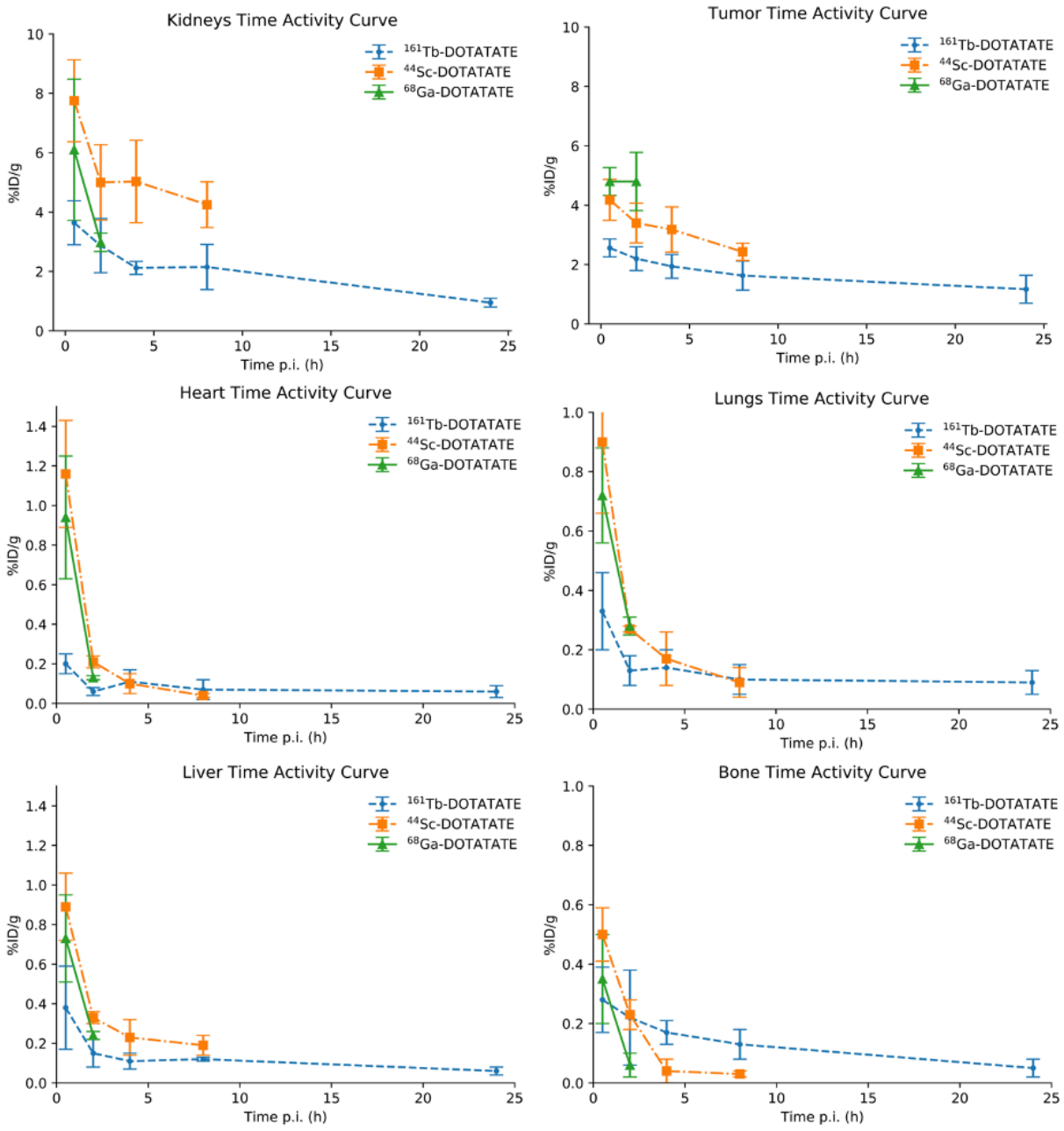


Figure 74: Uptake of [^{68}Ga]Ga-DOTA-TATE, [^{44g}Sc]Sc-DOTA-TATE, and [^{161}Tb]Tb-DOTA-TATE in several organs of interest.

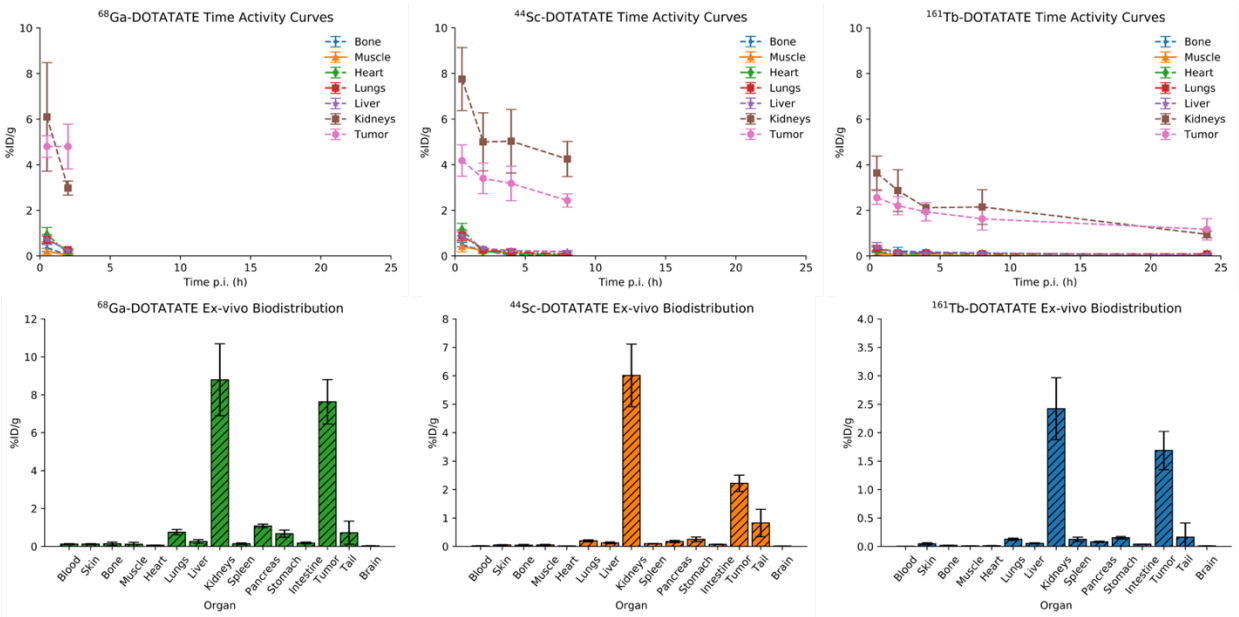


Figure 75: (Top row) Time-dependent uptake of the three radio-lignads investigated here determined from ROI analysis on CT-attenuation corrected PET and SPECT images. (Bottom row) *Ex vivo* biodistribution of the corresponding radio-ligand measured with a calibrated gamma counter.

Kidney and tumor uptake was highest for all three PET radiotracers at 30 min p.i. Kidney uptake decreased at a faster rate for [^{68}Ga] Ga-DOTA-TATE compared to the other two radio-ligands and resulted in a higher tumor-to-kidney ratio for [^{68}Ga] Ga-DOTA-TATE at 2 h p.i. (increasing from 0.87 ± 0.32 at 30 min p.i. to 1.63 ± 0.33 at 2 h p.i.). The tumor-to-kidney ratio increased after 30 min p.i. for [^{44g}Sc] Sc-DOTA-TATE as well, though to a lesser extent (0.54 ± 0.03 at 30 min p.i. and 0.71 ± 0.05 at 2 h p.i.). The tumor-to-kidney ratio for [^{161}Tb] DOTA-TATE remained relatively constant between 30 min and 8 h p.i. (0.72 - 0.93) until 24 h p.i. when most of the tracer cleared from the kidneys, resulting in a tumor-to-kidney ratio of 1.24 ± 0.43.

The accumulation of tracer in the tumor peaked for all three tracers at 30 min and high tumor uptake (>1 %IA/g) was observed even after 24 h p.i.

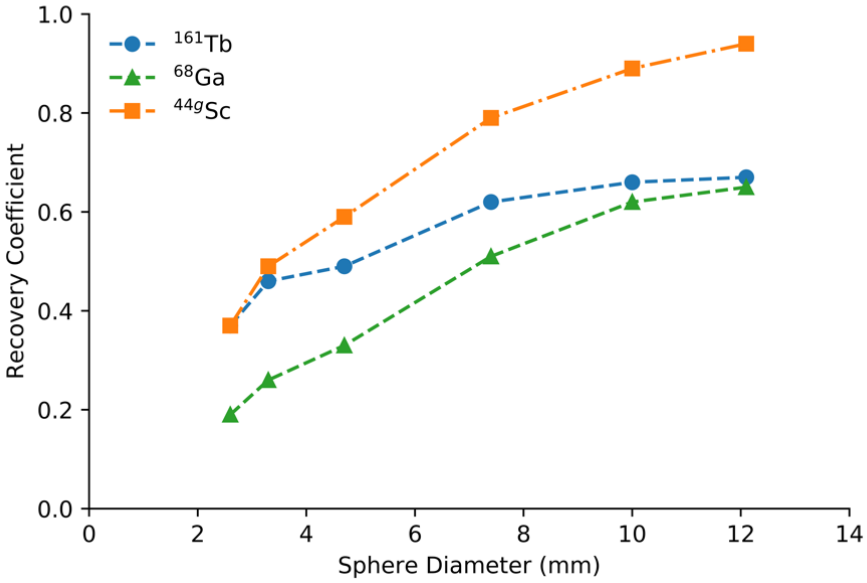


Figure 76: Activity recovery versus feature diameter.

Maximum intensity projection (MIP) PET/CT images of AR42J tumor-bearing mice injected with [^{68}Ga]Ga-DOTA-TATE and [^{44g}Sc]DOTA-TATE are shown in Figure 78. The higher tumor-to-kidney ratio for mice injected with [^{68}Ga]Ga-DOTA-TATE compared to [^{44g}Sc]DOTA-TATE can be seen in the brighter tumor region compared to the kidneys in the 2 h p.i. image for

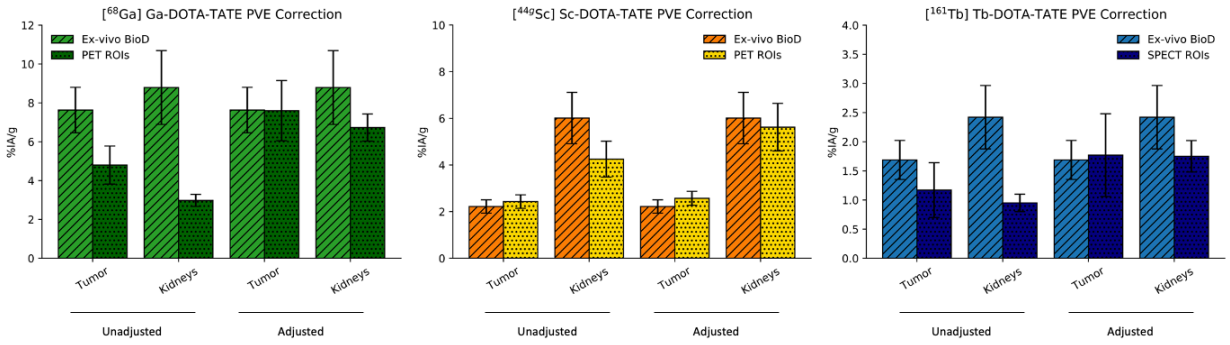


Figure 77: PVE-corrected uptake from PET/CT and SPECT/CT images compared to *ex vivo*-derived data.

the [^{68}Ga]Ga-DOTA-TATE injected mice, indicating higher tumor than kidney uptake. At 2 h p.i. for the [^{44g}Sc]DOTA-TATE injected mice, the kidneys remain brighter than the tumor region indicating higher kidney than tumor uptake. Tumor uptake can be seen at 30 min p.i. for all mice injected with both PET radio-ligands and remained high even at 2 - 8 h p.i.

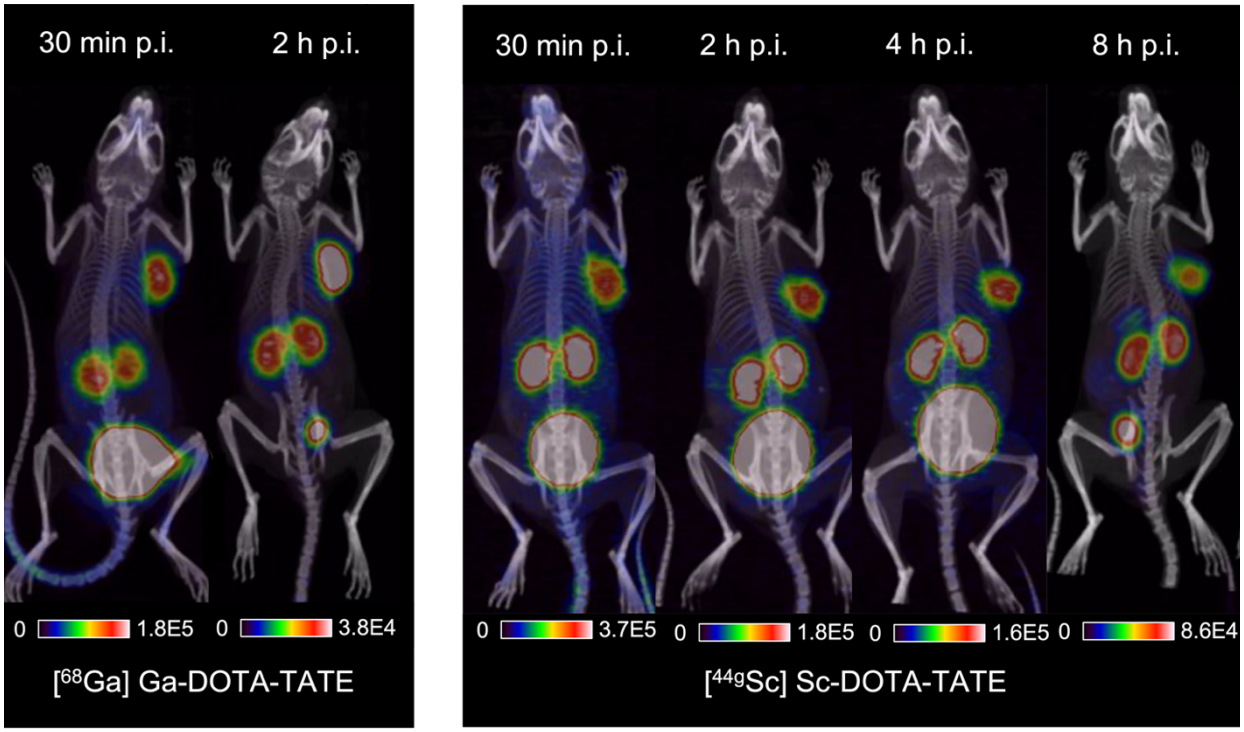


Figure 78: MIP PET/CT imaged of AR42J tumor-bearing mice injected with [^{68}Ga]Ga-DOTA-TATE (left) and [^{44g}Sc]Sc-DOTA-TATE (right). Scale bars are given in units of Bq/mL.

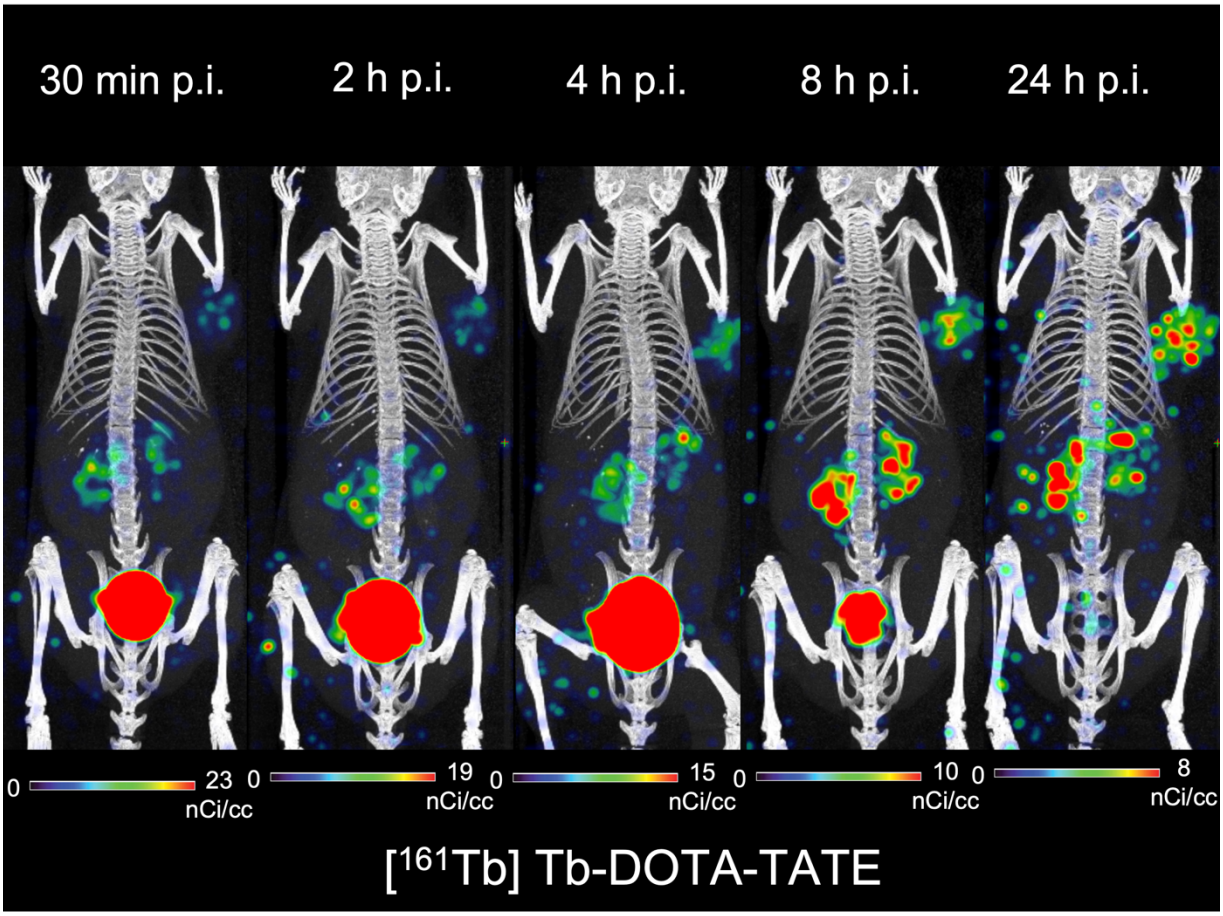


Figure 79: MIP SPECT/CT images of [^{161}Tb]Tb-DOTA-TATE uptake in AR42J tumor-bearing mice.

MIP SPECT/CT images of AR42J tumor-bearing mice injected with [^{161}Tb]Tb-DOTA-TATE are shown in Figure 79. Similar to mice injected with [^{44g}Sc]Sc-DOTA-TATE, the kidney uptake is higher than the tumor uptake at all time points except 24 h. Tumor uptake is seen beginning at 30 min p.i. and remains high even at 24 h p.i.

Accumulation of all three M-DOTA-TATE ligands in normal tissues (other than the kidneys) remained below 1.5 %IA/g for all time points. The distribution of the three M-DOTA-TATE ligands in the blood and normal tissues were nearly identical at all time points except for 30 min p.i. PET/CT images were acquired for 40 - 80 million counts while SPECT/CT images were

collected for 2 min per SPECT position. Thus, at early time points when the activity in the blood and bladder was high (30 min p.i.), the PET/CT images took approximately 5-10 min to collect while the SPECT/CT scan was collected for 40 min. Additionally, at early time points, the distribution of the tracer in the body is rapidly changing, particularly as the tracer circulates in the blood. The prolonged SPECT/CT scan resulted in a time-averaged uptake across 30 min to 1.2 h p.i. compared to the short scan duration for the PET/CT scans. This resulted in slightly varied uptake (particularly in the blood and the heart) for [^{161}Tb]Tb-DOTA-TATE compared to [^{68}Ga]Ga-DOTA-TATE and [^{44g}Sc]Sc-DOTA-TATE at 30 min p.i.

4.3.7 [^{161}Tb]Tb-DOTA-TATE toxicity

White blood cell counts for two mice injected with [^{161}Tb]Tb-DOTA-TATE are shown in Figure 80. Exposure to radiation can induce hematological changes which affect the body's immune system and decrease ability to heal wounds and fight off infection [167]. Thus, the white blood cell count was monitored in the two mice to determine whether approximately 500 μCi was enough activity to affect the immune system in a murine model.

In this preliminary study, a 63 ± 16% decline in leukocytes (n = 2) was observed at 8 d post 19.0 ± 0.1 MBq (515 ± 4 μCi) [^{161}Tb]Tb-DOTA-TATE injection. A similar study performed by Svenssona et. a. observed a 23 ± 2.9% decline in leukocytes at 10 d post 150 MBq (4.05 mCi) [^{177}Lu]Lu-DOTA-TATE injection (n = 7-8) and a 50 ± 4.4% decline for mice injected with 30 MBq (810.8 μCi) [^{90}Y]Y-DOTA-TATE [168]. The group of mice injected with [^{177}Lu]Lu-DOTA-TATE showed recovered leukocyte levels back to baseline at 30 d p.i. indicating minimal bone marrow toxicity. However, the mice injected with [^{90}Y]Y-DOTA-TATE had further decline to 20%-60% from baseline values and several mice had to be euthanized prior to the 30 d p.i.

time point. The authors mention that the need to euthanize several mice in the 30 MBq [^{90}Y]Y-DOTA-TATE cohort was likely due to bone marrow toxicity.

While this is a preliminary study with a small number of subjects, the results suggest that approximately 500 μCi of [^{161}Tb]Tb-DOTA-TATE could induce hematological changes in a murine model and result in bone marrow toxicity at a greater level than was observed for [^{177}Lu]Lu-DOTA-TATE In previous work [168].

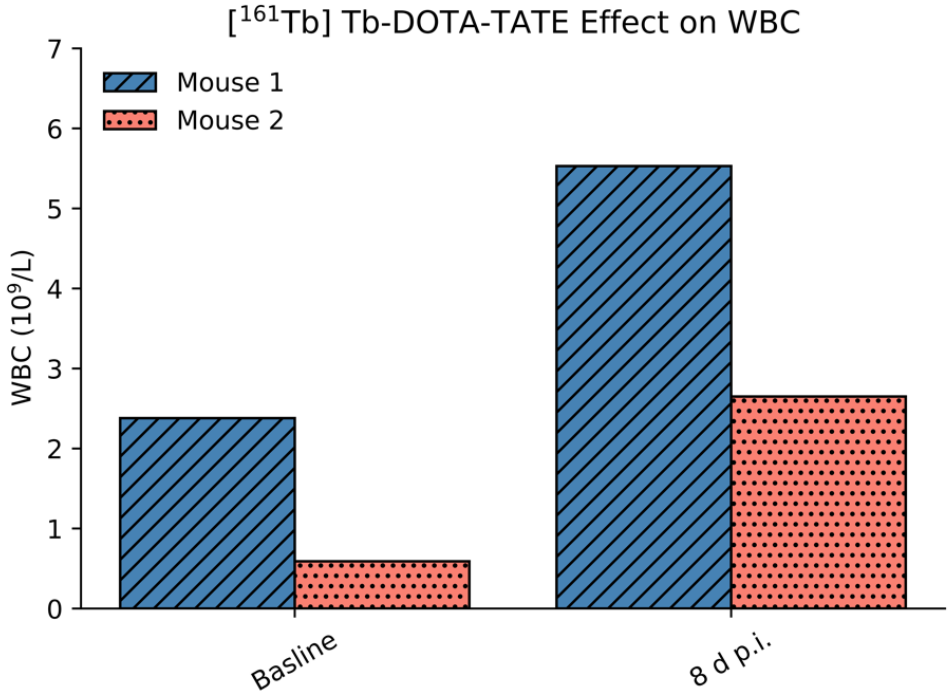


Figure 80: White blood cell counts for two mice before and after injection of [^{161}Tb]Tb-DOTA-TATE.

4.3.8 [^{161}Tb]Tb-DOTA-TATE dosimetry estimations

Figure 81 shows the estimated [^{161}Tb]Tb-DOTA-TATE dose to female human organs based on [^{68}Ga]Ga-DOTA-TATE (green hash), [^{44g}Sc]Sc-DOTA-TATE (orange dots), and [^{161}Tb]Tb-DOTA-TATE (blue hash) time activity curves up to 2 h p.i. Consistent with what was observed on the PET/CT images and the time activity curves from section 4.3.6, kidney and other normal

tissue uptake is within error for all three M-DOTA-TATE ligands but the tumor uptake for [^{68}Ga]Ga-DOTA-TATE is higher than [^{44g}Sc]Sc-DOTA-TATE or [^{161}Tb]Tb-DOTA-TATE. Estimated tumor dose from [^{161}Tb]Tb-DOTA-TATE was 11.7 ± 2.7 mGy/MBq from [^{68}Ga]Ga-DOTA-TATE time activity curves, 6.4 ± 1.6 mGy/MBq from [^{44g}Sc]Sc-DOTA-TATE time activity curves, and 5.6 ± 1.2 mGy/MBq from [^{161}Tb]Tb-DOTA-TATE time activity curves. The difference between [^{68}Ga]Ga-DOTA-TATE and [^{161}Tb]Tb-DOTA-TATE was statistically significant using an unpaired t-test (p value = .02) while the difference between [^{44g}Sc]Sc-DOTA-TATE and [^{161}Tb]Tb-DOTA-TATE was not statistically significant (p value = .51). Thus, estimating [^{161}Tb]Tb-DOTA-TATE tumor dose based on [^{68}Ga]Ga-DOTA-TATE imaging would result in overestimation of dose to the tumor but accurate dose to the kidney. In contrast, [^{44g}Sc]Sc-DOTA-TATE based dose estimations are much more similar to what was calculated from [^{161}Tb]Tb-DOTA-TATE SPECT/CT images.

^{44g}Sc's four-fold longer half-life also permitted [^{161}Tb]Tb-DOTA-TATE dose estimations at 4 h and 8 h p.i. (Figure 82). While the [^{44g}Sc]Sc-DOTA-TATE based dose estimations at 2 h p.i. were closer to [^{161}Tb]Tb-DOTA-TATE SPECT/CT based values than [^{68}Ga]Ga-DOTA-TATE, [^{44g}Sc]Sc-DOTA-TATE overestimates the dose to the tumor by approximately 60% at 4 h p.i. Notably, the dose to the kidneys is also overestimated by roughly 50% indicating universally higher uptake for [^{44g}Sc]Sc-DOTA-TATE as opposed to what was observed for [^{68}Ga]Ga-DOTA-TATE at 2 h p.i. where uptake in the tumor was higher, but not in the kidneys. Overall, estimating [^{161}Tb]Tb-DOTA-TATE dose based on > 2 h p.i. [^{44g}Sc]Sc-DOTA-TATE PET/CT images may result in overestimation of dose in both the tumor and the kidneys. However, the differences in dose estimations were not statistically significant using an unpaired t-test at 4 h p.i.

(p value = .16) and 8 h p.i. (p value = .22) due to the large errors in dose estimations at these time points.

Overall, [^{44g}Sc]Sc-DOTA-TATE uptake appears to be more representative to [^{161}Tb]Tb-DOTA-TATE uptake than [^{68}Ga]Ga-DOTA-TATE. Dose estimations at later time-points (> 2 h p.i.) is also possible with [^{44g}Sc]Sc-DOTA-TATE over [^{68}Ga]Ga-DOTA-TATE. While this study estimated dose to humans, time activity curves were taken from a murine model, and human dosimetry studies must be performed to further evaluate [^{44g}Sc]Sc-DOTA-TATE's potential to act as a diagnostic analogue for [^{161}Tb]Tb-DOTA-TATE.

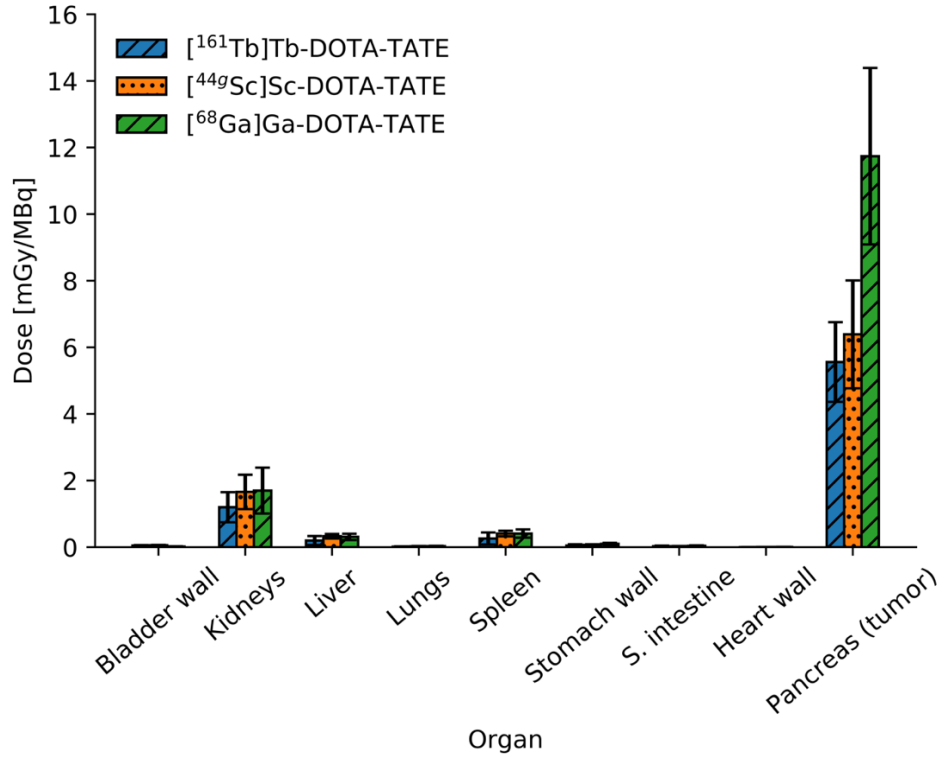


Figure 81: Estimated [^{161}Tb]Tb-DOTA-TATE dose to female human organs based on [^{68}Ga]Ga-DOTA-TATE and [^{44g}Sc]Sc-DOTA-TATE PET/CT imaging and [^{161}Tb]Tb-DOTA-TATE SPECT/CT imaging.

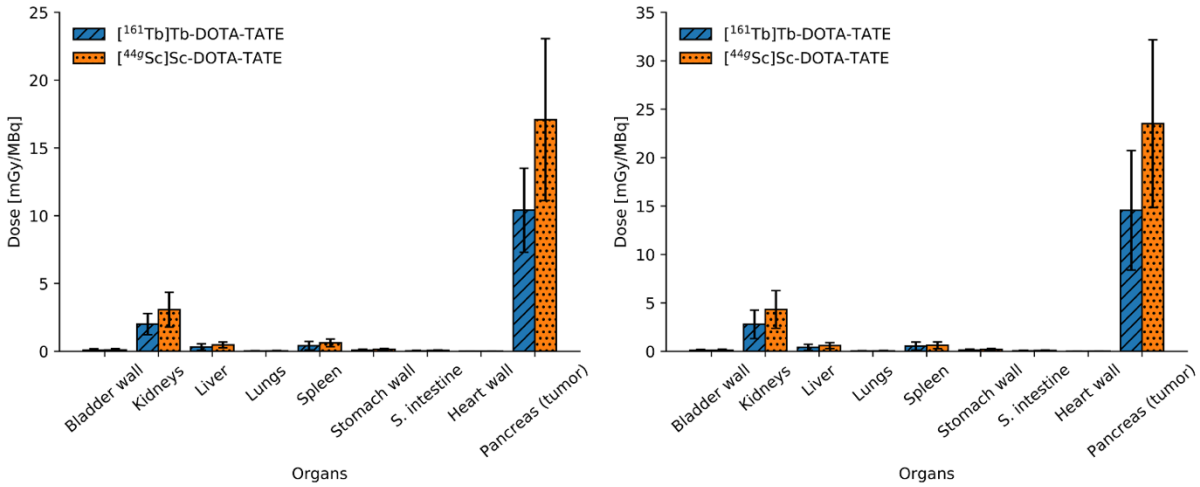


Figure 82: [^{161}Tb]Tb-DOTA-TATE dose estimates for female human organs at 4 h (left) and 8 h (right) p.i.

4.4 Conclusions

In this study, [^{68}Ga]Ga-DOTA-TATE, [^{44g}Sc]DOTA-TATE, and [^{161}Tb]Tb-DOTA-TATE were compared *in vitro* and in an *in vivo* model with AR42J tumor-bearing mice. The lipophilicity, binding affinity for SST2 receptors, and internalization rate into AR42J cells was compared across the three radiotracers.

[^{161}Tb]Tb-DOTA-TATE was successfully labeled at a molar activity of 10 nmol/mCi and found to be stable in PBS and human serum up to 24 h post incubation. At pH 4 - 5, ^{161}Tb was successfully complexed with DOTA-TATE; however inconsistent labeling results were found at pH 5.5 - 6 indicating that hydrolysis may be occurring at higher pHs.

Lipophilicity is the measurement of a radiopharmaceutical's affinity for a lipid environment and can affect the clearance route of the tracer. The transcellular passage of a pharmaceutical depends on its ability to permeate the phospholipid bilayer which is affected partially by the lipophilicity [169]. Additionally, more lipophilic molecules tend to have higher affinity for metabolic enzymes, speeding up the metabolism of the pharmaceutical [169]. The results of this

study found very similar lipophilicities across the three radiotracers with [^{161}Tb]Tb-DOTA-TATE demonstrating a slightly higher log$D_{7.4}$ value than [^{68}Ga]Ga-DOTA-TATE and [^{44g}Sc]Sc-DOTA-TATE, indicating a slightly higher affinity for lipid environments for [^{161}Tb]Tb-DOTA-TATE. While studies have demonstrated that the more lipophilic a radiopharmaceutical is, the more likely it is to partially clear through the hepatic clearance route, the differences in log$D_{7.4}$ values observed here (-2.14 ± 0.03 for [^{161}Tb]Tb-DOTA-TATE compared to -2.32 ± 0.24 for [^{68}Ga]Ga-DOTA-TATE and -2.36 ± 0.12 for [^{44g}Sc]Sc-DOTA-TATE) are unlikely to have a significant impact on clearance route. Image-derived uptake and *ex vivo* biodistribution also showed high kidney uptake and minimal liver uptake for all three M-DOTA-TATE ligands supporting the hypothesis that the change in lipophilicity was not substantial enough to alter the clearance of the most lipophilic M-DOTA-TATE molecule, [^{161}Tb]Tb-DOTA-TATE.

Similar equilibrium dissociation constants were observed across all M-DOTA-TATE ligands. The equilibrium dissociation constant is the radio-ligand concentration required to achieve half of the maximum binding at equilibrium and can be dependent on experimental conditions. Thus, the relative binding affinity, which is inversely related to the K_D, was compared across the radio-ligands. Comparable binding affinities were observed within error which was expected considering the chemical similarities between all three M-DOTA-TATE ligands. [^{44g}Sc]Sc-DOTA-TATE had a relative binding affinity of 1.16 and [^{68}Ga]Ga-DOTA-TATE had a relative binding affinity of 0.81 indicating that [^{44g}Sc]Sc-DOTA-TATE had a slightly higher binding affinity than [^{161}Tb]Tb-DOTA-TATE, and [^{68}Ga]Ga-DOTA-TATE had a slightly lower binding affinity. However, with the large errors associated with cell studies, the difference in binding affinity is not statistically significant.

The internalization rate in AR42J cells was also compared. While the internalization rate was comparable, [^{161}Tb]Tb-DOTA-TATE appeared to be taken into the cells at a moderately slower rate than [^{68}Ga]Ga-DOTA-TATE and [^{44g}Sc]Sc-DOTA-TATE. While this has a negligible effect on tissue uptake over time and [^{44g}Sc]Sc-DOTA-TATE's ability to act as a diagnostic analogue, this may have consequences for cellular-level dosimetry. In addition to β^- particles, ^{161}Tb emits lower range Auger-electrons which require proximity to the nucleus to have cytotoxic effects. Studies showed that ^{161}Tb's additional emitted Auger-electrons contributed to higher cytotoxicity and tumor control potential compared to similar doses of ^{177}Lu using a folate receptor targeting model [144]. The internalized fraction at 4 h was 50 - 80% for the cell models investigated in their study (KB and IGROV-1) compared to the roughly 20% internalization observed in this study. Thus, the dosimetric advantage of ^{161}Tb's Auger electrons in this model are likely significantly smaller than in targeting models that have a greater internalization rate.

Evaluation of tumor uptake over time showed favorable tumor uptake in all three M-DOTA-TATE ligands beginning at 30 min p.i.. Kidney and tumor uptake peaked at 30 min for all three M-DOTA-TATE and decreased with increasing time following injection. Kidney uptake dropped at a faster rate for [^{68}Ga]Ga-DOTA-TATE than [^{44g}Sc]Sc-DOTA-TATE or [^{161}Tb]Tb-DOTA-TATE resulting in a higher tumor-to-kidney ratio for [^{68}Ga]Ga-DOTA-TATE than the other two radio-ligands. SST2 receptors are natively expressed in murine kidneys resulting in specific uptake of the DOTA-TATE radio-ligands in addition to renal clearance. Thus, the faster kidney clearance for the [^{68}Ga]Ga-DOTA-TATE could be a result of the lower binding affinity or lipophilicity compared to [^{44g}Sc]Sc-DOTA-TATE and [^{161}Tb]Tb-DOTA-TATE which can influence the clearance of the radiopharmaceutical.

Due to the tendency of somatostatin analogues to primarily clear though the kidneys, nephrotoxicity is a major limitation for NET PRRT [170]. Barone et. al. investigated the impact of patient-specific adjustments to the standard dosimetric model for [^{90}Y]Y-DOTA-TOC using absorbed renal dose estimations from pre-treatment [^{86}Y]Y-DOTA-TOC PET/CT scans [170]. Their results showed large variation in renal absorbed dose between patients ranging from 1.2 to 5.1 mGy/MBq, concluding that patient-specific physiology cannot be neglected and that several patients would benefit from dose de-escalation to prevent nephrotoxicity. While renal dose was consistent across the three M-DOTA-TATE ligands, there was large deviation in tumor uptake for [^{68}Ga]Ga-DOTA-TATE compared to [^{44g}Sc]Sc-DOTA-TATE and [^{161}Tb]Tb-DOTA-TATE. Patient-specific nephrotoxicity evaluation is likely the most beneficial application of pre-treatment dosimetry for therapeutic NET PRRT and total injected dose is typically decided based on dose to the kidneys and the tumor. If dose to the tumor is overestimated, less dose may be prescribed to help spare the kidneys. This would result in lower tumor dose, potentially failing to control the disease.

This work suggests that [^{44g}Sc]Sc-DOTA-TATE is better suited than [^{68}Ga]Ga-DOTA-TATE for pre-treatment dosimetry evaluation for [^{161}Tb]Tb-DOTA-TATE from the similar renal and tumor uptake between [^{44g}Sc]Sc-DOTA-TATE and [^{161}Tb]Tb-DOTA-TATE and ability to image at later time points p.i, (> 2 h p.i.). Overall, the biodistribution of all three radio-ligands was comparable and either [^{68}Ga]Ga-DOTA-TATE or [^{44g}Sc]Sc-DOTA-TATE could likely be used to identify lesions and evaluate eligibility for [^{161}Tb]Tb-DOTA-TATE treatment, but [^{44g}Sc]Sc-DOTA-TATE is a superior option for pre-treatment dosimetry because of its more similar biodistribution compared to [^{161}Tb]Tb-DOTA-TATE. However, at later time points, overestimation of tumor and kidney dose was observed for [^{44g}Sc]Sc-DOTA-TATE and more

extensive studies investigating human biodistribution is needed to confirm [^{44g}Sc]Sc-DOTA-TATE's potential to act as an imaging surrogate for [^{161}Tb]Tb-DOTA-TATE.

Additionally, ^{44g}Sc's longer half-life compared to ^{68}Ga permits longer time-point imaging, providing more information about the distribution of the tracer at later time points. Due to ^{44g}Sc's longer half-life, transportation to local institutions is also possible. This would enable clinics without a cyclotron to still have access to ^{44g}Sc-based radiopharmaceuticals, increasing the accessibility of the radionuclide. The four-fold longer half-life also allows for imaging at time points where the background may be decreased while tumor uptake remains high, potentially enabling imaging of smaller lesions when tumor-to-background ratios (and consequently, contrast) are higher. The lower positron energy from ^{44g}Sc compared to ^{68}Ga also enables more accurate activity quantification and higher PET resolution which may be impactful for small features.

The potential for [^{44g}Sc]Sc-DOTA-TATE to act as a diagnostic analogue for [^{161}Tb]Tb-DOTA-TATE was demonstrated and compared to the diagnostic capabilities of [^{68}Ga]Ga-DOTA-TATE. The *in vitro* and *in vivo* characteristics between [^{68}Ga]Ga-DOTA-TATE, [^{44g}Sc]Sc-DOTA-TATE, and [^{161}Tb]Tb-DOTA-TATE were all similar. However, the tumor-to-kidney ratios were more comparable between [^{44g}Sc]Sc-DOTA-TATE, and [^{161}Tb]Tb-DOTA-TATE, indicating that [^{44g}Sc]Sc-DOTA-TATE is more suitable for pre-treatment dosimetric evaluation of tumor dose and neprotoxicity for [^{161}Tb]Tb-DOTA-TATE treatment than [^{68}Ga]Ga-DOTA-TATE. The additional benefits from ^{44g}Sc's longer half-life and lower average positron energy further support [^{44g}Sc]Sc-DOTA-TATE's use as a diagnostic analogue for [^{161}Tb]Tb-DOTA-TATE over [^{68}Ga]Ga-DOTA-TATE. Dosimetric estimations were performed assuming identical biodistribution (percent injected activity in an entire organ) between mice and

humans and thus, human-based biodistribution studies for [^{68}Ga]Ga-DOTA-TATE, [^{44g}Sc]Sc-DOTA-TATE, and [^{161}Tb]Tb-DOTA-TATE are needed to further evaluate [^{44g}Sc]Sc-DOTA-TATE's potential as an imaging surrogate for [^{161}Tb]Tb-DOTA-TATE.

Acknowledgements

We gratefully acknowledge Dr. Heather Hennkens, Patrick Bokolo, and Madhushan Serasinghe for their help producing and providing the ^{161}Tb used in this work.

Chapter 5: Conclusions and future directions

In this work, production methods for ^{43}Sc and ^{44g}Sc were evaluated and imaging and theranostic applications with PDAC and NETs in murine models were explored. Several production routes are accessible with small cyclotrons capable of accelerating 16 MeV protons and 8 MeV deuterons. When new institutions are determining whether to produce ^{43}Sc or ^{44g}Sc, factors such as production yield, radionuclidic purity, time, and cost are all important considerations. In Chapter 2, ^{43}Sc and ^{44g}Sc were produced through proton and deuteron bombardment of isotopically enriched calcium targets and compared their production yields and radionuclidic purities, describing benefits and drawbacks of several possible reaction routes. CaO was also investigated as an alternative target material to $CaCO_3$ and a radiochemical isolation scheme based on extraction chromatography using branched DGA resin that facilitated efficient recycling of the target material was developed. Though isotopically enriched calcium is currently expensive (\$22-267 mg^{-1}), following a 1 hour, 5 μA 13.6 MeV proton irradiation of a 150 mg ^{44}CaO target, the chemical isolation procedure described in Chapter 2 isolates 1.4 ± 0.3 GBq (38 ± 9 mCi) of ^{44g}Sc with 99.5 ± 0.05% radionuclidic purity in 2 mL 0.01 M HCl 2 hours after EoB. This is sufficient for multiple patient doses (5 - 10 mCi per patient) and the target material can be recovered with 95 ± 2% efficiency.

Measurement of the ^{42}Ca(d,n)^{43}Sc cross section was attempted but was complicated by target fabrication challenges. Precise cross section measurements require thin targets so that they do not significantly perturb the beam energy as it traverses the target. To achieve this goal, thin (3 μm) calcium deposits were evaporated on monitor foils (nickel and copper) but were highly susceptible to absorption of water from the atmosphere due to calcium's hygroscopic nature.

Future work on thin calcium target development is needed to ensure production of targets that can withstand 200 - 500 nA of 3 – 12 MeV deuterons. While production yield measurements made in Chapter 2 are in close agreement with previously reported cross section data, additional cross section measurements at energies higher than 10 MeV would be beneficial for institutions with higher energy deuteron machines and to verify previously reported data.

Chapter 3 investigated [^{43}Sc]Sc-FAPI-46's and [^{44g}Sc]Sc-FAPI-46's potential to detect PDAC in a murine model compared to [^{68}Ga]Ga-FAPI-46. Both a heterotopic and orthotopic model were investigated. The heterotopic model results showed that both [^{43}Sc]Sc-FAPI-46 and [^{44g}Sc]Sc-FAPI-46 had superior image quality over [^{68}Ga]Ga-FAPI-46 (higher tumor uptake, fewer artifacts from high bladder and kidney uptake, clearer tumor boundaries). The image quality between [^{43}Sc]Sc-FAPI-46 and [^{44g}Sc]Sc-FAPI-46 PET/CT images was comparable indicating that ^{44g}Sc's higher positron energy and 1157 keV prompt gamma emission does not significantly affect tumor visualization in this model.

There was uptake in the abdominal region observed at later time points (> 1 h p.i.) in many of the mice for both the heterotopic and orthotopic model. Comparison of the *ex vivo* stomach and intestinal uptake showed that the stomach and intestines with their contents had a higher %IA/g than the emptied stomach and intestines. These results suggest that the contents of the stomach and intestines contained M-FAPI-46, contributing to the signal seen in the MIP PET/CT images. In future Sc-FAPI-46 murine studies, it may be beneficial to either remove the bedding prior to injection, or to install a grate to limit access to the bedding material to prevent ingestion of the excreted radiopharmaceutical if later time points will be collected (> 1 h p.i.).

No tumors were confirmed on any PET/CT images of the orthotopic model mice, even when tumor diameters exceeded the size of the heterotopic model. Several factors likely contribute to

the inability to visualize orthotopic tumors in this work: [^{44g}Sc]Sc-FAPI-46 tumor uptake was lower in the orthotopic model than the heterotopic model and the pancreas is located in the abdomen near high uptake regions such as the bladder, kidneys, and intestines. Future work investigating the FAP-α expression within the orthotopic tumors would be beneficial to determine whether the tumor environment affects the FAP-α expression. While the [^{44g}Sc]Sc-FAPI-46 tumor uptake was lower in the orthotopic model than the heterotopic model, it was still higher than the [^{68}Ga]Ga-FAPI-46 heterotopic tumor uptake where the tumors were visible. This suggests that the location of the tumor was another primary factor complicating the visualization of the tumors. Bladder uptake could be reduced in future studies by removing the water source several hours prior to injection. Limiting access to the bedding to prevent intestinal uptake would further reduce the signal in the intestines and may provide lower background signal in the tumor region.

In addition to murine studies, this work investigated clinical phantom studies to compare the contrast and activity quantification of $^{43/44g}$Sc compared to other clinically used PET radionuclides. Derenzo phantom studies showed that ^{43}Sc, ^{44g}Sc, and the $^{43/44g}$Sc mixture all had comparable contrast that was between the calculated contrast of ^{68}Ga and ^{18}F/^{64}Cu which is expected based on their average positron energies. Interestingly, the recovery coefficients for the phantom filled with ^{43}Sc and the $^{43/44g}$Sc mixture (88% ^{43}Sc and 12% ^{44g}Sc) had recovery coefficients significantly greater than 1 (1.4 for the 1 cm sphere to 2.0 for the 3.7 cm sphere), indicating that the scanner was reconstructing more activity than the phantom was filled with. The ^{44g}Sc recovery coefficients ranged from 0.7 at the smallest sphere diameter to 1.1 at the largest sphere size which is comparable to what was observed for the other radionuclides (^{68}Ga, ^{18}F, ^{64}Cu), isolating the issue to ^{43}Sc alone. The only distinguishing feature of ^{43}Sc is it's 373

keV (22.5%) gamma that is near the energy window of clinical PET scanners (425 – 650 keV) that may scatter within the energy window and result in higher signal. Further work exploring the cause of the activity overestimation is warranted before moving to clinical studies.

In Chapter 4, the biodistribution and *in vitro* characteristics of [^{68}Ga]Ga-DOTA-TATE, [^{44g}Sc]Sc-DOTA-TATE, and [^{161}Tb]Tb-DOTA-TATE were compared. Lipophilicity and binding affinity were within error for all three M-DOTA-TATE ligands, so metabolic clearance and binding to the SST2 receptors should be very similar. The biodistribution of M-DOTA-TATE in AR42J tumor-bearing mice showed similar uptake in most organs between the three M-DOTA-TATE ligands. However, the kidney uptake was lower for mice injected with [^{68}Ga]Ga-DOTA-TATE. A major driving factor for personalized dosimetry and deviation from standard dose for all patients is the ability to escalate or de-escalate dose for a given patient depending on their specific tumor and kidney uptake (and corresponding nephrotoxicity). Thus, the deviation in tumor uptake and dose delivered to the tumor between [^{68}Ga]Ga-DOTA-TATE and [^{161}Tb]Tb-DOTA-TATE suggests that [^{44g}Sc]Sc-DOTA-TATE would be a better diagnostic analogue for [^{161}Tb]Tb-DOTA-TATE. Additionally, ^{68}Ga's short half-life would severely limit the pre-treatment dosimetry possible with [^{68}Ga]Ga-DOTA-TATE PET/CT scans. ^{44g}Sc's longer half-life permits dose estimations for time points up to four times as long p.i. compared to ^{68}Ga. However, the [^{161}Tb]Tb-DOTA-TATE dose to the tumor and kidneys was overestimated using [^{44g}Sc]Sc-DOTA-TATE activity curves at later time points (> 2 h p.i.). However, the dose estimates were within error and were only approximations taken from murine biodistribution curves. Further dosimetry estimations in humans are needed to fully evaluate [^{44g}Sc]Sc-DOTA-TATE's potential to act as an imaging analogue for [^{161}Tb]Tb-DOTA-TATE.

Applications for $^{43/44g}$Sc extend beyond what was discussed in this work. One unique application for ^{44g}Sc, is positronium imaging to determine the oxygen content in a tumor [171]. Because hypoxia is often linked to chemotherapy and radiation therapy resistance, determining oxygen content in a tumor could provide information that could inform treatment planning [172]. Positronium imaging can determine oxygen content because the oxygen concentration in the surroundings affects the lifetime of positronium. The lifetime of the positronium can be measured by triggering a timer with the signal from ^{44g}Sc's prompt 1157 keV (99.9%) gamma and ending the measurement with the 511 keV signal from the annihilated positron-electron pair. Work by Shibuya et. al. suggests that the differences in lifetime measured in this manner can inform clinicians about the oxygen content in the tumor [171]. However, generator-produced ^{44g}Sc would be better suited for this work compared to cyclotron-produced ^{44g}Sc due to the lack of co-produced ^{44m}Sc.

A therapeutic radioisotope of Sc also exists (^{47}Sc) and could form a chemically identical theranostic pair with ^{43}Sc or ^{44g}Sc. ^{47}Sc emits a low energy β^- particle (β^-_{mean} = 162 keV) with a half-life ($t_{1/2}$ = 3.35 d) that is suitable for PRRT. The advantage to using $^{43/44g}$Sc/^{47}Sc over $^{43/44g}$Sc/^{177}Lu or $^{43/44g}$Sc/^{161}Tb is that $^{43/44g}$Sc and ^{47}Sc would be chemically matched and have identical biodistributions. Additionally, work has shown that the tumor therapy efficacy between ^{47}Sc-folate and ^{177}Lu-folate were nearly identical [173] However, currently the production of ^{47}Sc is costly and work on optimizing ^{47}Sc would be beneficial to make the radionuclide more clinically feasible.

Appendix A: Cross section measurements for proton induced reactions on natural lanthanum

Introduction

Clinical treatment of cancer with alpha-emitting radioisotopes has been recently increasing with particular interest in ^{225}Ac ($t_{1/2}$ = 9.92 days, 100% α), which decays, emitting a total of 4 alpha particles in its decay chain, to stable ^{209}Bi [174, 175]. Alpha particles' high LET and short range in tissue give ^{225}Ac the potential to spare healthy tissue nearby targeted tumor cells when used in conjunction with an appropriate targeting vector [176, 177]. However, measurement of *in vivo* biokinetics to determine the efficacy of ^{225}Ac as a therapeutic radionuclide and quantification of dose delivered to healthy tissue versus target regions are areas that need further investigation [178].

Nuclear medicine imaging techniques are an established method of assaying biodistribution, but ^{225}Ac does not emit positrons imageable by positron emission tomography (PET) [174, 175]. Instead, radionuclides with similar chemical qualities may be used as analogues of ^{225}Ac to quantitatively assay pharmacokinetics and biodistribution of radiopharmaceutical agents [179]. Using surrogate radionuclides to describe the biodistribution of a therapeutic isotope has limitations because of the different *in vivo* behavior of targeting vectors labeled with different radioactive elements [180]. In spite of these limitations, use of chemically-similar radionuclides as imaging surrogates for therapeutic radionuclides is currently being performed clinically, such as the case of using the positron-emitting isotope ^{68}Ga to model the biodistribution of the therapeutic beta-emitter ^{177}Lu [181, 182, 183]. Cerium is more chemically similar to actinium than almost any other element in ionic radius and preferred oxidation states, and so has been proposed as a theranostic congener of several alpha-emitting actinide radioisotopes [184]. While

^{134}Ce ($t_{1/2}$ = 3.1625 days, 100% ec) does not emit positrons, its biodistribution can be indirectly assayed by detection of its daughter ^{134}La's ($t_{1/2}$ = 6.4 minutes, 100% ec) rapid β^+ decay [1].

In addition to biochemical knowledge of ^{134}Ce, nuclear data, including cross section measurements, are essential for determining the ideal irradiation energy so that the production yield is maximized, while contaminants are minimized. Theoretical models such as TALYS can be used to predict cross sections; however, models depend on measured data [88]. The goal of this work is to measure cross sections of proton induced reactions on natural lanthanum, informing ^{134}Ce production efforts and providing data for theoretical code developments.

Materials and Methods

Target Design

Cross sections for proton reactions on natural lanthanum targets were measured at ten proton energies from 88 MeV to 46 MeV. This was done using a stacked target design [185] comprised of an aluminum target box divided by aluminum degraders into ten compartments with an identical bundle of targets in each compartment (as seen in Figure 83).

In each compartment were 0.025 mm thick ^{nat}Al (99.999% Alfa Aesar, Ward Hill, MA, 01835), 0.1 mm thick ^{nat}La (99.9% BeanTown Chemical, Hudson, NH, 03051, USA), and 0.05 mm thick ^{nat}Cu (99.9999% Alfa Aesar, Ward Hill, MA, 01835, USA) foils in the order listed. Each foil was cut to approximately 25 mm by 25 mm and then cleaned with ethanol, measured, and weighed. When determining the width and height, the distance was measured with vernier calipers at three distinct points along the side of the foil. The thickness of each foil was measured using micrometers with a precision of 0.0005 mm. These measurements were used to calculate the areal density with an error calculated by adding the error on the thickness, mass, width, and length measurements in quadrature.

Between each compartment, 1100-aluminum alloy of varying thickness was used to sequentially degrade the beam by a few MeV. Calculations of the proton energy loss through the aluminum slabs were done using the Andersen and Ziegler semi-empirical formalism through an in–house excel program when determining the appropriate thickness for each degrader [85]. The degraders were designed to be slid into the target box to allow for accurate measurements of the degrader before assembly of the box. The thickness, width, height, and mass of each aluminum slab were all measured prior to assembly. After measurements were taken, the degraders were then cleaned with ethanol and placed in grooves machined in the interior of the box.

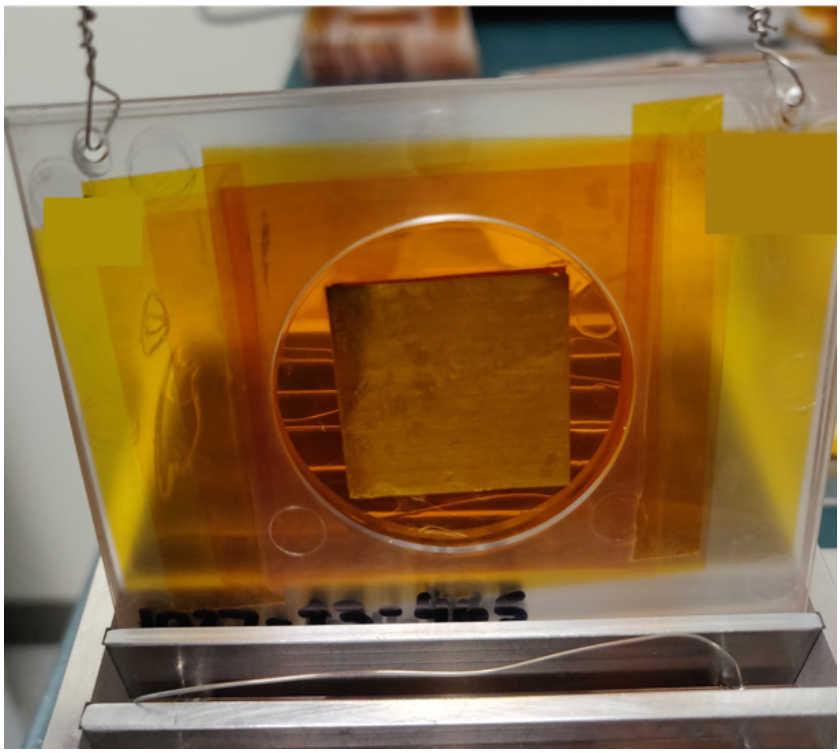


Figure 83: Aluminum foil affixed to an acrylic holder with 3M acrylic lined Kapton polyimide film tape.

To create the foil packets that were housed in each compartment, the target foils were sealed in two pieces of 0.046 mm thick 3 M acryliclined polyimide Kapton tape (7419 series) composed of 0.025 mm of Kapton polyimide film backing and 0.020 mm acrylic adhesive. The Kapton tape was used to prevent contamination and affix the foils in the center of an acrylic frame (Figure 79). Each compartment contained a target stack consisting of one aluminum, one lanthanum, and one copper foil all attached to their own acrylic plates. The three plates were bound together using wire as shown in Figure 79 to allow for disassembly with minimal radiation exposure.

In the front and rear of the box, a 0.127 mm thick, 25 mm by 25 mm stainless-steel sheet was placed to determine the beam profile. After irradiation, the stainless-steel sheets were exposed to gafchromic film and the beam slot was evaluated to ensure the entire fluence of the beam was incident on the foils. The full description of the target stack, along with the measured densities, is listed in Table 32.

Irradiation

The target stack was irradiated at the Isotope Production Facility at Los Alamos National Laboratory with a 100 MeV proton beam from the LANSCE accelerator. The stack was irradiated for one hour with a nominal current of 110 nA measured with an in-line induction type beam monitor which showed that the beam current remained stable other than 7 observed beam trips that lasted less than 3 s each during the irradiation. After irradiation, the stack was removed from the beam line and disassembled in a hot cell using robotic manipulators. The bundle of foils in each compartment was separated and individual foils were decontaminated before packing and transporting to the counting facilities for assay.

After disassembly, the stainless-steel foils at the front and rear of the stack were exposed to gafchromic film to compare the beam spot size to the dimensions of the foil. The full width-half

maximum of the beam spot exiting the stack was 1.9 cm. The width of the foils used was 2.5 cm, indicating that the beam fluence was within the dimensions of the foil.

Material	Thickness (mm)	Density (g/cm^3)	Δ Density (g/cm^3)
SS Beam Monitor	0.1270	7.930	–
Al(1)	0.025	2.935	0.06663
La(1)	0.1	6.2435	0.0388
Cu(1)	0.05	9.363	0.06241
Al Degrader(1)	6.3000	2.7161	0.004918
Al(2)	0.025	2.9998	0.06743
La(2)	0.1	6.2176	0.03864
Cu(2)	0.05	8.986	0.06101
Al Degrader(2)	3.1000	2.7836	0.005043
Al(3)	0.025	2.925	0.06585
La(3)	0.1	6.1664	0.03856
Cu(3)	0.05	9.823	0.06455
Al Degrader(3)	2.3000	2.7127	0.004915
Al(4)	0.025	2.8916	0.06675
La(4)	0.1	6.089	0.03816
Cu(4)	0.05	9.463	0.06295
Al Degrader(4)	1.5000	2.8565	0.005176
Al(5)	0.025	2.9712	0.06634
La(5)	0.1	6.1558	0.03800
Cu(5)	0.05	9.430	0.06236
Al Degrader(5)	1.0000	2.801	0.005079
Al(6)	0.025	2.9459	0.06674
La(6)	0.1	6.4905	0.03953
Cu(6)	0.05	9.684	0.06228
Al Degrader(6)	0.8000	2.8191	0.005116
Al(7)	0.025	2.8813	0.06579
La(7)	0.1	6.2241	0.03826
Cu(7)	0.05	9.684	0.06371
Al Degrader(7)	0.5080	2.7715	0.005037
Al(8)	0.025	2.9588	0.06676
La(8)	0.1	6.0515	0.03797
Cu(8)	0.05	9.070	0.06110
Al Degrader(8)	0.5080	2.7728	0.005039
Al(9)	0.025	2.9251	0.06653
La(9)	0.1	6.326	0.03908
Cu(9)	0.05	8.889	0.06044
Al Degrader(9)	0.5080	2.7711	0.005035
Al(10)	0.025	2.9008	0.06668
La(10)	0.1	6.043	0.03754
Cu(10)	0.05	8.880	0.06021
SS Beam Monitor	0.1270	7.930	–

Table 32: Description of each element in the stacked target

Analysis

End of bombardment activities for each radioisotope were calculated from gamma ray spectra that were collected using two efficiency calibrated HPGe detectors at LANL and the University of Wisconsin, Madison. At the IPF counting facilities, an ORTEC GEM HPGe detector with a p-type aluminum window was used. This detector has a FWHM of about 1.99 keV (at 1333 keV) and an efficiency of 10%. After transportation to the University of Wisconsin, Madison, a Canberra GC1519 model HPGe detector was used to collect the spectra. This detector has a FWHM of 1.78 keV (at 1333 keV), an efficiency of 18.7% and an aluminum window with a 1.5 mm thickness.

Approximately 5 h post irradiation, gamma spectra for the La foils were collected at the IPF counting facility using a mechanism that automatically positioned foils at selected, calibrated locations from the detector and counted for a designated duration. Spectra were collected continuously for the La target foils for 5 days after irradiation using this system. Periodic adjustments to the distance from the detector face were made as the foils decayed to get optimum efficiency, while keeping the dead time under 30%, before transporting the foils to the University of Wisconsin, Madison. Maximum dead time recorded was 31.97% while typical dead time was approximately 7%.

Collection of spectra for the La foils continued for one week after relocating to the University of Wisconsin, Madison to capture any longer-lived isotopes, such as ^{133g}Ba. The acrylic frames, with the foils positioned in the center, were placed an appropriate distance from the detector to ensure a dead time less than 5% . Typical dead time for the measurements taken at the University of Wisconsin, Madison were below 1%. Peaks were then fit from the spectra

using fitting software at LANL and the University of Wisconsin, Madison which both utilized SAMPO fitting algorithms [16].

Through use of both detectors, the gamma spectra for each foil were collected at approximately ten different time points after irradiation to get a well-characterized decay curve for each photopeak that could be used to determine end of bombardment activities. For reactions such as ^{134}Ce where no decay from a parent contributes to the measured daughter activity, the standard decay formula,

$$A(t) = A_0 e^{-\lambda t} \tag{11}$$

was used to determine end of bombardment activity, where A_0 is the initial activity, t is the time after irradiation, and λ is the parameter being fit. For two or more step decay chains, the Bateman equation was fit to the decay curve:

$$A(t) = A_p \frac{\lambda_p}{\lambda_d - \lambda_p}(e^{-\lambda_p t} - e^{-\lambda_d t}) + A_0 e^{-\lambda_d t} \tag{12}$$

where A_p is the activity of the parent, λ_p is the decay constant of the parent, and λ_d is the decay constant of the daughter.

A decay curve was fit to confirm the identity of the isotope and determine if there were nearby, indistinguishable, gammas from other isotopes contaminating any peaks. In cases where there was contamination, the contribution from the contaminating isotope was subtracted from the peak area, or the time point was removed from the collection of data used to calculate the final end of bombardment activity.

To calculate final activities, the activity from each time point was decay corrected to end of bombardment using well established values for the half-life. The final end of bombardment activity was then determined from an average of the individual activities weighted by the errors associated with each point. The errors for each point were calculated by adding the errors on the

half-life, branching ratio, detector efficiency (conservatively estimated at 5%), and peak fit in quadrature.

To better characterize an isotope's end of bombardment activity, more than one characteristic gamma was used when possible. In the cases where more than one gamma was quantifiable, the end of bombardment activity for each gamma was found and the final end of bombardment activity was calculated using an average weighted by the relative error of all end of bombardment activities. The final cross section was then calculated from this weighted end of bombardment activity (see Table 34 and Table 35). The nuclear decay data, including gamma energies, branching ratios, and half-lives, used for each isotope in the equations above are recorded in Table 33.

Product Nuclear Decay Data			
Reaction	Half-life	γ Energy (keV)	Branching Ratio (%)
^{27}Al(p,x)^{22}Na	2.6018(22) y	1274.537(7)	99.940(14)
^{27}Al(p,x)^{24}Na	14.997(12) h	1368.626(5)	99.9936(15)
^{nat}Cu(p,x)^{56}Co	77.236(66) d	846.770(2)	99.9399(1)*
^{nat}Cu(p,x)^{58}Co	70.86(6) d	810.7593(20)	99.450(1)*
^{nat}Cu(p,x)^{65}Zn	243.93(9) d	1115.539(2)	50.04(10)
^{139}La(p,8n)^{132}Ce	3.51(11) h	182.11(3)	77.4(1)*
^{139}La(p,7n)^{133m}Ce	5.1(3) h	477.22(4)	39.3(1)*
^{139}La(p,6n)^{134}Ce	3.16(4) d	162.306(10)	0.230(16)
		130.414(15)	0.209(15)
^{139}La(p,5n)^{135}Ce	17.7(3) h	265.56(2)	41.8(14)
		300.07(2)	23.5(5)
		606.76(2)	18.8(6)
^{139}La(p,4n)^{137g}Ce	9.0(3) h	447.15(8)	1.68(1)*
^{139}La(p,4n)^{137m}Ce	34.4(3) h	254.29(5)	11.1(4)
^{139}La(p,n)^{139}Ce	137.641(20)	165.8575(11)	80(8)
^{139}La(p,x)^{135}La	19.5(2) h	480.51(2)	1.52(1)*
^{139}La(p,x)^{131}Ba	11.50(6) d	496.321(5)	48.0(1)*
		123.804(3)	29.8(3)
^{139}La(p,x)^{133g}Ba	10.551(11) y	356.0129(7)	62.05(1)*
^{139}La(p,x)^{133m}Ba	38.93(10) h	275.925(7)	17.69
^{139}La(p,x)^{132}Cs	6.480(6) d	667.714(2)	97.59

Table 33: Tabulated nuclear decay data used in this work [1]. *An error equivalent to the magnitude of the last digit provided was assumed when no uncertainty was provided.

E(ΔE) (MeV)	σ(Δσ) ^{132}Ce (mb)	σ(Δσ) ^{133m}Ce (mb)	σ(Δσ) ^{134}Ce (mb)	σ(Δσ) ^{135135}Ce (mb)	σ(Δσ) $^{137\ g}$Ce (mb)	σ(Δσ) ^{137m}Ce (mb)	σ(Δσ) ^{139}Ce (mb)
46.96(2.5)	–	–	–	297.94(16.67)	27.28(2.01)	89.08(5.35)	13.95(1.68)
51.58(1.7)	–	–	–	359.78(28.96)	–	75.71(6.10)	13.51(1.28)
54.93(1.6)	–	–	41.12(3.59)	400.73(30.15)	21.42(1.96)	63.57(4.98)	10.98(1.47)
58.87(1.6)	–	–	127.79(15.99)	347.67(25.02)	20.69(1.76)	57.84(4.30)	9.98(1.03)
63.32(1.0)	–	4.96(0.07)	204.94(20.71)	217.45(13.79)	18.86(1.43)	51.81(3.47)	9.26(1.22)
67.99(1.4)	–	33.74(0.65)	224.66(26.59)	145.69(11.15)	13.96(2.38)	44.26(3.53)	9.15(1.52)
78.05(0.2)	61.82(4.33)	106.61(2.15)	135.24(12.90)	97.74(6.18)	13.93(1.48)	36.03(2.46)	5.43(0.43)
88.66(0.6)	3.79(0.22)	97.71(2.09)	72.83(7.20)	69.74(5.19)	10.77(1.19)	30.37(2.41)	5.69(0.74)

Table 34: Tabulated measured cross sections for all Cerium radioisotope excitation functions.

E(ΔE)	^{133}La σ(Δσ)	^{135}La σ(Δσ)	^{131}Ba σ(Δσ)	^{133g}Ba σ(Δσ)	^{133m}Ba σ(Δσ)	^{132}Cs σ(Δσ)
46.96(2.5)	–	29.89(2.50)	–	0.24(0.04)	10.11(0.60)	–
51.58(1.7)	–	73.55(8.02)	–	0.27(0.05)	10.12(0.82)	–
54.93(1.6)	–	70.67(6.86)	–	0.20(0.03)	8.95(0.71)	–
58.87(1.6)	–	94.38(8.91)	0.95(0.16)	0.17(0.05)	7.14(0.55)	0.43(0.03)
63.32(1.0)	–	122.88(10.79)	5.64(0.65)	0.26(0.03)	5.63(0.40)	0.96(0.07)
67.99(1.4)	69.02(1.34)	128.54(12.52)	15.03(1.39)	1.01(0.10)	4.57(0.40)	1.70(0.14)
78.05(0.2)	149.89(2.98)	122.91(10.94)	16.83(1.66)	–	4.45(0.42)	1.86(0.13)
88.66(0.6)	200.82(4.55)	108.13(10.41)	14.55(1.39)	–	8.15(0.67)	2.34(0.19)

Table 35: Tabulated measured cross sections for all remaining radioisotope excitation functions.

Proton Fluence Determination

Proton fluences were determined from the end of bombardment activities of the radionuclides produced in the copper and aluminum monitor foils. The ^{nat}Cu(p,x)^{56}Co, ^{nat}Cu(p,x)^{58}Co, ^{nat}Cu(p,x)^{65}Zn, ^{27}Al(p,x)^{22}Na, and ^{27}Al(p,x)^{24}Na reactions were used due to the abundant experimental data that exists for these reactions, and their monotonically increasing excitation functions in the energy range of interest [186]. Theoretical proton energies for each position in the stack were determined from MCNP6 [187] simulations and these energies were used to solve for the cross section from the cumulative monitor reaction data [84]. The current was then determined by:

$$I = \frac{A_0}{\sigma \rho x (1 - e^{-\lambda t})} \tag{13}$$

where I is the proton fluence (protons/s), σ is the cross section, ρ is the measured density of the foil (kg/m3), and x is the foil thickness (m).

Figure 84 (left) shows the monitor reaction-calculated fluences using the energies obtained from MCNP6 simulations and the monitor reaction determined cross sections. Attenuation of the beam between the aluminum and copper foils in the same energy position is negligible, so the fluences among all five monitor reactions should be approximately equal. The spread in fluence

towards the rear of the stack in Figure 84 (left) is likely due to inaccurate densities, improper characterization of stopping powers, incorrect incident beam energies, or errors in the initial fluence of the beam. Towards the front of the stack, there is still reasonable agreement due to the minimal effect that slight errors in density and stopping power have at these higher energies.

The variance minimization technique discussed by Graves et al. was used to remedy the disagreement amongst the fluences [185]. Figure 85 shows the standard deviation between all five of the monitor reaction calculated fluences for a range of energies in the final compartment of the stack where the discrepancy is expected to be largest. The variance is minimized at an energy of 46.96 MeV, which is approximately 6 MeV lower than the MCNP6 calculated energy of 52.89 MeV and about 4 MeV lower than the Andersen and Ziegler calculated energy of 50.99 MeV. This process was repeated for the remaining foils and the fluences for the full stack were recalculated using the energies where the variance was minimized as seen in Figure 84 (right). The change in energy that was employed for each position was treated as a lump correction for all the potential errors mentioned previously; most notably being the density of the aluminum degraders which contributes the most to potential errors. To determine the fluence in the La foils, linear interpolation between the Al and Cu foils was performed. To do this, MCNP6 was first used to simulate proton bombardment on the stack and determine the rate that the protons were attenuated through the stack. A linear fit to the monitor reaction-obtained fluences in Figure 84 (right), with the rate of attenuation from the MCNP6 simulations as the slope, was used to determine the fluence in the La foils. The uncertainty in the proton fluence was calculated from taking the standard deviation of the monitor reaction-obtained fluences in each compartment.

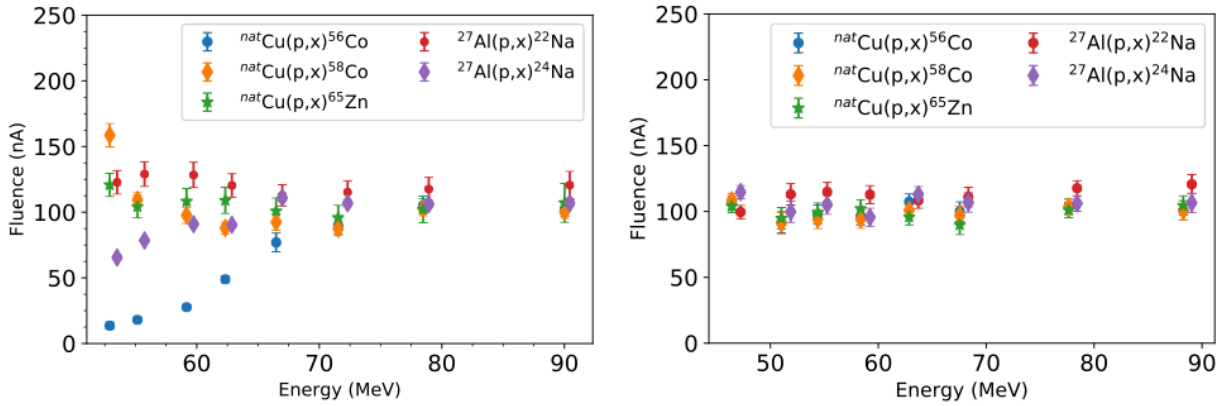


Figure 84: Fluences before (left) and after (right) minimization.

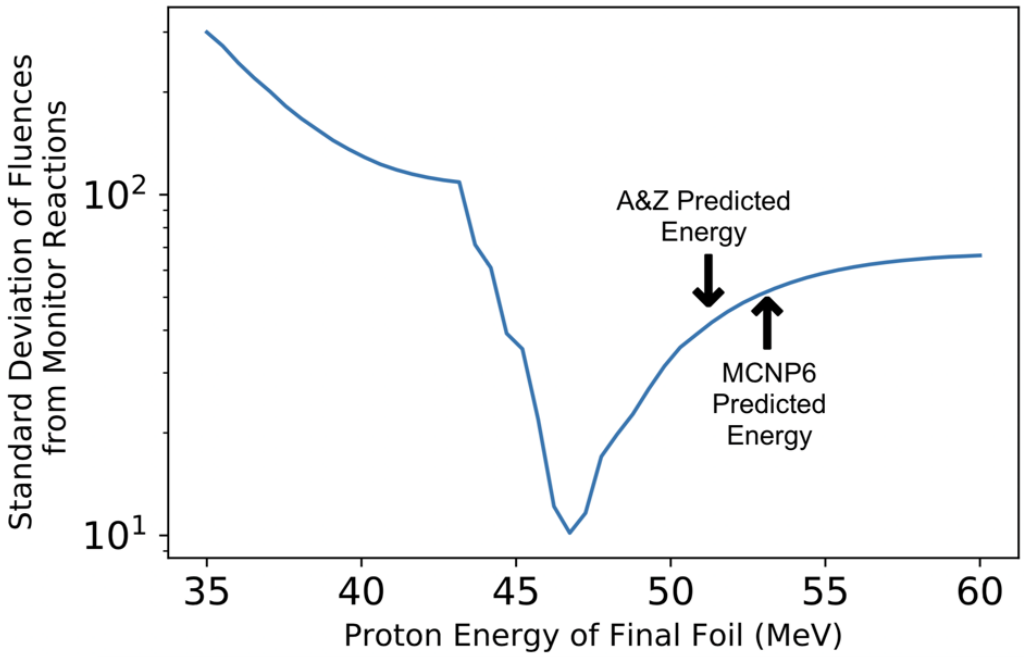


Figure 85: Result of varying exit energy of the protons to minimize the variance between the predicted fluences among the 5 monitor reactions measured.

Cross section calculation

The variance-minimized proton fluences, energies, and final end of bombardment activities were used to calculate cross sections using the formula:

$$\sigma = \frac{A_0}{I\rho x(1-e^{-\lambda t})} \quad (14)$$

When possible, the independent cross sections were calculated for each isotope. In some cases, it was not possible to separate the decay of a parent from the created daughter due to a lack of visible gammas or half-lives that were too short to allow for quantification of the parent. In these cases, the cumulative cross section for that isotope was reported.

The error in the cross section was calculated by summing the error on the fluence, density, and the end of bombardment activity in quadrature.

Results

Calculated cross sections are reported for ^{132}Ce, ^{133m}Ce, ^{134}Ce, ^{135}Ce, ^{137}Ce, ^{137m}Ce, ^{139}Ce, ^{133}La, ^{135}La, ^{131}Ba, ^{133}Ba, ^{133m}Ba, and ^{132}Cs. Measured values are compared to theoretical cross sections calculated using the TENDL-2017 predictions [88] and previously reported experimental data [188, 189].

Ce isotopes

Ce isotopes other than ^{134}Ce produced on La at these proton energies are of particular interest due to their inability to be chemically separated. Below, the cross sections for all detectable Ce isotopes are reported.

^{139}La(p,8n)^{132}Ce

^{132}Ce's excitation function was measured as a cumulative cross section due to the short half-life of the metastable state (^{132m}Ce; $t_{1/2}$ = 9.4 ms) that prevented us from quantifying the individual activities. Only the two highest energy foils were used to calculate the cross section due to the

high threshold energy of this reaction as shown in Figure 86. There are no other reported cross sections for this reaction in the literature, though a shift towards higher energies in our cross section data was observed compared to what is predicted by TENDL.

^{139}La(p,7n)^{133m}Ce

The ground state, ^{133}Ce, has a short half-life of only 97 min, and was not quantifiable in any foil.

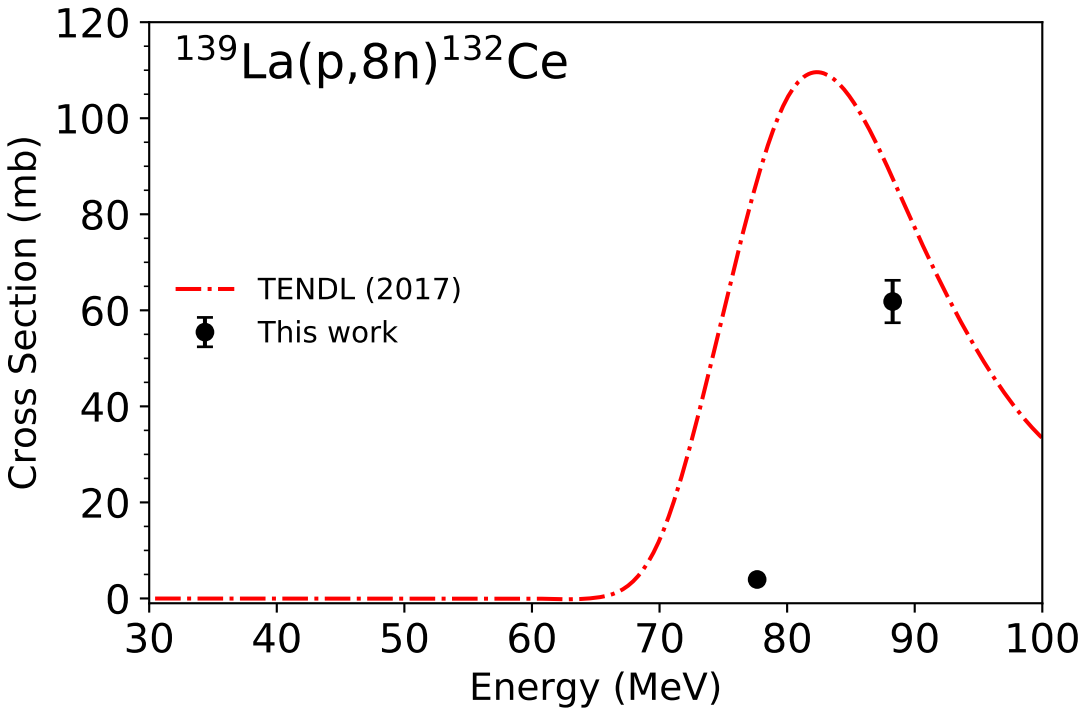


Figure 86: Experimental and theoretical cross sections for ^{132}Ce [88].

The metastable state has a longer half-life and was calculated in the 4 highest energy foils.

Cross sections for two energies were reported by Tarkanyi [188], and agree with the data measured here in the energies where the two works overlap. When compared to TENDL calculations, the peak observed in this work occurs at a higher energy than predicted by TENDL (Figure 87). In addition, the peak in this work was also broader, and of a lower magnitude.

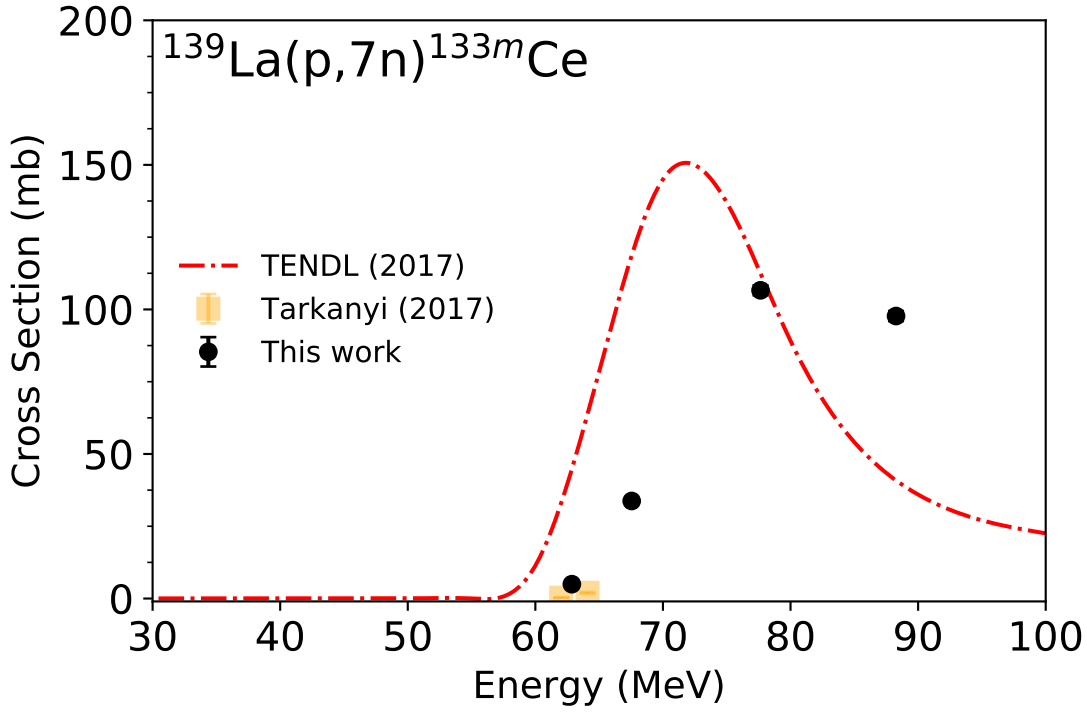


Figure 87: Experimental and theoretical cross sections for ^{133m}Ce [188, 88].

^{139}La(p,6n)^{134}Ce

Two other experiments have measured the cross section for ^{139}La(p,6n)^{134}Ce in a similar energy range to this work [188, 189]. The data in this work (Figure 88) sit between the values recorded by Tarkanyi [188] and Morrell [189]. In addition, the peak of the excitation function appears to be overestimated in magnitude by the TENDL prediction and the TENDL peak is shifted towards a lower energy than what was observed experimentally (approximately 68 MeV) [88].

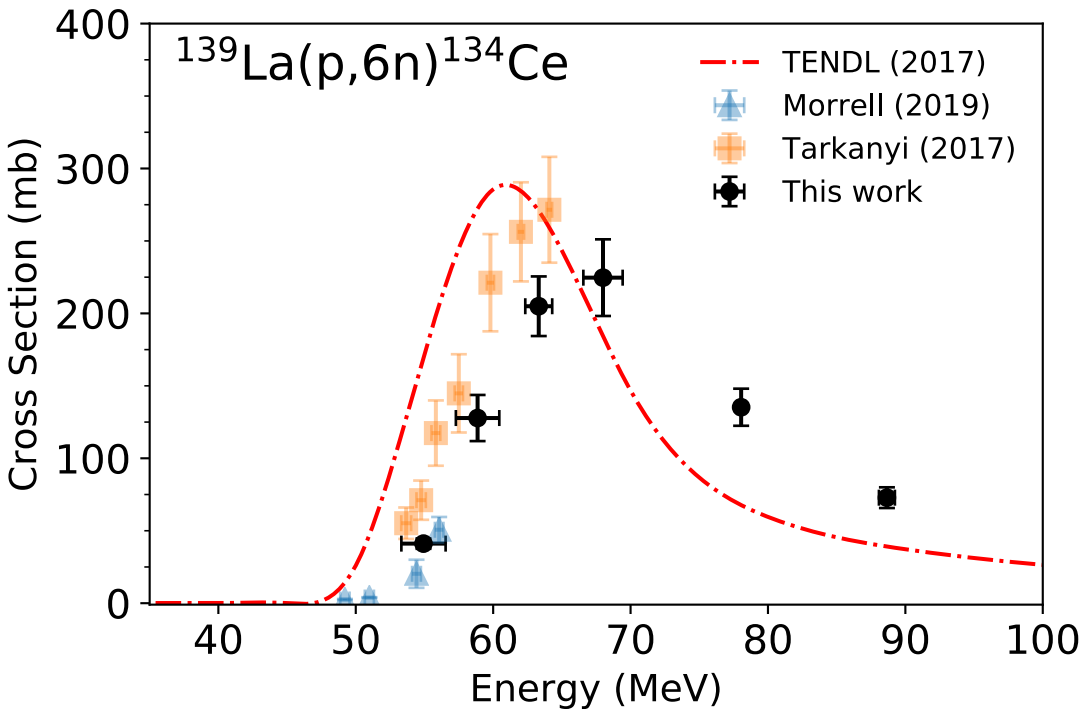


Figure 88: Experimental and theoretical cross sections for ^{134}Ce [188, 189, 88].

^{139}La(p,5n)^{135}Ce

The shorter-lived isomeric state ^{135m}Ce, which decays through internal conversion, was not detectable at the time of measurement due to its short half-life of only 20 s. Thus, the cross sections reported here are cumulative. ^{135}Ce has many strong characteristic gammas so an end of bombardment activity was calculated with relatively low uncertainty. There is excellent agreement between the cross sections measured in this work (Figure 89) and those calculated by Tarkanyi and Morrell [188, 189]. In addition, the TENDL prediction exhibits a shift towards lower energies, similar to what was observed in the case of ^{134}Ce.

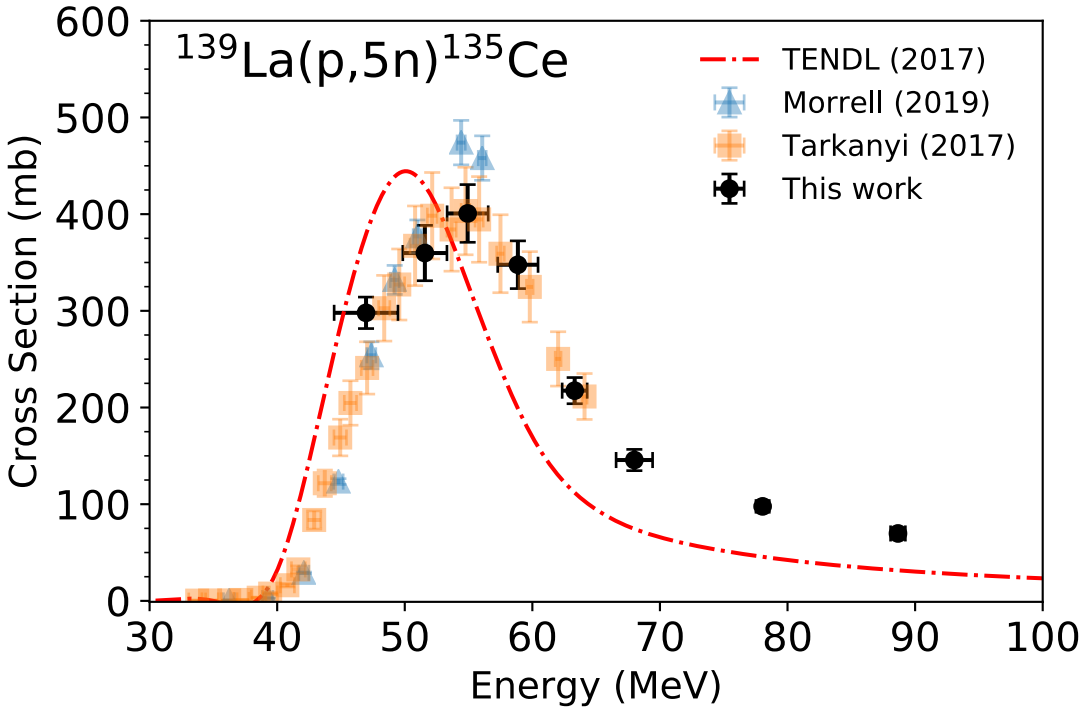


Figure 89: Experimental and theoretical cross sections for ^{135}Ce [188, 189, 88].

^{139}La(p,3n)^{137}Ce

Both the isomeric state, ^{137m}Ce, and the ground state, ^{137}Ce, were observed and cross sections reported here are independent. The ground state cross sections (as seen in Figure 90) are between the values reported by Tarkanyi and Morrell for each energy measured [188, 189]. In addition, the TENDL predicted excitation function's shape resembles the work measured here but appears to underestimate the cross section in the energy range observed. In the case of the isomeric state ^{137m}Ce, our data agrees with the data reported by Tarkanyi shown in Figure 91. In addition, the TENDL predicted cross sections agree very well and overlap within the error bars reported here. The data from Morrell [189] appear to disagree slightly where the energy overlaps, and is

slightly higher in magnitude than what was observed here and in the work presented by Tarkanyi.

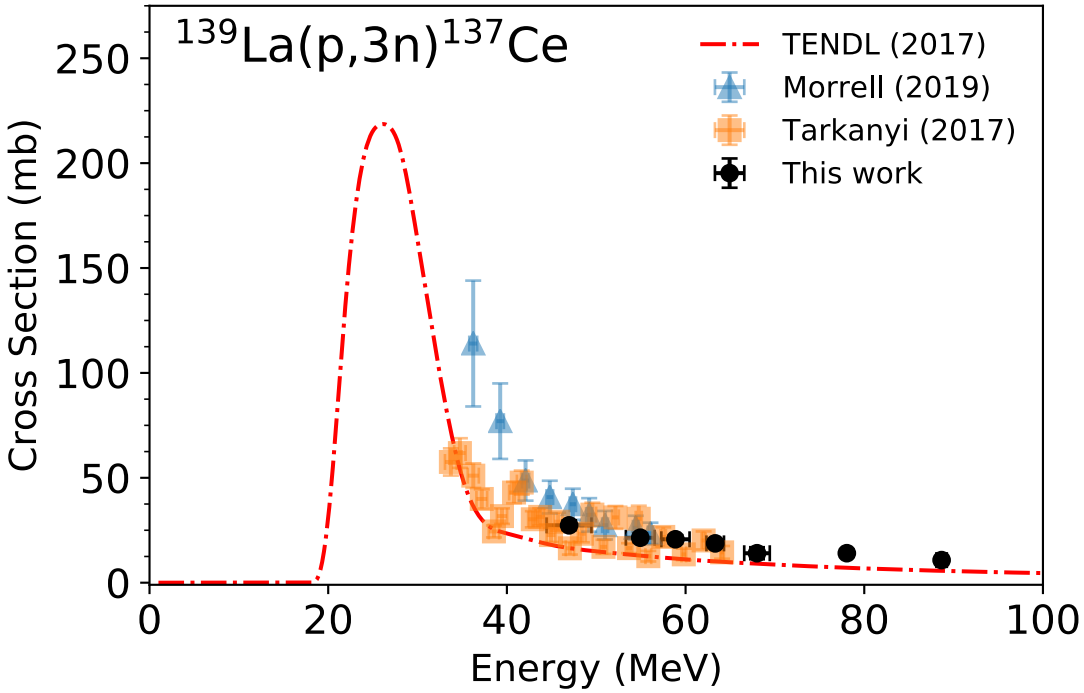


Figure 90: Experimental and theoretical cross sections for ^{137}Ce [188, 189, 88].

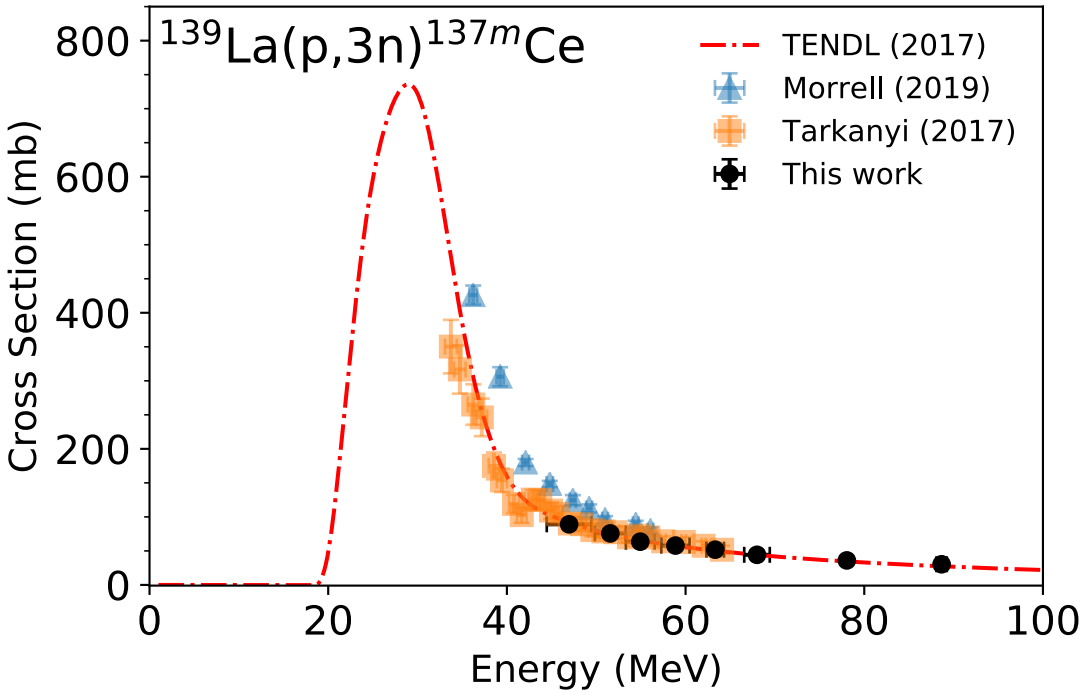
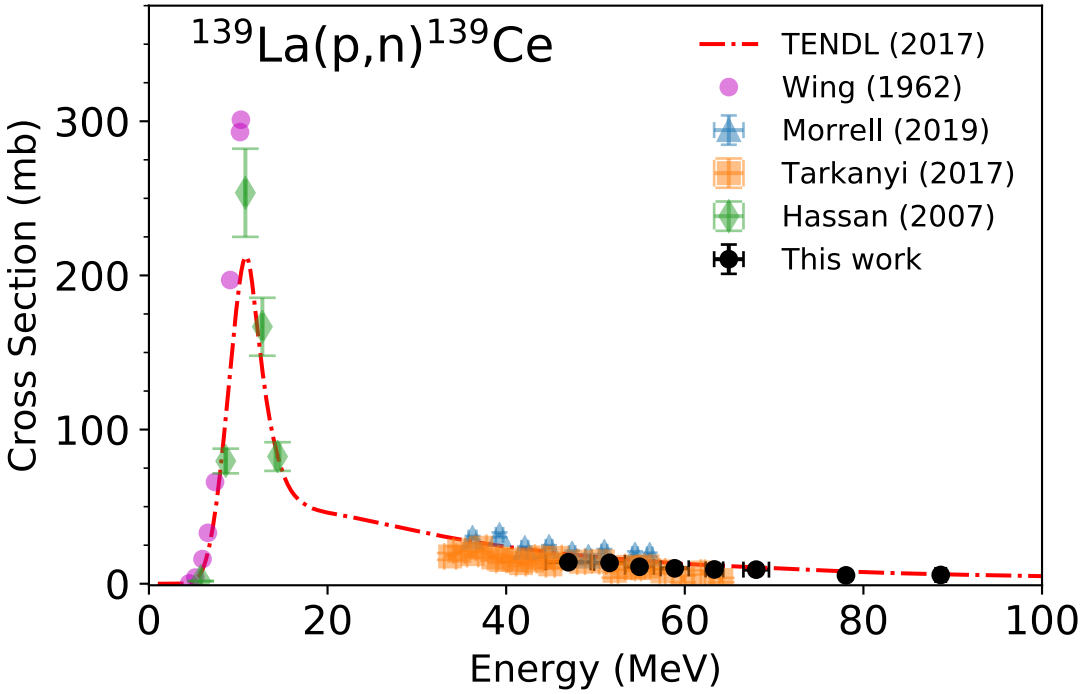


Figure 91: Experimental and theoretical cross sections for ^{137m}Ce [188, 189, 88].

^{139}La(p,n)^{139}Ce

^{139}Ce has both a short-lived isomeric state, ^{139m}Ce, and a longer lived ground state ^{139}Ce. Due to the short half-life of ^{139m}Ce ($t_{1/2}$ = 57.58 s), we could not quantify the activity of ^{139m}Ce produced directly and the cross sections reported here are cumulative. Our data in Figure 92 match closely with what was reported by Tarkanyi [188] in the area where the energies investigated overlap. The data reported by Morrell [189] are slightly higher in magnitude than the cross sections we observed in this work, but the shape of the trend is consistent. The TENDL predicted values appear to agree well with the data reported by Morrell but overestimate the magnitude of the cross sections in the energy range we measured according to the cross sections reported in this work and by Tarkanyi. Additional cross sections reported by Wing and Herman are shown here, though the energy range is lower than the scope of this work [190].


^{139}La(p,n)^{139}Ce
TENDL (2017)
Wing (1962)
Morrell (2019)
Tarkanyi (2017)
Hassan (2007)
This work
Cross Section (mb)
Energy (MeV)
0
100
200
300
0
20
40
60
80
100

Other isotopes

^{139}La(p,x)^{135}La

The measured cross sections for this work, along with data reported by Tarkanyi and Morrell, are shown in Figure 93 [20,21]. In the higher energy range, we begin to see deviation of the TENDL predicted cross sections from the data observed here. The cross sections calculated in this work begin to decrease before the TENDL predicted values and are lower in magnitude than the predictions, though the error bars in this range are large and overlap the TENDL predictions up to 88.7 MeV.

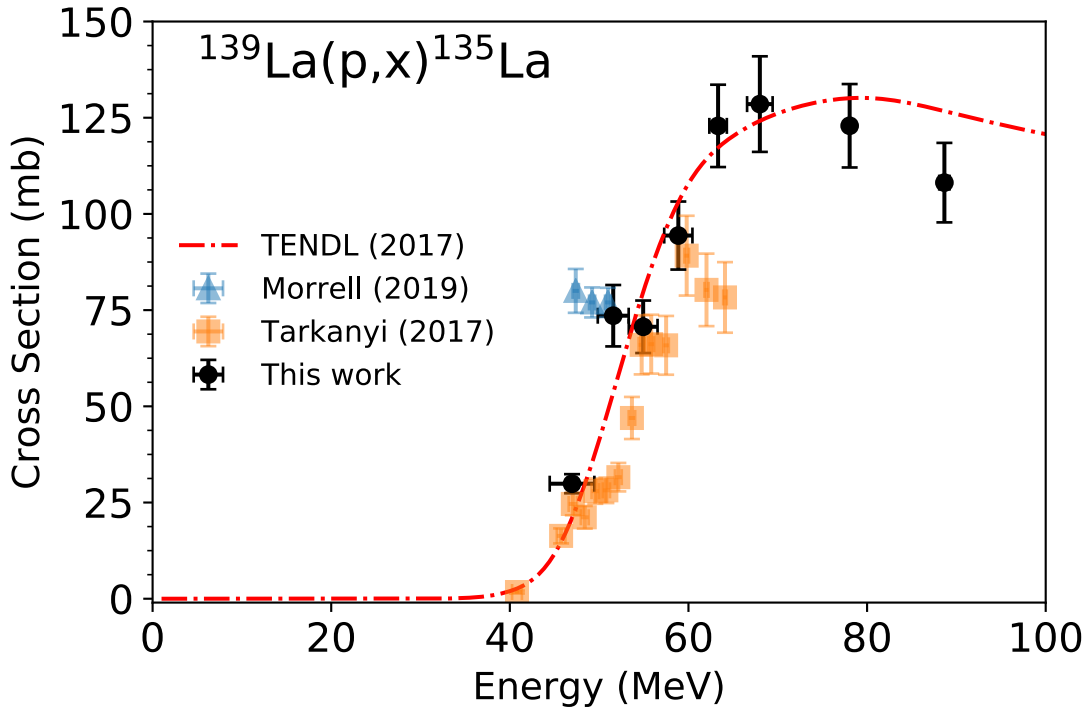


Figure 93: Experimental and theoretical cross sections for ^{135}La [188, 189, 88].

^{139}La(p,x)^{131}Ba

^{131}Ba has a short-lived isomeric state, ^{131m}Ba, that decays via internal conversion, but was not directly observed due to its short half-life ($t_{1/2}$ = 14.6 min), so we report the cumulative cross section. In the energies where this work overlaps with Tarkanyi's, the data reported from this [188]experiment match well (Figure 94) . The TENDL predictions also agree well with what was observed experimentally in this lower energy range; however, the magnitude of the peak in this energy range appears to be underestimated in the TENDL model according to what we observed in this work.

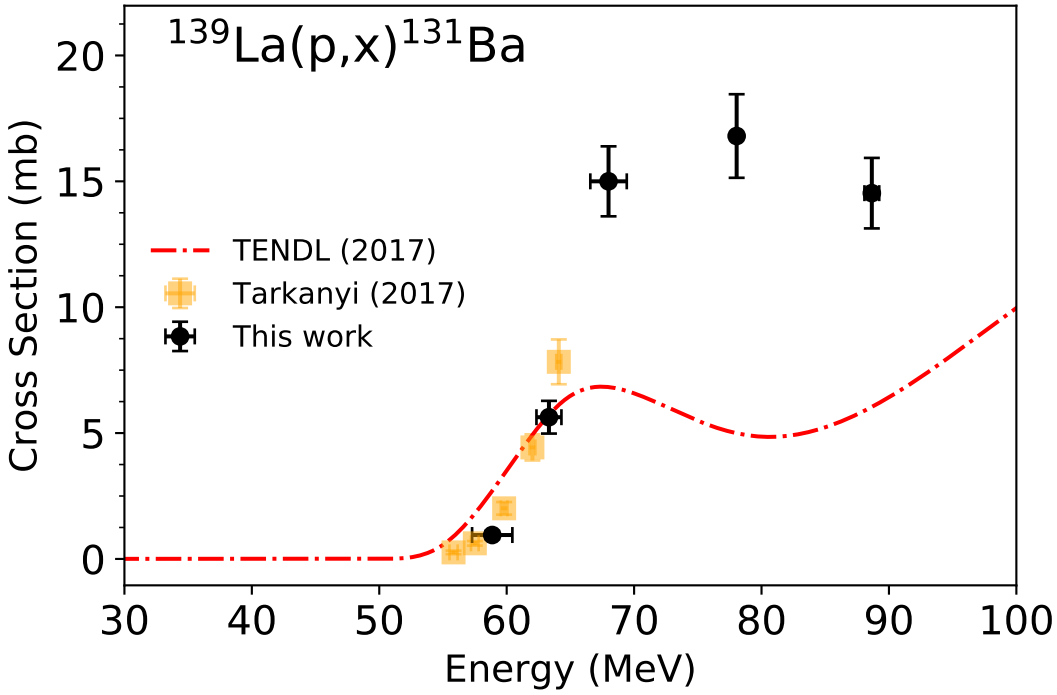


Figure 94: Experimental and theoretical cross sections for ^{131}Ba [188, 88].

^{139}La(p,x)^{133}Ba

^{133}Ba has both a metastable, ^{133m}Ba, and ground state, ^{133}Ba, that were distinguishable from one another. To quantify the ground state's activity, we waited about a week after irradiation to let shorter-lived isotopes decay. We then quantified this isotope through its 356.0129 keV (62.05%)

gamma once nearby gammas were no longer contaminating this peak. Our measured data in Figure 95 are lower than both Tarkanyi's and Morrell's data in the energies where the two experiments overlap [188, 189], though agreeing more with Morrell's lower values. The TENDL predictions appear to have a similar shape to what was observed experimentally, though the cross sections we observed are still lower in magnitude. The measured cross sections for the metastable state have great agreement with Tarkanyi's data [188], though our data are lower than that reported by Morrell (Figure 96) [189]. The TENDL model underestimates the peak in this region and then overestimates the cross sections in the energies greater than 60 MeV where we have measured data.

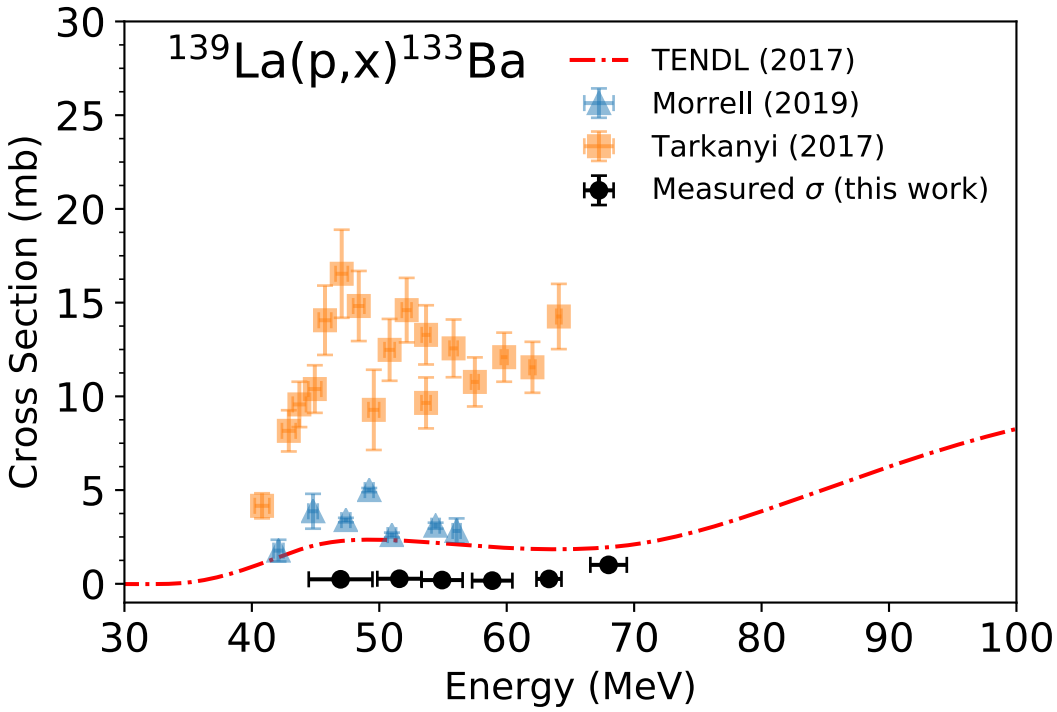


Figure 95: Experimental and theoretical cross sections for ^{133}Ba [188, 189, 88].

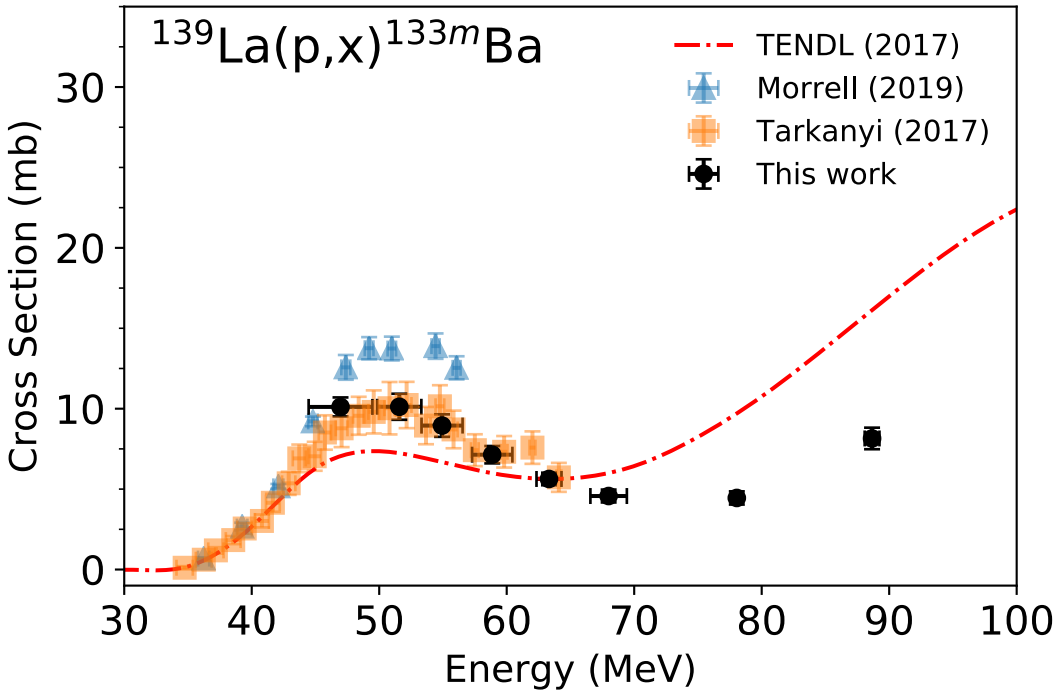


Figure 96: Experimental and theoretical cross sections for ^{133m}Ba [188, 189, 88].

^{139}La(p,x)^{132}Cs

The data reported from other experiments does not overlap in energy in the areas where we quantified the activity for ^{132}Cs. However, the lower energy trend matches well with what was reported by Morrell as seen in Figure 97 [189]. The TENDL predictions also may be underestimating the magnitude of the cross section in the energies investigated here according to the data we measured.

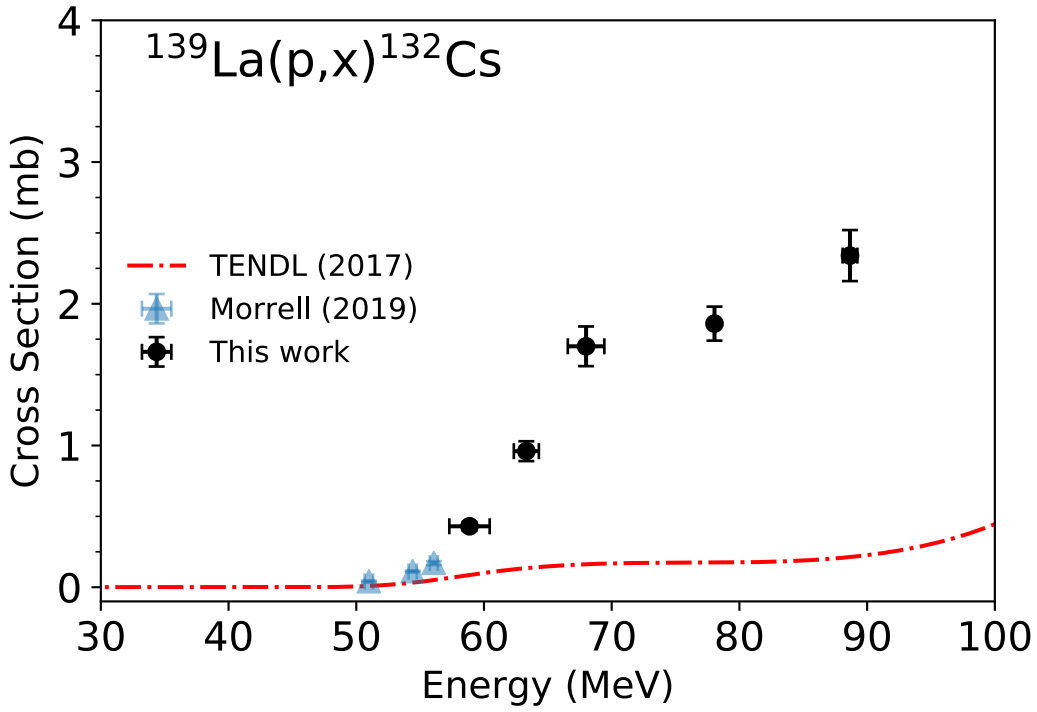


Figure 97: Experimental and theoretical cross sections for ^{132}Cs [188, 189, 88].

Predicted yields

Approximate thick target yields were calculated using the cross sections that were calculated in this work (Figure 98). To get a function of the cross section over the entire energy range from 0 to 100 MeV, the TENDL theoretical model for each isotope was stretched and adjusted to get a best fit with the data from this work. In addition, since the energy range investigated in this work did not include energies below 40 MeV, data from other experiments were also used to get an appropriate shape for the excitation function in the lower energy range. Using all published data, the TENDL curve was altered by stretching the curve in both the energy and cross section, as well as performing a shift in the two dimensions. The transformation of the TENDL curve that provided the minimum distance between the data points and the adjusted curve was then used to determine the cross section for each energy in the yield calculation.

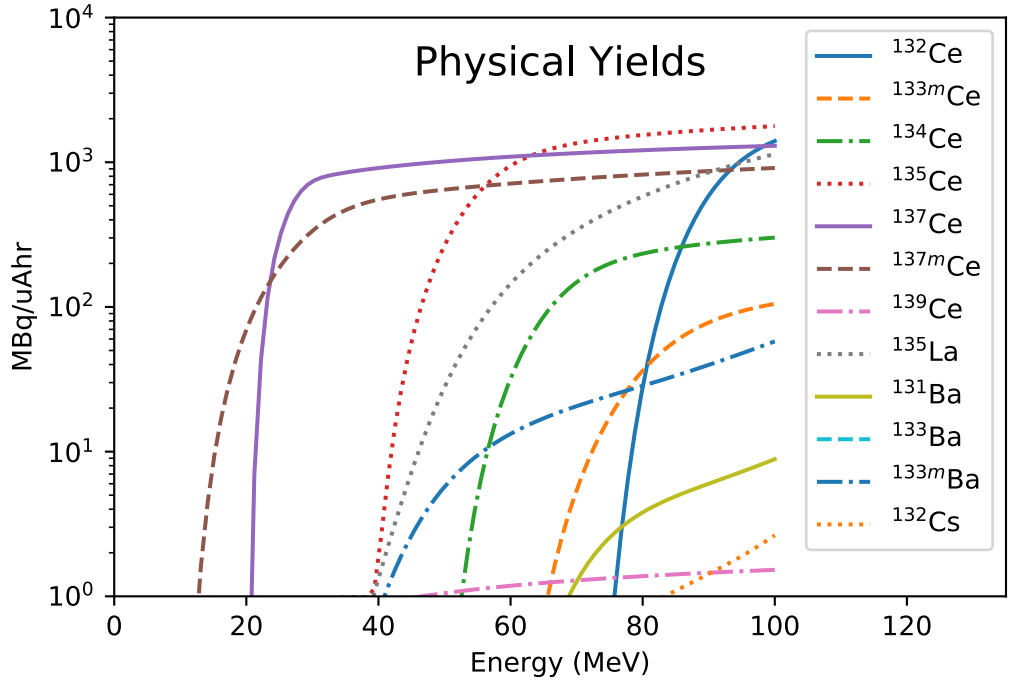


Figure 98: Yields calculated from a combination of experimental and theoretical data.

Conclusions

We presented measured cross sections for ten isotopes produced from proton bombardment on natural lanthanum targets in the energy range from 45 MeV to 90 MeV. These measurements were compared to previously measured data as well as the TENDL 2017 theoretical models. Nearly all cross sections reported here are independent cross sections and are the first measurements to be made in the energy range investigated here.

In these measurements, we were able to capture the peak of the excitation function for the ^{nat}La(p,6n)^{134}Ce reaction. In addition, we measured the excitation function of other by-products of proton bombardment on natural La. The excitation function of ^{nat}La(p,5n)^{135}Ce is important due to the large quantity of ^{135}Ce produced, which is difficult to separate from ^{134}Ce. Figures 88

and 89 show that ^{nat}La(p,5n)^{135}Ce's excitation curve peak and threshold energy are lower than that of ^{nat}La(p,6n)^{134}Ce. From this, we can conclude that irradiating at a higher energy, in particular an energy near the tail of ^{nat}La(p,6n)^{134}Ce's excitation curve, will give us a more pure sample of ^{134}Ce, with less ^{135}Ce contamination. This is also true of ^{137}Ce, ^{137m}Ce, and ^{139}Ce. However, doing so will give us larger amounts of ^{132}Ce and ^{133m}Ce.

Overall, we were able to make quantitative measurements of ^{nat}La(p,6n)^{134}Ce's excitation function in conjunction with other potential contaminants, which is of particular interest in the field of medicine because of ^{134}Ce's ability to act as an imaging analogue for the therapeutic isotope ^{225}Ac.

Appendix B: Optimization of automatic chemistry FASTLab module for ^{89}Zr and ^{68}Ga

Motivation

The cyclotron lab at the University of Wisconsin, Madison produces approximately 20 - 50 mCi of ^{89}Zr for weekly distribution to institutions across the continental United States. Additionally, ^{68}Ga access from the ^{68}Ge/^{68}Ga GalliaPharm generator at the University of Wisconsin, Madison's radiopharmaceutical facility is limited based on clinical demands, increasing the need for cyclotron-produced ^{68}Ga.

Manual processing of irradiated ^{nat}Y and ^{68}Zn targets requires operator handling of the target when transferring from the cyclotron, during radiochemical separation, reformulation, and packaging. Automating this process will not only reduce the dose to the operator but will also provide a reproduceable and streamlined method to increase efficiency and reproducibility. In this work, we optimized an automated target retrieval, dissolution, and chemical processing procedure to produce ^{89}Zr from spot welded ^{nat}Y targets and ^{68}Ga from electroplated $^{nat/68}$Zn targets using a GE FASTLab cassette-based radiochemistry system and an ARTMS QiS^{TM} solid-target transfer and dissolution system.

Materials and Methods

Equipment

A GE FASTLab automated radiochemistry system was installed in a hot cell with connection to an ARTMS QiS^{TM} pneumatic target transfer and dissolution system. The capsule containing a Y or Zn target could be sent to, and retrieved from, the target station on the cyclotron via a 2-way pneumatic transfer system. A separate dissolution module was connected directly to the

FASTLab to facilitate delivery of the dissolved target to FASTLab cassette (see Figure 99). A sample cassette for the $^{nat}Y/^{89}Zr$ procedure is shown in Figure 100.



Figure 99: ARTMS QiS^{TM} target transfer and dissolution system (left) and GE FASTlab (right).

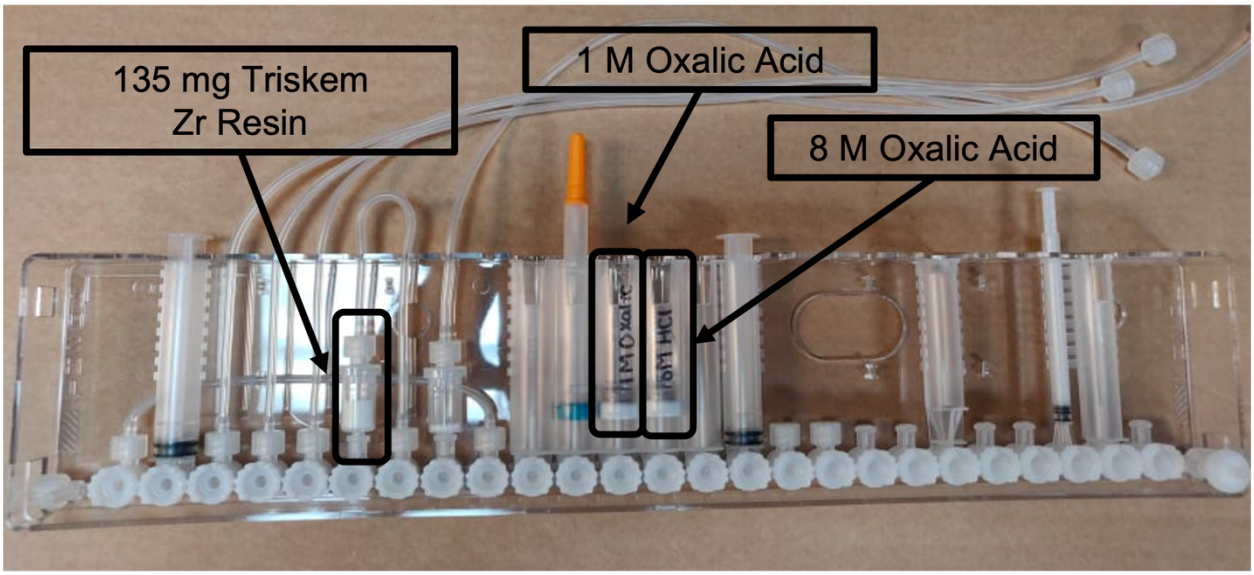


Figure 100: FASTLab cassette for the $^{nat}Y/^{89}Zr$ radiochemical separation, labeling key components.

^{89}Zr sequence development

Development of the FASTLab separation sequence for ^{89}Zr from ^{nat}Y target disks was modelled after the manual process used at the University of Wisconsin, Madison for weekly productions.



Figure 101: Spot-welded ^{nat}Y foil target on a tantalum backing.

Spot-welded Y targets (approximately 275 mg; Figure 101) were irradiated with 12.96 MeV protons (incident 16 MeV protons degraded with 0.127 mm tantalum foil) on the University of

Wisconsin, Madison's GE PETtrace cyclotron. In the manual radiochemical separation process, a column containing 120 mg of Zr resin (Eichrom) is preconditioned with 10 mL of 18 MΩ cm^{-1} water and 2 M HCl using a homemade peristaltic pump-driven device. The ^{nat}Y targets were dissolved with 5 mL 6 M HCl and then diluted with 10 mL of 18 MΩ cm^{-1} water and loaded onto the preconditioned resin. The column is then washed with 10 mL 2 M HCl followed with 10 mL of 18 MΩ cm^{-1} water. The ^{89}Zr is eluted slowly from the resin with 1 mL 1 M oxalic acid and the first 2 drops are sent to waste (low activity concentration). The second fraction containing 12-14 drops is collected as the main, high activity concentration, fraction. While the remaining volume from the 1 mL elution is usable, it is a lower concentration than the main fraction.

After setup of the FASTLab system was complete, optimization of the dissolution sequence was performed. A schematic showing the dissolution sequence is outlined in Figure 102. Small changes were made to four successive iterations of the original test sequence. The changes are outlined below:

- **181205_Zr89_Seq**: Original test sequence based off the manual separation procedure.
- **181205_Zr89_SeqB**: The volumes eluted to each fraction were increased to improve yields.
- **181205_Zr89_SeqC**: The volume eluted in fraction 1 was decreased to improve yield in fraction 2.
- **181205_Zr89_SeqF**: The volume eluted in fraction 2 was increased and the syringe used to hold the oxalic acid was swapped with another syringe to reduce activity lost in the cassette.

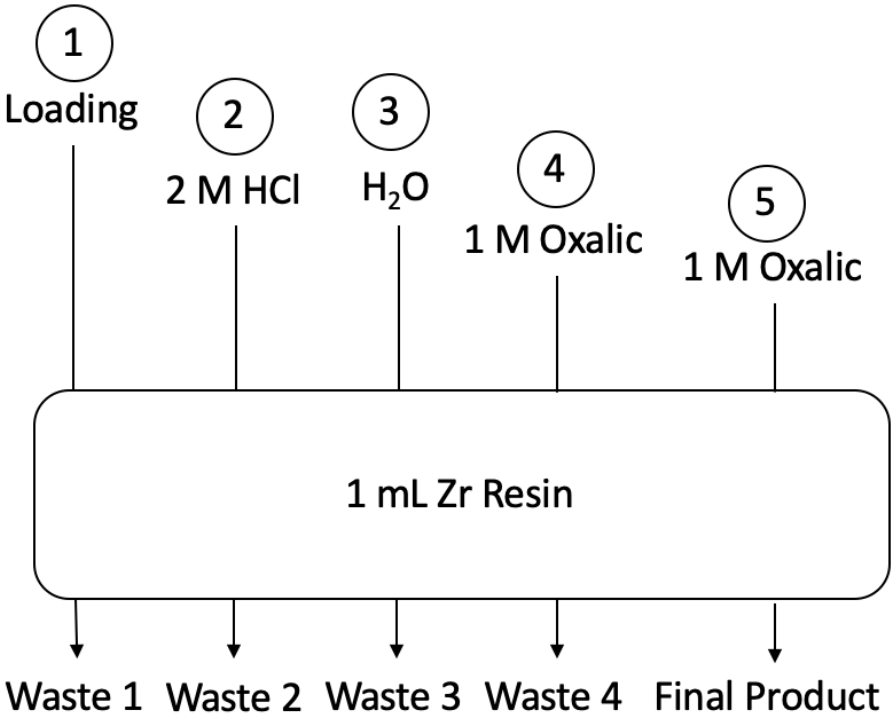


Figure 102: Separation scheme used for radiochemical isolation of ^{89}Zr from Y targets.

Each of the above sequences were designed to be used in conjunction with the ARTMS QiS™ dissolution system. After irradiation, the capsule was placed on the ARTMS QiS™ dissolution system and heated to 80 °C (Figure 95, left). 10 mL of 6 M HCl was circulated to the capsule for 14 min before transferring to the FASTLab. To accommodate a situation where the ARTMS QiS™ dissolution system may not be available, an additional sequence was designed for manual dissolution. This sequence was identical to sequence D above, but with the target dissolved manually in a 50 mL vial and then sent to the FASTLab. Once the sequence was optimized, quality tests and tests for consistency were performed.

In addition to the sequence alterations listed above, the mass of the Zr resin was varied to investigate the effect of resin mass on yields and purity of the final sample. Additionally, to lower the iron presence in the final product, and to improve the apparent molar activity, 0.1 M

ascorbic acid was added in the dissolution step in place of 18 MΩ cm^{-1} water and compared to the water-only dissolution [191].

Targets of sedimented Y were procured from ARTMS and irradiated and separated using the same methodology as the spot-welded Y targets. Radiochemical yield, radionuclidic purity, and apparent molar activity were compared across the two target types.

^{89}Zr results

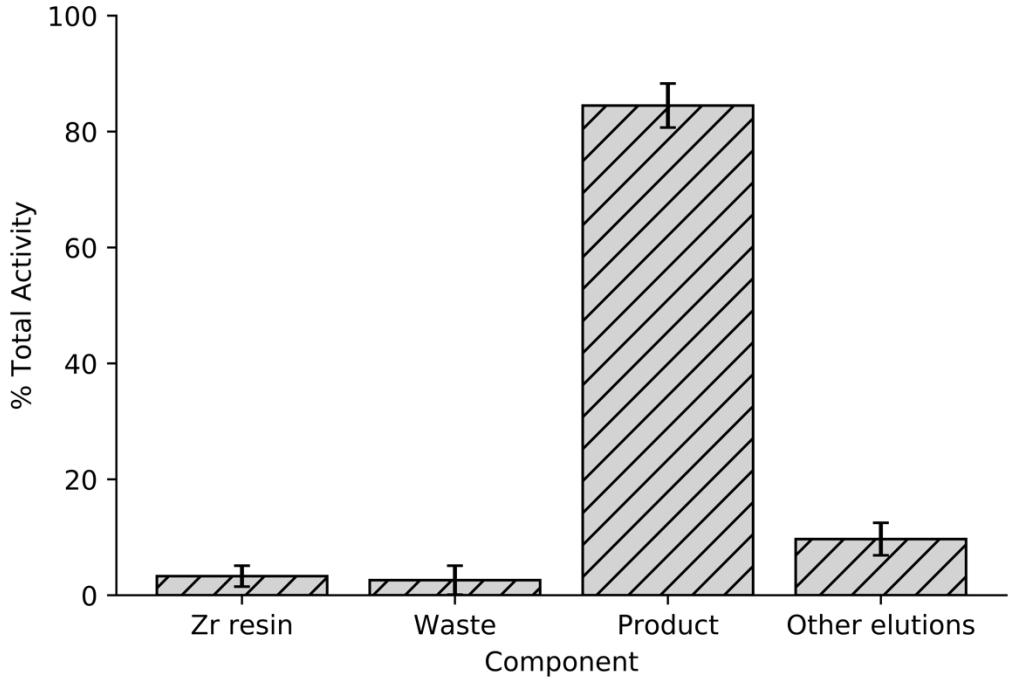


Figure 103: Activity distribution of the final, optimized ^{nat}Y/^{89}Zr FASTLab separation sequence.

The results of the progressive sequence optimization are shown in Table 36. In the first test sequence (sequence A), the activity concentration of the final product was lower than what was achieved manually, so the volumes of each elution fraction were increased for sequence B. The increase in elution volume raised the activity in both the low concentration fraction and the high concentration fraction for sequence B. To reduce the amount of activity lost in fraction 1, the volume eluted in fraction 1 was decreased for sequence C. However, this also decreased the total

activity in fraction 2 and increased the activity concentration of fraction 3. The elution volume for fraction 2 was increased for the final sequence D and resulted in high activity concentration in fraction 2 (82.53%).

The activity distribution for the final optimized sequence is shown in Figure 103. The distribution of activity among waste, resin, and final fractions is comparable to what is seen when the separation is done manually while the amount of activity in the final fraction is roughly 2-5% better than what is achieved manually.

Sequence	Resin mass (mg)	Dissol-ution vial	Resin	Waste	Fraction 1	Fraction 2 (target)	Fraction 3
Sequence A	167	4.89%	29.35%	2.17%	1.47%	**30.27%**	36.74%
Sequence B	98	7.15%	7.15%	7.80%	7.70%	**61.52%**	15.83%
Sequence C	127	6.90%	14.67%	6.10%	0.067%	**19.40%**	59.77%
Sequence D	134	6.89%	2.31%	10.27%	0.97%	**82.53%**	3.93%

Table 36: Effects on activity distribution from sequence optimization.

To determine the quality of the separation process, several radiochemical tests were performed. Fractions 1 and 3 were both discarded and the volume that was eluted in fraction 2 was assessed to determine the radioactive yield, pH, and apparent molar activity (Table 37).

Property	Average value across 20 runs
Yield (in final eluted volume)	84.5 ± 3.8 %
Apparent molar activity	1.7 ± 0.4 Ci/μmol
pH	7.5
Half-life	77.3 ± 5.6 h
Radionuclidic purity	No detectable ^{88m}Zr

Table 37: Assessment of the final ^{89}Zr product from the FASTLab separation (n = 20).

Element	Concentration (mg/L)
Zn	0.73
Fe	0.20
Cu	0.20
Y	0.58

Table 38: Microwave plasma – atomic emission spectrometry trace metals analysis of ^{89}Zr from FASTLab separation procedure (n = 15).

In addition, 15 out of the 20 final runs were tested for trace metal analysis using MP-AES. Amounts of stable Ni, Fe, Y, and Cu are all reported for each sample and listed in Table 38. Addition of ascorbic acid to the dissolution vial did not significantly change the measured apparent molar activity (1.3 vs 1.7 Ci/μmol) and the amount of iron measured via MP-AES was small, indicating that iron in the final solution was not significantly impacting the apparent molar activity. Apparent molar activity was also compared across the ARTMS Y targets (1.4 ± 0.3 Ci/μmol) and the spot-welded targets (1.7 ± 0.4 Ci/μmol) but no significant difference was noted between the two target types.

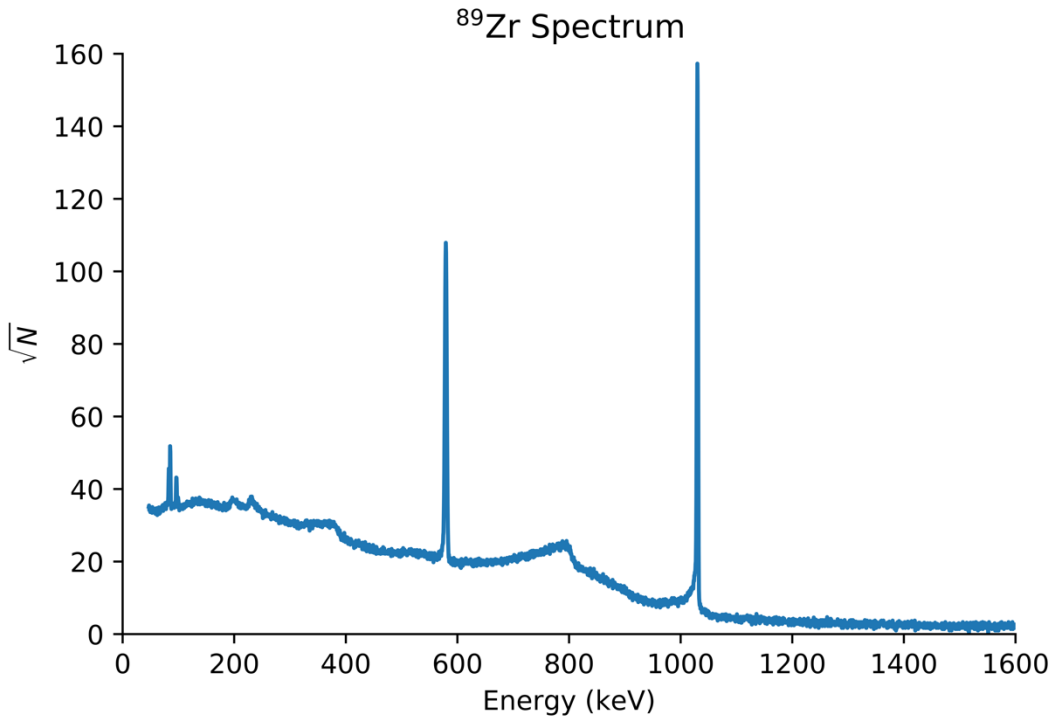


Figure 104: HPGe spectrum of a final ^{89}Zr product sample. No detectable peaks from ^{88m}Zr were present.

Spectra were taken of each final sample using a calibrated HPGe detector (Figure 104). The spectra were used to determine the radionuclidic purity of the sample and determine the half-life (n = 3 spectra were collected at different time points). From the results of the HPGe spectra, we concluded that there is no traceable amount of other radioactive isotopes (of particular interest was the metastable state Zr^{88m}) and the half-life matched the theoretical half-life within error.

^{68}Ga sequence optimization

A FastLab sequence was developed to separate cyclotron-produced ^{68}Ga from solid $^{nat/68}$Zn targets. Both ^{nat}Zn and isotopically enriched ^{68}Zn targets were electroplated on silver backings using the methodology described by Engle et. al [192]. ^{68}Zn (metal; 99.26%) was purchased from Isoflex (San Francisco, CA). Approximately 250 – 300 mg $^{nat/68}ZnCl_2$ was dissolved in 2 – 2.5 mL 0.05 M HCl. A 0.5 mm silver backing disk was used as the cathode and a platinum wire

was placed in the solution as the anode. A current of 30 - 60 mA and a voltage of 5 – 7 V was applied across the solution and approximately 3.5 – 4.5 h after the voltage was applied, 100 µL of 0.1 M HCl was added to the solution. The voltage and current were applied for approximately 20 – 25 h and yielded a plating efficiency of 93.1 ± 6.9%. A sample ^{68}Zn electroplated target is shown in Figure 105.

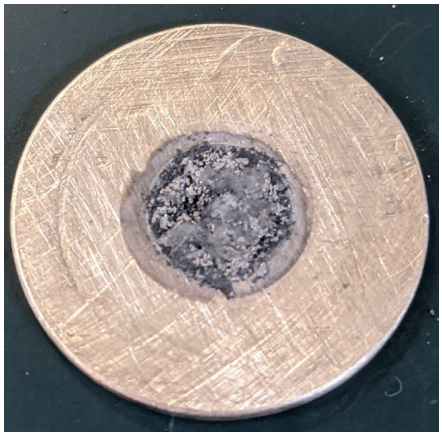


Figure 105: Electroplated ^{68}Zn target.

The initial solid target ^{68}Ga FASTLab sequence was based off the commercially available liquid target FASTLab sequence developed by GE. Optimization steps for the radiochemical separation procedure are outlined below:

- **Sequence A:** The original separation sequence based on liquid target separation.
- **Sequence B:** The Zr resin conditioning step was removed.
- **Sequence C:** A manual Zr resin conditioning was performed (before loading on the cassette).
- **Sequence D:** A filter was added in to prevent large particles from the dissolution step from loading on the resin.

The final, optimized Zn/^{68}Ga radiochemical separation procedure (sequence D) is shown in Figure 106. The cassette layout displayed on the GE FASTLab developer platform software is also shown in Figure 107.

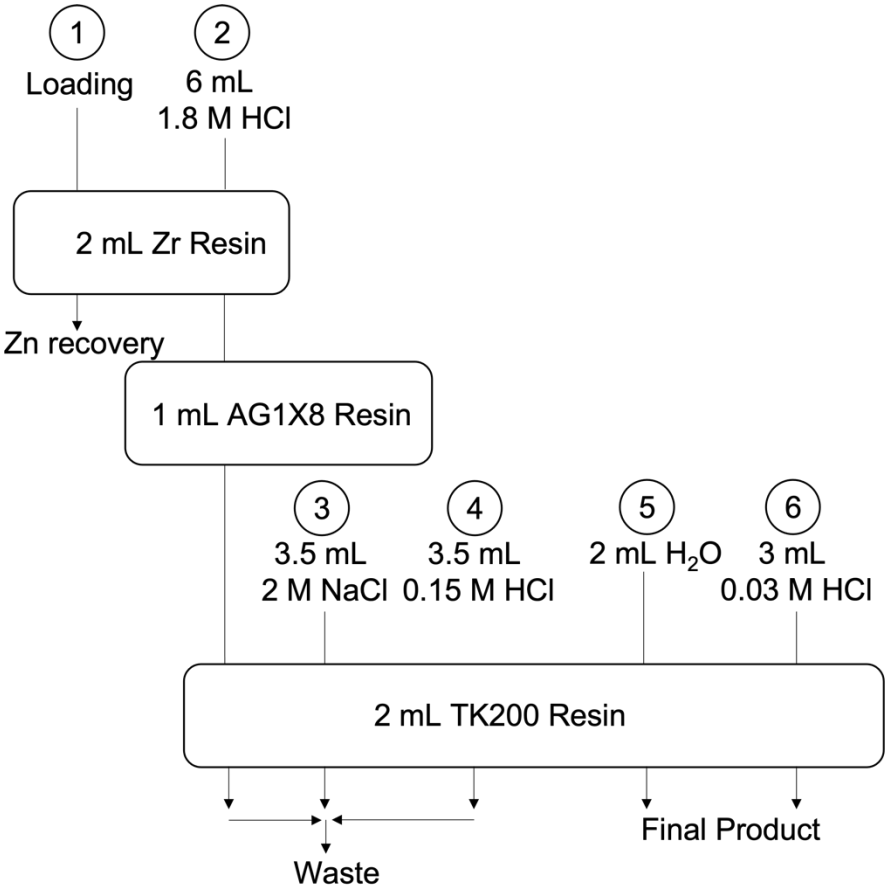


Figure 106: Final Zn/^{68}Ga FASTLab sequence.

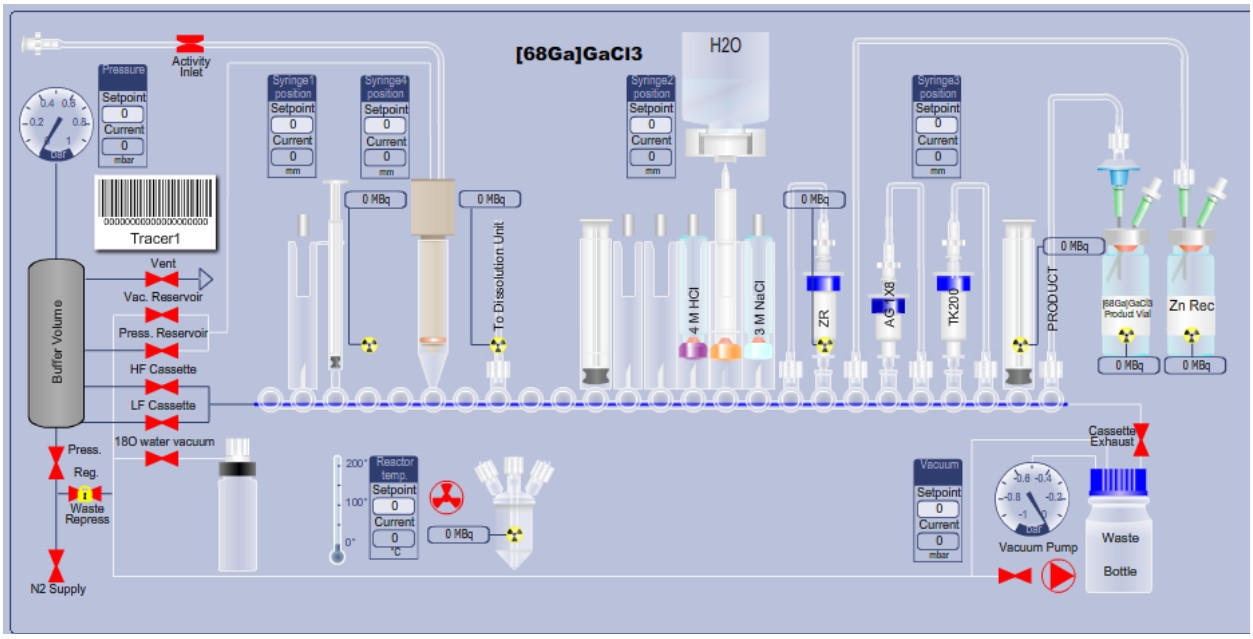


Figure 107: Zn/^{68}Ga FASTLab cassette layout on the GE FASTLab developer platform software.

An external recycling vial was attached to the FASTLab to facilitate collection of the ^{68}Zn from the loading step for isotopically enriched targets. To recycle the target, the solution collected from the FASTLab was first heated to dryness and then reconstituted in 2 – 2.5 mL 0.05 M HCl. The resulting solution could be added to the electrochemical cell and electroplated using the procedure described above.

Following sequence optimization, apparent molar activity measurements with DOTA were performed (n = 4). For these measurements, the product was allowed to decay for at least 12 hours before labelling to obtain a sample of predominantly ^{66}Ga.

^{68}Ga results

The results for each sequence optimization step are shown in Table 39. With the removal of the Zr resin conditioning step, there was a slight increase in activity in the product, but also an increase in the activity that did not load on the column and was passed to the Zn recycling vial.

Thus, the conditioning step was reintroduced but was performed manually before placing the column on the cassette. There was a significant increase in activity present in the waste vial that is not explained by the changes between sequences B and C. Sequence C was rerun and a decrease in waste activity was observed. Finally, to reduce the activity stuck on the Zr resin, a filter was added to prevent undissolved Zn from loading on the Zr resin. The activity distribution of the final, optimized separation sequence (sequence D) is shown in Figure 108.

Sequence	Zr resin	AG-1X-8 resin	TK200 resin	Zn vial	Product	Waste
Sequence A	16.29%	4.14%	7.52%	0.88%	67.42%	3.76%
Sequence B	18.63%	2.39%	0.52%	7.02%	71.18%	0.26%
Sequence C_1	14.31%	0.92%	0.53%	6.23%	56.50%	21.51%
Sequence C_2	15.77%	2.87%	2.38%	0.57%	78.08%	0.34%
Sequence D	10.62%	2.69%	0.40%	5.63%	74.16%	3.41%

Table 39: Activity distribution for each sequence optimization step.

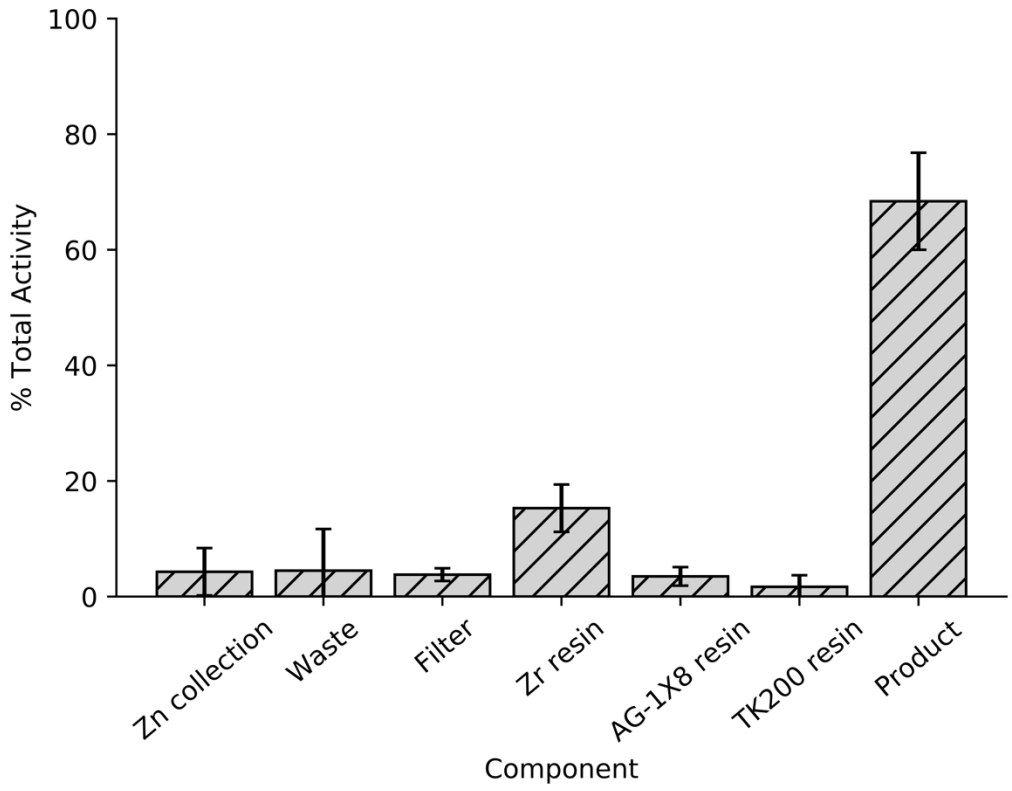


Figure 108: Activity distribution of the final, optimized FASTLab Zn/^{68}Ga separation sequence.

The yield in the final four ^{68}Ga product vial and the apparent molar activity are shown in Table 40. The amount of Zn. Fe, and Cu in the final product vial determined via MP-AES are shown in Table 41.

Property	**Average value across 4 runs**
Yield (in final eluted volume)	68.4 ± 8.4 %
Apparent molar activity	1.05 ± 0.57 Ci/μmol

Table 40: Yield and apparent molar activity of final ^{68}Ga produced from FASTLab separation.

Element	Concentration (mg/L)
Zn	0.09 ± 0.03
Fe	0.13 ± 0.14
Cu	0.05 ± 0.007

Table 41: Microwave plasma – atomic emission spectrometry trace metals analysis of ^{89}Zr from FASTLab separation procedure (n = 4).

A sample spectrum is shown in Figure 109. The peak at 1077 keV is ^{68}Ga's characteristic gamma emission (1077.34; 3.22%). No ^{66}Ga ($t_{1/2}$ = 9.49 h; E_γ = 1039.220 keV, I_γ = 37.0%) or ^{67}Ga ($t_{1/2}$ = 3.2617 d; E_γ = 93.310, I_γ = 38.81%) peaks were observed. Recycling of the isotopically enriched ^{68}Zn targets yielded and efficiency of 83 ± 14% and there was no significant change in the measured apparent molar activity for recycled versus enriched targets.

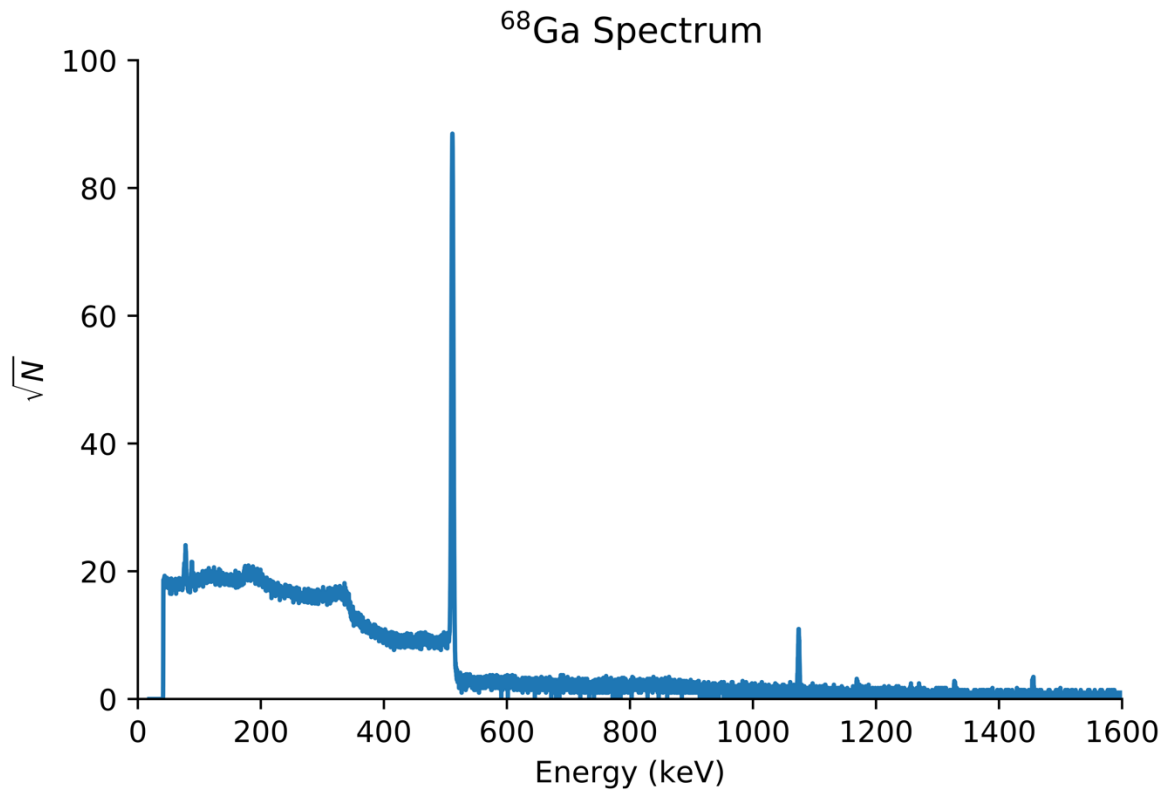


Figure 109: Sample ^{68}Ga HPGe spectrum of the final product vial.

Conclusions

In this work, we developed automated radiochemical separation sequences for production of ^{89}Zr from ^{nat}Y targets and ^{68}Ga from solid $^{nat/68}$Zn targets using the ARTMS QiS target transfer and dissolution system and a GE FASTLab. The GE FASTLab sequences had similar radiochemical yields while lowering exposure to staff and providing an easy to implement and reproduceable procedure.

REFERENCES

[1] "Nudat 3.0," Accessed on (17 April 2023). [Online]. Available: https://www.nndc.bnl.gov/nudat3/.

[2] M. Brandt, J. Cardinale, M. L. Aulsebrook, G. Gasser and T. L. Mindt, "An Overview of PET Radiochemistry, Part 2: Radiometals," *The Journal of Nuclear Medicine,* vol. 59, no. 10, pp. 1500-1506, 2018.

[3] M. D. Bartholomä, "Recent developments in the design of bifunctional chelators for metal-based radiopharmaceuticals used in Positron Emission Tomography," *Inorganica Chimica Acta,* vol. 389, no. 1, pp. 36-51, 2012.

[4] E. Aluicio-Sarduy, P. A. Ellison, T. E. Barnhart, W. Cai, R. J. Nickles and J. W. Engle , "PET radiometals for antibody labeling," *Labelled Compounds and Radiopharmaceuticals,* vol. 61, no. 9, pp. 636-651, 2018.

[5] J. Lau, E. Rousseau, D. Kwon, K.-S. Lin, F. Bénard and X. Chen, "Insight into the Development of PET Radiopharmaceuticals for Oncology," *Cancers,* vol. 12, no. 5, 2020.

[6] W. R. Strohl, "Fusion Proteins for Half-Life Extension of Biologics as a Strategy to Make Biobetters," *BioDrugs,* vol. 29, no. 4, p. 215–239, 2015.

[7] B. Grubmüller, D. Senn, G. Kramer, P. Baltzer, D. D'Andrea, K. H. Grubmüller, M. Mitterhauser, H. Eidherr, A. R. Haug, W. Wadsak, S. Pfaff, S. Shariat, M. Hacker and Hartenba, "Response assessment using ^{68}Ga-PSMA ligand PET in patients undergoing ^{177}Lu-PSMA radioligand therapy for metastatic castration-resistant prostate cancer," *European Journal of Nuclear Medicine and Molecular Imaging,* vol. 46, p. 1063–1072, 2018.

[8] A. Heinzel, D. Boghos, F. M. Mottaghy, F. Gaertner, M. Essler, D. von Mallek and H. Ahmadzadehfar, "^{68}Ga-PSMA PET/CT for monitoring response to ^{177}Lu-PSMA-617 radioligand therapy in patients with metastatic castration-resistant prostate cancer," *European Journal of Nuclear Medicine and Molecular Imaging,* vol. 46, p. 1054–1062, 2019.

[9] M. Weineisen, M. Schottelius, J. Simecek, R. P. Baum, A. Yildiz, S. Beykan, H. R. Kulkarni, M. Lassmann, I. Klette, M. Eiber, M. Schwaiger and H.-J. Wester, "^{68}Ga- and

^{177}Lu-Labeled PSMA I&T: Optimization of a PSMA-Targeted Theranostic Concept and First Proof-of-Concept Human Studies," *The Journal of Nuclear Medicine,* vol. 56, no. 8, pp. 1169-1176, 2015.

[10] J. E. Gains, J. B. Bomanji, N. L. Fersht, T. Sullivan, D. D'Souza, K. P. Sullivan, M. Aldridge, W. Waddington and M. N. Gaze, "177Lu-DOTATATE Molecular Radiotherapy for Childhood Neuroblastoma," *The Journal of Nuclear Medicine,* vol. 52, no. 7, pp. 1041-1047, 2011.

[11] A. Sainz-Esteban, V. Prasad, C. Schuchardt, C. Zachert, J. M. Carril and R. P. Baum, "Comparison of sequential planar ^{177}Lu-DOTA-TATE dosimetry scans with ^{68}Ga-DOTA-TATE PET/CT images in patients with metastasized neuroendocrine tumours undergoing peptide receptor radionuclide therapy," *European Journal of Nuclear Medicine and Molecular Imaging,* vol. 39, p. 501–511, 2012.

[12] K. Kim and S.-J. Kim, "Lu-177-Based Peptide Receptor Radionuclide Therapy for Advanced Neuroendocrine Tumors," *Nuclear Medicine and Molecular Imaging,* vol. 52, p. 208–215, 2018.

[13] L. Santoro, , E. Mora-Ramirez, D. Trauchessec, S. Chouaf, P. Eustache, J.-P. Pouget, P.-O. Kotzki, M. Bardiès and E. Deshayes , "Implementation of patient dosimetry in the clinical practice after targeted radiotherapy using [^{177}Lu-[DOTA0, Tyr3]-octreotate," *EJNMMI Research,* vol. 8, 2018.

[14] S. A. Graves and R. F. Hobbs, "Dosimetry for Optimized, Personalized Radiopharmaceutical Therapy," *Seminars in Radiation Oncology,* vol. 31, no. 1, pp. 37-44, 2021.

[15] J. Wang, J. Zang, H. Wang, Q. Liu, F. Li, Y. Lin, L. Huo, O. Jacobson, G. Niu, X. Fan, Z. Zhu and X. Chen, "Pretherapeutic ^{68}Ga-PSMA-617 PET may indicate the dosimetry of ^{177}Lu-PSMA-617 and ^{177}Lu-EB-PSMA-617 in main organs and tumor lesions," *Clin Nucl Med,* vol. 44, no. 6, p. 431–438, 2019.

[16] J. Capala, S. A. Graves, A. Scott, G. Sgouros, S. St. James, P. Zanzonico and B. E. Zimmerman, "Dosimetry for Radiopharmaceutical Therapy: Current Practices and Commercial Resources," *The Journal of Nuclear Medicine,* vol. 62, 2021.

[17] D. K. Soulek, M. E. Martin, N. J. Mastascusa and S. A. Graves, "Practical Considerations

for Implementation of ^{177}Lu-DOTATATE Neuroendocrine Tumor Treatment Programs," *Journal of Nuclear Medicine Technology,* vol. 50, no. 3, pp. 195-202, 2022.

[18] A. Sainz-Esteban, V. Prasad, C. Schuchardt, C. Zachert, J. M. Carril and R. P. Baum , "Comparison of sequential planar ^{177}Lu-DOTA-TATE dosimetry scans with ^{68}Ga-DOTA-TATE PET/CT images in patients with metastasized neuroendocrine tumours undergoing peptide receptor radionuclide therapy," *European Journal of Nuclear Medicine and Molecular Imaging,* vol. 39, p. 501–511, 2012.

[19] C. Müller, K. A. Domnanich, C. A. Umbricht and N. P. van der Meulen, "Scandium and terbium radionuclides for radiotheranostics: current state of development towards clinical application," *The British Journal of Radiology,* vol. 91, no. 1091, 2018.

[20] S. Huclier-Markai, R. Kerdjoudj, C. Alliot, A. C. Bonraisin, N. Michel, F. Haddad and J. Barbet, "Optimization of reaction conditions for the radiolabeling of DOTA and DOTA-peptide with $^{44m/44}$Sc and experimental evidence of the feasibility of an in vivo PET generator," *Nuclear Medicine and Biology,* vol. 41, no. e36-e43, 2014.

[21] M. Chernysheva , S. C. Loveless, T. Brossard, K. Becker, S. Cingoranelli, E. Alucio-Sarduy, J. Song, P. Ellison, J. Nolen, D. A. Rotsch, S. E. Lapi and J. W. Engle, "Accelerator Production of Scandium Radioisotopes: Sc-43, Sc-44, and Sc-47," *Current Radiopharmaceuticals,* vol. 14, no. 4, pp. 359-373, 2021.

[22] R. D. Shannon, "Revised effective ionic radii and systematic studies of interatomic distances in halides and chalcogenides," *Acta Crystallographica Section A: crystal physics, diffraction, theoretical and general crystallography ,* vol. 32, no. 5, pp. 751-767, 1976.

[23] G. W. Severin, J. W. Engle, H. F. Valdovinos, T. E. Barnhart and R. J. Nickles, "Cyclotron produced ^{44g}Sc from natural calcium," *Applied Radiation and Isotopes,* vol. 70, no. 8, pp. 1526-1530, 2012.

[24] K. Szkliniarz, M. Sitarz, R. Walczak, J. Jastrzębski, A. Bilewicz, J. Choiński, A. Jakubowski, A. Majkowska, A. Stolarz, A. Trzcińska and W. Zipper, "Production of medical Sc radioisotopes with an alpha particle beam," *Applied Radiation and Isotopes,* vol. 118, pp. 182-189, 2016.

[25] A. A. Ahmed, R. Misiak, M. Bartyzel, J. W. Mietelski and B. Wąs, "Study of (p,x) reactions in the natCaO targets," *Radiation Physics and Chemistry,* 2023.

[26] N. Benabdallah, H. Zhang, R. Unnerstall, A. Fears, L. Summer, M. Fassbender, B. E. Rodgers, D. Abou, V. Radchenko and D. L. J. Thorek , "Engineering a modular ^{44}Ti/^{44}Sc generator: eluate evaluation in preclinical models and estimation of human radiation dosimetry," *EJNMMI Research ,* vol. 13, no. 1, p. 17, 2023.

[27] H. F. Valdovinos, "Production, Labeling and In Vivo Studies with the Theranostic Positron-Emitting Radiometals ^{44}Sc, $^{55/58m/58g}$Co, $^{61/64}$Cu, ^{86}Y and ^{69}Ge," (Doctoral dissertation). *University of Wisconsin, Madison,* 2017. Retreived from https://www.proquest.com/docview/1892817968?pq-origsite=gscholar&fromopenview=true.

[28] A. J. Koning, D. Rochman, J. Sublet, N. Dzysiuk, M. Fleming and S. van der Marck, "TENDL: Complete Nuclear Data Library for Innovative Nuclear Science and Technology," *Nuclear Data Sheets 155,* vol. 1, 2019.

[29] T. S. Carzaniga, M. Auger, S. Braccini, M. Bunka, A. Ereditato, K. P. Nesteruk, P. Scampoli, A. Türler and N. van der Meulen, "Measurement of ^{43}Sc and ^{44}Sc production cross-section with an 18 MeV medical PET cyclotron," *Applied Radiation and Isotopes,* vol. 129, pp. 96-102, 2017.

[30] S. Krajewski, I. Cydzik, K. Abbas, A. Bulgheroni, F. Simonelli, U. Holzwarth and A. Bilewicz, "Cyclotron production of ^{44}Sc for clinical application," *Radiochimica Acta,* vol. 101, p. 333, 2013.

[31] T. J. de Waal, M. Peisach and R. Pretorius, "Activation cross sections for proton-induced reactions on calcium isotopes up to 5·6 MeV," *Journal of Inorganic and Nuclear Chemistry,* vol. 33, no. 9, pp. 2783-2789, 1971.

[32] M. Al-Abyad, I. Spahn, S. Sudár, M. Morsy, M. N. Comsan, J. Csikai, S. M. Qaim and H. H. Coenen, "Nuclear data for production of the therapeutic radionuclides ^{32}P, ^{64}Cu, ^{67}Cu, ^{89}Sr, ^{90}Y and ^{153}Sm via the (n,p) reaction: Evaluation of excitation function and its validation via integral cross-section measurement using a 14 MeV d(Be) neutron source," *Applied Radiation and Isotopes,* vol. 64, no. 6, pp. 717-724, 2006.

[33] T. S. Carzaniga, N. P. van der Meulen, R. Hasler, C. Kottler, P. Peier, A. Türler, E. Vermeulen, C. Vockenhuber and S. Braccini, "Measurement of the ^{43}Sc production cross-section with a deuteron beam," *Applied Radiation and Isotopes,* vol. 145, pp. 205-208,

2019.

[34] C. Alliot, R. Kerdjoudj , N. Michel, F. Haddad and S. Huclier-Markai, "Cyclotron production of high purity ^{44m,44}Sc with deuterons from ^{44}CaCO3 targets," *Nuclear Medicine and Biology,* vol. 42, no. 5, pp. 524-529, 2015.

[35] T. S. Carzaniga, M. Augera, S. Braccinia, M. Bunkac, A. Ereditato, K. P. Nesteruka, P. Scampolia, . A. Türler and N. van der Meulen, "Measurement of ^{43}Sc and ^{44}Sc production cross-section with an 18 MeV medical PET cyclotron," *Applied Radiation and Isotopes,* vol. 129, pp. 96-102, 2017.

[36] . V. N. Levkovski, "Cross sections of medium mass nuclide activation (A= 40-100) by medium energy protons and alpha-particles (E= 10-50 MeV)," *Inter-Vesi,* 1991.

[37] C. S. Loveless, J. R. Blanco, G. L. Diehl, R. T. Elbahrawi, T. S. Carzaniga, S. Braccini and S. E. Lapi, "Cyclotron Production and Separation of Scandium Radionuclides from Natural Titanium Metal and Titanium Dioxide Targets," *The Journal of Nuclear Medicine,* vol. 62, no. 1, pp. 131-136, 2021.

[38] K. A. Domnanich, R. Eichler, C. Müller, S. Jordi, V. Yakusheva, S. Braccini, M. Behe, R. Schibli, A. Türler and N. P. van der Meulen , "Production and separation of ^{43}Sc for radiopharmaceutical purposes," *EJNMMI Radiopharmacy and Chemistry,* vol. 2, no. 14, 2017.

[39] D. Schumann, S. Horn and J. Neuhausen , "Design of a ^{44}Ti/^{44}Sc Generator System," *Annual Report,* p. 41, 2006.

[40] N. Loktionova, D. Filosofov and M. Pruszy, "Design and performance of a novel 5 mCi ^{44}Ti/^{44}Sc-radionuclide generator," *The Journal of Nuclear Medicine,* vol. 51, p. 1467, 2010.

[41] D. V. Filosofov , N. S. Loktionova and F. Rösch, "A ^{44}Ti/^{44}Sc radionuclide generator for potential application of ^{44}Sc-based PET-radiopharmaceuticals," *rca-Radiochimica Acta,* vol. 98, no. 3, pp. 149-156, 2010.

[42] M. Pruszyński, N. S. Loktionova, D. V. Filosofov and F. Rösch, "Post-elution processing of ^{44}Ti/^{44}Sc generator-derived ^{44}Sc for clinical application," *Applied Radiation and Isotopes,* vol. 68, no. 9, pp. 1636-1641, 2010.

[43] V. Radchenko, C. A. Meyer, J. W. Engle, C. M. Naranjo, G. A. Unc, T. Mastren, M. Brugh, E. R. Birnbaum, K. D. John, F. M. Nortier and M. E. Fassbender, "Separation of ^{44}Ti from proton irradiated scandium by using solid-phase extraction chromatography and design of ^{44}Ti/^{44}Sc generator system," *Journal of Chromatography A,* vol. 1477, pp. 39-46, 2016.

[44] V. Radchenko, J. W. Engle, D. G. Medvedev, J. M. Maassen, C. M. Naranjo, G. A. Unca, C. A. Meyer, T. Mastren, M. Brugh, L. Mausner, C. S. Cutler, E. R. Birnbaum, K. D. John, F. M. Nortier and Fassbend, "Proton-induced production and radiochemical isolation of ^{44}Ti from scandium metal targets for ^{44}Ti/^{44}Sc generator development," *Nuclear Medicine and Biology,* vol. 50, pp. 25-32, 2017.

[45] S. Rane, J. T. Harris and V. N. Starovoitova, "^{47}Ca production for ^{47}Ca/^{47}Sc generator system using electron linacs," *Applied Radiation and Isotopes,* vol. 97, pp. 188-192, 2015.

[46] R. Kerdjoudj , M. Pniok , C. Alliot , V. Kubíč, J. Havlíčková , F. Rösch , . P. Hermann and S. Huclier-Markai , "Scandium(III) complexes of monophosphorus acid DOTA analogues: a thermodynamic and radiolabelling study with ^{44}Sc from cyclotron and from a ^{44}Ti/^{44}Sc generator," *Dalton Transactions,* vol. 45, pp. 1398-1409, 2016.

[47] D. Pawlak, W. Wojdowska, L. J. Parus, I. Cieszykowska, M. Zoltowska, P. Garnuszek and R. Mikolajczak, "Comparison of separation methods for ^{47}Ca/^{47}Sc radionuclide generator," *Applied Radiation and Isotopes,* vol. 151, pp. 140-144, 2019.

[48] V. N. Starovoitova, P. L. Cole and T. L. Grimm , "Accelerator-based photoproduction of promising beta-emitters ^{67}Cu and ^{47}Sc," *Journal of Radioanalytical and Nuclear Chemistry,* vol. 305, p. 127–132, 2015.

[49] L. F. Mausner, K. L. Kolsky, V. Joshi and S. C. Srivastava, "Radionuclide development at BNL for nuclear medicine therapy," *Applied Radiation and Isotopes,* vol. 49, no. 4, pp. 285-294, 1998.

[50] T. S. Carzaniga and S. Braccini, "Cross-section measurement of ^{44m}Sc,^{47}Sc, ^{48}Sc and ^{47}Ca for an optimized ^{47}Sc production with an 18 MeV medical PET cyclotron," *Applied Radiation and Isotopes,* vol. 143, pp. 18-23, 2019.

[51] R. Misiak, R. Walczak, B. Wąs, M. Bartyzel, J. W. Mietelski and A. Bilewicz , "^{47}Sc production development by cyclotron irradiation of 48Ca," *Journal of Radioanalytical and*

Nuclear Chemistry, vol. 313, p. 429–434, 2017.

[52] T. S. Carzaniga and S. Braccini, "Cross-section measurement of ^{44m}Sc,^{47}Sc, ^{48}Sc and ^{47}Ca for an optimized ^{47}Sc production with an 18 MeV medical PET cyclotron," *Applied Radiation and Isotopes,* vol. 143, pp. 18-23, 2019.

[53] K. Minegishi, K. Nagatsu, M. Fukadaa, H. Suzuki, T. Ohya and M.-R. Zhanga, "Production of scandium-43 and -47 from a powdery calcium oxide target via the $^{nat/44}$Ca(α,x)-channel," *Applied Radiation and Isotopes,* vol. 116, pp. 8-12, 2016.

[54] M. Aikawa, Y. Hanada, D. Jichinkhorloo, H. Haba, S. Takács, F. Ditróif and Z. Szűcs, "Production cross sections of ^{47}Sc via alpha-particle-induced reactions on natural calcium up to 29 MeV," *Nuclear Instruments and Methods in Physics Research Section B: Beam Interactions with Materials and Atoms,* vol. 515, pp. 1-6, 2022.

[55] F. A. Wibowo and I. Kambali, "Calculated cyclotron-based scandium-47 production yields via ^{48}Ca(p, 2n)^{47}Sc nuclear reaction," *Journal of Physics: Conference Series,* vol. 1816, no. 1, 2021.

[56] M. Sitarz, K. Szkliniarz, J. Jastrzębski, J. Choiński, A. Guertin, F. Haddad, A. Jakubowski, K. Kapinos, M. Kisieliński, A. Majkowska, E. Nigron, M. Rostampour, A. Stolarz and Trzcińska, "Production of Sc medical radioisotopes with proton and deuteron beams," *Applied Radiation and Isotopes,* vol. 142, pp. 104-112, 2018.

[57] C. S. Loveless, L. L. Radford, S. J. Ferran, S. L. Queern, M. R. Shepherd and S. E. Lapi , "Photonuclear production, chemistry, and in vitro evaluation of the theranostic radionuclide ^{47}Sc," *EJNMMI Research,* vol. 9, no. 42, 2019.

[58] D. A. Rotsch, M. A. Brown, J. A. Nolen, T. Brossard, W. F. Henning, S. D. Chemerisov, R. G. Gromov and J. Greene, "Electron linear accelerator production and purification of scandium-47 from titanium dioxide targets," *Applied Radiation and Isotopes,* vol. 131, pp. 77-82, 2018.

[59] R. A. Aliev, S. S. Belyshev, E. B. Furkina, V. V. Khankin, A. A. Kuznetsov, L. Z. Dzhilavyan, A. B. Priselkova and B. S. Ishkhanov , "Photonuclear production of medically relevant radionuclide ^{47}Sc," *Journal of Radioanalytical and Nuclear Chemistry,* vol. 326, p. 1099–1106, 2020.

[60] A. G. Kazakov, T. Y. Ekatova and J. S. Babenya, "Photonuclear production of medical radiometals: a review of experimental studies," *Journal of Radioanalytical and Nuclear Chemistry,* vol. 328, p. 493–505, 2012.

[61] K. A. Domnanich, C. Müller, M. Benešová, R. Dressler, S. Haller, U. Köster, B. Ponsard, . R. Schibli, A. Türler and N. P. van der Meulen, "^{47}Sc as useful β–-emitter for the radiotheragnostic paradigm: a comparative study of feasible production routes," *EJNMMI Radiopharmacy and Chemistry ,* vol. 2, no. 5, 2017.

[62] H. F. Valdovinos, R. Hernandez, T. E. Barnhart, S. Graves, W. Cai and R. J. Nickles, "Separation of cyclotron-produced 44Sc from a natural calcium target using a dipentyl pentylphosphonate functionalized extraction resin," *Applied Radiation and Isotopes,* vol. 95, pp. 23-29, 2015.

[63] C. Müller, M. Bunka, J. Reber, C. Fischer, K. Zhernosekov, A. Türler and R. Schibli, "Promises of Cyclotron-Produced ^{44}Sc as a Diagnostic Match for Trivalent β−-Emitters: In Vitro and In Vivo Study of a ^{44}Sc-DOTA-Folate Conjugate," *The Journal of Nuclear Medicine,* vol. 5, no. 12, pp. 2168-2174, 2013.

[64] N. P. van der Meulen, M. Bunkac, K. A. Domnanichbc, C. Müllera, S. Hallera, C. Vermeulena, A. Türlerbc and R. Schibliad, "Cyclotron production of ^{44}Sc: From bench to bedside," *Nuclear Medicine and Biology,* vol. 42, no. 9, pp. 745-751, 2015.

[65] A. T. Rane and K. S. Bhatki, "Rapid Radiochemical Separations of Strontium-90-Yttrium-90 and Calcium-45-Scandium-46 on a Cation Exchange Resin," *Analytical Chemistry,* vol. 38, no. 11, pp. 1598-1601, 1966.

[66] K. Minegishi, K. Nagatsu, M. Fukada, H. Suzuki, T. Ohya and M.-R. Zhang, "Production of scandium-43 and -47 from a powdery calcium oxide target via the $^{nat/44}$Ca(α,x)-channel," *Applied Radiation and Isotopes,* vol. 116, pp. 8-12, 2016.

[67] B. Bartoś, A. Majkowska, S. Krajewski and A. Bilewicz, "New separation method of no-carrier-added ^{47}Sc from titanium targets," *Radiochimica Acta,* vol. 100, no. 7, pp. 457-462, 2012.

[68] K. L. Kolsky, V. Joshi, L. F. Mausner and S. C. Srivastava, "Radiochemical purification of no-carrier-added scandium-47 for radioimmunotherapy," *Applied Radiation and Isotopes,* vol. 49, no. 12, pp. 1541-1549, 1998.

[69] M. Yagi and K. Kondo, "Preparation of carrier-free ^{47}Sc by the ^{48}Ti (γ,p) reaction," *The International Journal of Applied Radiation and Isotopes,* vol. 28, no. 5, pp. 463-468, 1977.

[70] M. Połosak, A. Piotrowska, S. Krajewski and A. Bilewicz , "Stability of ^{47}Sc-complexes with acyclic polyamino-polycarboxylate ligands," *Journal of Radioanalytical and Nuclear Chemistry,* vol. 295, p. 1867–1872, 2013.

[71] L. Li, M. de Guadalupe Jaraquemada-Peláez, E. Aluicio-Sarduy , X. Wang, T. E. Barnhart, W. Cai, V. Radchenko , P. Schaffer, J. W. Engle and C. Orvig , "Coordination chemistry of [Y(pypa)]− and comparison immuno-PET imaging of [^{44}Sc]Sc- and [^{86}Y]Y-pypa-phenyl-TRC105," *Royal Society of Chemistry,* vol. 49, pp. 5547-5562, 2020.

[72] B. A. Vaughn , S. H. Ahn, E. Aluicio-Sarduy, J. D. Devaraj, A. P. Olson, J. Engle and E. Boros, "Chelation with a twist: a bifunctional chelator to enable room temperature radiolabeling and targeted PET imaging with scandium-44," *Royal Society of Chemistry,* vol. 11, pp. 333-342, 2020.

[73] L. Li, M. d. G. Jaraquemada-Peláez, E. Aluicio-Sarduy, X. Wang, D. Jiang, M. Sakheie, H.-T. Kuo, T. E. Barnhart, W. Cai, V. Radchenko, P. Schaffer, K.-S. Lin, J. W. Engle and Bénard, "[$^{nat/44}$Sc(pypa)]−: Thermodynamic Stability, Radiolabeling, and Biodistribution of a Prostate-Specific-Membrane-Antigen-Targeting Conjugate," *Inorganic Chemistry,* vol. 59, no. 3, pp. 1985-1995, 2020.

[74] B. A. Vaughn, A. J. Koller, Z. Chen, S. H. Ahn, C. S. Loveless, S. J. Cingoranelli, Y. Yang, A. Cirri, C. J. Johnson, S. E. Lapi, K. W. Chapman and E. Boros, "Homologous Structural, Chemical, and Biological Behavior of Sc and Lu Complexes of the Picaga Bifunctional Chelator: Toward Development of Matched Theranostic Pairs for Radiopharmaceutical Applications," *Bioconjugate Chemistry,* vol. 32, no. 7, p. 1232–1241, 2020.

[75] C. Fersing , N. Masurier, L. Rubira, E. Deshayes and V. Lisowski , "AAZTA-Derived Chelators for the Design of Innovative Radiopharmaceuticals with Theranostic Applications," *Pharmaceuticals,* vol. 15, no. 2, p. 234, 2022.

[76] A. Singh, N. P. van der Meulen, C. Müller, I. Klette, H. R. Kulkarni, A. Türler, R. Schibli and R. P. Baum, "First-in-Human PET/CT Imaging of Metastatic Neuroendocrine Neoplasms with Cyclotron-Produced ^{44}Sc-DOTATOC: A Proof-of-Concept Study,"

Cancer Biotherapy and Radiopharmeceuticals, vol. 32, no. 4, 2017.

[77] E. Eppard, A. de la Fuente, M. Benešová, A. Khawar, R. A. Bundschuh, F. C. Gärtner, B. Kreppel, K. Kopka, M. Essler and F. Rösch, "Clinical Translation and First In-Human Use of [^{44}Sc]Sc-PSMA-617 for PET Imaging of Metastasized Castrate-Resistant Prostate Cancer," *Theranostics,* vol. 7, no. 18, pp. 4359-4369, 2017.

[78] R. Hernandez, H. F. Valdovinos, Y. Yang, R. Chakravarty, H. Hong, T. E. Barnhart and W. Cai, "^{44}Sc: An Attractive Isotope for Peptide-Based PET Imaging," *Molecular Pharmaceuticals,* vol. 11, no. 8, p. 2954–2961, 2014.

[79] S. Ghiani, I. Hawala, D. Szikra, G. Trencsényi, Z. Baranyai, G. Nagy, A. Vágner, R. Stefania, S. Pandey and A. Maiocchi , "Synthesis, radiolabeling, and pre-clinical evaluation of [^{44}Sc]Sc-AAZTA conjugate PSMA inhibitor, a new tracer for high-efficiency imaging of prostate cancer," *European Journal of Nuclear Medicine and Molecular Imaging,* vol. 48, p. 2351–2362, 2021.

[80] J.-P. Sinnes, U. Bauder-Wüst, M. Schäfer, E. S. Moon, K. Kopka and F. Rösch, "^{68}Ga, ^{44}Sc and ^{177}Lu-labeled AAZTA5-PSMA-617: synthesis, radiolabeling, stability and cell binding compared to DOTA-PSMA-617 analogues," *EJNMMI Radiopharmacy and Chemistry,* vol. 5, no. 28, 2020.

[81] R. Chakravarty, S. Goel, H. F. Valdovinos, R. Hernandez, H. Hong, R. J. Nickles and W. Cai, "Matching the Decay Half-Life with the Biological Half-Life: ImmunoPET Imaging with ^{44}Sc-Labeled Cetuximab Fab Fragment," *Bioconjugate Chemistry,* vol. 25, no. 12, p. 2197–2204, 2014.

[82] T. S. Carzaniga, N. P. van der Meulen, R. Hasler, C. Kottler, P. Peier, A. Türler, E. Vermeulen, C. Vockenhuber and S. Braccini, "Measurement of the ^{43}Sc production cross-section with a deuteron beam," *Applied Radiation and Isotopes,* vol. 145, pp. 205-208, 2019.

[83] C. Duchemin, A. Guertin, F. Haddad, N. Michel and V. Métivier, "Production of scandium-44m and scandium-44g with deuterons on calcium-44: cross section measurements and production yield calculations," *Physics in Medicine & Biology,* vol. 60, no. 17, 2015.

[84] A. Hermanne, A. V. Ignatyuk, R. Capote, B. V. Carlson, J. W. Engle, M. A. Kellett, T.

Kibédi, G. Kim, F. G. Kondev, M. Hussain, O. Lebeda, A. Luca, Y. Nagai, H. Naik, A. L. Nichols, F. M. Nortier, S. V. Suryanarayana, S. Takács and Tárkányi, "Reference Cross Sections for Charged-particle Monitor Reactions," *Nuclear Data Sheets,* vol. 148, pp. 338-382, 2018.

[85] J. F. Ziegler, M. D. Ziegler and J. P. Biersack, "SRIM – The stopping and range of ions in matter (2010)," *Research Section B: Beam Interactions with Materials and Atoms,* vol. 268, pp. 1818-1823, 2010.

[86] H. A. Bethe, "Passage of radiations through matter," *Experimental nuclear physics,* 1953.

[87] T. J. de Waal, M. Peisach and R. Pretorius, "Activation cross sections for proton-induced reactions on calcium isotopes up to 5·6 MeV," *Journal of Inorganic and Nuclear Chemistry,* vol. 33, no. 9, pp. 2783-2789, 1971.

[88] A. J. Koning and D. Rochman, "Modern Nuclear Data Evaluation with the TALYS Code System," *Nuclear Data Sheets,* vol. 113, no. 12, pp. 2841-2934, 2012.

[89] S. Krajewski, I. Cydzik , K. Abbas, A. Bulgheroni , F. Simonelli , U. Holzwarth and A. Bilewicz , "Cyclotron production of ^{44}Sc for clinical application," *Radiochimica Acta,* pp. 333-338, 2013.

[90] E. Aluicio-Sarduy, R. Hernandez, H. F. Valdovinos, C. J. Kutyref, P. A. Ellison, T. E. Barnhart, R. J. Nickles and J. W. Engle, "Simplified and automatable radiochemical separation strategy for the production of radiopharmaceutical quality ^{86}Y using single column extraction chromatography," *Applied Radiation and Isotopes,* vol. 142, pp. 28-31, 2018.

[91] B. Coto, C. Martos, J. L. Peña and R. Rodríguez , "Effects in the solubility of CaCO3: Experimental study and model description," *Fluid Phase Equilibria,* vol. 324, pp. 1-7, 2012.

[92] T. J. de Waal , M. Peisach and R. Pretorius, "Activation cross sections for deuteron-induced reactions on calcium isotopes up to 5.5 MeV," *Radiochim. Acta,* vol. 15, pp. 123-127, 1971.

[93] Z. Talip, C. Favaretto, S. Geistlich and N. P. van der Meulen, "A Step-by-Step Guide for the Novel Radiometal Production for Medical Applications: Case Studies with ^{68}Ga, ^{44}Sc,

^{177}Lu and ^{161}Tb," *Molecules,* vol. 25, no. 4, p. 966, 2020.

[94] Council of Europe (2013), "Gallium (^{68}Ga) Edotreotide injection," 2013.

[95] A. F. Hezel, A. C. Kimmelman, B. Z. Stanger, N. Bardeesy and R. A. Depinho, "Genetics and biology of pancreatic ductal adenocarcinoma," *Genes and Development,* vol. 20, no. 10, pp. 1218-1249, 2006.

[96] A. Bengtsson, R. Anderson and D. Ansari, "The actual 5-year survivors of pancreatic ductal adenocarcinoma based on real-world data," *Scientific Reports,* vol. 10, 2020.

[97] "National Cancer Institute," National Cancer Institute, 2022. [Online]. Available: https://seer.cancer.gov/statfacts/html/pancreas.html. [Accessed 24 May 2022].

[98] T. T. Poels, F. A. Vuijk, L.-F. de Geus-Oei, A. L. Vahrmeijer, D. E. Oprea-Lager and R.-J. Swijnenburg, "Molecular Targeted Positron Emission Tomography Imaging and Radionuclide Therapy of Pancreatic Ductal Adenocarcinoma," *Cancers,* vol. 13, no. 24, 2021.

[99] L. Zhang, S. Sanagapalli and A. Stoita, "Challenges in diagnosis of pancreatic cancer," *World journal of gastroenterology,* vol. 24, no. 19, pp. 2047-2060, 2018.

[100] R. Yeh, L. Dercle, I. Garg, Z. J. Wang, D. M. Hough and A. H. Goenka , "The Role of 18F-FDG PET/CT and PET/MRI in Pancreatic Ductal Adenocarcinoma," *Abdominal Radiology,* vol. 43, p. 415–434, 2018.

[101] K. Y. Elbanna, H.-J. Jang and T. K. Kim, "Imaging diagnosis and staging of pancreatic ductal adenocarcinoma: a comprehensive review," *Insights into Imaging,* vol. 11, p. 2020, 2020.

[102] P. Tummala, O. Junaidi and B. Agarwal, "Imaging of pancreatic cancer: An overview," *J Gastrointest Oncol.,* vol. 2, no. 3, p. 168–174, 2011.

[103] J. D. Kang, S. E. Clarke and A. F. Costa, "Factors associated with missed and misinterpreted cases of pancreatic ductal adenocarcinoma," *European Radiology,* vol. 31, p. 2422–2432, 2021.

[104] Y. Pang, L. Zhao, Q. Shang, T. Meng, . L. Zhao, L. Feng, S. Wang, P. Guo, X. Wu, Q. Lin, H. Wu, W. Huang, L. Sun and H. Chen , "Positron emission tomography and computed tomography with [^{68}Ga]Ga-fibroblast activation protein inhibitors improves tumor

detection and staging in patients with pancreatic cancer," *European Journal of Nuclear Medicine and Molecular Imaging,* vol. 49, p. 1322–1337, 2022.

[105] E. Pauwels, M. Ribeiro, J. Stoot and V. McCready, "FDG Accumulation and Tumor Biology," *Nuclear Medicine and Biology,* vol. 25, no. 4, pp. 317-322, 1998.

[106] M. V. Liberti and J. W. Locasale, "The Warburg Effect: How Does it Benefit Cancer Cells?," *Trends Biochem Sci.,* vol. 41, no. 3, pp. 211-218, 2016.

[107] M. Röhrich, P. Naumann, F. L. Giesel, P. L. Choyke, F. Staudinger, A. Wefers, D. P. Liew, C. Kratochwil, H. Rathke, J. Liermann, K. Herfarth, D. Jäger, J. Debus, U. Haberkorn and La, "Impact of ^{68}Ga-FAPI PET/CT Imaging on the Therapeutic Management of Primary and Recurrent Pancreatic Ductal Adenocarcinomas," *The Journal of Nuclear Medicine,* vol. 62, no. 6, pp. 779-786, 2021.

[108] J. Liermann, M. Syed, E. Ben-Josef, K. Schubert, I. Schlampp, S. D. Sprengel, J. Ristau, F. Weykamp, M. Röhrich, S. A. Koerber, U. Haberkorn, J. Debus, K. Herfarth and F. Giesel, "Impact of FAPI-PET/CT on Target Volume Definition in Radiation Therapy of Locally Recurrent Pancreatic Cancer," *Cancers,* vol. 13, no. 4, p. 796, 2021.

[109] M. Awaji and R. K. Singh, "Cancer-Associated Fibroblasts' Functional Heterogeneity in Pancreatic Ductal Adenocarcinoma," *Cancers,* vol. 11, no. 3, p. 290, 2019.

[110] M. Röhrich, P. Naumann, F. Giesel, P. L. Choyke, F. Staudinger, A. Wefers, D. P. Liew, C. Kratochwil, ,. H. Rathke, J. Liermann, K. Herfarth, D. Jäger, J. Debus, U. Habe and M. Lang, "Impact of ^{68}Ga-FAPI PET/CT Imaging on the Therapeutic Management of Primary and Recurrent Pancreatic Ductal Adenocarcinomas," *Journal of Nuclear Medicine,* vol. 62, no. 6, pp. 779-786, 2021.

[111] A. A. Fitzgerald and L. M. Weiner, "The role of fibroblast activation protein in health and malignancy," *Cancer Metastasis Rev.,* vol. 39, no. 3, pp. 783-803, 2020.

[112] Z. Zhang, G. Jia, G. Pan, K. Cao, Q. Yang, H. Meng, J. Yang, L. Zhang, T. Wang and Cheng, "Comparison of the diagnostic efficacy of ^{68}Ga-FAPI-04 PET/MR and ^{18}F-FDG PET/CT in patients with pancreatic cancer," *European Journal of Nuclear Medicine and Molecular Imaging,* 2022.

[113] S. Ferguson , H.-S. Jans, M. Wuest, T. Riauka and F. Wuest, "Comparison of scandium-44

g with other PET radionuclides in pre-clinical PET phantom imaging," *EJNMMI Physics,* vol. 6, no. 23, 2019.

[114] F. Rosar, H.-G. Buchholz, S. Michels, . M. A. Hoffmann, M. Piel, C. M. Waldmann, F. Rösch, S. Reuss and M. Schreckenberger, "Image quality analysis of ^{44}Sc on two preclinical PET scanners: a comparison to ^{68}Ga," *EJNMMI Physics,* vol. 7, no. 16, 2020.

[115] T. V. M. Lima , S. Gnesin, K. Strobel, M. del Sol Pérez , J. E. Roos, C. Müller and N. P. van der Meulen, "Fifty Shades of Scandium: Comparative Study of PET Capabilities Using Sc-43 and Sc-44 with Respect to Conventional Clinical Radionuclides," *Diagnostics,* vol. 11, no. 10, 2021.

[116] S. R. Hingorani, L. Wang, A. S. Multani, C. Combs, T. B. Deramaudt, R. H. Hruban, A. K. Rustgi, S. Chang and D. A. Tuveson, "Trp53R172H and KrasG12D cooperate to promote chromosomal instability and widely metastatic pancreatic ductal adenocarcinoma in mice," *Cancer Cell,* vol. 7, no. 5, pp. 469-483, 2005.

[117] D. J. Erstad, M. Sojoodi, M. S. Taylor, S. Ghoshal , A. A. Razavi, K. A. Graham-O'Regan, N. Bardeesy, C. R. Ferrone, . M. Lanuti, P. Caravan, K. K. Tanabe and B. C. Fuchs, "Orthotopic and heterotopic murine models of pancreatic cancer and their different responses to FOLFIRINOX chemotherapy," *Dis Model Mech,* vol. 11, no. 7, 2018.

[118] P. Bainbridge, "Wound healing and the role of fibroblasts," *J. Wound Care,* vol. 22, no. 8, pp. 407-408, 2013.

[119] M. Soret, S. L. Bacharach and I. Buvat, "Partial-Volume Effect in PET Tumor Imaging," *The Journal of Nuclear Medicine,* vol. 48, no. 6, pp. 932-945, 2007.

[120] W. Lehnert, M.-C. Gregoire, A. Reilhac and S. R. Meikle, "Characterisation of partial volume effect and region-based correction in small animal positron emission tomography (PET) of the rat brain," *NeuroImage,* vol. 60, pp. 2144-2157, 2012.

[121] J. A. Disselhorst, M. Brom, P. Laverman, C. H. Slump, O. C. Boerman, W. J. Oyen, M. Gotthardt and E. P. Visser, "Image-Quality Assessment for Several Positron Emitters Using the NEMA NU 4-2008 Standards in the Siemens Inveon Small-Animal PET Scanner," *The Journal of Nuclear Medicine,* vol. 51, no. 4, pp. 610-617, 2010.

[122] H. J. Yoon, . Y. J. Jeong, H. J. Son, D.-Y. Kang, K.-Y. Hyun and M.-K. Lee ,

"Optimization of the Spatial Resolution for the GE Discovery PET/CT 710 by Using NEMA NU 2-2007 Standards," *Journal of the Korean Physical Society,* vol. 66, pp. 287-294, 2015.

[123] D. F. Hsu, E. Ilan, W. T. Peterson, J. Uribe, M. Lubberink and C. S. Levin, "Studies of a Next-Generation Silicon-Photomultiplier–Based Time-of-Flight PET/CT System," *The Journal of Nuclear Medicine,* vol. 58, no. 9, pp. 1511-1518, 2017.

[124] M. Röhrich, P. Naumann, F. L. Giese, P. L. Choyke, F. Staudinger, A. Wefers, D. P. Liew, C. Kratochwil, H. Rathke, J. Liermann, K. Herfarth, D. Jäger, J. Debus, U. Haberkorn and Lang, "Impact of 68Ga-FAPI PET/CT Imaging on the Therapeutic Management of Primary and Recurrent Pancreatic Ductal Adenocarcinomas," *The Journal of Nuclear Medicine,* vol. 62, no. 6, pp. 779-786, 2021.

[125] K. V. Becker, E. Aluicio-Sarduy, T. Bradshaw, S. A. Hurley, A. P. Olson, K. E. Barrett, J. Batterton, P. E. Ellison, T. E. Barnhart, A. Pirasteh and J. E. Engle, "Cyclotron production of ^{43}Sc and ^{44g}Sc from enriched ^{42}CaO, ^{43}CaO, and ^{44}CaO targets," under review.

[126] K. Zukotynski, H. Jadvar, J. Capala and F. Fahey, "Targeted Radionuclide Therapy: Practical Applications and Future Prospects," *Biomark Cancer,* vol. 8, no. 2, p. 35–38, 2016.

[127] E. L. Mazzaferri and S. M. Jhiang, "Long-term impact of initial surgical and medical therapy on papillary and follicular thyroid cancer," *The American Journal of Medicine,* vol. 97, no. 5, pp. 418-428, 1994.

[128] K. V. Kokov, B. V. Egorova, M. N. German, I. D. Klabukov, M. E. Krasheninnikov, A. A. Larkin-Kondrov, K. A. Makoveeva, M. V. Ovchinnikov and Sidorov, "^{212}Pb: Production Approaches and Targeted Therapy Applications," *Pharmaceutics,* vol. 14, no. 1, p. 189, 2022.

[129] C. Kratochwil, P. Flechsig, T. Lindner, L. Abderrahim, A. Altmann, W. Mier, S. Adeberg, H. Rathke, M. Röhrich, H. Winter, P. K. Plinkert, F. Marme, M. Lang, H.-U. Kauczor and J, "68Ga-FAPI PET/CT: Tracer Uptake in 28 Different Kinds of Cancer," *Journal of Nuclear Medicine,* vol. 60, no. 6, pp. 801-805, 2019.

[130] R. Marcus, "Use of ^{90}Y-ibritumomab tiuxetan in non-Hodgkin's lymphoma," *Seminars in Oncology,* vol. 32, no. 1, pp. 36-43, 2005.

[131] R. L. Wahl, "Tositumomab and ^{131}I Therapy in Non-Hodgkin's Lymphoma," *The Journal of Nuclear Medicine,* vol. 46, no. 1, pp. 128S-140S, 2005.

[132] F. Kraeber-Bodéré, L. Campion, C. Rousseau, S. Bourdin, J.-F. Chatal and I. Resche , "Treatment of bone metastases of prostate cancer with strontium-89 chloride: efficacy in relation to the degree of bone involvement," *European Journal of Nuclear Medicine,* vol. 27, p. 1487–1493, 2000.

[133] C. L. Maini, S. Bergomi, L. Romano and R. Sciuto , "^{153}Sm-EDTMP for bone pain palliation in skeletal metastases," *European Journal of Nuclear Medicine and Molecular Imaging,* vol. 31, p. S171–S178, 2004.

[134] B. Rojas, D. R. McGowan, M. J. Guy, J. Tipping, M. Aldridge and J. Gear, "Eighty per cent more patients in 10 years of UK molecular radiotherapy: Internal Dosimetry Users Group survey results from 2007 to 2017," *Nucl Med Commun,* vol. 40, no. 7, p. 657–661, 2019.

[135] W. P. Fendler, K. Rahbar, K. Herrmann, C. Kratochwil and M. Eiber, "^{177}Lu-PSMA Radioligand Therapy for Prostate Cancer," *The Journal of Nuclear Medicine,* vol. 58, no. 8, pp. 1196-1200, 2017.

[136] L. Bodei, M. Cremonesi, C. M. Grana, N. Fazio, S. Iodice, S. M. Baio, M. Bartolomei, D. Lombardo, M. E. Ferrari, M. Sansovini, M. Chinol and G. Paganelli , "Peptide receptor radionuclide therapy with ^{177}Lu-DOTATATE: the IEO phase I-II study," *European Journal of Nuclear Medicine and Molecular Imaging,* vol. 38, p. 2125–2135, 2011.

[137] J. C. Yao, M. Hassan, A. Phan, C. Dagohoy, C. Leary, J. E. Mares, E. K. Abdalla, J. B. Fleming, J.-N. Vauthey, A. Rashid and D. B. Evans, "One Hundred Years After "Carcinoid": Epidemiology of and Prognostic Factors for Neuroendocrine Tumors in 35,825 Cases in the United States," *Journal of Clinical Oncology,* vol. 26, no. 18, pp. 3063-3072, 2008.

[138] R. Simoneaux, "A Look at the Increasing Incidence of Neuroendocrine Tumors," *Oncology Times,* vol. 42, no. 6, pp. 1-4, 2020.

[139] F. Costa and B. Gumz, "Octreotide – A Review of its Use in Treating Neuroendocrine Tumours," *Eur Endocrinol.,* vol. 10, no. 1, p. 70–74, 2014.

[140] B. J. Burkett , A. Dundar, J. R. Young, A. T. Packard, G. B. Johnson, T. R. Halfdanarson, R. A. Eiring, D. N. Gansen, C. M. Patton and A. T. Kendi, "How We Do It: A Multidisciplinary Approach to ^{177}Lu DOTATATE Peptide Receptor Radionuclide Therapy," *Radiology,* vol. 298, no. 2, 2020.

[141] P. L. Kunz, D. Reidy-Lagunes, L. B. Anthony, E. M. Bertino, K. Brendtro, J. A. Chan, H. Chen, R. T. Jensen, M. K. Kim, D. S. Klimstra, M. H. Kulke, E. H. Liu, D. C. Metz and A. Phan, "Consensus Guidelines for the Management and Treatment of Neuroendocrine Tumors," *Pancreas,* vol. 42, no. 4, pp. 557-577, 2013.

[142] K. E. Öberg, J. Reubi, D. J. Kwekkeboom and E. P. Krenning, "Role of Somatostatins in Gastroenteropancreatic Neuroendocrine Tumor Development and Therapy," *Gastroenterology,* vol. 139, no. 3, pp. 742-753, 2010.

[143] S. Lehenberger, C. Barkhausen, S. Cohrs, E. Fischer, J. Grünberg, A. Hohn, U. Köster, R. Schibli, A. Türler and K. Zhernosekov, "The low-energy β− and electron emitter ^{161}Tb as an alternative to ^{177}Lu for targeted radionuclide therapy," *Nuclear Medicine and Biology,* vol. 38, no. 6, pp. 917-924, 2011.

[144] C. Müller, J. Reber, S. Haller, H. Dorrer, P. Bernhardt, K. Zhernosekov, A. Türler and R. Schibli , "Direct in vitro and in vivo comparison of 161Tb and 177Lu using a tumour-targeting folate conjugate," *European Journal of Nuclear Medicine and Molecular Imaging,* vol. 41, p. 476–485, 2014.

[145] N. Naskar and S. Lahiri, "Theranostic Terbium Radioisotopes: Challenges in Production for Clinical Application," *Frontiers in Medicine,* vol. 8, 2021.

[146] T. I. Kostelnik and C. Orvig, "Radioactive Main Group and Rare Earth Metals for Imaging and Therapy," *Chemical Reviews,* vol. 119, pp. 902-956, 2019.

[147] A. Sainz-Esteban, V. Prasad, C. Schuchardt, C. Zachert, J. M. Carril and R. P. Baum , "Comparison of sequential planar ^{177}Lu-DOTA-TATE dosimetry scans with ^{68}Ga-DOTA-TATE PET/CT images in patients with metastasized neuroendocrine tumours undergoing peptide receptor radionuclide therapy," *European Journal of Nuclear Medicine and Molecular Imaging,* vol. 39, p. 501–511, 2012.

[148] L. Zidan, A. Iravani, K. Oleinikov, S. Ben-Haim, D. J. Gross, A. Meirovitz, O. Maimon, T. Akhurst, M. Michael, R. J. Hicks, S. Grozinsky-Glasberg and G. Kong, "Efficacy and

Safety of ^{177}Lu-DOTATATE in Lung Neuroendocrine Tumors: A Bicenter study," *The Journal of Nuclear Medicine,* vol. 63, no. 2, pp. 218-225, 2022.

[149] C. A. Umbricht, M. Benešová, . R. M. Schmid, A. Türler, . R. Schibli, N. P. van der Meulen and C. Müller, "^{44}Sc-PSMA-617 for radiotheragnostics in tandem with ^{177}Lu-PSMA-617—preclinical investigations in comparison with ^{68}Ga-PSMA-11 and ^{68}Ga-PSMA-617," *EJNMMI,* vol. 7, no. 9, 2017.

[150] C. L. Loirec and C. Champion, "Track structure simulation for positron emitters of medical interest. Part I: The case of the allowed decay isotopes," *Nuclear Instruments and Methods in Physics Research Section A: Accelerators, Spectrometers, Detectors and Associated Equipment ,* vol. 582, no. 2, pp. 644-653, 2007.

[151] Z. Talip, C. Favaretto, S. Geistlich and N. P. van der Meulen, "A Step-by-Step Guide for the Novel Radiometal Production for Medical Applications: Case Studies with ^{68}Ga, ^{44}Sc, ^{177}Lu and ^{161}Tb," *molecules,* vol. 25, no. 4, p. 966, 2020.

[152] E. Hindié, P. Zanotti-Fregonara, M. A. Quinto, C. Morgat and C. Champion, "Dose Deposits from ^{90}Y, ^{177}Lu, ^{111}In, and ^{161}Tb in Micrometastases of Various Sizes: Implications for Radiopharmaceutical Therapy," *The Journal of Nuclear Medicine,* vol. 57, no. 5, pp. 759-764, 2016.

[153] C. Champion, M. A. Quinto, C. Morgat, P. Zanotti-Fregonara and E. Hindié, "Comparison between Three Promising ß-emitting Radionuclides, ^{67}Cu, ^{47}Sc and ^{161}Tb, with Emphasis on Doses Delivered to Minimal Residual Disease," *Theranostics,* vol. 6, no. 10, p. 1611–1618, 2016.

[154] C. Müller, C. A. Umbricht, N. Gracheva, V. J. Tschan, G. Pellegrini, P. Bernhardt, J. R. Zeevaart, U. Köster, R. Schibli and N. P. van der Meulen , "Terbium-161 for PSMA-targeted radionuclide therapy of prostate cancer," *European Journal of Nuclear Medicine and Molecular Imaging,* vol. 46, p. 1919–1930, 2019.

[155] J. J. Parry, M. Eiblmaier, R. Andrews, L. A. Meyer, R. Higashikubo, C. J. Anderson and B. E. Rogers, "Characterization of Somatostatin Receptor Subtype 2 Expression in Stably Transfected A-427 Human Cancer Cells," *Molecular Imaging,* vol. 6, no. 1, 2007.

[156] J. A. Reddy, L.-C. Xu, N. Parker, M. Vetzel and C. P. Leamon, "Preclinical Evaluation of ^{99m}Tc-EC20 for Imaging Folate Receptor–Positive Tumors," *The Journal of Nuclear*

Medicine, vol. 45, no. 5, pp. 857-866, 2004.

[157] W. E. Bolch, K. F. Eckerman, G. Sgouros and S. R. Thomas, "MIRD Pamphlet No. 21: A Generalized Schema for Radiopharmaceutical Dosimetry—Standardization of Nomenclature," *Journal of Nuclear Medicine,* vol. 50, no. 3, pp. 477-484, 2009.

[158] W. Lin, E. Aluicio-Sarduy, H. A. Houson, T. E. Barnhart, V. Tekin, J. J. Jeffery, A. M. Weichmann, . K. E. Barrett, S. E. Lapi and J. W. Engle, "Theranostic cobalt-55/58m for neurotensin receptor-mediated radiotherapy in vivo: A pilot study with dosimetry," *Nuclear Medicine and Biology,* Vols. 118-119, 2023.

[159] M. Chauvin, D. Borys, F. Botta, P. Bzowski, J. Dabin, A. M. Denis-Bacelar, A. Desbrée, N. Falzone, B. Q. Lee, A. Mairani, A. Malaroda, G. Mathieu, E. McKay, E. Mora-Ramirez and Robinson, "OpenDose: Open-Access Resource for Nuclear Medicine Dosimetry," *Journal of Nuclear Medicine,* vol. 61, no. 10, pp. 1514-1519, 2020.

[160] C. H. Clement, "Adult Reference Computation Phantoms: Joint ICRP/ICRU Report," Elsevier, Amsterdam, 2009.

[161] D. S. Abou, T. Ku and P. M. Smith-Jones, "In vivo biodistribution and accumulation of 89Zr in mice," *Nuclear Medicine and Biology,* vol. 38, no. 5, pp. 675-681, 2011.

[162] T. Kostou, P. Papadimitroulas, G. Loudos and G. C. Kagadis, "A preclinical simulated dataset of S-values and investigation of the impact of rescaled organ masses using the MOBY phantom," *Physics in Medicine & Biology,* vol. 61, 2016.

[163] L. Bestervelt, B. Barr and L. Dethloff, "Divergent proliferative responses to a gastrin receptor ligand in synchronized and unsynchronized rat pancreatic AR42J tumour cells," *Cellular Signalling,* vol. 12, p. 53–61, 2000.

[164] K. P. Willowson, E. Eslick, H. Ryu, A. Poon, E. J. Bernard and D. L. Bailey, "Feasibility and accuracy of single time point imaging for renal dosimetry following ^{177}Lu-DOTATATE (‘Lutate’) therapy," *EJNMMI Physics,* vol. 5, no. 33, 2018.

[165] N. K. Tafreshi, H. Kil, D. N. Pandya, C. J. Tichacek, M. L. Doligalski, M. M. Budzevich, N. C. Delva, M. L. Langsen, J. A. Vallas, D. C. Boulware, R. W. Engelman, K. L. Gage and E. Moros, "Lipophilicity Determines Routes of Uptake and Clearance, and Toxicity of an Alpha-Particle-Emitting Peptide Receptor Radiotherapy," *ACS Pharmacol Transl Sci.,*

vol. 4, no. 2, p. 953–965, 2021.

[166] A. Grings, C. Jobic, T. Kuwert and P. Ritt, "The magnitude of the partial volume effect in SPECT imaging of the kidneys: a phantom study," *EJNMMI Phys,* vol. 9, no. 18, 2022.

[167] J. K. Sanzari, X. S. Wan,, G. S. Krigsfeld, A. J. Wroe, D. S. Gridley and A. R. Kennedy, "The Effects of Gamma and Proton Radiation Exposure on Hematopoietic Cell Counts in the Ferret Model," *Gravit Space Res.,* vol. 1, no. 1, p. 79–94, 2013.

[168] J. Svenssona, J. Mölne, E. Forssell-Aronsson, M. Konijnenberg and P. Bernhardt, "Nephrotoxicity profiles and threshold dose values for [^{177}Lu]-DOTATATE in nude mice," *Nuclear Medicine and Biology,* vol. 39, no. 6, pp. 756-762, 2012.

[169] M. S. Alavijeh, M. Chishty, M. Z. Qaiser and A. M. Palmer, "Drug Metabolism and Pharmacokinetics, the Blood-Brain Barrier, and Central Nervous System Drug Discovery," *NeuroRx,* vol. 2, no. 4, p. 554–571, 2005.

[170] R. Barone, F. Borson-Chazot, R. Valkema, S. Walrand, F. Chauvin, L. Gogou, L. K. Kvols, E. P. Krenning, F. Jamar and S. Pauwels, "Patient-Specific Dosimetry in Predicting Renal Toxicity with ^{90}Y-DOTATOC: Relevance of Kidney Volume and Dose Rate in Finding a Dose–Effect Relationship," *Journal of Nuclear Medicine,* vol. 46, no. 1 suppl, pp. 99S-106S, 2005.

[171] K. Shibuya, H. Saito, F. Nishikido, M. Takahashi and T. Yamaya , "Oxygen sensing ability of positronium atom for tumor hypoxia imaging," *Communications Physics,* vol. 3, no. 173, 2020.

[172] J. M. Brown, "Tumor Hypoxia in Cancer Therapy," *Methods in Enzymology,* vol. 435, pp. 297-321, 2007.

[173] K. Siwowska, P. Guzik, K. A. Domnanich, J. M. Monné Rodríguez, P. Bernhardt, B. Ponsard, R. Hasler, F. Borgna , R. Schibli, U. Köster, N. P. van der Meulen and C. Müller, "Therapeutic Potential of ^{47}Sc in Comparison to 177Lu and 90Y: Preclinical Investigations," *Pharmaceutics,* vol. 11, no. 8, p. 424, 2019.

[174] M. Miederer, D. A. Scheinberg and M. R. McDevitt, "Realizing the potential of the Actinium-225 radionuclide generator in targeted alpha particle therapy applications," *Advanced Drug Delivery Reviews,* vol. 60, no. 12, pp. 1371-1382, 2008.

[175] R. A. Boll, D. Malkemus and S. Mirzadeh, "Production of actinium-225 for alpha particle mediated radioimmunotherapy," *Applied Radiation and Isotopes,* vol. 62, no. 5, pp. 667-679, 2005.

[176] D. A. Scheinberg and M. R. McDevitt, "Actinium-225 in Targeted Alpha-Particle Therapeutic Applications," *Current Radiopharmaceuticals,* vol. 4, no. 4, pp. 306-320, 2011.

[177] B. J. Allen, "Clinical Trials of Targeted Alpha Therapy for Cancer," *Reviews on Recent Clinical Trials,* vol. 3, 2008.

[178] I. A. Davis, K. A. Glowienka, R. A. Boll, K. A. Deal, M. W. Brechbiel, M. Stabin, P. N. Bochsler, S. Mirzadeh and S. J. Kennel, "Comparison of 225actinium chelates: tissue distribution and radiotoxicity," *Nuclear Medicine and Biology,* vol. 26, no. 5, pp. 581-589, 1999.

[179] S. S. Kelkar and T. M. Reineke, "Theranostics: Combining Imaging and Therapy," *Bioconjugate Chem.,* vol. 22, no. 10, p. 1879–1903, 2011.

[180] A. Lorenzoni, A. Capozza, E. Seregni and L. Giovanella , "Nuclear Medicine Theranostics: Between Atoms and Patients," *Nuclear Medicine Therapy,* pp. 1-9, 2019.

[181] R. P. Baum and H. R. Kulkarni, "THERANOSTICS: From Molecular Imaging Using Ga-68 Labeled Tracers and PET/CT to Personalized Radionuclide Therapy - The Bad Berka Experience," *Theranostics,* vol. 2, no. 5, p. 437–447, 2012.

[182] G. Wunderlich, E. Schiller, R. Bergmann and H.-J. Pietzsch, "Comparison of the stability of Y-90-, Lu-177- and Ga-68- labeled human serum albumin microspheres (DOTA-HSAM)," *Nucl Med Biol ,* vol. 37, no. 8, pp. 861-867, 2010.

[183] B. Baur, C. Solbach, E. Andreolli, G. Winter, H.-J. Machulla and S. N. Reske, "Synthesis, Radiolabelling and In Vitro Characterization of the Gallium-68-, Yttrium-90- and Lutetium-177-Labelled PSMA Ligand, CHX-A"-DTPA-DUPA-Pep," *Pharmaceuticals,* vol. 7, no. 5, pp. 517-529, 2014.

[184] T. Bailey, A. Lakes, D. An, t. Gauny and R. Abergel, "Biodistribution Studies of Chelated Ce-134/La-134 as Positron-Emitting Analogues of Alpha-Emitting Therapy Radionuclides," *Journal of Nuclear Medicine,* vol. 60, no. Supplemental 1, p. 130, 2019.

[185] S. A. Graves, P. A. Ellison, T. E. Barnhart, H. F. Valdovinos, E. R. Birnbaum, F. M. Nortier, R. J. Nickles and J. W. Engle, "Nuclear excitation functions of proton-induced reactions (Ep = 35–90 MeV) from Fe, Cu, and Al," *Nuclear Instruments and Methods in Physics Research Section B: Beam Interactions with Materials and Atoms,* vol. 386, pp. 44-53, 2016.

[186] A. Hermanne, A. V. Ignatyuk, R. Capote, B. V. Carlson, J. W. Engle, M. A. Kellett, T. Kibédi, G. Kim, F. G. Kondev, M. Hussain, O. Lebeda, A. Luca, Y. Nagai, H. Naik, A. L. Nichols, F. M. Nortier, S. V. Suryanarayana, S. Takács and Tárkány, "Reference Cross Sections for Charged-particle Monitor Reactions," *Nuclear Data Sheets,* vol. 138, pp. 338-382, 2018.

[187] T. Goorley, M. James, T. Booth, F. Brown, J. Bull, L. Cox, J. Durkee, J. Elson, M. Fensin, R. A. Forster, J. Hendricks, H. G. Hughes, R. Johns, B. Kiedrowski, R. Martz, S. Mashnik, G. McKinney, D. Pelowitz, R. Prael, J. Sweezy and Waters, "Initial MCNP6 Release Overview," *Nuclear Technology,* vol. 180, no. 3, pp. 298-315, 2012.

[188] F. Tárkányi, A. Hermanne, F. Ditrói and S. Takács, "Activation cross section data of proton induced nuclear reactions on lanthanum in the 34–65 MeV energy range and application for production of medical radionuclides," *Journal of Radioanalytical and Nuclear Chemistry,* vol. 312, p. 691–704, 2017.

[189] J. T. Morrell, A. S. Voyles, M. S. Basunia, J. C. Batchelder, E. F. Matthews and L. A. Bernstein , "Measurement of ^{139}La(p,x) cross sections from 35–60 MeV by stacked-target activation," *The European Physical Journal A,* vol. 56, 2020.

[190] J. Wing and J. R. Huizenga, "(p , n) Cross Sections of V 51 , Cr 52 , Cu 63 , Cu 65 , Ag 107 , Ag 109 , Cd 111 , Cd 114 , and La 139 from 5 to 10.5 MeV," *Physical Review,* vol. 128, no. 280, 1962.

[191] "Triskem INFOS, No 15," http://www.triskem-international.com/scripts/files/59d1f4fc31f796.50370140/ tki_15_en_web.pdf, 2016.

[192] J. W. Engle, V. Lopez-Rodriguez, R. E. Gaspar-Carcamo, H. F. Valdovinos, M. Valle-Gonzalez, F. Trejo-Ballado, G. W. Severin, T. E. Barnhart, R. J. Nickles and M. A. Avila-Rodriguez, "Very high specific activity $^{66/68}$Ga from zinc targets for PET," *Applied Radiation and Isotopes,* vol. 70, no. 8, pp. 1792-1796, 2012.

[193] M. Nurmik, P. Ullmann, F. Rodriguez, S. Haan and E. Letellier, "In search of definitions: Cancer-associated fibroblasts and their markers," *International Journal of Cancer,* 2019.

[194] E. Aluicio-Sarduy, R. Hernandez, A. P. Olson, T. E. Barnhart, W. Cai, P. A. Ellison and J. W. Engle, "Production and in vivo PET/CT imaging of the theranostic pair $^{132/135}$La," *Scientific Reports,* vol. 9, 2019.

[195] Y. Shou, Q. Xue, J. Yuan and J. Zhao, "68Ga-FAPI-04 PET/MR is helpful in differential diagnosis of pancreatitis from pancreatic malignancy compared to ^{18}F-FDG PET/CT: a case report," *European Journal of Hybrid Imaging,* vol. 5, no. 12, 2021.

[196] D. V. Filosofov, N. S. Loktionova and F. Rösch, "A 44Ti/44Sc radionuclide generator for potential application of ^{44}Sc-based PET-radiopharmaceuticals," *Radiochimica Acta,* vol. 98, no. 3, pp. 149-156, 2010.

[197] F. Roesch, "Scandium-44: Benefits of a Long-Lived PET Radionuclide Available from the 44Ti/44Sc Generator System," *Current Radiopharmeceuticals,* vol. 5, no. 3, pp. 187-201, 2012.

[198] M. Bunka, C. Müller, C. Vermeulen, S. Haller, A. Türler, R. Schibli and N. P. van der Meulen, "Imaging quality of ^{44}Sc in comparison with five other PET radionuclides using Derenzo phantoms and preclinical PET," *Applied Radiation and Isotopes,* vol. 110, pp. 129-133, 2016.

[199] B. Lommel, A. Beusch, W. Hartmann, A. Hübner, B. Kindler, J. Steiner and V. Yakusheva, "Reduction of isotopically enriched ^{50}Ti-dioxide for the production of high-intensity heavy-ion beam," *Journal of Radioanalytical and Nuclear Chemistry,* vol. 299, p. 977–980, 2014.

[200] S. D. Robert, "Revised effective ionic radii and systematic studies of interatomic distances in halides and chalcogenides," *Acta crystallographica section A: crystal physics, diffraction, theoretical and general crystallography,* vol. 32, no. 5, pp. 751-767, 1976.

[201] G. W. Severin, K. Gagnon and J. W. Engle, "^{44g}Sc from metal calcium targets for PET," in *AIP Conference Proceedings*, 2012.

[202] A. Azzam, M. S. Hamada, S. A. Said, G. Y. Mohamed and M. Al-abyad, "Excitation functions for proton-induced reactions on Te and natTi targets: Measurements and model

calculations special relevant to the ^{128}Te(p,n)^{128}I reaction," *Nuclear Physics A,* vol. 999, p. 121790, 2020.

[203] A. R. Usman, M. U. Khandaker, H. Haba, N. Otuka and M. Murakami, "Excitation functions of alpha particles induced nuclear reactions on natural titanium in the energy range of 10.4–50.2 MeV," *Nuclear Instruments and Methods in Physics Research Section B: Beam Interactions with Materials and Atoms,* vol. 399, pp. 34-47, 2017.

[204] O. Lebeda, J. Štursa and J. Ráliš, "Experimental cross-sections of deuteron-induced reaction on ^{89}Y up to 20 MeV; comparison of ^{nat}Ti(d,x)^{48}V and ^{27}Al(d,x)^{24}Na monitor reactions," *Nuclear Instruments and Methods in Physics Research Section B: Beam Interactions with Materials and Atoms,* vol. 360, pp. 118-128, 2015.

[205] M. U. Khandaker, H. Haba, J. Kanaya, N. Otuka and H. A. Kassima, "Activation Cross-sections of Deuteron-induced Nuclear Reactions on Natural Titanium," *Nuclear Data Sheets,* vol. 119, pp. 252-254, 2014.

[206] M. U. Khandaker, H. Haba, J. Kanaya and N. Otukac, "Excitation functions of (d,x) nuclear reactions on natural titanium up to 24 MeV," *Nuclear Instruments and Methods in Physics Research Section B: Beam Interactions with Materials and Atoms,* vol. 296, pp. 14-21, 2013.

[207] S. Takácss, M. Sonck, B. Scholten, A. Hermanne and F. Tárkány, "Excitation functions of deuteron induced nuclear reactions on ^{nat}Ti up to 20 MeV for monitoring deuteron beams," *Applied Radiation and Isotopes,* vol. 48, pp. 657-665, 1997.

[208] B. Liu, R. Han, C. Yuan, H. Sun, Z. Chen, G. Tian, F. Shi, X. Zhang, P. Luo and H. Jia, "Excitation functions of proton induced reactions on titanium and copper," *Applied Radiation and Isotopes,* vol. 173, p. 109713, 2021.

[209] J. Červenák and O. Lebeda, "New cross-section data for proton-induced reactions on ^{nat}Ti and ^{nat}Cu with special regard to the beam monitoring," *Nuclear Instruments and Methods in Physics Research Section B: Beam Interactions with Materials and Atoms,* vol. 480, pp. 78-97, 2020.

[210] M. Shahid, K. Kim, G. Kim and H. Naik , "Measurement of excitation functions of residual radionuclides from ^{nat}Ti(p,x) reactions up to 44 MeV," *Journal of Radioanalytical and Nuclear Chemistry,* vol. 318, p. 2049–2057, 2018.

[211] E. Garrido, C. Duchemin, A. Guertin, F. Haddad, N. Michela and V. Métivier, "New excitation functions for proton induced reactions on natural titanium, nickel and copper up to 70 MeV," *Nuclear Instruments and Methods in Physics Research Section B: Beam Interactions with Materials and Atoms,* vol. 383, pp. 191-212, 2016.

[212] K. Zarie, N. Al-Hammad and A. Azzam, "Experimental study of excitation functions of some proton induced reactions on natTi for beam monitoring purposes," *Radiochimica Acta,* pp. 795-799, 2009.

[213] P. Kopecky, F. Szelecsényi, T. Molnár, P. Mikecz and F. Tárkányi, "Excitation functions of (p, xn) reactions on ^{nat}Ti: Monitoring of bombarding proton beams," *Applied Radiation and Isotopes,* vol. 44, pp. 687-692, 1993.

[214] S. Holländer and D. Birk, "Pancreatic Cancer Within the Uncinate Process," in *The Pancreas: An Integrated Textbook of Basic Science, Medicine, and Surgery, Third Edition*, 2018, pp. 724-727.

[215] L. Bodei, J. A. Chan, G. El-Haddad, N. Fidelman, P. L. Kunz, J. Mailman, Y. Menda, D. C. Metz, E. S. Mittra, D. A. Pryma, D. L. Reidy-Lagunes, S. Singh and J. R. Strosberg, "NANETS/SNMMI Consensus Statement on Patient Selection and Appropriate Use of 177Lu-DOTATATE Peptide Receptor Radionuclide Therapy," *Journal of Nuclear Medicine,* vol. 61, no. 2, pp. 222-227, 2020.

[216] J. T. Routti, "SAMPO, a Fortran IV program for computer analysis of gamma spectra from Ge (Li) detectors, and for other spectra with peaks," *Lawrence Berkley National Laboratory,* 1969.